

**COMPREHENSIVE MODELLING AND ITS APPLICATION TO
SIMULATION OF FLUIDIZED-BED REACTORS FOR
EFFICIENT PRODUCTION OF HYDROGEN AND OTHER
HYDROCARBON PROCESSES**

by

Andrés Mahecha-Botero

B.Sc., Universidad Pontificia Bolivariana, Medellín, Colombia, 2003

A THESIS SUBMITTED IN PARTIAL FULFILLMENT OF THE
REQUIREMENTS FOR THE DEGREE OF

DOCTOR OF PHILOSOPHY

in

The Faculty of Graduate Studies

(Chemical and Biological Engineering)

THE UNIVERSITY OF BRITISH COLUMBIA
(Vancouver)

March 2009

© Andrés Mahecha-Botero, 2009

ABSTRACT

A generalized comprehensive model, coupled with experimentation in a pilot reactor, is developed to simulate the performance of fluidized-bed catalytic reactors. The model characterizes multiple phases and regions (low-density phase, high-density phase, staged membranes, freeboard region) in different geometries. It accounts for conventional and balancing interphase transfer, catalytic reaction, solid sorption, change in molar/volumetric flow, temperature and pressure profiles, anisotropic dispersion, hydrodynamic regime variation, catalyst deactivation, energy options, feed distribution along the reactor, selective membranes, fluidization hydrodynamics and dynamic behaviour. It also allows for seamless introduction of features and/or simplifications depending on the system of interest. The literature is comprehensively analyzed, reviewing the most important models proposed since 1952. A systematic algorithm for formulating chemical/biochemical reaction engineering problems is developed for systems of different complexity. Simulations are conducted for specific processes including: 1) steam methane reforming (SMR) for production of ultra-pure hydrogen, 2) oxychlorination of ethylene to ethylene dichloride, 3) partial oxidation of n-butane to maleic anhydride, and 4) partial oxidation of naphthalene to phthalic anhydride.

Special emphasis is dedicated to steam reforming in fluidized-bed membrane reactors comparing their performance under bubbling, turbulent and fast fluidization regimes in a variety of configurations. Bubbling regime simulations predict somewhat less hydrogen production due to the effects of conventional and balancing interphase mass transfer. Overall reactor performance is predicted to be best under turbulent fluidization operation. A concomitant experimental program was performed to collect detailed experimental data in a novel pilot scale prototype reactor operated under SMR and auto-thermal reforming (ATR) conditions, without and with membranes of different areas under diverse operating conditions. Hydrogen permeate purity of up to 99.995+% as well as a pure-H₂-to-methane yield of 2.07 were achieved with only half of the full complement of membrane panels active. A permeate-H₂-to reactor methane feed molar ratio >3 was achieved when all of the membrane panels were installed. The reactor model is tested with no adjustable parameters by comparing predictions against axially distributed concentration in the pilot reactor, leading to reasonable agreement and better understanding of a variety of phenomena.

TABLE OF CONTENTS

ABSTRACT	ii
TABLE OF CONTENTS	iii
LIST OF TABLES	viii
LIST OF FIGURES	x
LIST OF SYMBOLS	xvi
ACKNOWLEDGEMENTS	xxii
DEDICATION	xxiv
CO-AUTHORSHIP STATEMENT	xxv
1. INTRODUCTION	1
1.1. Thesis Overview	1
1.1.1. Research Approach	1
1.1.2. Motivation and Outstanding Issues	2
1.1.3. Research Scope and Objectives	4
1.1.4. Thesis Outline	4
1.2. Comprehensive Model Development	8
1.2.1. Introduction	8
1.2.2. System Theory and Comprehensive Modelling Workflow	8
1.2.2.1. <i>System characterization</i>	9
1.2.2.2. <i>Identification of state variables</i>	9
1.2.2.3. <i>Identification of independent variables</i>	9
1.2.2.4. <i>Model development</i>	9
1.2.2.5. <i>Parameter values (design, operational and physico-chemical)</i>	10
1.2.2.6. <i>Simplifying assumptions</i>	10
1.2.2.7. <i>Simulations and numerical analysis</i>	10
1.2.2.8. <i>Model validation</i>	11
1.2.3. General Form of Conservation Equations	11
1.2.3.1. <i>Model features</i>	12
1.2.3.2. <i>Mole balance</i>	14
1.2.3.3. <i>Energy balance</i>	19
1.2.3.4. <i>Pressure balance</i>	23
1.2.3.5. <i>Boundary and initial conditions</i>	24
1.2.4. Model Reduction and Simplification	26
1.2.5. Simulation Tools	26
1.2.5.1. <i>Software and codes</i>	26
1.2.5.2. <i>Verification of numerical solutions</i>	29
1.2.5.3. <i>Computational resources</i>	30
1.3. References	30
2. MODELLING OF FLUIDIZED-BED CATALYTIC REACTORS: A COMPREHENSIVE REVIEW	33
2.1. Introduction	33
2.2. Previous Fluidized-Bed Reactor Modelling Reviews	34
2.3. Analysis of Fluidized-Bed Catalytic Reactor Models	36
2.4. Discussion and Concluding Remarks	60
2.4.1. Model Comparison	60
2.5. References	61

3. PURE HYDROGEN GENERATION IN FLUIDIZED-BED MEMBRANE REACTOR: EXPERIMENTAL FINDINGS	67
3.1. Introduction	67
3.2. Experimental Studies	69
3.2.1. Operation Modes	69
3.2.1.1. Steam methane reforming (SMR) with external heating:.....	69
3.2.1.2. Autothermal reforming (ATR) with addition of air or oxygen:.....	70
3.2.2. Experimental Equipment.....	70
3.2.3. Pilot Fluidized-Bed Membrane Reactor.....	72
3.2.4. Membranes for Hydrogen Removal.....	73
3.2.5. Catalyst.....	75
3.2.6. Experimental design	76
3.2.7. Gas Sampling	77
3.3. Results and Discussion	78
3.3.1. Overall Reactor Performance.....	78
3.3.3. Influence of Key Operating Parameters.....	80
3.3.3.1. Membrane isothermality.....	80
3.3.3.2. Heat effects.....	81
3.3.3.3. Thermodynamic effect of reactor pressure.....	82
3.3.3.4. Effect of membrane area.....	83
3.3.3.5. Effect of pressure driving force.....	85
3.3.3.6. Effect of air input (SMR vs ATR)	87
3.3.3.7. Effect of air split	87
3.3.3.8. Gas backmixing	88
3.3.3.9. Effect of feed rates.....	89
3.4. Conclusions.....	91
3.5. References.....	91
4. PURE HYDROGEN GENERATION IN FLUIDIZED-BED MEMBRANE REACTOR: APPLICATION OF GENERALIZED COMPREHENSIVE MODEL	96
4.1. Introduction	96
4.2. Model Implementation	96
4.2.1. Mole Balance Equations for the Two Phases	98
4.2.2. Energy Balance	99
4.2.2.1. Preliminary heat studies:.....	99
4.2.2.2. Simplified temperature profiles:.....	100
4.2.3. Pressure Balance.....	101
4.2.4. Selective Removal of Species via Membranes.....	102
4.2.5. Equi-molar Interphase Mass Transfer	102
4.2.6. Interphase Balancing Mass Transfer.....	103
4.2.7. Variation in Volumetric Flowrate Due to Expansion/Compression and Changes in Total Molar Flows	105
4.2.8. Feed Distribution along the Reactor	106
4.2.9. Boundary Conditions	108
4.2.10. Calculation of Reactor Parameters.....	109
4.2.10.1. Mass transfer coefficients.....	111
4.2.10.2. Bed volume fractions profiles.....	113
4.2.10.3. Velocity profiles	114
4.2.10.4. Bed expansion and freeboard.....	114

4.2.10.5. Voidage profiles	115
4.2.10.6. Heat dispersion:	116
4.2.10.7. Gas dispersion:.....	117
4.3. Reacting System and Kinetics.....	117
4.4. Concentration Profiles and Reactor Performance	119
4.4.1. Differences between Model Predictions and Experimental Measurements.....	131
4.5. Conclusions.....	131
4.6. References.....	133
5. COMPARISON OF FLUIDIZED-BED FLOW REGIMES FOR STEAM METHANE REFORMING IN MEMBRANE REACTORS	137
5.1. Introduction	137
5.1.1. Steam Methane Reforming.....	138
5.1.2. Fluidized-Bed Membrane Reformers	139
5.2. Description of Reactor Models	140
5.2.1. Single-Stage Equilibrium Model (Model 1).....	144
5.2.2. Plug Flow Reactor Model with Complete Conversion Regenerator (Model 2)	145
5.2.4. Generic Reactor Model (Model 3).....	148
5.3. Flow Regimes of Fluidization	148
5.3.1. Introduction	148
5.3.2. Simulations and Discussion.....	148
5.3.2.1. Plug flow reactor model with complete conversion regenerator (Model 2) ...	151
5.3.2.3 Generic reactor model (Model 3)	154
5.4. Other Factors Affecting Choice of Flow Regime	162
5.5. Conclusions.....	163
5.6. References.....	164
6. OTHER CONFIGURATIONS FOR STEAM REFORMING	169
6.1. Introduction	169
6.2. Sorbent-Enhanced/Membrane-Assisted Steam-Methane Reforming	170
6.2.1. Predictions and Discussion.....	171
6.3. 2-D Modelling of a Fast Fluidization Reactor	177
6.3.1. Model Implementation	177
6.3.2. Discussion	179
6.3.2.1. Membrane gas removal via sweep gas.	179
6.3.2.2. Membrane removal via vacuum.	184
6.4. Conclusions.....	184
6.5. References.....	188
7. MODELLING OF OXY-CHLORINATION FLUIDIZED-BED REACTOR FOR PRODUCTION OF ETHYLENE DICHLORIDE	189
7.1. Introduction	189
7.2 Overview of the PVC Production Process	189
7.2.1. Byproducts	190
7.2.2. PVC	191
7.3. Application of Model to an Oxychlorination Fluidized-Bed Reactor	191
7.3.1. Model Implementation	191
7.3.2. Reaction Pathways and Kinetics	192
7.3.2.1. Estimation of proprietary kinetic parameters.....	193

7.4. Results and Discussion	193
7.5. Conclusions.....	199
7.6. References.....	199
8. TIME-SCALE ANALYSIS OF MALEIC ANHYDRIDE FLUIDIZED-BED CATALYTIC REACTOR BASED ON DYNAMIC MODEL	201
8.1. Introduction	201
8.2. Application to an Industrial MA Fluidized-Bed Reactor	201
8.2.1. Reaction Kinetics	202
8.2.2. Proposed Stoichiometry	203
8.2.3. Implementation of General Model	203
8.3. Results and Discussion	204
8.3.1. Mass Transfer/Reaction Time Scale	204
8.3.2. Heat Transfer Time Scale	205
8.4. Conclusions.....	207
8.5. References.....	207
9. FLUIDIZED-BED REACTOR FOR PRODUCTION OF PHTHALIC ANHYDRIDE	209
9.1. Introduction	209
9.2. Reaction Kinetics	209
9.3. Results and Discussion	211
9.4. Conclusions.....	215
9.5. References.....	215
10. GLOBAL DISCUSSION, CONCLUSIONS AND RECOMMENDATIONS FOR FUTURE WORK.....	216
10.1. Global Discussion.....	216
10.2. Conclusions.....	218
10.3. Outlook and Recommendations for Future Work	219
10.3.1. Modelling.....	219
10.3.2. Future of Reactor Modelling	220
10.3.3. Experimental Set-up.....	221
10.3.4. Future of Reforming Technologies	222
10.4. References.....	222
APPENDIX A. NUMERICAL SOLVERS	224
A.1. Introduction.....	224
A.2. Solution of Systems of Ordinary Differential Equations (ODEs)	224
A.3. Solution of Systems of Partial Differential Equations (PDEs).....	225
A.4. Conclusions.....	226
A.5. References.....	226
APPENDIX B. PRESSURE VESSEL CALCULATIONS FOR FLUIDIZED-BED MEMBRANE REACTOR	228
B.1. Introduction.....	228
B.2. Calculations	228
B.2.1. Wall Thickness	228
<i>B.2.1.1. Effect of temperature</i>	<i>232</i>
B.2.2. Distance Between Bolts.....	234
B.2.3. Number of Bolts	235

B.2.4. Bolt Size.....	235
B.3 Notation.....	236
B.4. Conclusions	236
B.5. References	237
APPENDIX C. COMMISSIONING OF FLUIDIZED-BED MEMBRANE REACTOR	238
C.1. Introduction.....	238
C.2. Cold Commissioning.....	238
C.3. Hot Commissioning	239
C.4. Start-Up and Experimental Runs.....	239
C.5. Conclusion	239
APPENDIX D. DETAILS OF PILOT FLUIDIZED-BED MEMBRANE REACTOR.	240
D.1. Overview	240
APPENDIX E. EFFECT OF AIR SPLIT IN A MULTI-STAGE MODEL WITH INTERNAL RECYCLE.....	250
E.1. Introduction.....	250
E.2. Results and Discussion.....	250
E.3. Conclusions	258
E.4. References	258
APPENDIX F. DESIGN OF A SOLIDS CIRCULATION LOOP FOR A REFORMER- CALCINER SYSTEM	259
F.1. Introduction	259
F.2. Practical Considerations.....	259
F.3. Conclusions	261
F.4. References	263
APPENDIX G. A COMPREHENSIVE APPROACH TO REACTION ENGINEERING	264
G.1. Introduction	264
G.2. Generalized Governing Equations for Reaction Engineering.....	264
G.2.1. Lumped Systems (Continuous Stirred Tank Reactors, Stirred Batch and Semi- Batch Reactors).....	265
G.2.1.1. Mole balance.....	265
G.2.1.2. Energy balance	267
G.2.1.3. Initial conditions	269
G.2.1.4. Simplifications	270
G.2.2. Distributed Systems (Plug Flow Reactors, Packed Beds, Fluidized-Beds, etc)	271
G.2.2.1. Mole balance	271
G.2.2.2. Energy balance	273
G.2.2.3. Initial and boundary conditions	275
G.2.2.4. Simplifications	275
G.2.3. Additional Relations	276
G.2.4. Summary of Mechanistic Modeling Algorithm for Reaction Engineering Systems	278
G.4. Conclusions	278
G.5. References	279
APPENDIX H. PUBLICATIONS	280

LIST OF TABLES

Table 1-1. Typical boundary and initial conditions.....	25
Table 1-2. Computers used for case studies.	30
Table 2-1. Common model assumptions. Table 2-2 shows how these assumptions apply to specific models.....	37
Table 2-2. Summary of fluidized-bed models. A to Z below refer to Table 2-1 characteristics.	40
Table 2-3. Summary of conservation equations for selected models.	46
Table 3-1. Controlled parameters for experimental program.....	72
Table 3-2. Experimental conditions. (All experiments were carried out at 550°C with a steam-to-carbon molar ratio of 3.0).	77
Table 3-3. Justification of selected operating conditions.	77
Table 3-4. Typical feed natural gas analysis.	79
Table 3-5. Experimental results.	79
Table 3-6. Typical reactor gas composition (dry basis). Samples taken at central membrane level.	79
Table 4-1. Model reduction and simplification of conservation equations.	97
Table 4-2. Reaction and kinetics for methane steam reforming/oxidative reforming. See Table 4-3 for parameter values.	118
Table 4-3. List of kinetic parameters.	119
Table 5-1. Summary of reactor models.....	142
Table 5-2. Reaction kinetics applied to membrane reformer.....	146
Table 5-3. Steady state equations for Model 2.	147
Table 5-4. Base values for reactor comparison.	148
Table 5-5. Comparison of simulation results for base case (as specified in Table 5.4) for different models.	149
Table 5-6. Parameters for different fluidization flow regimes.	150
Table 5-7. Configurations for reactor simulations.	150
Table 6-1. Basis for kinetic reactor simulation	171
Table 7-1. Reactor parameters.	192
Table 8-1. Key reactor parameters.	202
Table 8-2. Maleic anhydride kinetic parameters from Centi <i>et al.</i> (1985).	203
Table 9-1. Key reactor parameters.	210
Table 9-2. Kinetic parameters from Johnsson <i>et al.</i> (1987)	211

Appendix A.

Table A. 1. COMSOL Multiphysics PDE solvers. Adapted from (COMSOL, 2006). 226

**Table A. 2. COMSOL Multiphysics linear system solvers. Adapted from (COMSOL, 2006).
..... 226**

Appendix C.

Table C. 1. Cold commissioning test procedure..... 238

Table C. 2. Hot commissioning test procedure 239

Appendix E.

Table E. 1. Simulation conditions..... 251

Table E. 2. Simulation conditions for different cases..... 251

Table E. 3. Case 1 Simulation results. Input and output streams..... 252

Table E. 4. Case 1 Simulation results. Permeation zones..... 253

Table E. 5. Case 2 Simulation results. Input and output streams..... 254

Table E. 6. Case 2 Simulation results. Permeation zones..... 255

Table E. 7. Case 3 Simulation results. Input and output streams..... 256

Table E. 8. Case 3 Simulation results. Permeation zones..... 257

LIST OF FIGURES

Figure 1.1. Comprehensive modeling iterative process.....	12
Figure 1.2. Two pseudo-phase reactor model schematics.	15
Figure 1.3. Differential control volume for derivation of conservation equations.	16
Figure 1.4. Schematic representation of Matlab code levels.....	27
Figure 1.5. Schematic representation of the developed program.....	28
Figure 2.1. Fluidization regimes. (A) Packed bed; (B) Homogeneous / Bubble-free expansion (only for group A particles); (C) Bubbling fluidization regime; (D) Slugging fluidization regime (only in small scale vessels); (E) Turbulent fluidization regime; (F) Fast fluidization regime; (G) Dense suspension upflow (only for large solids carrying rates) (H) Pneumatic conveying. U = Superficial gas velocity; U_{mf} = Minimum fluidization velocity; U_{mb} = Minimum bubbling velocity; U_c = Velocity of transition from bubbling to turbulent fluidization regime; U_{se} = Velocity of transition from turbulent to fast fluidization regime / significant entrainment.	51
Figure 3.1. Experimental setup schematic drawing. ROG = reactor off-gas.	71
Figure 3.2. Reactor configuration.	75
Figure 3.3. Palladium membrane details.....	76
Figure 3.4. Temperature vs height for experiments 4 to 8. Membrane isothermality. For experimental conditions, see Table 3.2.	81
Figure 3.5. Methane conversion and temperature vs height for typical ATR operation (experiment 10). For experimental conditions, see Table 3.2.	82
Figure 3.6. Methane conversion vs height for Experiments 1 (650 kPa) and 2.....	83
Figure 3.7. Methane conversion vs height for experiments 6 (3 membranes) and 2 (no membranes). Effect of membrane area during SMR operation. For experimental conditions, see Table 3.2.....	84
Figure 3.8. Methane conversion and dry H ₂ molar fraction inside the reactor vs height for experiments 11 (6 membranes) and 3 (no membranes). Effect of membrane area during ATR operation. For experimental conditions, see Table 3.2.....	85
Figure 3.9. Hydrogen production vs reactor pressure and permeate pressure. (Experiments 4, 5 and 6). Effect of pressure driving force on hydrogen removal. For experimental conditions, see Table 3.2.....	86
Figure 3.10. Effect of reactor pressure on methane conversion vs height. For experimental conditions, see Table 3.2, for Experiments 5 and 6.....	86
Figure 3.11. Methane conversion and temperature vs reactor height for experiments 2 (SMR) and 3 (ATR). Effect of oxygen input. For experimental conditions, see Table 3.2.	87
Figure 3.12. Effect of air distribution on methane conversion vs height. For experimental conditions, see Table 3.2, Experiments 10 and 11.....	88

Figure 3.13. Nitrogen concentration vs height for experiments 10 (50% air at top), 11 (25% air at top) and 12 (10.4% air at top). Gas backmixing. For experimental conditions see Table 3.2.	89
Figure 3.14. Effect of methane feed rate on axial methane conversion. For experimental conditions, see Table 3.2, Experiments 11 and 12.....	90
Figure 3.15. Yield of hydrogen, i.e. molar ratio of H₂ permeation rate divided by methane feed rate, as a function of methane feed rate for operation at 900 kPa(g), for 3 and 6 membranes, SMR and ATR operation. For experimental conditions see Table 3.2....	90
Figure 4.1. Simulated 2-D adiabatic temperature profile.	100
Figure 4.2. Simulated reactor pressure drop vs height (Experiment 10). For experimental/simulation parameters see Table 3.2.	101
Figure 4.3. Simulated volumetric flow rates vs height (Experiment 10). For experimental/simulation parameters see Table 3.2.	106
Figure 4.4. a) Simulated impulse Dirac function and molar flow rate of inerts vs height (Experiment 10, 50% air at top). b) Enlargement of a) at the top air distributor section (z=1.45 to z=1.6). For experimental/simulation parameters see Table 3.2.....	107
Figure 4.5. Regime mapping for the FBMR experiments. Simulated probability distribution for bubbling, turbulent and fast fluidization flow regimes vs superficial gas velocity.....	110
Figure 4.6. Simulated species diffusivity vs height. (Experiment 10). For experimental/simulation parameters see Table 3.2.	112
Figure 4.7. Methane conversion and two-phase species concentrations vs height. (Experiment 1). a) Overall methane conversion. b) Dry hydrogen concentration. c) Dry methane concentration. d) Dry carbon dioxide concentration. Points indicate experimental measurements. Lines show model predictions. For experimental/simulation parameters see Table 3.2.	121
Figure 4.8. Methane conversion and two-phase species concentrations vs height. (Experiment 3). a) Overall methane conversion. b) Dry hydrogen concentration. c) Dry methane concentration. d) Dry carbon dioxide concentration. Points indicate experimental measurements. Lines show model predictions. For experimental/simulation parameters see Table 3.2.	122
Figure 4.9. Methane conversion and two-phase species concentrations vs height. (Experiment 6). a) Overall methane conversion. b) Dry hydrogen concentration. c) Dry methane concentration. d) Dry carbon dioxide concentration. Points indicate experimental measurements. Lines show model predictions. For experimental/simulation parameters see Table 3.2.	123
Figure 4.10. Methane conversion and two-phase species concentrations vs height. (Experiment 10). a) Overall methane conversion. b) Dry hydrogen concentration. c) Dry methane concentration. d) Dry carbon dioxide concentration. Points indicate experimental measurements. Lines show model predictions. For experimental/simulation parameters see Table 3.2.	124
Figure 4.11. Methane conversion and two-phase species concentrations vs height. (Experiment 11). a) Overall methane conversion. b) Dry hydrogen concentration. c)	

Dry methane concentration. d) Dry carbon dioxide concentration. Points indicate experimental measurements. Lines show model predictions. For experimental/simulation parameters see Table 3.2.	125
Figure 4.12. Methane conversion and two-phase species concentrations vs height. (Experiment 12). a) Overall methane conversion. b) Dry hydrogen concentration. c) Dry methane concentration. d) Dry carbon dioxide concentration. Points indicate experimental measurements. Lines show model predictions. For experimental/simulation parameters see Table 3.2.	126
Figure 4.13. Two-phase species concentrations vs height. (Experiment 11). a) Dry carbon monoxide. b) Dry nitrogen. c) Dry oxygen. d) Steam concentration. Points indicate experimental measurements. For experimental/simulation parameters see Table 3.2.	127
Figure 4.14. Two-phase species concentrations vs height. (Experiment 12). a) Dry carbon monoxide. b) Dry nitrogen. c) Dry oxygen. d) Steam concentration. Points indicate experimental measurements. For experimental/simulation parameters see Table 3.2.	128
Figure 4.15. Pure hydrogen production vs height. (Experiments 5, 7, 13 and 14). For experimental/simulation parameters see Table 3.2.	130
Figure 5.1. a) Comparison of pure hydrogen production rates and b) methane conversion for different membrane thicknesses, different permeation area per unit volume of reactor and for different fluidization flow regimes based on Model 2 for fast fluidization. For conditions see Tables 5.6 and 5.7.	152
Figure 5.2. Predicted profiles of key variables for base case (i.e. configuration 2). Simulations using Model 2 for fast fluidization. For conditions see Tables 5.6 and 5.7.	153
Figure 5.3. Predicted profiles of species molar flow-rates for base case (i.e. configuration 2). Simulations using Model 2 under fast fluidization. For conditions see Tables 5.6 and 5.7.	153
Figure 5.4. Comparison of pure hydrogen production rates for different membrane thicknesses and different permeation area per unit volume of reactor. (a) Bubbling fluidization regime, (b) Turbulent fluidization regime, (c) Fast fluidization regime. Simulations using Model 3. For conditions see Tables 5.6 and 5.7.	155
Figure 5.5. Comparison of methane conversion for different flow regimes: bubbling (blue), turbulent.(black) and fast fluidization (red). (a) Configuration 1 (50μm, 200m^2/m^3), (b) Configuration 2 (25μm, 200m^2/m^3), (c) Configuration 3 (3μm, 200m^2/m^3). Simulations using Model 3. For conditions see Tables 5.6 and 5.7.	156
Figure 5.6. Comparison of methane conversion for different flow regimes: bubbling (blue), turbulent.(black) and fast fluidization (red). (a) Configuration 4 (5μm, 200m^2/m^3), (b) Configuration 5 (1μm, 200m^2/m^3), (c) Configuration 6 (25μm, 1000m^2/m^3). Simulations using Model 3. For conditions see Tables 5.6 and 5.7.	157
Figure 5.7. Comparison of CH₄ and H₂O concentrations in the high and low density pseudo-phases for different flow regimes (base case). (a) bubbling regime, (b) turbulent regime, (c) fast fluidization regime. Simulations using Model 3. For conditions see Tables 5.6 and 5.7.	158

Figure 5.8. Comparison of H₂ and CO₂ concentrations in the high and low density pseudo-phases for different flow regimes (base case). (a) bubbling regime, (b) turbulent regime, (c) fast fluidization regime. Simulations using Model 3. For conditions see Tables 5.6 and 5.7.	159
Figure 5.9. Comparison of CO and O₂ concentrations in the high and low density pseudo-phases for different flow regimes (base case). (a) bubbling regime, (b) turbulent regime, (c) fast fluidization regime. Simulations using Model 3. For conditions see Tables 5.6 and 5.7.	160
Figure 6.1. Effect of CO₂ capture on reformer performance. For conditions, see Table 6.1. (a.) Isothermal methane conversion; (b.) Isothermal CO₂ yield in the reformer; (c.) Isothermal CO₂ yield in the regenerator; (d.) Isothermal CaO conversion.....	173
Figure 6.2. Effect of CO₂ capture on reformer performance. For conditions, see Table 6.1. (a.) Isothermal pure hydrogen production rate; (b.) Isothermal fraction of hydrogen removed by membranes; (c.) Non-isothermal reformer temperature. (d.) Non-isothermal heat supply rate from CO₂ capture. The parameter “b” is the ratio of CaO sorbent to total solids.....	175
Figure 6.3. Effect of CO₂ capture on reformer performance. For conditions, see Table 6.1. (a.) Non-isothermal methane conversion; (b.) Non-isothermal CO₂ yield in the reformer; (c.) Non-isothermal CaO conversion. (d.) Non-isothermal fraction of hydrogen removed by membranes. The parameter “b” is the ratio of CaO sorbent to total solids.....	176
Figure 6.4. Reactor cross-section (Not to scale).	177
Figure 6.5. Membrane reactor (Not to scale). Note that the zx-plane is adopted as the plane of symmetry.....	179
Figure 6.6. 2-D H₂ concentration profile using sweep gas (Geometry not to scale).....	181
Figure 6.7. 2-D local conversion profile using sweep gas (Geometry not to scale).	181
Figure 6.8. Predicted local axial and radial H₂ concentration profiles using sweep gas. (a.) Axial H₂ concentration profile. H₂ concentration vs height (at y = 0 m). (b.) Horizontal H₂ concentration profile. H₂ concentration vs horizontal distance (at z = 1.5 m). (c.) Axial H₂ concentration profile. H₂ concentration vs height (at y = 20 mm).....	182
Figure 6.9. Predicted local axial and radial conversion profiles using sweep gas. (a.) Axial conversion profile. Conversion vs height (at y = 0 m). (b.) Horizontal conversion profile. Conversion vs horizontal distance (at z = 1.5 m).	183
Figure 6.10. 2-D H₂ concentration profile using vacuum (Geometry not to scale).....	185
Figure 6.11. 2-D local conversion profile using vacuum (Geometry not to scale).	185
Figure 6.12. Predicted local axial and radial H₂ concentration profiles using vacuum. (a.) Axial H₂ concentration profile. H₂ concentration vs height (at y = 0 m). (b.) Horizontal H₂ concentration profile. H₂ concentration vs horizontal distance (at z = 1.5 m). (c.) Axial H₂ concentration profile. H₂ concentration vs height (at y = 20 mm).....	186
Figure 6.13. Predicted local axial and radial conversion profiles using vacuum. (a.) Axial conversion profile. Conversion vs height (at y = 0 m). (b.) Horizontal conversion profile. Conversion vs horizontal distance (at z = 1.5 m).	187

Figure 7.1. Predicted steady-state ETY molar flows in the high- and low-density pseudo-phases vs height in the reactor. For operating conditions see Table 7.1. Values are normalized by their maximum value.	194
Figure 7.2. Predicted steady-state HCl molar flows in the high- and low-density pseudo-phases vs height. For conditions see Table 7.1. Values are normalized by their maximum value.	194
Figure 7.3. Predicted steady-state oxygen molar flows in the high- and low-density pseudo-phases vs height. For operating conditions see Table 7.1. Values are normalized by their maximum value.	195
Figure 7.4. Predicted steady-state EDC molar flows in the high- and low-density pseudo-phases vs height. For operating conditions see Table 7.1. Values are normalized by their maximum value.	195
Figure 7.5. Predicted steady-state H₂O molar flows in the high- and low-density pseudo-phases vs height. For operating conditions see Table 7.1. Values are normalized by their maximum value.	196
Figure 7.6. Predicted steady-state CO_x molar flows in the high- and low-density pseudo-phases vs height. For operating conditions see Table 7.1. Values are normalized by their maximum value.	196
Figure 7.7. Predicted steady-state impurity molar flows in the high- and low-density pseudo-phases vs height. For operating conditions see Table 7.1. Values are normalized by their maximum value.	197
Figure 7.8. Pressure vs reactor height. For conditions see Table 7.1. Values are normalized by their maximum value.	197
Figure 7.9. Predicted axial profile of steady-state overall ETY conversion. For operating conditions see Table 7.1. Values are normalized by their maximum value.	198
Figure 8.1. Conversion vs Height [m] for different times (one profile every 0.5 s).	205
Figure 8.2. Reactor temperature vs height for different times (profiles at: t = 0 s, t = 1 s, t = 2 s, t = 5 s, t = 10 s, t = 1,000 s and t = 150,000 s).	206
Figure 8.3. Reactor shell temperature vs height at different times (one profile every 3,000 s).	206
Figure 9.1. Molar flows in the low and high density phases vs reactor height for phthalic anhydride process in fluidized bed reactor. For reactor size and operating conditions, see (Johnsson <i>et al.</i>, 1987): (a) Molar flows of naphthalene and phthalic anhydride. (b) Molar flows of maleic anhydride and naphthoquinone.	212
Figure 9.2. Species concentrations in the low and high density phases vs reactor height for phthalic anhydride process in fluidized bed reactor. For reactor size and operating conditions, see (Johnsson <i>et al.</i>, 1987): (a) Concentrations of naphthalene and phthalic anhydride. (b) Concentrations of maleic anhydride and naphthoquinone.	213
Figure 9.3. Conversion, yield and pressure vs reactor height. For reactor size and operating conditions, see (Johnsson <i>et al.</i>, 1987).	214
Appendix A.	

Figure A. 1. Example of a three-dimensional mesh created using COMSOL Multiphysics.	225
Appendix B.	
Figure B. 1. Schematic representation of FBMR flange.	229
Figure B. 2. Schematic representation of the pressure force acting on the reactor walls..	230
Figure B. 3. Bending moment on reactor walls.....	231
Figure B. 4. Tensile strength vs temperature for stainless steel. (The orange line is the maximum temperature tolerable by the H₂ membranes).	233
Figure B. 5. Required wall thickness vs temperature for stainless steel. (The orange line is the maximum temperature tolerable by the H₂ membranes).	233
Appendix D.	
Figure D. 1. Pilot reactor under operation.....	241
Figure D. 2. Fluidized-bed reactor insulation at different stages of the project.....	242
Figure D. 3. Close-up photo of membrane panel.....	243
Figure D. 4. Palladium membrane panel.....	244
Figure D. 5. Side flange supporting two panels.	245
Figure D. 6. Top flange with gas filters and air distributor.....	246
Figure D. 7. Close-up of top air distributor.....	246
Figure D. 8. Placement of external electrical heaters.....	247
Figure D. 9. External heaters above the gas distributor.	247
Figure D. 10. Fluidization catalysts.....	248
Figure D. 11. PID diagram for pilot reactor.	249
Appendix E.	
Figure E. 1. Required membrane area for different configurations. Gibbs reactors in series with 10 permeation zones are used to simulate the fluidized-bed membrane reformer.	258
Appendix F.	
Figure F. 1. Reformer-calciner system.	260
Figure F. 2. Mapping for J-valve.....	261
Figure F. 3. PID for calciner and solids circulation system.....	262
Appendix G.	
Figure G. 1. Mole and energy fundamental balances for lumped systems.....	265
Figure G. 2. Mole and energy balances for distributed systems.	272

LIST OF SYMBOLS

A	Reactor cross-sectional area, (m ²)
a	Parameter for the numerical calculation of Dirac delta functions, (dimensionless)
A_{eff}	Effective membrane area, (m ²)
$a_{I(n \rightarrow \varphi)}$	Interphase transfer area per unit volume between phases φ and (n), (m ⁻¹)
$a_{j\varphi}$	Catalyst activity (associated with catalyst deactivation), (dimensionless)
A_M	Membrane cross sectional area, (m ²)
A_{Panel}	Membrane panel effective membrane surface area, (m ²)
Ar	Archimedes number, $\rho_{gas} \cdot (\rho_{solids} - \rho_{gas}) \cdot g \cdot \bar{d}_p^3 / \mu^2$, (dimensionless)
a_{SR}	External heat transfer surface area per unit reactor volume, (m ⁻¹)
A_{TM}	Total effective membrane surface area, (m ²)
C	Courant number, (dimensionless)
$C_{eq,i}$	Molar concentration of component i at equilibrium state, (mol/m ³)
$C_{i\varphi}$	Concentration of species i in phase φ , (mol/m ³)
$c_{i\varphi}$	Surface concentration of species i in phase φ , (mol/m ²)
C_k	Concentration of deposited coke on catalyst, (g/gcatalyst)
$C_{pi\varphi}$	Specific heat of species i in phase φ , (J/mol.K)
d_b	Bubble diameter, (m)
$\vec{D}_{i\varphi}$	Vector of diffusion coefficients of species i in phase φ , (m ² /s)
\bar{d}_p	Mean particle diameter, (m)
D_T	Reactor diameter, (m)
$E_{i\varphi}$	Internal energy of species i in phase φ , (J/mol)
$E_{i_{cat},\varphi}$	Internal energy of species i chemisorbed on catalyst surface in phase φ , (J/mol)
$E_{cat,\varphi}$	Internal energy of catalyst in phase φ , (J/kg)
$E_{sorb,\varphi}$	Internal energy of solids sorbent in phase φ , (J/kg)
E_{H_2}	Activation energy for hydrogen permeation, (J/mol)
$E_{i_{sorb},\varphi}$	Internal energy of species i chemisorbed on solids sorbent surface in phase φ , (J/mol)
$E_{sorb,\varphi}$	Internal energy of solid sorbent in phase φ , (J/kg)
$F_{H_2,\varphi}$	Molar flow rate of hydrogen extracted through permselective membranes, (mol/s)
$F_{i\varphi}$	Molar flow rate of species i in phase φ , (mol/s)
$Fines$	Fraction of powder less than 45 μ m, (dimensionless)
$F_{T\varphi}$	Total molar flow rate in phase φ , (mol/s)
f_C	Catalyst chemisorption function, (mol/m ²)
f_S	Solid sorbent chemisorption function, (mol/m ²)

g	Gravitational acceleration, (m/s ²)
G_s	Net solids circulation flux, (kg/m ² s)
G_{so}	Average solids flux under fast fluidization conditions, (kg/m ² s)
h_{Cool}	Cooling heat transfer coefficient, (W.m ⁻² .K ⁻¹)
ΔH^0	Enthalpy change, (J/mol)
ΔH_C^0	Heat of combustion, (J/mol)
h_{Surf}	Surface-to-bed heat transfer coefficient, (W.m ⁻² .K ⁻¹)
$h_{heaters}$	Surroundings-to-reactor surface heat transfer coefficient, (W.m ⁻² .K ⁻¹)
$H_{i\varphi}$	Enthalpy of species i in phase φ , (J/mol)
ΔH_j	Heat of reaction j , (J/mol)
$J_{H_2,\varphi}$	Membrane flux of hydrogen, (mol.m ⁻² .s ⁻¹)
$J_{i\varphi}$	Permeation flux of component i in phase φ , (mol m ⁻² s ⁻¹)
k	Reaction rate constant, (various units)
\vec{K}	Vector of heat diffusion coefficients in phase φ , (J.s ⁻¹ . m ⁻¹ .K ⁻¹)
$k_{c_{i,(n\rightarrow\varphi)}}$	Interphase mass transfer coefficient of component i , (m/s)
k_{H_2}	Membrane pre-exponential factor, (mol.m ⁻¹ .s ⁻¹ .Pa ^{-0.5})
m	Parameter for modified two-phase theory, (dimensionless)
M_s	Solids inventory, (kg)
MW_i	Molecular weight of species i , (g/mol)
N_C	Total number of species in phase φ , (dimensionless)
N_{CM}	Total number of chemical species inside membrane panel, (dimensionless)
$\vec{N}_{i\varphi}$	Vector of dispersive molar fluxes of species i in phase φ , (mol/m ² .s)
N_I	Number of inputs to pseudo-phase φ , (dimensionless)
N_o	Number of outputs from pseudo-phase φ , (dimensionless)
N_{or}	Number of distributor orifices, (dimensionless)
N_R	Total number of reactions, (dimensionless)
N_φ	Number of phases, (dimensionless)
P_φ	Pressure in phase φ , (Pa)
$P_{H_2,\varphi}$	Partial pressure of hydrogen on reactor side, (kPa)
$P_{H_2,M}$	Partial pressure of hydrogen inside hydrogen permselective membranes, (kPa)
P_i	Partial pressure of component i , (kPa)
P_M	Total permeate pressure, (kPa)
p_M	Membrane perimeter per unit area of reactor cross section, (m/m ²)
P_r	Probability of being in regime r , (dimensionless)
\vec{q}_φ	Vector of dispersive molar fluxes in phase φ , (W/m ²)
\dot{Q}	Rate of heating along the reactor length, (J m ⁻¹ s ⁻¹)
Q_g	Heat generated rate, (J/s)

Q_P	Preheating rate, (J/s)
R	Gas constant, (8.314 J.mol ⁻¹ .K ⁻¹)
Re	Reynolds number, $\rho_{gas} U \bar{d}_p / \mu$, (dimensionless)
$r_{j\varphi}'$	Rate of production by chemical reaction j in phase φ per mass of catalyst, (mol.kg ⁻¹ .s ⁻¹)
$r_{j\varphi}$	Rate of production by chemical reaction j in phase φ , (mol.(m of phase φ) ⁻³ .s ⁻¹)
S	Surface area per unit volume of solids, (m ² /m ³)
$Split_H$	H -phase flow split factor, (dimensionless)
$Split_{top}$	Top flow split factor, (dimensionless)
t	Time, (s)
tp_{H_2}	Total perimeter of hydrogen membranes, (m)
T_φ	Temperature of phase φ , (K)
T_{Cool}	Coolant temperature, (K)
$T_{heaters}$	Temperature of heaters, (K)
T_M	Membrane temperature, (K)
T_{SUR}	Surroundings temperature, (K)
T_{Surf}	Reactor surface temperature, (K)
T_∞	Ambient air temperature, (K)
U	Superficial gas velocity, (m/s)
U^*	Dimensionless superficial gas velocity, $U \left(\frac{\rho_g^2}{\mu g (\rho_p - \rho_g)} \right)^{1/3}$, (dimensionless)
\vec{U}_φ	Vector of convective velocities of the catalyst in phase φ , (m/s)
u_{br}	Bubble rise velocity, (m/s)
U_c	Transition velocity from bubbling to turbulent fluidization, (m/s)
U_{DSU}	Onset of dense suspension upflow, (m/s)
U_{mb}	Minimum bubbling velocity, (m/s)
U_{mf}	Minimum fluidization velocity, (m/s)
U_{se}	Transition gas superficial velocity to fast fluidization regime, corresponding to significant solids entrainment, (m/s)
$v_{Bulk_{(H \rightarrow L)}}''''$	Volumetric flow rate convectively transferred from (H)-phase to (L)-phase per unit volume of phase, (1/s).
$v_{Bulk_{(L \rightarrow H)}}''''$	Volumetric flow rate convectively transferred from (L)-phase to (H)-phase per unit volume of phase, (1/s).
v_c	Normalized transition velocity from bubbling to turbulent fluidization, (dimensionless)
v_M	Membrane volumetric flow rate, (m ³ /s)
v_{se}	Normalized transition velocity to fast fluidization regime, corresponding to significant solids entrainment, (dimensionless)
$v_{Solids(\varphi)}$	Volumetric flow rate of solids in pseudo-phase φ , (m ³ /s)
v_{VB}	Visible bubble flow, (m ³ /s)
v_φ	Volumetric flow rate of phase φ , (m ³ /s)

ΔV	Differential volume, (m^3)
W	Catalyst mass, (Kg)
\dot{W}_s	Rate of work done by system on the surroundings, (W)
x, y, z	Cartesian coordinates, with z vertical, (m)
X_i	Conversion of component i , (dimensionless)
Y	Parameter for modified two-phase theory, (dimensionless)
Y_i	Mole fraction of component i in gas phase, (dimensionless)
z_d	Expanded dense bed height, (m)
z_R	Total reactor height, (m)
z_{Top}	Height of top air distributor, (m)
ΔZ	Integration step-size, (m)

Greek Letters

α_φ	Volume of solid sorbent per unit of total solids, $\left(\frac{m^3_{sorb_\varphi}}{m^3_{cat_\varphi+sorb_\varphi}} \right)$, (dimensionless)
$(1 - \alpha_\varphi)$	Volume of catalyst per unit of total solids, $\left(\frac{m^3_{cat_\varphi}}{m^3_{cat_\varphi+sorb_\varphi}} \right)$, (dimensionless)
α_c	Deactivation constant, (gcatalyst/gcoke)
α_m	Heat balance control indexes (dimensionless, may be 0 or 1)
β	Parameter in logistic regression function, (dimensionless)
β_m	Mole balance control indexes (dimensionless, may be 0 or 1)
Δ_{H_2}	Thickness of hydrogen membranes, (m)
δ	Dirac delta, (dimensionless)
ε_φ	Voidage in phase φ , $\left(\frac{m^3_{gas_\varphi}}{m^3_\varphi} \right)$, (dimensionless).
ε^*	$(1 - \phi^*)$, (dimensionless).
$(1 - \varepsilon_\varphi)$	Solids holdup in phase φ , $\left(\frac{m^3_{solids_\varphi}}{m^3_\varphi} \right)$, (dimensionless).
ε_M	Surface emissivity, (dimensionless)
$\hat{\theta}$	Averaged value of the operating conditions and physical properties
θ_r	Operating conditions and physical properties
μ	Viscosity, (kg/m.s)
π	Circumference/Diameter ratio of a circle, (dimensionless)
ρ	Density, (kg/m^3)
σ	Boltzmann constant, ($W/m^2.K^4$)

σ_c	Standard deviation of uncertainty in critical regime boundary correlation, (m/s)
σ_{se}	Standard deviation of uncertainty in significant entrainment regime boundary correlation, (m/s)
τ	Gap width between flat surfaces, (m)
ν_{ij}	Stoichiometric coefficient of species i in reaction j , (dimensionless)
ϕ	Solids volume fraction, (dimensionless)
ϕ^*	Saturation carrying capacity, (dimensionless)
ψ_ϕ	Volume fraction of phase, $\left(\frac{m_\phi^3}{m_{system}^3} \right)$, (dimensionless)
ψ_{slip}	Slip factor, (dimensionless)
$\Omega_{j\phi}$	Overall effectiveness factor of reaction j in phase, ϕ , (dimensionless)

Subscripts

<i>bubb</i>	Bubbling flow regime
<i>c</i>	Transition from bubbling to turbulent fluidization regime
<i>cat</i>	Catalyst
<i>f</i>	Feed condition
<i>fast</i>	Fast fluidization flow regime
<i>gas</i>	Gas
<i>H</i>	High-density phase
<i>i</i>	Compound i
<i>I</i>	Interphase
<i>in</i>	Input condition
<i>j</i>	Reaction j
<i>L</i>	Low-density phase
<i>max</i>	Maximum
<i>mb</i>	Minimum bubbling
<i>mix</i>	Mixture
<i>mf</i>	Minimum fluidization
<i>n</i>	Phase in contact with phase ϕ
<i>(R)</i>	Reactor shell
<i>T</i>	Total value. For reactor parameters: average between H and L phases
<i>TM</i>	Membrane total value
<i>r</i>	Regime r
<i>se</i>	Transition from turbulent to fast fluidization regime / significant entrainment
<i>solids</i>	Catalyst + sorbent
<i>sorb</i>	Solid sorbent
<i>turb</i>	Turbulent flow regime
x, y, z	x, y and z directions, with z vertical
ϕ	phase ϕ

Abbreviations

< Parameter >	Denotes mean value of the parameter.
ATR	Autothermal reforming
CFB	Circulating fluidized-bed

DEN	DEN term (in SMR kinetics equations)
ET	Energy transfer
EDC	Ethylene dichloride
ETY	Ethylene
FBMR	Fluidized bed membrane reactor
FEM	Finite element method
GB	Gigabyte (1024^3 bytes)
GC	Gas chromatograph
GHz	Gigahertz, (10^9 Hz)
GMRES	Generalised minimum residual solver
H-phase	Dense, particulate, emulsion or continuous phase
IMP	Impurities
L-phase	Bubble, dilute, void or discontinuous phase
MA	Maleic anhydride
MRT	Membrane Reactor Technologies Ltd.
MT	Mass transfer
NA	Naphthalene
NEDO	New Energy and Industrial Technology Development Organization, Japan
NQ	Naphthoquinone
ODE	Ordinary differential equation
PA	Phthalic anhydride
PC	Personal computer
PDE	Partial differential equation
RAM	Random-access memory
ROG	Reactor off-gas
SMR	Steam methane reforming
SPOOLES	Sparse object oriented linear equations solver
TCD	Thermal conductivity detector
UBC	The University of British Columbia
UMFPACK	Unsymmetric multifrontal sparse LU factorization package
Superscripts	
*	Dimensionless variable

ACKNOWLEDGEMENTS

To Dr. John R. Grace – You provided me with opportunities, constant guidance and support during my doctoral studies. Your knowledge, experience and consistency were invaluable when dealing with a variety of challenges.

To Dr. Said S.E.H. Elnashaie – You have been my mentor for so many years and because of you I had the opportunity of doing my Ph.D. Your creative ideas, energy and input were vital in the development of this thesis.

To Dr. C. Jim Lim – Thank you very much for your encouragement, confidence, strategy and practical advice. I am also thankful for your flexibility in the execution of my research and for your support.

Working with the *three* of you has been a privilege because of your personal qualities and values, and I will strive with my future students to be the type of advisor that you have been to me.

To Dr. Jorge Mahecha-Gómez – Thank you for countless things related to every single aspect of my life, which incidentally include valuable advice regarding mathematical modeling and solution of a variety of technical problems.

To Monica N. Danon-Schaffer and Boris Schaffer – Your friendship is probably the most valuable product of my stay in Vancouver. I am grateful to you for your unconditional and consistent support and especially for being a family to me.

To Dr. Tony Boyd – The experience I had working with you was absolutely fantastic. As a result of your effort, the work environment was positive, efficient and quite productive. Thank you for all your teachings, your patience and for being absolutely instrumental during the experimental program at MRT.

To Zhongxiang Chen and Ali Gulamhusein – I acknowledge the important collaboration provided for this thesis.

To Wajeeh O. Moughrabiah – Thank you for being my officemate, for your friendship and timely advice.

To Professors Fabio Castrillón-Hernández, Antonio Quintero, Carlos A. Henao, Fabio Martínez-Uribe and Javier Escobar-Montoya – The instruction I received from you at

Universidad Pontificia Bolivariana during my undergraduate studies gave me a strong foundation for developing the model of this thesis.

To Helsa Leong – I really appreciate your availability, assistance and efficiency starting from my admission process until today.

To my examining committee: Dr. Martha Salcudean, Dr. Xiaotao Bi, Dr. Susan A. Baldwin, Dr. Donald S. Mavinic and Dr. Robert R. Hudgins – I am grateful for your availability and dedication.

To my colleagues and friends: Lucas Bustamante-Valencia, Jorge Juan David Martínez-Arboleda, Heping Cui, Clara Gómez-Henao, Fábio Bentes-Freire, Renaud Escudié, Ramn Toor, Celia Sobrino-Fernández, Kim Johnsen, Ibrahim Abba, Siamak Elyasi, Adnan Al-Muttahar, Nicholas Comyn, Anwu Li, Hongbo Jiang, Maxime Foucault, Isaias Ochoa, Omar Delgadillo-Velázquez, Raymond Alava, Sophie Pantin, Miguel A. Portillo-Ceballos, Siva Sarathy, Alexandre Vigneault, Graham Liebelt, Doug Yuen, Richard Ryoo, Darcy Westfall, Max Read and Hank Yu – Thank you for your support and many useful discussions during different stages of my studies.

I am also grateful to the *Cordula and Gunter Paetzold Fellowship* and *UGF fellowships* at the *University of British Columbia* for providing funding for this project.

This thesis is dedicated to Laura, who offered me unconditional love during this endeavour. It is also dedicated to Clara, Jorge and Eduardo, for being a constant source of inspiration, guidance, support, care and encouragement.

CO-AUTHORSHIP STATEMENT

This is a manuscript-based thesis. Chapters 2, 3, 4, 5, 7, 8, 9 as well as section 6.2 are independent manuscripts that are either published papers in peer-reviewed journals/international conference proceedings or manuscripts prepared for publication in peer-reviewed journals. I declare that I am the main investigator as well as the corresponding author for all these publications, except for the manuscript briefly presented in Section 6.2, as described in Appendix H. The co-authors listed for each paper have/will assist with final editing of the manuscripts and the use of these papers is under their permission. I also declare that while discussing with my research advisors, my contributions to these manuscripts have consisted of:

- Proposing research work and designing research plan.
- Development of the mechanistic models.
- Setup of workstations as well as coding, debugging and simulation of computer models.
- Operation, proposing commissioning and experimental plan, set-up of distributed concentration measurements for pilot reactor, as well as the collection, interpretation and analysis of all experimental data.
- Preparation and writing of manuscripts (including digital photography and elaboration of figures).

Chapter 3 contains experimental work conducted at *Membrane Reactor Technologies Ltd.* (MRT). The assembling, commissioning, start-up and operation of the pilot scale reactor were performed in collaboration with Dr. Tony Boyd and Ali Gulamhusein.

A single-phase model was run by Dr. Zhongxiang Chen to verify simulations in the fast fluidization regime for Chapter 5.

Section 6.2 contains modelling work elaborated in collaboration with Dr. Zhongxiang Chen.

Appendices E and F include results obtained in collaboration with Dr. Tony Boyd.

1. INTRODUCTION¹

1.1. Thesis Overview

1.1.1. Research Approach

Chemical reactors represent the heart of many industrial processes. The high complexity of fluidized-beds and their number of variables make model development a complicated process, usually requiring coupling with experimentation. Although the ultimate objective of modelling is the prediction of reactor performance for different scales and configurations, scale-up methods tend to be uncertain, typically requiring multiple testing stages from the laboratory scale to final industrial applications.

Modelling is an important tool for describing a large variety of complex systems (Aris, 1978; Haken, 1983; Aris, 1999; Mahecha-Botero *et al.*, 2004, 2005a, b, c; Garhyan *et al.*, 2006). As modelling tools evolve, simulation has become a key player in the creation of new technologies and applications. In the case of industrial fluidized-bed reactors, theoretical modelling turns out to be very attractive given the huge cost, safety concerns and potential for large economic impact on commercial scale processes. For instance, for large petrochemical units, the prevention of one day of reactor shutdown or increase in performance by a fraction of one percent can pay for years of fundamental work. Development of mechanistic models for the design, scale-up, optimization, operation and control of these processes is therefore essential. Furthermore this type of modelling plays an important role in advancing fundamental knowledge of multiphase engineering systems, for example by indicating aspects which require further experimental or theoretical investigation.

¹ *Section 1.1 gives a brief introduction to the thesis and presents the strategy implemented in the modelling and experimental program. Some outstanding issues of the field of study are identified. The scope of work, research objectives and an overview of the main aspects of the remaining chapters are also presented. Section 1.2 compiles the development of the generalized comprehensive model implemented in the thesis. The model is derived in as general a manner as possible explaining all its features and covering all modelling cases presented in the remaining chapters.*

In this thesis a modelling and experimental program were designed to advance the fundamental knowledge of fluidized-beds reactors. Both programs were carefully defined following the general workflow, so they can be seamlessly linked to investigate several phenomena of gas solids fluidized-bed reactors. A comprehensive model is developed to describe fluidized-bed catalytic reactors using fewer simplifying assumptions than previously reported in the literature. The model is general enough that it can deal with a wide spectrum of systems, while special attention is given to non-conventional fluidized-bed membrane reactors (FBMRs).

Simulations are carried out using different versions of the model, with varying degrees of sophistication according to the system of study and stage of model development. The modelling work was performed at the *Chemical and Biological Engineering Department* of the *University of British Columbia* in contact with chemical companies such as *LG Chemical Ltd.* of Korea for studies on oxychlorination of ethylene to ethylene dichloride, and *Tokyo Gas Co.* of Japan and *Membrane Reactor Technologies Ltd.* of Canada for studies on methane steam reforming for the production of ultra-pure hydrogen. Some contact also was made with *Sasol Technology Ltd.* of South Africa.

An experimental program was also carried out in this thesis. A pilot scale prototype reactor of a nominal capacity of 1.0 Nm³/h hydrogen was constructed, commissioned, and operated at *Membrane Reactor Technologies, Ltd.* (MRT) with financial support from *Tokyo Gas Co.* and the *New Energy and Industrial Technology Development Organization (NEDO)*, of Japan. In addition, some contributions to design of the solids circulation loop for reactor/regenerator system for hydrogen production coupled with carbon dioxide capture were also performed at MRT.

1.1.2. Motivation and Outstanding Issues

Given the importance of fluidized-bed reactors, a number of models and experimental methods have been proposed to study their behaviour. However, it is clear that considerable work is needed to create a robust methodology that allows for design and simulation with minimal uncertainties. Some outstanding issues that need to be addressed are:

- Catastrophic environmental and social damage is expected to occur due to global warming if its mitigation does not become a priority for mankind. The Intergovernmental

Panel on Climate Change suggests that most of the recent temperature increase is due to the increase in anthropogenic greenhouse gas concentrations. Hydrogen technologies are promising means to reduce greenhouse gas emissions and in turn mitigate global warming. One of the major hurdles for the implementation of a hydrogen economy is to improve hydrogen production processes. Steam reforming of natural gas in inefficient fixed bed furnaces is the dominant process for hydrogen production. Although fluidized-bed membrane reforming is more efficient than conventional reforming, significant improvements to this technology are still needed.

- Most fluidized-beds reactor models available in the literature are developed for specific processes under pre-defined operating conditions. For this reason, modelling equations are often limited in their applicability to a certain flow regime, an existing geometry and/or a specific chemical system. Moreover, simplifications and assumptions are introduced before their derivation, further constraining model flexibility.
- Many modelling and experimentation projects proposed by the same researchers appear to be disconnected from each other. It is quite common to see that experimental measurements are not conducted in a way that they can be used for model validation and analysis. A major example of this situation is the widespread use of exit reactor conversions to “validate” distributed models.
- Reactant conversion is predominantly used to review reactor performance. In general, concentration of individual species and selectivity to specific products are more valuable variables in the analysis of experimental measurements and validation of reactor models.
- While progress has been made in adding some of the complexities encountered in practice, e.g. allowance for multiple phases and regions, gradual transitions between flow regimes, interphase transfer and dispersion of mass and heat, volume change due to reaction, membranes to selectively introduce or remove one species, and use of a sorbent to selectively capture one product component, there are no models general enough to incorporate all of these features.
- Much work is needed to address key issues such as interphase balancing mass transfer, especially for systems with large changes in volumetric flows. Conventional multiphase models may fail, predicting unrealistic fluidization conditions (e.g. defluidization).

- Available fluidized-bed reactor models are overwhelmingly limited to steady state operation. Significant progress is needed to analyze the reactor time-scales and to investigate dynamic behaviour.

1.1.3. Research Scope and Objectives

The overall objective of this research project was to develop and work towards the validation of a comprehensive model for multiphase reacting systems. Specific objectives contributing to the achievement of this overall goal were:

- To obtain a set of mathematical expressions to simulate complex multiphase catalytic reactions taking place in a wide range of fluidized-bed reactors (e.g. with different configurations, different processes);
- To simulate different reacting systems and obtain insights on their operation, dynamics and sensitivity to key design and operative parameters;
- To use different versions of the model to simulate catalytic fluidized-bed reactor systems including: methane steam reforming for the production of ultra-pure hydrogen, oxychlorination of ethylene to ethylene dichloride, partial oxidation of n-butane to maleic anhydride, and partial oxidation of naphthalene to phthalic anhydride;
- To assemble, commission, start-up and operate a novel pilot scale fluidized-bed membrane reactor to produce ultra-pure hydrogen;
- To gain new pilot plant experimental data, measuring distributed species concentrations at various levels for the pilot reactor; and
- To compare the experimental results with the simulations implementing the comprehensive model at a higher degree of sophistication than previously reported in the literature.

1.1.4. Thesis Outline

This thesis is presented in manuscript form, with a few modifications to avoid overlap or repetition that could hinder its readability and quality of presentation. Most notably, the development of the general model conservation equations is carefully presented in Section 1.2

(i.e. compiling elements from different papers), and individual versions of the model applied in the individual chapters, are presented by simply explaining their unique simplifications. This approach establishes clear connections between models without repetition. Also the equations for model parameter calculations are compiled and presented only once in Chapter 4. The following is a summary of the topics covered in this dissertation:

In **Chapter 1** a concise overview of this thesis identifying its motivation, research objectives, scope of work and organization is presented. In **Section 1.2** a comprehensive modelling workflow applicable to modelling and experimental programs is also introduced. The general model equations are developed starting from fundamental conservation principles. The model is derived in as general a manner as possible, explaining its features covering all modelling cases in the remaining chapters. Simulation and computational tools are also discussed.

Chapter 2 provides a comprehensive review of these models, ranging from the classic and pioneering reactor models found in the literature to the current state-of-the-art. Each model incorporates a different set of assumptions, leading to different expressions for simulating reactor performance. Forty models are analyzed depending on the characteristics of their conservation equations and their underlying assumptions, by reducing each model to a sequential combination of assumptions. This review contributes to the elucidation process for choosing the most appropriate model to simulate a specific fluidized-bed reactor.

Chapter 3 treats an experimental pilot-scale fluidized-bed membrane reactor for the production of hydrogen. The prototype reactor operated under steam methane reforming (SMR) and auto-thermal reforming (ATR) conditions, without membranes and with membranes of different total areas. Heat was added either externally or via direct air addition. Hydrogen permeate purity of up to 99.995+% as well as a pure-H₂-to-methane yield of 2.07 were achieved with only half of the full complement of membrane panels active under SMR conditions. A permeate-H₂-to reactor methane feed molar ratio >3 was achieved when all of the membrane panels were installed under SMR conditions. Experimental tests investigated the influence of such parameters as reactor pressure, hydrogen permeate pressure (vacuum vs. atmospheric pressure), air top/bottom split, feed flowrate and membrane area.

Chapter 4 demonstrates the implementation of the generalized comprehensive model derived in Section 1.2 to simulate the pilot reactor described in Chapter 3. The reactor model is tested by comparing its simulation predictions against axially distributed concentration in the

pilot reactor. This chapter also discusses phenomena along the reactor including: mass transfer, distributed selective removal of species, interphase cross-flow, flow regime variations, changes in volumetric flow, feed distribution, and fluidization hydrodynamics. The model does not require any adjustable parameters and is shown to give reasonably good predictions for the system under study.

Chapter 5 examines the performance of fluidized bed methane reformers for different flow regimes and membrane configurations. Overall reactor performance is studied for the three fluidization regimes indicating which simulations give the best results and analyzing the mechanistic reasons for this occurrence. Practical considerations, advantages and shortcomings of the flow regimes are considered as well.

Chapter 6 investigates methane steam reforming for production of ultra-pure hydrogen implementing different approaches. This chapter discusses issues such as: 1) carbon dioxide capture (sorption enhancement), 2) effect of sweep gas and vacuum in the membrane side implementing a two-dimensional dispersive model.

Chapter 7 summarizes a case study that simulates an oxy-chlorination fluidized-bed reactor for the production of ethylene dichloride from ethylene. Steady state and dynamic simulations are conducted for an industrial scale reactor.

Chapter 8 focuses on the simulation of partial oxidation of n-butane to maleic anhydride (MA) in an industrial scale fluidized-bed reactor with special emphasis on its dynamic behaviour. Different assumptions are studied with special attention to the resulting simulated time scales. The mass transfer and reaction time scales were compared with a heat transfer time scale to identify the appropriate degree of complexity needed to predict the dynamics of complex reacting systems.

Chapter 9 discusses predictions for an industrial scale fluidized-bed reactor for the partial oxidation of naphthalene to phthalic anhydride.

Chapter 10 provides general discussions and conclusions resulting from this research work. Some recommendations for future work are also examined.

Appendix A briefly describes the most important numerical solvers implemented in the Matlab and COMSOL Multiphysics codes.

Appendix B discusses pressure vessel calculations performed for the pilot FBMR described in Chapter 3.

Appendix C explains the commissioning procedure put into practice for the pilot reactor (Chapter 3).

Appendix D shows detailed photographic documentation of the construction of the pilot plant (Chapter 3).

Appendix E discusses the effect of air split ratio in membrane reformers using a HYSYS model as an extension to what is discussed in Chapter 4.

Appendix F presents the design of a solids circulation system for an experimental integrated reformer-regenerator unit. This is a practical implementation of the system discussed in the first part of Chapter 6.

Appendix G introduces a systematic algorithm for formulating and solving chemical/biochemical reaction engineering problems. This systematic approach is general enough that it can treat different systems with varying degrees of complexity utilizing the same methodology. The suggested procedure can be used in both introductory and advanced chemical/biochemical reaction engineering courses. This provides students with a powerful “toolkit” to tackle a wide range of academic and industrial engineering problems, as well as a useful starting point for developing research projects in this field. This may also allow students to have a better understanding of the multiple phenomena encountered in chemical/biochemical engineering systems and encourage them to prepare models at an optimum level of sophistication for design, optimization, and exploration of novel ideas.

Appendix H provides the list of journal publications, international conference proceedings and conference presentations generated from this thesis.

1.2. Comprehensive Model Development

1.2.1. Introduction

To significantly improve the performance of chemical processes, as well as to advance the fundamental knowledge of complex systems, a synergistic methodology is required combining experimental investigation with detailed mechanistic modelling. The experimental design must be interrelated with the model development so that the experimental data can be used to test and improve the model. In the present chapter, a comprehensive model is presented to simulate a prototype reactor and gain insights into the phenomena experienced inside fluidized-bed reactors, compiling the model developed by Mahecha-Botero *et al.* (2006a, 2007a, b; 2008; 2008a; 2008b; 2009a; 2009b).

In modelling fluidized-bed reactors, several phenomena need to be coupled to accurately characterize the main performance variables. Conservation balances of matter and energy need to be established to track the evolution of system state variables such as species concentrations and temperature along the reactor. These equations need to be coupled with information on the geometry, physics, stoichiometry, thermodynamics, heat and mass transfer, reaction rates and flow patterns of the different phases in the reactor. Models from the literature were reviewed in Chapter 2. These models typically account for a limited number of phenomena under a restricted range of operating parameters. In this chapter, a general fluidized-bed reactor model is presented which can simulate a wide variety of fluidized-bed reactors.

1.2.2. System Theory and Comprehensive Modelling Workflow

Mechanistic modeling is an iterative process of representing a system found in nature by an abstract mathematical description based on physical and chemical principles in order to make predictions and gain insights about the system's underlying phenomena. This process attempts to match observations with a set of equations describing and explaining what is observed and/or measured in nature, and predicting the behaviour of a system. Such models are currently utilized in virtually all fields of knowledge, including psychology, medicine, politics, economics, as well as in all branches of science and engineering.

1.2.2.1. System characterization

The first step in mechanistic modeling is to define the system and its boundaries. This step should include a description of how the system interacts with its surroundings. Thus in reaction engineering systems one needs to emphasize the exchange of species and energy to include this information in mole and energy balances.

1.2.2.2. Identification of state variables

The modeler should define what kind of information he/she wants to obtain from the model. The state variables should be chosen to describe the key features of the system and all the relevant information required to define the system. The most important state variables are the concentrations or molar flows of each species, system temperature, and pressure.

1.2.2.3. Identification of independent variables

This step defines the functional relation of the state variables to the system geometry and their time dependence. This is a very important step which sets the tone for the complexity/simplicity of the system. Independent variables should be chosen carefully depending on the system because they determine the model robustness and usefulness. If time dependence is included, the model is said to be *dynamic*; otherwise it is assumed to be *steady-state*. If variation within the system geometry is considered, the model is said to be *distributed*; otherwise it is *lumped*. The most widely used dependent variables are time and a single distance coordinate, e.g. distance, volume passed, or weight of catalyst passed in travelling streamwise along a reactor.

1.2.2.4. Model development

The modeler should define the relation among the system variables and parameters based on a set of *governing equations*. In general, all systems involve multiple phenomena of different complexity and nature (Froment and Bischoff, 1990; Rodrigues and Minceva, 2005). One of the most important duties of the modeler is to understand, organize and couple these phenomena to represent the system. A good model must represent key elements of the most important phenomena and the interactions of the state variables in order to reproduce synergistic effects. One may begin with a very simple representation, adding additional elements until an adequate representation of the particular case at hand has been formulated. It is preferable to develop a

very general model in order to account for the most important characteristics of an overall system. This model can then be simplified by judicious introduction of different assumptions, depending on the particular case to be studied. In reaction engineering the overall process usually involves a combination of fundamental/conservation equations, differential balances and empirical relations. The goal is to reach “the optimum degree of sophistication” (Aris, 1961), i.e. models which satisfy Occam’s razor principle, with all elements that are needed, but without extra embellishments.

1.2.2.5. Parameter values (design, operational and physico-chemical)

A set of parameter values is required to solve the model. These can be taken from the literature or from separate, but linked, experimental efforts designed to reproduce or simulate the conditions of the system under study. Obtaining accurate *reaction kinetics* and thermo-chemical data is a key requirement for reliable chemical reaction engineering models. The calculation procedure of the many parameters required for the present fluidized bed model, are presented in Chapter 4.

1.2.2.6. Simplifying assumptions

If the same predictions can be obtained by different models, one should prefer the simplest one. For many systems, many different assumptions can be introduced without significantly affecting the accuracy of the results. For example, if the overall rate of reaction is dominated by chemical kinetics, then many different mass transfer approaches could be used with negligible overall impact on the ultimate predictions. Each assumption should be justified either by physical reasoning, experimental findings, mathematical derivations or by the experience of the modeler. Robustness and accuracy should be balanced by the modeler. Each modelling chapter of this thesis describes the simplifying assumptions implemented for the particular system of study.

1.2.2.7. Simulations and numerical analysis

After providing a complete set of equations describing the interactions of all system phenomena in terms of the main system variables, a solution is required to obtain the desired results. Solution methods vary in complexity. In the simplest cases this solution may be obtained analytically, but in most applications of practical interest, especially in reaction engineering,

numerical simulation is required. Step 1.2.2.3 of the above sequence determines the numerical technique and software required to solve the model. If the number of independent variables is zero, the resulting equations are transcendental. When only one independent variable is considered, the system can be described by ordinary differential equations (ODEs). If more than one independent variable is included, partial differential equations (PDEs) must be solved. The number of state variables defines the number of equations to be solved. The number of linearly independent equations should equal the number of state variables. Specific details of the simulation techniques implemented in this thesis are presented in Section 1.2.5.

1.2.2.8. Model validation

Every model should be tested against experimental data in order to check its accuracy. In some cases, experimental data must be utilized to establish values of parameters by fitting the model to experimental results. The ultimate test of a model is to be able to predict experimental results without any adjustable parameters. Benchmarks using well-known systems, limiting case analysis and experimental tests for individual elements of the model should be performed whenever possible (Post and Votta, 2005). Any discrepancy should be analyzed and fed back into the previous steps to improve the model. Final results should be published for future improvements when exposed to the scrutiny of the scientific community.

Figure 1.1 depicts the iterative process for model development. In this thesis, the first six steps for the generalized mathematical modeling of reaction engineering systems are treated in a systematic way in order to facilitate learning and implementation.

1.2.3. General Form of Conservation Equations

In this work priority is given to model flexibility and comprehensiveness. Therefore the model is initially developed to account for as many phenomena as possible so that it can be applied to a variety of systems without changing its fundamental structure. Depending on the system characteristics, some model terms can be retained, while others of less relevance are neglected, facilitating a transparent manipulation of the model equations.

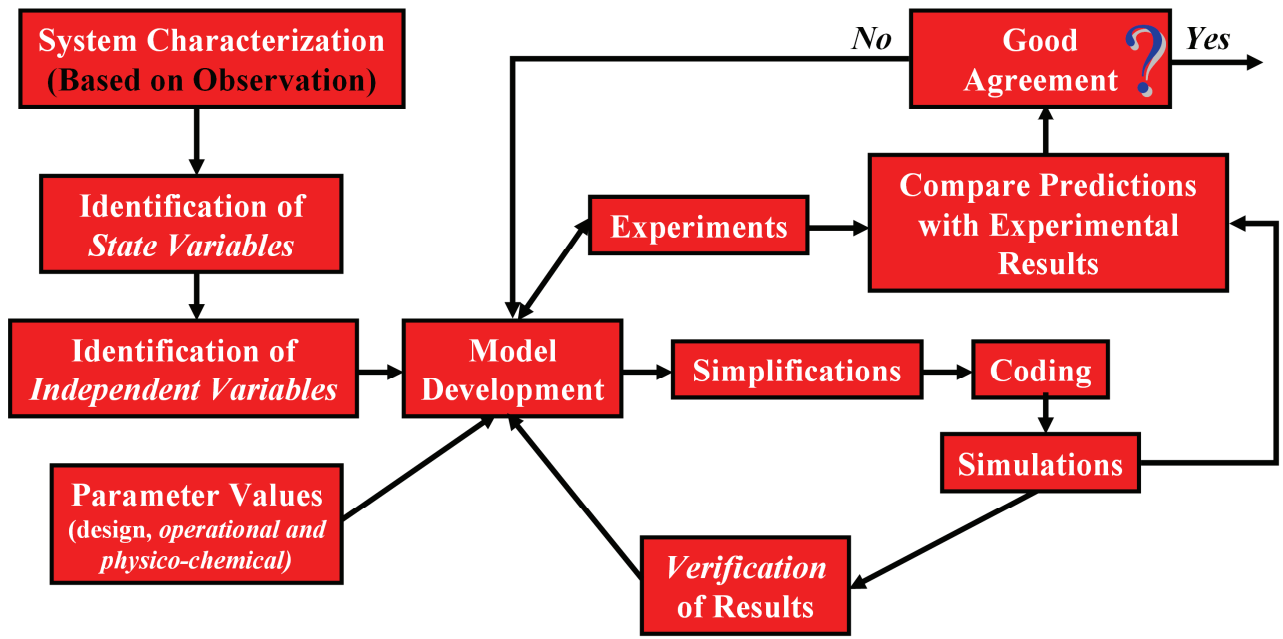


Figure 1.1. Comprehensive modeling iterative process.

1.2.3.1. Model features

The set of generalizations for the model is as follows:

- **Model flexibility:** The mechanistic model treats a system of N_ϕ phases, N_C components and N_R reactions. The conservation equations can be written in any coordinate system with different geometries in one, two, or three dimensions using vector operators.
- **Pseudo-phase approach:** Control volumes for the conservation balances include both gas and solid based on two pseudo-phases: a high-density (also called dense, emulsion, continuous) H-phase and low-density (also referred to as bubble, dilute, void, discontinuous) L-phase. For simplicity the term “pseudo-phase” is replaced by “phase” in the text below.
- **Convective transport:** The convective velocities account for changes in molar and gas volumetric flows (Abba *et al.*, 2002). Changes with time, temperature and pressure are also treated.
- **Equi-molar interphase mass transfer:** For interpenetrating phases, mass transfer is calculated depending on a concentration gradient (Sit and Grace, 1981). In addition, a specific mass transfer coefficient is calculated for each chemical species to account for

different mass transfer resistances encountered by molecules having different diffusion coefficients.

- **Balancing interphase cross-flow:** Convective bulk mass transport of fluid from/to each phase is considered independent of concentration gradients. The fluid leaving each phase is determined by fluidization conditions and has the same concentration as the source phase.
- **Catalytic reactions:** Species generation/consumption is based on intrinsic chemical kinetics. Overall reaction effectiveness factors, as well as deactivation functions, may also be included if needed (Elnashaie and Elshishini, 1993; Chen *et al.*, 2004).
- **Flow regime variation:** The model is not restricted to a single flow regime. Its hydrodynamic parameters are calculated by probabilistic averaging of adjacent flow regimes (Abba *et al.*, 2003b), with hydrodynamic parameters from appropriate correlations and equations relevant to the different flow regimes (Grace *et al.*, 1999a). For instance the voidage distribution within the bed is calculated as explained below allowing for exponential decay in the freeboard. For more details on the implications of flow regime variation, see Chapter 5.
- **Selective removal of species:** The model considers membranes to remove certain products (thereby breaking the thermodynamic barrier) or to supply reactants (e.g. to improve selectivity to a desired product). The membranes fit the reactor geometry and are not necessarily continuously distributed as is often assumed in the literature. Membrane deactivation functions can also be included when available (Raich & Foley, 1995).
- **Feed distribution along the reactor:** The developed model can deal with distributed reactant feeding along the reactor, e.g. for the addition of oxidants to improve heat integration.
- **Other features:** Dynamic behaviour may also be addressed (see Chapter 8). Mass dispersion and anisotropic heat dispersion can also be included (Bird *et al.*, 2002). In addition, if solids chemisorption (Elnashaie and Elshishini, 1993) and solid capture of species by means of a solid sorbent (e.g. for carbon dioxide capture to enhance steam reforming and separate CO₂ for subsequent sequestration (Johnsen *et al.*, 2006; Chen *et al.*, 2008)), can be simulated. Not all model features are needed to represent a particular system, and attention should be paid to practical simplifying assumptions (Aris, 1999).

1.2.3.2. Mole balance

The number of mole balance equations is $N_C \cdot N_\varphi$ where N_C is the number of chemical species and N_φ is the number of phases. For a fluidized-bed membrane reactor depicted schematically in Figures 1.2 and 1.3, a mole balance equation must be applied to all chemical species in the two fluidization phases, as well as permeating species in the membrane phase. The equation below is an extension of that given in Mahecha-Botero *et al.* (2006a, 2007b; 2008b), but incorporates model parameters inside the derivatives when appropriate and adds terms for balancing interphase crossflow and feed distribution along the reactor. The molar rate balance over a differential element (see Figure 1.3) for phase (φ) is given by:

$$\boxed{[Convective\ input - Convective\ output]_{(gas+cat+sorb)} + [Diffusive\ input - Diffusive\ output]_{(gas)} + [Reaction\ generation/consumption]_{(cat+sorb)} + [Exchange]_{(\varphi)} = [Accumulation\ rate]_{(gas+cat+sorb)}}$$

The terms in the general mole balance in symbols for component i in phase φ are as follows:

[Convective input – Convective output]_(gas):

$$\left. \begin{aligned} & A_x \cdot \left[\left(\psi_\varphi \cdot \varepsilon_\varphi \cdot U_{x_{gas_\varphi}} \cdot C_{i_\varphi} \right)_{(x,y,z)} - \left(\psi_\varphi \cdot \varepsilon_\varphi \cdot U_{x_{gas_\varphi}} \cdot C_{i_\varphi} \right)_{(x+\Delta x,y,z)} \right] \\ & + A_y \cdot \left[\left(\psi_\varphi \cdot \varepsilon_\varphi \cdot U_{y_{gas_\varphi}} \cdot C_{i_\varphi} \right)_{(x,y,z)} - \left(\psi_\varphi \cdot \varepsilon_\varphi \cdot U_{y_{gas_\varphi}} \cdot C_{i_\varphi} \right)_{(x,y+\Delta y,z)} \right] \\ & + A_z \cdot \left[\left(\psi_\varphi \cdot \varepsilon_\varphi \cdot U_{z_{gas_\varphi}} \cdot C_{i_\varphi} \right)_{(x,y,z)} - \left(\psi_\varphi \cdot \varepsilon_\varphi \cdot U_{z_{gas_\varphi}} \cdot C_{i_\varphi} \right)_{(x,y,z+\Delta z)} \right] \end{aligned} \right\} \quad (1.1)$$

where for phase φ : C_{i_φ} is the concentration of species i (i.e. mole balance state variables), ψ_φ the volume fraction, ε_φ the void fraction and U_{gas_φ} the convective velocity vector given by

$$\overrightarrow{U_{gas_\varphi}} = \left(U_{x_{gas_\varphi}}, U_{y_{gas_\varphi}}, U_{z_{gas_\varphi}} \right).$$

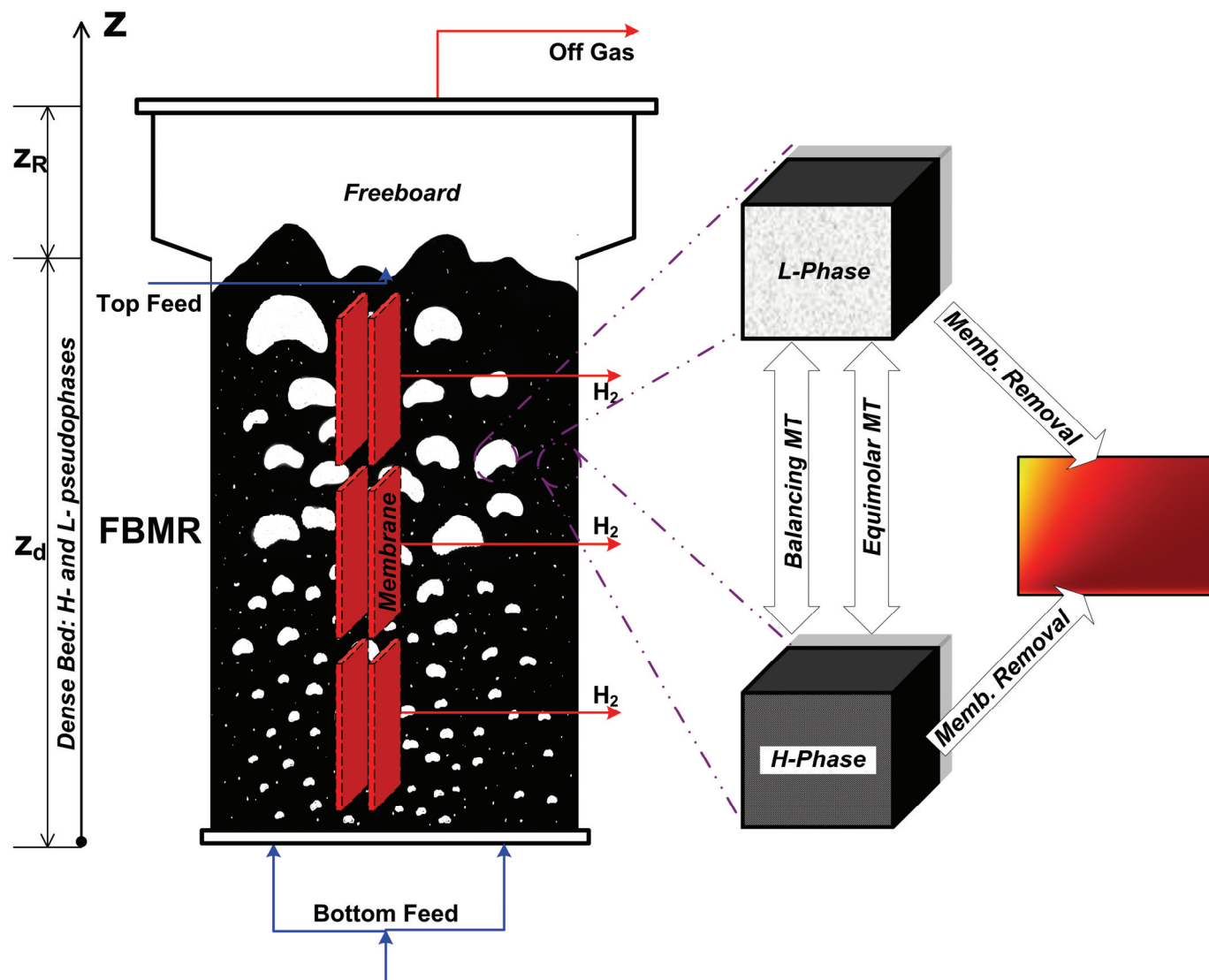


Figure 1.2. Two pseudo-phase reactor model schematics.

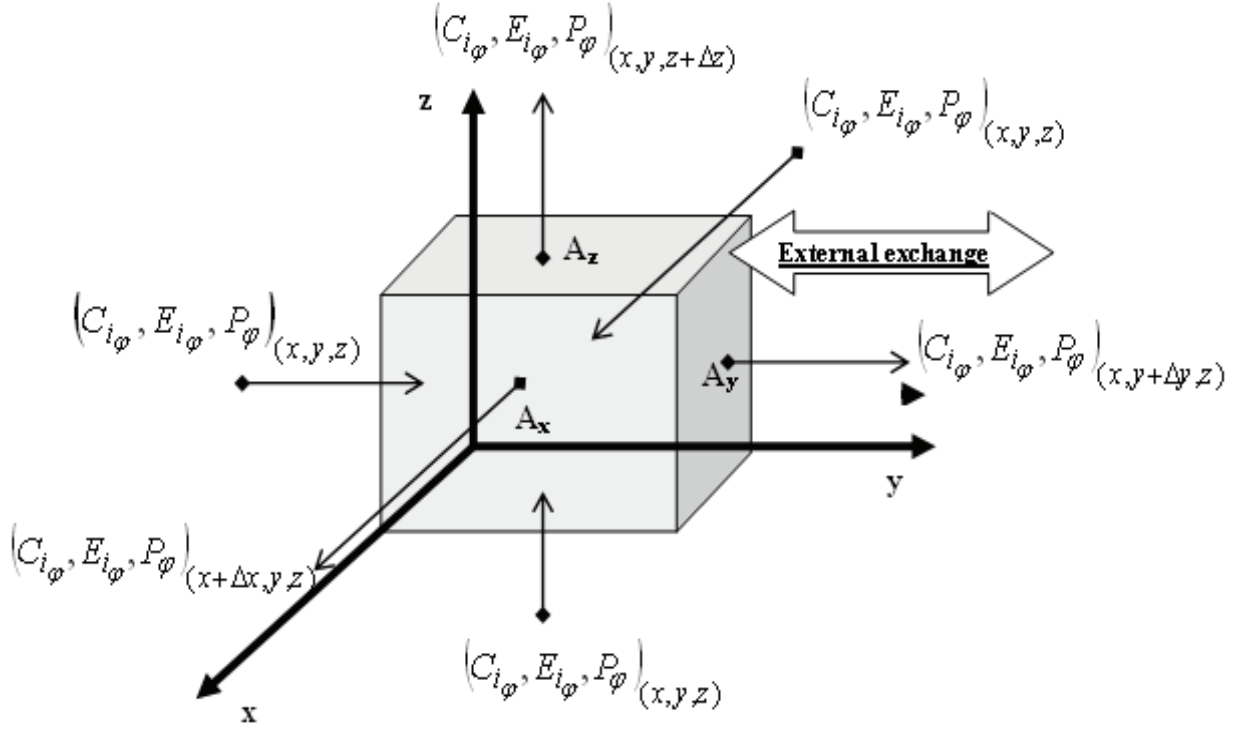


Figure 1.3. Differential control volume for derivation of conservation equations.

[Convective input – Convective output]_(cat):

$$\left. \begin{aligned}
 & A_x \cdot \left[\left(\psi_\phi (1 - \varepsilon_\phi) (1 - \alpha_\phi) U_{x_{cat\phi}} \cdot S_{cat\phi} \cdot c_{i_{cat\phi}} \right)_{(x,y,z)} - \left(\psi_\phi (1 - \varepsilon_\phi) (1 - \alpha_\phi) U_{x_{cat\phi}} \cdot S_{cat\phi} \cdot c_{i_{cat\phi}} \right)_{(x+\Delta x,y,z)} \right] \\
 & + A_y \cdot \left[\left(\psi_\phi (1 - \varepsilon_\phi) (1 - \alpha_\phi) U_{y_{cat\phi}} \cdot S_{cat\phi} \cdot c_{i_{cat\phi}} \right)_{(x,y,z)} - \left(\psi_\phi (1 - \varepsilon_\phi) (1 - \alpha_\phi) U_{y_{cat\phi}} \cdot S_{cat\phi} \cdot c_{i_{cat\phi}} \right)_{(x,y+\Delta y,z)} \right] \\
 & + A_z \cdot \left[\left(\psi_\phi (1 - \varepsilon_\phi) (1 - \alpha_\phi) U_{z_{cat\phi}} \cdot S_{cat\phi} \cdot c_{i_{cat\phi}} \right)_{(x,y,z)} - \left(\psi_\phi (1 - \varepsilon_\phi) (1 - \alpha_\phi) U_{z_{cat\phi}} \cdot S_{cat\phi} \cdot c_{i_{cat\phi}} \right)_{(x,y,z+\Delta z)} \right]
 \end{aligned} \right\} \tag{1.2}$$

[Convective input – Convective output]_(sorb):

$$\left. \begin{aligned}
 & A_x \cdot \left[\left(\psi_\phi (1 - \varepsilon_\phi) \alpha_\phi U_{x_{sorb\phi}} \cdot S_{sorb\phi} \cdot c_{i_{sorb\phi}} \right)_{(x,y,z)} - \left(\psi_\phi (1 - \varepsilon_\phi) \alpha_\phi U_{x_{sorb\phi}} \cdot S_{sorb\phi} \cdot c_{i_{sorb\phi}} \right)_{(x+\Delta x,y,z)} \right] \\
 & + A_y \cdot \left[\left(\psi_\phi (1 - \varepsilon_\phi) \alpha_\phi U_{y_{sorb\phi}} \cdot S_{sorb\phi} \cdot c_{i_{sorb\phi}} \right)_{(x,y,z)} - \left(\psi_\phi (1 - \varepsilon_\phi) \alpha_\phi U_{y_{sorb\phi}} \cdot S_{sorb\phi} \cdot c_{i_{sorb\phi}} \right)_{(x,y+\Delta y,z)} \right] \\
 & + A_z \cdot \left[\left(\psi_\phi (1 - \varepsilon_\phi) \alpha_\phi U_{z_{sorb\phi}} \cdot S_{sorb\phi} \cdot c_{i_{sorb\phi}} \right)_{(x,y,z)} - \left(\psi_\phi (1 - \varepsilon_\phi) \alpha_\phi U_{z_{sorb\phi}} \cdot S_{sorb\phi} \cdot c_{i_{sorb\phi}} \right)_{(x,y,z+\Delta z)} \right]
 \end{aligned} \right\} \tag{1.3}$$

Sub-indexes “*cat*” and “*sorb*” denote the catalyst and sorbent, respectively. $c_{i_{cat},\varphi}$ and $c_{i_{sorb},\varphi}$ are the concentrations of species i on the catalyst and solid sorbent surface per unit surface area respectively. These surface concentrations can be expressed as functions of the corresponding volumetric gas concentrations, i.e.: $c_{i_{cat},\varphi} = f_C(C_{i_\varphi})$, and $c_{i_{sorb},\varphi} = f_S(C_{i_\varphi})$. $S_{cat,\varphi}$ and $S_{sorb,\varphi}$ are the surface area of catalyst and solid sorbent surface per unit volume, respectively, and α_φ is the volume fraction of solid sorbent per unit volume of total solids

[Diffusive input – Diffusive output] (gas):

$$\left\{ \begin{aligned} & A_x \cdot \left[(\psi_\varphi \cdot \varepsilon_\varphi \cdot N_{i\varphi_x})_{(x,y,z)} - (\psi_\varphi \cdot \varepsilon_\varphi \cdot N_{i\varphi_x})_{(x+\Delta x,y,z)} \right] \\ & + A_y \cdot \left[(\psi_\varphi \cdot \varepsilon_\varphi \cdot N_{i\varphi_y})_{(x,y,z)} - (\psi_\varphi \cdot \varepsilon_\varphi \cdot N_{i\varphi_y})_{(x,y+\Delta y,z)} \right] \\ & + A_z \cdot \left[(\psi_\varphi \cdot \varepsilon_\varphi \cdot N_{i\varphi_z})_{(x,y,z)} - (\psi_\varphi \cdot \varepsilon_\varphi \cdot N_{i\varphi_z})_{(x,y,z+\Delta z)} \right] \end{aligned} \right\}, \quad (1.4)$$

where $\overline{N_{i\varphi}}$ is the vector of dispersive molar fluxes. This term can be calculated using Fick’s (or alternatively Stefan –Maxwell) diffusion.

[Reaction generation/consumption] (cat):

$$\Delta V \left\{ \psi_\varphi \cdot (1 - \varepsilon_\varphi) \cdot (1 - \alpha_\varphi) \cdot \rho_{cat} \cdot \sum_{j=1}^{N_{Rcat}} \nu_{ij_{cat},\varphi} \cdot \Omega_{j_{cat},\varphi} \cdot a_{j_{cat},\varphi} \cdot r'_{j_{cat},\varphi} \right\}, \quad (1.5)$$

[Reaction generation/consumption] (sorb):

$$\Delta V \left\{ \psi_\varphi \cdot (1 - \varepsilon_\varphi) \cdot \alpha_\varphi \cdot \rho_{sorb} \cdot \sum_{j=1}^{N_{Rsorb}} \nu_{ij_{sorb},\varphi} \cdot \Omega_{j_{sorb},\varphi} \cdot a_{j_{sorb},\varphi} \cdot r'_{j_{sorb},\varphi} \right\}, \quad (1.6)$$

where the stoichiometric coefficients $\nu_{ij_{cat},\varphi}$ are positive for products, negative for reactants and zero for non-reacting species. $\Omega_{j_{cat},\varphi}$ is the effectiveness factor, and $a_{j_{cat},\varphi}$ is a catalyst deactivation coefficient. The volumetric reaction rates are given by: $r_j = \rho_{cat} \cdot (1 - \varepsilon_{(\varphi)}) \cdot r'_j$.

[Exchange with other phases] (φ):

Mass exchange, as well as feed distribution, along the reactor which do not affect all differential control volumes (i.e. are dependent on the system’s geometry) need to be included in

the boundary conditions. For example, membrane removal, as well as feed distribution along the reactor terms in 3-D and 2-D geometries must be included as boundary conditions, contrary to one-dimensional distributed models where they may be introduced in the differential equations. For equimolar interphase mass transfer and balancing mass transfer we have:

$$\Delta V \cdot \left\{ \left[\psi_{\varphi} \cdot \sum_{\substack{n=1 \\ n \neq \varphi}}^{N_{\varphi}} a_{I_{(n \rightarrow \varphi)}} \cdot k_{c_{i,(n \rightarrow \varphi)}} \cdot (C_{i_n} - C_{i_{\varphi}}) \right] - \left[\psi_{\varphi} \cdot \sum_{\substack{n=1 \\ n \neq \varphi}}^{N_{\varphi}} v_{Bulk_{(\varphi \rightarrow n)}}^{\text{'''}} \cdot C_{i_{\varphi}} \right] + \left[\psi_n \cdot \sum_{\substack{n=1 \\ n \neq \varphi}}^{N_{\varphi}} v_{Bulk_{(n \rightarrow \varphi)}}^{\text{'''}} \cdot C_{i_n} \right] \right\} \quad (1.7)$$

where $a_{I_{(n \rightarrow \varphi)}}$ is the interphase transfer area per unit volume between phases φ and (n) , $k_{c_{i,(n \rightarrow \varphi)}}$ the equimolar interphase mass transfer coefficient of component i , C_{i_n} the concentration of species i in a phase in contact with phase φ , and $v_{Bulk}^{\text{'''}}$ is the interphase balancing volumetric flow per unit volume.

[Accumulation rate] _(gas+cat+sorb):

$$\Delta V \cdot \left\{ \frac{d}{dt} \left[\psi_{\varphi} \cdot \varepsilon_{\varphi} \cdot C_{i_{\varphi}} \right] + \frac{d}{dt} \left[\psi_{\varphi} \cdot (1 - \varepsilon_{\varphi}) \cdot (1 - \alpha_{\varphi}) \cdot (S_{cat_{\varphi}} \cdot c_{i_{cat,\varphi}}) \right] + \frac{d}{dt} \left[\psi_{\varphi} \cdot (1 - \varepsilon_{\varphi}) \cdot \alpha_{\varphi} \cdot (S_{sorb_{\varphi}} \cdot c_{i_{sorb,\varphi}}) \right] \right\}, \quad (1.8)$$

Adding the terms from 1.1 to 1.8, equating to 0, dividing by ΔV , taking the limit as $\Delta V \rightarrow 0$ and introducing the vector operator “ ∇ ”, we obtain the following generalized mole balance of each compound in phase (φ) :

$$\begin{aligned}
& -\vec{\nabla} \cdot [\psi_\varphi \cdot \varepsilon_\varphi \cdot C_{i_\varphi} \cdot \overline{U}_{gas_\varphi}] + \left[\begin{array}{c} \text{Equimolar interphase mass transfer} \\ \psi_\varphi \cdot \sum_{\substack{n=1 \\ n \neq \varphi}}^{N_\varphi} a_{I(n \rightarrow \varphi)} \cdot k_{c_{i,(n \rightarrow \varphi)}} \cdot (C_{i_n} - C_{i_\varphi}) \end{array} \right] - \left[\begin{array}{c} \text{Balancing M.T. from } \varphi \\ \psi_\varphi \cdot \sum_{\substack{n=1 \\ n \neq \varphi}}^{N_\varphi} v_{Bulk(\varphi \rightarrow n)} \cdot C_{i_\varphi} \end{array} \right] \\
& + \left[\begin{array}{c} \text{Balancing M.T. to } \varphi \\ \psi_n \cdot \sum_{\substack{n=1 \\ n \neq \varphi}}^{N_\varphi} v_{Bulk(n \rightarrow \varphi)} \cdot C_{i_n} \end{array} \right] + \left[\begin{array}{c} \text{Catalytic reaction generation/consumption} \\ \psi_\varphi \cdot (1 - \varepsilon_\varphi) \cdot (1 - \alpha_\varphi) \cdot \rho_{cat} \cdot \sum_{j=1}^{N_{R_{cat}}} v_{ij_{cat,\varphi}} \cdot \Omega_{j_{cat,\varphi}} \cdot a_{j_{cat,\varphi}} \cdot r'_{j_{cat,\varphi}} \end{array} \right] \\
& + \left[\begin{array}{c} \text{Sorbent reaction generation/consumption} \\ \psi_\varphi \cdot (1 - \varepsilon_\varphi) \cdot \alpha_\varphi \cdot \rho_{sorb} \cdot \sum_{j=1}^{N_{R_{sorb}}} v_{ij_{sorb,\varphi}} \cdot \Omega_{j_{sorb,\varphi}} \cdot a_{j_{sorb,\varphi}} \cdot r'_{j_{sorb,\varphi}} \end{array} \right] - \left[\begin{array}{c} \text{Gas dispersion} \\ \vec{\nabla} \cdot [\psi_\varphi \cdot \varepsilon_\varphi \cdot \overline{N}_{i_\varphi}] \end{array} \right] \\
& - \vec{\nabla} \cdot [\psi_\varphi \cdot (1 - \varepsilon_\varphi) \cdot (1 - \alpha_\varphi) \cdot (S_{cat_\varphi} \cdot c_{i_{cat,\varphi}}) \cdot \overline{U}_{cat_\varphi}] + \vec{\nabla} \cdot [\psi_\varphi \cdot (1 - \varepsilon_\varphi) \cdot \alpha_\varphi \cdot (S_{sorb_\varphi} \cdot c_{i_{sorb,\varphi}}) \cdot \overline{U}_{sorb_\varphi}] \\
& = \frac{\partial}{\partial t} [\psi_\varphi \cdot \varepsilon_\varphi \cdot C_{i_\varphi}] + \frac{\partial}{\partial t} [\psi_\varphi \cdot (1 - \varepsilon_\varphi) \cdot (1 - \alpha_\varphi) \cdot (S_{cat_\varphi} \cdot c_{i_{cat,\varphi}})] + \frac{\partial}{\partial t} [\psi_\varphi \cdot (1 - \varepsilon_\varphi) \cdot \alpha_\varphi \cdot (S_{sorb_\varphi} \cdot c_{i_{sorb,\varphi}})]
\end{aligned}$$

(1.9)

for $i=1,2,\dots,N_C$ and $\varphi=1,2,\dots,N_\varphi$,

M.T. = Mass Transfer

1.2.3.3. Energy balance

The differential energy balance (see Figures 1.2 and 1.3) for phase (φ) is given by:

$$\boxed{[Convective\ heat\ input - Convective\ heat\ output]_{(gas+cat+sorb)} + [Diffusive\ heat\ input - Diffusive\ heat\ output]_{(gas)} + [Chemical\ reaction\ heat\ generation/consumption]_{(cat+sorb)} + [Heat\ exchange\ with\ other\ phases\ and\ surroundings]_{(\varphi)} = [Heat\ accumulation\ rate]_{(gas+cat+sorb)}}$$

The terms in the general balance are shown in symbols below. Energy dissipation due to viscous effects is neglected. Also it is assumed that there is no stirrer or other mechanical devices dissipating heat within the control volume. The number of energy balance equations is N_φ .

[Convective heat input – Convective heat output]_(gas):

$$\left. \begin{aligned} & A_x \cdot \left[\left(\psi_\varphi \cdot \varepsilon_\varphi \cdot \left(\sum_{i=1}^{NC} C_{i_\varphi} \cdot E_{i_\varphi} \right) \cdot U_{x_{gas\varphi}} \right)_{(x,y,z)} - \left(\psi_\varphi \cdot \varepsilon_\varphi \cdot \left(\sum_{i=1}^{NC} C_{i_\varphi} \cdot E_{i_\varphi} \right) \cdot U_{x_{gas\varphi}} \right)_{(x+\Delta x,y,z)} \right] \\ & + A_y \cdot \left[\left(\psi_\varphi \cdot \varepsilon_\varphi \cdot \left(\sum_{i=1}^{NC} C_{i_\varphi} \cdot E_{i_\varphi} \right) \cdot U_{y_{gas\varphi}} \right)_{(x,y,z)} - \left(\psi_\varphi \cdot \varepsilon_\varphi \cdot \left(\sum_{i=1}^{NC} C_{i_\varphi} \cdot E_{i_\varphi} \right) \cdot U_{y_{gas\varphi}} \right)_{(x,y+\Delta y,z)} \right] \\ & + A_z \cdot \left[\left(\psi_\varphi \cdot \varepsilon_\varphi \cdot \left(\sum_{i=1}^{NC} C_{i_\varphi} \cdot E_{i_\varphi} \right) \cdot U_{z_{gas\varphi}} \right)_{(x,y,z)} - \left(\psi_\varphi \cdot \varepsilon_\varphi \cdot \left(\sum_{i=1}^{NC} C_{i_\varphi} \cdot E_{i_\varphi} \right) \cdot U_{z_{gas\varphi}} \right)_{(x,y,z+\Delta z)} \right] \end{aligned} \right\}, \quad (1.10)$$

where E_{i_φ} is the internal energy of component i in phase (φ) .

[Convective heat input – Convective heat output]_(cat):

$$\left. \begin{aligned} & A_x \cdot \left(\psi_\varphi \cdot (1 - \varepsilon_\varphi) \cdot (1 - \alpha_\varphi) \cdot \left(\sum_{i=1}^{N_C} (S_{cat_\varphi} \cdot c_{i_{cat,\varphi}}) E_{i_{cat,\varphi}} + \rho_{cat} \cdot E_{cat_\varphi} \right) \cdot U_{x_{cat\varphi}} \right)_{(x,y,z)} \\ & - A_x \cdot \left(\psi_\varphi \cdot (1 - \varepsilon_\varphi) \cdot (1 - \alpha_\varphi) \cdot \left(\sum_{i=1}^{N_C} (S_{cat_\varphi} \cdot c_{i_{cat,\varphi}}) E_{i_{cat,\varphi}} + \rho_{cat} \cdot E_{cat_\varphi} \right) \cdot U_{x_{cat\varphi}} \right)_{(x+\Delta x,y,z)} \\ & + A_y \cdot \left(\psi_\varphi \cdot (1 - \varepsilon_\varphi) \cdot (1 - \alpha_\varphi) \cdot \left(\sum_{i=1}^{N_C} (S_{cat_\varphi} \cdot c_{i_{cat,\varphi}}) E_{i_{cat,\varphi}} + \rho_{cat} \cdot E_{cat_\varphi} \right) \cdot U_{y_{cat\varphi}} \right)_{(x,y,z)} \\ & - A_y \cdot \left(\psi_\varphi \cdot (1 - \varepsilon_\varphi) \cdot (1 - \alpha_\varphi) \cdot \left(\sum_{i=1}^{N_C} (S_{cat_\varphi} \cdot c_{i_{cat,\varphi}}) E_{i_{cat,\varphi}} + \rho_{cat} \cdot E_{cat_\varphi} \right) \cdot U_{y_{cat\varphi}} \right)_{(x,y+\Delta y,z)} \\ & + A_z \cdot \left(\psi_\varphi \cdot (1 - \varepsilon_\varphi) \cdot (1 - \alpha_\varphi) \cdot \left(\sum_{i=1}^{N_C} (S_{cat_\varphi} \cdot c_{i_{cat,\varphi}}) E_{i_{cat,\varphi}} + \rho_{cat} \cdot E_{cat_\varphi} \right) \cdot U_{z_{cat\varphi}} \right)_{(x,y,z)} \\ & - A_z \cdot \left(\psi_\varphi \cdot (1 - \varepsilon_\varphi) \cdot (1 - \alpha_\varphi) \cdot \left(\sum_{i=1}^{N_C} (S_{cat_\varphi} \cdot c_{i_{cat,\varphi}}) E_{i_{cat,\varphi}} + \rho_{cat} \cdot E_{cat_\varphi} \right) \cdot U_{z_{cat\varphi}} \right)_{(x,y,z+\Delta z)} \end{aligned} \right\}, \quad (1.11)$$

where $E_{i_{cat,\varphi}}$ is the internal energy of species i chemisorbed on the catalyst surface, and E_{cat_φ} is the internal energy of the catalyst.

[Convective heat input – Convective heat output]_(sorb):

$$\left. \begin{aligned} & A_x \cdot \left(\psi_\varphi \cdot (1 - \varepsilon_\varphi) \alpha_\varphi \cdot \left(\sum_{i=1}^{N_C} (S_{sorb_\varphi} \cdot c_{i_{sorb,\varphi}}) E_{i_{sorb,\varphi}} + \rho_{sorb} \cdot E_{sorb_\varphi} \right) \cdot U_{x_{sorb_\varphi}} \right)_{(x,y,z)} \\ & - A_x \cdot \left(\psi_\varphi \cdot (1 - \varepsilon_\varphi) \alpha_\varphi \cdot \left(\sum_{i=1}^{N_C} (S_{sorb_\varphi} \cdot c_{i_{sorb,\varphi}}) E_{i_{sorb,\varphi}} + \rho_{sorb} \cdot E_{sorb_\varphi} \right) \cdot U_{x_{sorb_\varphi}} \right)_{(x+\Delta x,y,z)} \\ & + A_y \cdot \left(\psi_\varphi \cdot (1 - \varepsilon_\varphi) \alpha_\varphi \cdot \left(\sum_{i=1}^{N_C} (S_{sorb_\varphi} \cdot c_{i_{sorb,\varphi}}) E_{i_{sorb,\varphi}} + \rho_{sorb} \cdot E_{sorb_\varphi} \right) \cdot U_{y_{sorb_\varphi}} \right)_{(x,y,z)} \\ & - A_y \cdot \left(\psi_\varphi \cdot (1 - \varepsilon_\varphi) \alpha_\varphi \cdot \left(\sum_{i=1}^{N_C} (S_{sorb_\varphi} \cdot c_{i_{sorb,\varphi}}) E_{i_{sorb,\varphi}} + \rho_{sorb} \cdot E_{sorb_\varphi} \right) \cdot U_{y_{sorb_\varphi}} \right)_{(x,y+\Delta y,z)} \\ & + A_z \cdot \left(\psi_\varphi \cdot (1 - \varepsilon_\varphi) \alpha_\varphi \cdot \left(\sum_{i=1}^{N_C} (S_{sorb_\varphi} \cdot c_{i_{sorb,\varphi}}) E_{i_{sorb,\varphi}} + \rho_{sorb} \cdot E_{sorb_\varphi} \right) \cdot U_{z_{sorb_\varphi}} \right)_{(x,y,z)} \\ & - A_z \cdot \left(\psi_\varphi \cdot (1 - \varepsilon_\varphi) \alpha_\varphi \cdot \left(\sum_{i=1}^{N_C} (S_{sorb_\varphi} \cdot c_{i_{sorb,\varphi}}) E_{i_{sorb,\varphi}} + \rho_{sorb} \cdot E_{sorb_\varphi} \right) \cdot U_{z_{sorb_\varphi}} \right)_{(x,y,z+\Delta z)} \end{aligned} \right\} \quad (1.12)$$

where $E_{i_{sorb,\varphi}}$ is the internal energy of species i chemisorbed on the solid sorbent surface, and E_{sorb_φ} is the internal energy of the solid sorbent.

[Diffusive heat input – Diffusive heat output]_(\varphi):

$$\left. \begin{aligned} & A_x \cdot \left[(\psi_\varphi \cdot q_{\varphi_x})_{(x,y,z)} - (\psi_\varphi \cdot q_{\varphi_x})_{(x+\Delta x,y,z)} \right] + A_y \cdot \left[(\psi_\varphi \cdot q_{\varphi_y})_{(x,y,z)} - (\psi_\varphi \cdot q_{\varphi_y})_{(x,y+\Delta y,z)} \right] \\ & + A_z \cdot \left[(\psi_\varphi \cdot q_{\varphi_z})_{(x,y,z)} - (\psi_\varphi \cdot q_{\varphi_z})_{(x,y,z+\Delta z)} \right] \end{aligned} \right\} \quad (1.13)$$

where \vec{q}_φ is the vector of conductive heat fluxes, which is a function of the temperature profile.

This term can be calculated using Fourier's law of conduction.

[Chemical reaction heat generation/consumption]_(cat):

$$\Delta V \left\{ \psi_\varphi \cdot (1 - \varepsilon_\varphi) (1 - \alpha_\varphi) \rho_{cat} \cdot \sum_{j=1}^{N_{Rcat}} \Delta H_{j_{cat}} \cdot \Omega_{j_{cat,\varphi}} \cdot a_{j_{cat,\varphi}} \cdot r'_{j_{cat,\varphi}} \right\} \quad (1.14)$$

where $\Delta H_{j_{cat}}$ is the heat of reaction j in the catalyst.

[Chemical reaction heat generation/consumption] _(sorb):

$$\Delta V \left\{ \psi_{\varphi} \cdot (1 - \varepsilon_{\varphi}) \alpha_{\varphi} \cdot \rho_{sorb} \cdot \sum_{j=1}^{N_{R_{sorb}}} \Delta H_{j_{sorb}} \cdot \Omega_{j_{sorb}, \varphi} \cdot a_{j_{sorb}, \varphi} \cdot r'_{j_{sorb}, \varphi} \right\}, \quad (1.15)$$

where $\Delta H_{j_{sorb}}$ is the heat of reaction j in the solid sorbent particles.

[Heat exchange with other phases and surroundings] _(\varphi):

The expressions for the exchange with other phases and the surroundings depend on the particular configurations adopted by the reacting system. Heat exchange terms which do not affect all differential control volumes (i.e. those dependent on the system's geometry) must be included in the boundary conditions. Reactor heat losses in 3-D and 2-D geometries must be included as boundary conditions depending on the system configuration. For heat transfer associated with equimolar interphase mass transfer and balancing mass transfer, we have:

$$\Delta V \left\{ \begin{array}{l} \left[\sum_{i=1}^{N_C} \psi_{\varphi} \cdot \left(\sum_{\substack{n=1 \\ n \neq \varphi}}^{N_{\varphi}} a_{I(n \rightarrow \varphi)} \cdot k_{c_{i, (n \rightarrow \varphi)}} \cdot (C_{i_n} - C_{i_{\varphi}}) \right) \cdot E_{i_{\varphi n}} \right] \\ - \left[\sum_{i=1}^{N_C} \psi_{\varphi} \cdot \left(\sum_{\substack{n=1 \\ n \neq \varphi}}^{N_{\varphi}} v_{Bulk(\varphi \rightarrow n)} \cdot C_{i_{\varphi}} \right) \cdot E_{i_{\varphi}} \right] + \left[\sum_{i=1}^{N_C} \psi_n \cdot \left(\sum_{\substack{n=1 \\ n \neq \varphi}}^{N_{\varphi}} v_{Bulk(n \rightarrow \varphi)} \cdot C_{i_n} \right) \cdot E_{i_n} \right] \end{array} \right\} \quad (1.16)$$

[Heat accumulation rate] _(gas+cat+sorb):

$$\Delta V \left\{ \begin{array}{l} \left[\frac{\partial}{\partial t} \left[\psi_{\varphi} \cdot \varepsilon_{\varphi} \cdot \sum_{i=1}^{N_C} C_{i_{\varphi}} \cdot E_{i_{\varphi}} \right] + \frac{\partial}{\partial t} \left[\psi_{\varphi} \cdot (1 - \varepsilon_{\varphi}) (1 - \alpha_{\varphi}) \left(\sum_{i=1}^{N_C} (S_{cat_{\varphi}} \cdot c_{i_{cat, \varphi}}) E_{i_{cat, \varphi}} + \rho_{cat} \cdot E_{cat_{\varphi}} \right) \right] \right] \\ + \frac{\partial}{\partial t} \left[\psi_{\varphi} \cdot (1 - \varepsilon_{\varphi}) \alpha_{\varphi} \cdot \left(\sum_{i=1}^{N_C} (S_{sorb_{\varphi}} \cdot c_{i_{sorb, \varphi}}) E_{i_{sorb, \varphi}} + \rho_{sorb} \cdot E_{sorb_{\varphi}} \right) \right] \end{array} \right\}, \quad (1.17)$$

Adding the terms from 1.10 to 1.17, equating to 0, dividing by ΔV , taking the limit as $\Delta V \rightarrow 0$ and using the definition of vector operator “ ∇ ”, we obtain the generalized energy balance for phase (φ) :

$$\begin{aligned}
& -\vec{\nabla} \cdot \left[\psi_\varphi \cdot \varepsilon_\varphi \cdot \left(\sum_{i=1}^{N_C} C_{i_\varphi} \cdot E_{i_\varphi} \right) \overrightarrow{U}_{gas_\varphi} \right] + \left[\sum_{i=1}^{N_C} \psi_\varphi \cdot \left(\sum_{\substack{n=1 \\ n \neq \varphi}}^{N_\varphi} a_{I_{(n \rightarrow \varphi)}} \cdot k_{c_{i,(n \rightarrow \varphi)}} \cdot (C_{i_n} - C_{i_\varphi}) \right) E_{i_\varphi} \right] \\
& \text{E.T. from Balancing Crossflow from } \varphi \quad \text{Catalytic reaction generation/consumption} \\
& - \left[\sum_{i=1}^{N_C} \psi_\varphi \cdot \left(\sum_{\substack{n=1 \\ n \neq \varphi}}^{N_\varphi} v_{Bulk_{(\varphi \rightarrow n)}} \cdot C_{i_\varphi} \right) \cdot E_{i_\varphi} \right] + \left[\psi_\varphi \cdot (1 - \varepsilon_\varphi) (1 - \alpha_\varphi) \cdot \rho_{cat} \cdot \sum_{j=1}^{N_{Rcat}} \Delta H_{jcat} \cdot \Omega_{jcat,\varphi} \cdot a_{jcat,\varphi} \cdot r'_{jcat,\varphi} \right] \\
& \text{E.T. from Balancing Crossflow to } \varphi \quad \text{Sorbent reaction generation/consumption} \\
& + \left[\sum_{i=1}^{N_C} \psi_n \cdot \left(\sum_{\substack{n=1 \\ n \neq \varphi}}^{N_\varphi} v_{Bulk_{(n \rightarrow \varphi)}} \cdot C_{i_n} \right) \cdot E_{i_n} \right] + \left[\psi_\varphi \cdot (1 - \varepsilon_\varphi) \alpha_\varphi \cdot \rho_{sorb} \cdot \sum_{j=1}^{N_{Rsorb}} \Delta H_{jsorb} \cdot \Omega_{jsorb,\varphi} \cdot a_{jsorb,\varphi} \cdot r'_{jsorb,\varphi} \right] \\
& \text{Heat dispersion} \quad \text{Convection due to catalyst chemisorption and catalyst solids} \\
& - \vec{\nabla} \cdot \left[\psi_\varphi \cdot \overrightarrow{q}_\varphi \right] - \vec{\nabla} \cdot \left[\psi_\varphi \cdot (1 - \varepsilon_\varphi) (1 - \alpha_\varphi) \cdot \left(\sum_{i=1}^{N_C} (S_{cat_\varphi} \cdot c_{i_{cat,\varphi}}) E_{i_{cat,\varphi}} + \rho_{cat} \cdot E_{cat_\varphi} \right) \overrightarrow{U}_{cat_\varphi} \right] \\
& \text{Convection due to sorbent chemisorption and sorbent solids} \\
& - \vec{\nabla} \cdot \left[\psi_\varphi \cdot (1 - \varepsilon_\varphi) \alpha_\varphi \cdot \left(\sum_{i=1}^{N_C} (S_{sorb_\varphi} \cdot c_{i_{sorb,\varphi}}) E_{i_{sorb,\varphi}} + \rho_{sorb} \cdot E_{sorb_\varphi} \right) \overrightarrow{U}_{sorb_\varphi} \right] \\
& \text{Gas Accumulation} \quad \text{Accumulation due to catalyst chemisorption and catalyst solids} \\
& = \frac{\partial}{\partial t} \left[\psi_\varphi \cdot \varepsilon_\varphi \cdot \sum_{i=1}^{N_C} C_{i_\varphi} \cdot E_{i_\varphi} \right] + \frac{\partial}{\partial t} \left[\psi_\varphi \cdot (1 - \varepsilon_\varphi) (1 - \alpha_\varphi) \cdot \left(\sum_{i=1}^{N_C} (S_{cat_\varphi} \cdot c_{i_{cat,\varphi}}) E_{i_{cat,\varphi}} + \rho_{cat} \cdot E_{cat_\varphi} \right) \right] \\
& \text{Accumulation due to sorbent chemisorption and sorbent solids} \\
& + \frac{\partial}{\partial t} \left[\psi_\varphi \cdot (1 - \varepsilon_\varphi) \alpha_\varphi \cdot \left(\sum_{i=1}^{N_C} (S_{sorb_\varphi} \cdot c_{i_{sorb,\varphi}}) E_{i_{sorb,\varphi}} + \rho_{sorb} \cdot E_{sorb_\varphi} \right) \right].
\end{aligned}$$

(1.18)

for $\varphi=1,2,\dots,N_\varphi$

E.T. = Energy Transport

The state variable for Equation 18, is the temperature T_φ , because E_{i_φ} corresponds to the internal energy of component i which can be expressed using the ideal relation: $E_{i_\varphi} \approx H_{i_\varphi} \approx C_{p_{i_\varphi}} \cdot T_\varphi$ (i.e. it is assumed that the residual value of the internal energy is negligible and that there is no change of phase).

1.2.3.4. Pressure balance

Strategies differing greatly in complexity have been proposed in the literature to account for the hydrodynamics and pressure variation in fluidized-bed reactors. In this work a simplified differential pressure balance is implemented where the reactor pressure drop is assumed to be

solely caused by the static head of phase φ . A simplified differential pressure balance in the z direction is then given by:

$$A_z \cdot \left\{ (P_\varphi)_{(x,y,z)} - (P_\varphi)_{(x,y,z+\Delta z)} \right\} + \Delta V \cdot \{ \rho_\varphi \cdot g \} = 0, \quad (1.19)$$

The density of phase (φ) can be calculated using the void fraction:

$$\rho_\varphi = \left[(1 - \varepsilon_\varphi) \cdot (1 - \alpha_\varphi) \cdot \rho_{cat} \cdot g \right] + \left[(1 - \varepsilon_\varphi) \cdot \alpha_\varphi \cdot \rho_{sorb} \cdot g \right] + \left[\varepsilon_\varphi \cdot \rho_{gas} \cdot g \right] \quad (1.20)$$

Dividing both sides by ΔV and taking the limit as $\Delta V \rightarrow 0$, we obtain:

Pressure drop	Catalyst gravity	Sorbent gravity	Gas gravity		(1.21)
$-\frac{dP_\varphi}{dz} = \left[(1 - \varepsilon_\varphi) \cdot (1 - \alpha_\varphi) \cdot \rho_{cat} \cdot g \right] + \left[(1 - \varepsilon_\varphi) \cdot \alpha_\varphi \cdot \rho_{sorb} \cdot g \right] + \left[\varepsilon_\varphi \cdot \rho_{gas} \cdot g \right]$					

where the phase voidage and gas density are distributed functions. Note that Equation 1.21 originates from an overall momentum balance where inter-particle forces, the time rate of increase of momentum, the rate of momentum addition by convection and shear forces (Bird *et al.*, 2002) are all neglected.

1.2.3.5. Boundary and initial conditions

The differential control volume of phase φ may or may not have external exchange with other phases and in general has no external exchange with the system surroundings. Interaction with the surroundings must therefore be included in the boundary conditions. These boundary conditions need be specified according to the geometric arrangement of the specific physical system. Where appropriate, they may assume axial symmetry, zero flux at the walls and Danckwerts (1953) criteria at closed entrances and exits. Typical boundary conditions are provided in Table 1.1.

Table 1-1. Typical boundary and initial conditions.

Boundary Conditions				
	Boundary condition	Location	Equations	
Typical boundary conditions	Input convective flow	At $z = 0$	$-D_{i\varphi_z} \cdot \frac{\partial C_{i\varphi}}{\partial z} = U_{gas\varphi_z} \cdot (C_{i\varphi}]_{0^-} - C_{i\varphi}]_{0^+})$	
			$-K_z \cdot \frac{\partial T_\varphi}{\partial z} = U_{gas\varphi_z} \cdot \rho_\varphi \cdot \langle C_{p\varphi} \rangle \cdot (T_\varphi]_{0^-} - T_\varphi]_{0^+})$	
			$P_\varphi = (P_\varphi)_{(z=0)}$	
	Output convective flow	At $z = z_R$	$\frac{\partial C_{i\varphi}}{\partial z} = 0$	$\frac{\partial T_\varphi}{\partial z} = 0$
Radial symmetry	At $r = 0$	$\frac{\partial C_{i\varphi}}{\partial r} = 0$	$\frac{\partial T_\varphi}{\partial r} = 0$	
Insulation at reactor wall	At $r = \frac{D}{2}$	$\frac{\partial C_{i\varphi}}{\partial r} = 0$	$\frac{\partial T_\varphi}{\partial r} = 0$	
Other boundary conditions	Selective membrane flux	Depending on reactor geometry	For permeable species:	$-D_{i\varphi_x} \cdot \frac{\partial C_{i\varphi}}{\partial x} + U_{gas\varphi} \cdot C_{i\varphi}]_{0^+} = J_{i\varphi}$ e.g. For hydrogen membranes: $J_{H_2\varphi} = \frac{k_{H_2}}{\delta_{H_2}} \cdot e^{\left(\frac{-E_{H_2}}{R \cdot T_\varphi}\right)} \cdot \left(\sqrt{P_{H_2\varphi}} - \sqrt{P_{H_2M}}\right)$
			For all other species:	$\frac{\partial C_{i\varphi}}{\partial x} = 0$
	Constant (fixed) state variable	Depending on reactor geometry	$C_{i\varphi} = (C_{i\varphi})_{x=x_0}$	$T_\varphi = (T_\varphi)_{x=x_0}$
Heat exchange (heating or cooling)	Depending on reactor geometry	$-K_z \cdot \frac{\partial T_\varphi}{\partial z} + U_{gas\varphi} \cdot \rho_\varphi \cdot \langle C_{p\varphi} \rangle \cdot T_\varphi]_{0^+} = q_\varphi$ e.g. For heating: $q_\varphi = h_{heaters} \cdot (T_\varphi - T_{heaters})$ e.g. For heat losses and cooling: $q_\varphi = -h_{Surf} \cdot (T_{Surf} - T_\infty) - h_{Cool} \cdot (T_\varphi - T_{Cool})$ $- \epsilon_M \cdot \sigma \cdot (T_{Surf}^4 - T_{SUR}^4)$		
Initial Conditions				
	Initial condition	Time	Equations	
	Initial condition according to start-up policy	At $t = 0$	$C_{i\varphi} = (C_{i\varphi})_{(t=0)}$	$T_\varphi = (T_\varphi)_{(t=0)}$ $P_\varphi = (P_\varphi)_{(t=0)}$

1.2.4. Model Reduction and Simplification

The general model described above needs to be simplified for practical implementation for the specific system being studied. By eliminating some terms in the general equations, simpler cases can be simulated with the desired level of complexity. Many terms are not applicable to all systems, for example due to the unavailability of certain reactor parameters and due to computational constraints. For many fluidized-bed systems, features such as gas chemisorption, gas sorption (no sorbent particles in the solids), intra-particle diffusion (e.g. for small particles), selective membrane permeation (only applicable for membrane reactors), diffusive and crossflow interphase heat transfer can be excluded from the practical computer simulations, thereby simplifying the model. The later chapters of this thesis explain the kinds of model reduction implemented to simulate several systems of interest.

1.2.5. Simulation Tools

1.2.5.1. Software and codes

The model is solved for different systems utilizing such software as: *COMSOL Multiphysics 3.4* (for Multi-physics modelling, formerly known as *FEMLAB*) and *Matlab 7.5* (Technical computing language). Appendix A briefly describes the most important numerical solvers implemented in the Matlab and COMSOL Multiphysics codes. Software such as *FORTRAN 90* (very fast programming language), and *Mathematica 5.0* (Integrated environment for technical computing specialized for symbolic calculations) were also tested during the initial stages of this research, but because of their features, *Matlab* and *COMSOL* were chosen for model simulation. The software *EASY-FIT* was used to fit proprietary kinetic parameters for an oxychlorination reaction in Chapter 7, by fitting laboratory data provided by LG Chem to ordinary differential equations. In addition, *LogMein* software was used to remotely monitor case study simulations when needed.

1.2.5.1.1. Programming based on Matlab®

An in-house code was developed for the simulation of two-phase, steady state distributed cases accounting for features such as feed distribution, balancing interphase crossflow, membrane removal and probabilistic averaging and catalytic reaction. *Matlab* was chosen for this task

because of its very robust solvers for algebraic and ordinary differential equations, as well as its customizability and ability to seamlessly handle arrays and figures. Figures 1.4 and 1.5 schematically represent the code in a detailed schematic manner.

A study was performed to test the different *Matlab* solvers (i.e. *ode45*, *ode23*, *ode113*, *ode15s*, *ode23s*, *ode23*, *ode23tb* and *ode15i*). It was concluded that the routines *ode15s* and *ode23tb* were stable when other solvers crashed. Also it was found that *ode15s* provided less numerical noise in the distributed profiles after running several tests. Therefore, *ode15s* with user defined parameters (absolute tolerance, relative tolerance, maximum step-size, minimum step-size, initial step-size) was chosen as the optimum routine. It was found to be necessary, however, to adapt the mesh to allow for smaller step sizes in the lower section of the bed where reaction rates are quite high, and at any top distributor where an input pulse was injected into the bed. This process was performed on a trial and error basis to make sure that the solution was independent of the solver parameters. The solver was provided with a “*non-negative*” statement to stabilize the concentrations of the chemical species. Moreover, two versions of *Matlab* were compared to identify the most adequate software. Although the solutions based on *Matlab* 7.5 (of 2007) appeared to be ~20% slower than for *Matlab* 6.5 (of 2002), the former was chosen since it provides greater solver stability and control of numerical parameters.

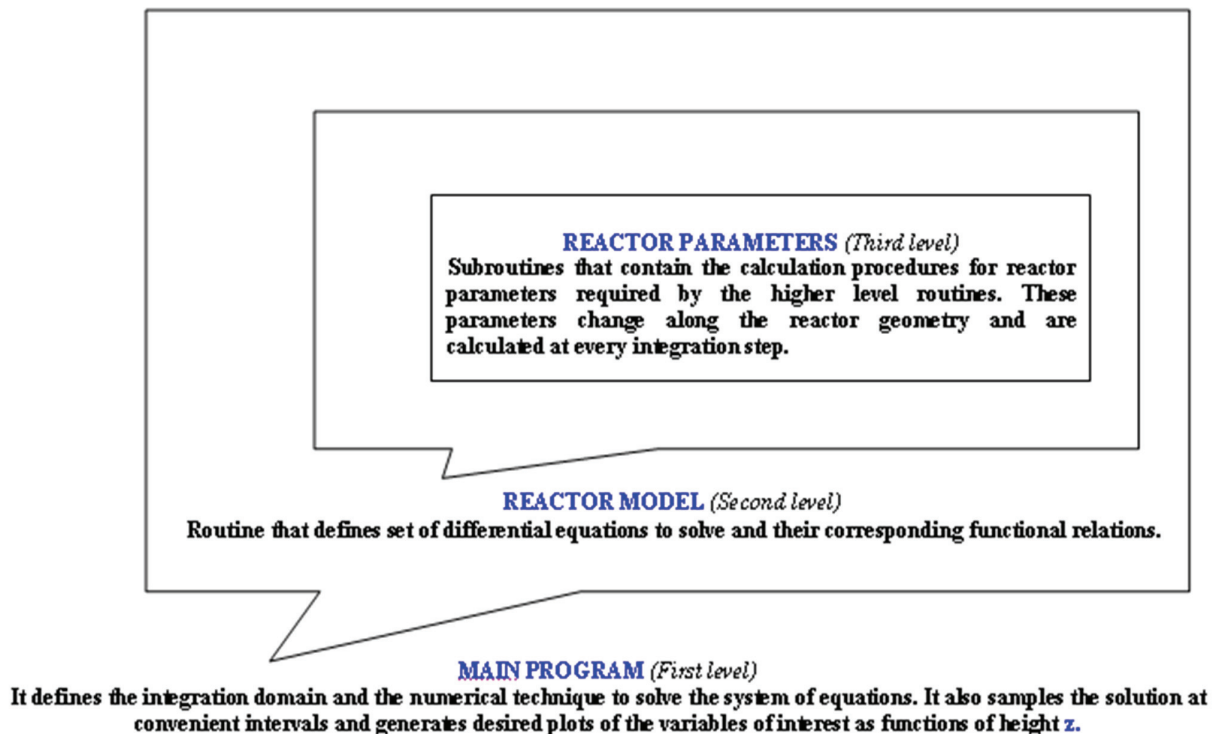


Figure 1.4. Schematic representation of Matlab code levels.

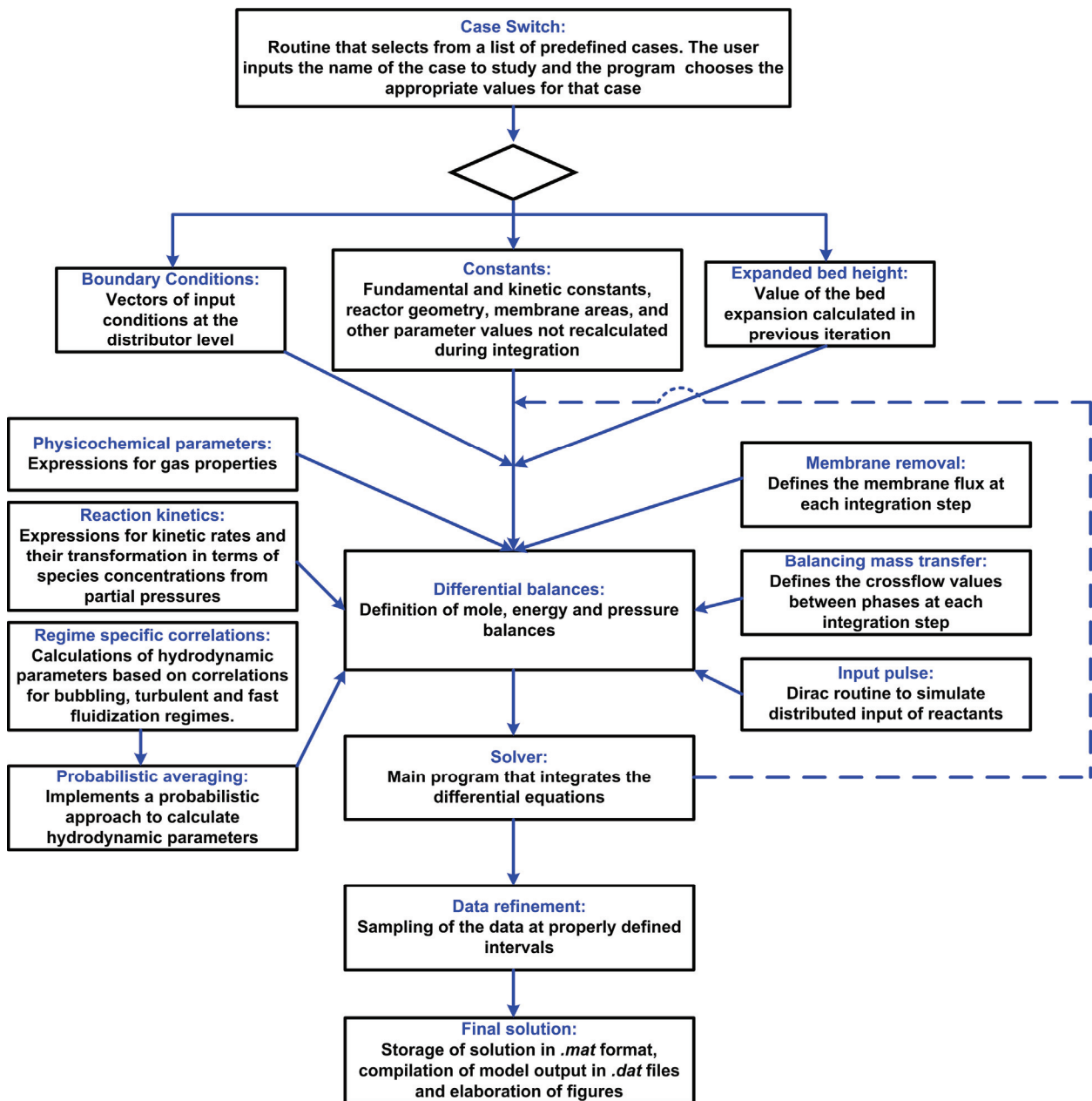


Figure 1.5. Schematic representation of the developed program.

1.2.5.1.2. Programming based on COMSOL Multiphysics®

COMSOL Multiphysics was implemented to simulate all cases requiring partial differential equations (i.e. multidimensional models and time-dependent models). The PDE general form was utilized during the initial stages of the modelling work, but the more efficient *COMSOL Chemical Engineering Module* was preferred due to its optimized solvers. For two-phase simulations, the code consisted of three interrelated multiphysics routines (i.e. *Convection-Diffusion* for the H- and L-phases, and *Convection-Conduction* for the entire bed). The mesh was

constructed with Lagrange-quadratic elements, and each simulation was completed with less than 100,000 degrees of freedom due to computational constraints.

Some important features of *COMSOL* are:

- It can be used for a wide range of physical phenomena and chemical processes.
- It is equation oriented.
- It facilitates models systems involving coupled phenomena.
- It features a *Chemical Engineering Module* for standard applications.

Although the modelling capabilities of *COMSOL* are undeniable, the overall simulation experience was frustrating due to frequent crashes caused by numerical instabilities. Clearly, considerable work needs to be done by the software developers to significantly improve the solver capabilities. *COMSOL Direct solvers* such as *UMFPACK* and *SPOOLES* were frequently unstable and inefficient. Therefore, the linear systems were solved by *GMRES* using Incomplete LU preconditioners with asymmetric matrices.

To overcome the convergence issues of *COMSOL*, a parametric solver was implemented. This parametric solver stored the solution of a simple case, and then used it as initial guess for more complex cases. For instance, for fast chemical reactions, the model was initially solved with the catalyst activity equal to zero. This solution was used as an interpolated initial guess for the next simulation that allowed for a catalyst activity of 0.1%. Similarly the second solution was taken as starting value for simulations of larger catalyst activities until 100% was reached.

1.2.5.2. Verification of numerical solutions

The results from each simulation were tested to verify the correctness and robustness of the numerical solution. Solver parameters such as the mesh size and time step were varied to study their effect on the modeling results. A test of *mesh-independence* was undertaken for each system of study, and the overall performance variables changed by less than 1 percent.

To improve the convergence of the model in the time-dependent simulations, the Courant–Friedrichs–Lewy (Courant *et al.*, 1928, 1967) condition is taken into account:

$$C = \frac{U \cdot \Delta t}{\Delta x} \tag{1.22}$$

where C is the Courant number which is advised to be set below 1.0.

1.2.5.3. Computational resources

Computers continue to follow Moore's law (i.e. "the number of transistors that can be placed inexpensively on an integrated circuit has increased exponentially, doubling approximately every two years"). Table 1.2 was created to put this thesis in context of the actual technology available at this point in time. The computers listed in this table were used to perform case studies since the solutions often required several hours to converge.

Table 1-2. Computers used for case studies.

#	Name	Processor	RAM*	Operating system
1.	Hewlet Packard (HP) Dual Workstation XW8000 SCSI	Dual Intel Xeon 2*3.06 GHz	3.0 GB	Windows XP SP3
2.	NCIX PC	Intel Core 2 Duo, 2.33GHz	4.0 GB	Windows XP SP3
3.	Acer Aspire E700	Intel Core 2 Quad, 2.4 GHz	2.0 GB	Windows Vista
4.	Dell Vostro 1310	Intel Core 2 Duo, 1.8GHz	4.0 GB	Windows XP SP3
5.	Dell Precision Workstation	Intel Pentium 4, 3.4 GHz	3.0 GB	Windows XP SP2
6.	HP nx9500	Intel Pentium 4, 3.0 GHz	2.0 GB	Windows XP SP3
7.	PC	Intel Pentium 4, 2.8 GHz	2.0 GB	Windows XP SP3
8.	PC	Intel Pentium 4, 2.6 GHz	1.5 GB	Windows XP SP3

*The *paging file* (virtual RAM on hard drive) size was increased to the maximum value allowed in all of the computers. This value is 8.19 GB for the HP Workstation and 4.1 GB in all others.

1.3. References

Abba, I.A., Grace, J.R. and Bi, H.T. (2002). Variable-gas-density fluidized bed reactor model for catalytic processes. *Chem. Eng. Sci.*, 57, 4797-4807.

Abba, I.A., Grace, J.R., Bi, H.T. and Thompson, M.L. (2003b). Spanning the flow regimes: A generic fluidized bed reactor model. *AIChE J.*, 49, 1838-1848.

Aris, R. (1961). *The optimal design of chemical reactors; a study in dynamic programming.* Academic Press, New York.

Aris, R. (1978). *Mathematical modelling techniques.* Pitman Publisher Limited, London.

Aris, R. (1999). *Mathematical modeling: A chemical engineer's perspective.* Academic Press, San Diego.

Bird, R.B., Stewart, W.E. and Lightfoot, E.N. (2002). *Transport phenomena.* Wiley, New York

Chen, Z., Po, F., Grace, J.R., Lim, C.J., Elnashaie, S.S.E.H., Mahecha-Botero, A., Rakib, M., Shirasaki, Y. and Yasuda, I. (2008). Sorbent enhanced/membrane-assisted steam methane reforming. *Chem. Eng. Sci.*, 63, 170-182.

Chen, Z., Yan, Y. and Elnashaie, S.S.E.H. (2004). Catalyst deactivation and engineering control for steam-reforming of higher hydrocarbons in a novel membrane reformer. *Chem. Eng. Sci.*, 59, 1965-1978.

Courant, R., Friedrichs, K. and Lewy, H. (1928). Über die partiellen Differenzgleichungen der mathematischen Physik. *Mathematische Annalen*, 100, 32-74.

Courant, R., Friedrichs, K. and Lewy, H. (1967). On the partial difference equations of mathematical physics. English translation of the 1928 German original. *IBM Journal*, 215-234.

Danckwerts, P.V. (1953). Continuous flow systems: Distribution of residence times. *Chem. Eng. Sci.*, 2, 1-13.

Elnashaie, S.S.E.H. and Elshishini, S.S. (1993). Modelling, simulation and optimization of industrial fixed-bed catalytic reactors. Gordon and Breach science publishers, Amsterdam.

Froment, G.F. and Bischoff, K.B. (1990). Chemical reactor design and analysis. Wiley, New York.

Garhyan, P., Elnashaie, S.S.E.H. and Mahecha-Botero, A. (2006). Complex bifurcation/chaotic behavior of acetylcholinesterase and choline-acetyltransferase enzymes system. *Applied Mathematical Modelling*, 30, 824-853.

Grace, J.R., Abba, I.A., Bi, H.T. and Thompson, M.L. (1999a). Fluidized bed catalytic reactor modeling across the flow regimes. *Can. J. Chem. Eng.*, 77, 305-311.

Haken, H. (1983). Synergetics: Introduction and advanced topics. Springer-Verlag, Berlin.

Johnsen, K., Ryu, H.J., Grace, J.R. and Lim, C.J. (2006). Sorption-enhanced steam reforming of methane in a fluidized bed reactor with dolomite as CO₂-acceptor. *Chem. Eng. Sci.*, 61, 1195-1202.

Mahecha-Botero, A., Boyd, T., Gulamhusein, A., Comyn, N., Lim, C.J., Grace, J.R., Shirasaki, Y. and Yasuda, I. (2008a). Pure hydrogen generation in a fluidized bed membrane reactor: Experimental findings. *Chem. Eng. Sci.*, 63, 2752-2762.

Mahecha-Botero, A., Chen, Z., Grace, J.R., Elnashaie, S.S.E.H., Lim, C.J., Rakib, M., Yasuda, I. and Shirasaki, Y. (2008b). Comparison of fluidized bed flow regimes for steam methane reforming in membrane reactors: A simulation study. *Chem. Eng. Sci.*, In review.

Mahecha-Botero, A., Garhyan, P. and Elnashaie, S.S.E.H. (2004). Bifurcation and chaotic behaviour of a coupled acetylcholinesterase/choline acetyltransferase diffusion-reaction enzymes system. *Chem. Eng. Sci.*, 59, 581-597.

Mahecha-Botero, A., Garhyan, P. and Elnashaie, S.S.E.H. (2005a). Modeling, bifurcation and chaotic behaviour of a coupled acetylcholinesterase/choline acetyltransferase enzymes neurocycle. *Mathematical and Computer Modelling*, 41, 655-678.

Mahecha-Botero, A., Garhyan, P. and Elnashaie, S.S.E.H. (2005b). Modeling, bifurcation and stabilization of a membrane fermentor for the production of ethanol. *Mathematical and Computer Modelling*, 41, 391-406.

Mahecha-Botero, A., Garhyan, P. and Elnashaie, S.S.E.H. (2005c). Non-linear characteristics of a membrane fermentor for ethanol production and their implications. *Nonlinear Analysis: Real World Applications*, 7, 432-457.

Mahecha-Botero, A., Grace, J.R., Elnashaie, S.S.E.H. and Lim, C.J. (2006a). Comprehensive modelling of gas fluidized-bed reactors allowing for transients, multiple flow regimes and selective removal of species. *Int. J. Chem. Reactor Eng.*, 4, A11.

Mahecha-Botero, A., Grace, J.R., Elnashaie, S.S.E.H. and Lim, C.J. (2007a). A comprehensive approach to reaction engineering. *Int. J. Chem. Reactor Eng.*, 5: A17.

Mahecha-Botero, A., Grace, J.R., Elnashaie, S.S.E.H. and Lim, C.J. (2007b). Time scale analysis of a fluidized-bed reactor based on a generalized dynamic model. in *Fluidization XII*. Eds. Bi, X.T., Berruti, F. and Pugsley, T. Harrison Hot Springs, BC, Canada., ECI Symposium Series. United Engineering Conferences, Brooklyn. http://services.bepress.com/eci/fluidization_xii/76.

Mahecha-Botero, A., Grace, J.R., Elnashaie, S.S.E.H. and Lim, C.J. (2009a). Advances in modelling of fluidized-bed catalytic reactors: A comprehensive review. *Chem. Eng. Commun.*, in press.

Mahecha-Botero, A., Grace, J.R., Lim, C.J., Elnashaie, S.S.E.H., Boyd, T. and Gulamhusein, A. (2009b). Pure hydrogen generation in a fluidized bed membrane reactor: Application of the generalized comprehensive reactor model. *Chem. Eng. Sci.*, in review.

Post, D.E. and Votta, L.G. (2005). Computational science demands a new paradigm. *Phys. Today*, 58, 35-41.

Rodrigues, A.E. and Minceva, M. (2005). Modelling and simulation in chemical engineering : Tools for process innovation. *Comput. Chem. Eng.* , 29, 1167-1183.

Sit, S.P. and Grace, J.R. (1981). Effect of bubble interaction on interphase mass transfer in gas fluidized beds. *Chem. Eng. Sci.*, 36, 327-335.

2. MODELLING OF FLUIDIZED-BED CATALYTIC REACTORS: A COMPREHENSIVE REVIEW ²

2.1. Introduction

A number of fluidized-bed catalytic reactor models have been proposed during the past half century based on conservation equations as well as empirical relations. This chapter presents a comprehensive review of these models, ranging from the classical and pioneering reactor models found in the literature to the current state-of-the-art. Each model incorporates a different set of assumptions, leading to different expressions for simulating reactor performance. Thirty-nine models are analyzed according to the characteristics of their conservation equations and their underlying assumptions, by reducing each model to a sequential combination of assumptions. This review contributes to the elucidation process for choosing the appropriate model to simulate a specific fluidized-bed reactor.

The present review analyzes existing reactor models based on the characteristics of their conservation equations and also discusses each of their assumptions. We focus on non-CFD models dedicated to predict reactive multiphase flow, although a few CFD models are also commented on when addressing the future of reactor modelling. We limit our attention to catalytic processes, since non-catalytic fluidized-bed reactors require extra elements as explained by Grace (1986b). We also treat only cases where the fluidizing fluid is a gas, i.e. we do not consider liquid-solid or gas-liquid-solid fluidized-bed reactors.

Each reactor model is based on an interpretation of key aspects of reactor mechanics as well as a series of assumptions (which may or not be valid). This review is intended to be useful to designers choosing a model for a specific system, as well as for researchers to indicate where significant progress is needed.

² A version of this Chapter will be published as: *Mahecha-Botero, A., Grace, J.R., Elnashaie, S.S.E.H. and Lim, C.J. (2009). "Advances in modelling of fluidized-bed catalytic reactors: A comprehensive review". Chemical Engineering Communications, in press.*

2.2. Previous Fluidized-Bed Reactor Modelling Reviews

The concept of two-phase fluidization (Toomey and Johnstone, 1952) and the first fluidized-bed reactor model (Shen and Johnstone, 1955) date from the 1950's. Most previous reviews of fluidized-bed reactor modelling were performed in the 1970's and 1980's, and deal only with reactors operating in the bubbling flow regime. Significant advances in reactor modelling have been attained in recent years which have not been covered in these reviews. Nevertheless, they are valuable references depicting the historical developments in reactor modelling.

In the review of fluidized-bed reactor models by Grace (1971), models were classified in two groups according to their complexity. Models composed of two parallel one-dimensional single-phase reactors containing three or more parameters were defined as "simple models", whereas models based on the properties of single rising bubbles were denoted as "bubbling bed models". Key assumptions were tabulated for models existing at time, showing that competing models differed in multiple features. It was indicated that the higher complexity of the latter group did not necessarily lead to better predictions. Furthermore it was recommended that more research was needed regarding bubble interactions and gas-solid contacting, topics which continue to be important in reactor modelling.

Calderbank and Toor (1971) discussed how the reacting system can define the complexity of model required. For example, very fast reactions are likely to be controlled by gas exchange whereas slow reacting systems may be modeled as simple CSTRs. This work also derived analytical expressions based on the Orcutt *et al.* (1962) model using different assumptions regarding mixing, extending earlier work (Toor and Calderbank, 1967). The authors concluded that gas exchange, bubble size and coalescence and gas bypassing are key variables affecting reactor performance.

Pyle (1972) pointed out the need to establish features important or critical for reactor design and questioned whether those features could be incorporated into reactor models. The models of Partridge and Rowe (1966), Davidson and Harrison (1963) and Kunii and Levenspiel (1969) were analyzed qualitatively.

Yates (1975) qualitatively discussed some models based on the same classification scheme proposed by Grace (1971). This work was further extended by Yates (1983), providing more details about the applicability of the most popular models of that time.

Three levels of sophistication were proposed by Horio and Wen (1977) to classify reactor models. The first consisted of two-phase models containing more than three adjustable experimental parameters, making them incapable of predicting behaviour at different scales. The second level used average parameters estimated from operating conditions in the middle of the reactor. The more complex third level comprised models that calculate parameters varying along the bed height. This review also suggested that for systems operating with a superficial gas velocity several times greater than U_{mf} , the prediction of dense phase concentrations is not very critical since the dense phase accounts for only a small fraction of the total gas flow.

Grace (1981) investigated the main focus of research in different decades, and presented a timeline of the most important topics studied since the 1940's. He classified a few models presented in a Symposium based on the phases considered, mixing in the emulsion phase, equimolar mass transfer, bubble size, time variation, isothermality and application.

Fane and Wen (1982) offered some practical advice on model application. They also gave some insights for gas-phase as well as gas-solid reactions according to the kinetics of the reaction. The model classification utilized the method proposed by Horio and Wen (1977).

Van Swaaij (1985) implemented the classification system of Horio and Wen (1977). He also provided some analysis of the model characteristics divided into three levels of complexity. Difficulties commonly encountered in identifying key fluidization parameters such as bubble size and rising velocity estimation, were also mentioned. The author emphasized the importance of calculating reactor parameters as a function of vertical coordinate instead of adopting average values. Other features such as bubble rising velocity, bubble hold-up, interfacial area and mass transfer coefficients were also discussed.

Grace (1986b) identified some key advantages (e.g. temperature uniformity, high heat transfer, solids handling capabilities, low pressure drop, large/small scale of operation) and disadvantages (e.g. backmixing, bypassing, entrainment, attrition and complexity) of fluidized beds. He classified reactor models according to the number of phases accounted for (single-phase, two-phase and three phase) and provided some useful analytical expressions for simple reaction systems. Several popular models were also analyzed according to their main characteristics.

Grace (1986c) presented a complete review of the features of two-phase models of the time. Special attention was given to the models of May (1959), Orcutt *et al.* (1962) and Grace

(1984). This review contains information on fluidization regimes, phase division, equimolar mass transfer, dense phase mixing and bubble size estimation. Models for specific flow regimes were also discussed.

Grace and Lim (1997) summarized models for circulating fluidized-bed reactors. The authors classified high-velocity fluidized-bed reactor models as single-region one-dimensional and core/annulus models. These two kinds of models were further classified based on their capability of calculating axial gradients for their hydrodynamic parameters. Other non-conventional models were also summarized.

More recently Ho (2003) classified reactor models as pseudo-homogeneous, two-phase and multiple-region. A general overview of such models was given together with a listing of experimental investigations to obtain model parameters. The author emphasized the art aspect of multiphase modelling, indicating that no single model is likely to be applicable in all cases. Finally, Grace and Abba (2005) provided an overview of several aspects and problems associated with fluidized-bed reactor modelling.

2.3. Analysis of Fluidized-Bed Catalytic Reactor Models

Different authors have used various assumptions to model fluidized-bed reactors. Pioneering and more advanced models from the literature are described and analyzed below with special emphasis on their distinct assumptions. These characteristics and assumptions are used as building blocks that synergistically constitute each specific model.

To grasp the different models by means of the present analysis, Tables 2.1 and 2.2 must be used together. Table 2.1 contains the main characteristics and assumptions implemented by most workers. Each characteristic (i.e. letters **A** to **Z**) can be tackled using different possible approaches listed to its left (i.e. numbers). Table 2.1 classifies model characteristics in three main categories: general, and applicable to the mole, energy or pressure balances. Note that a given model may adopt more than one approach for a given characteristic. Table 2.2 assigns information from Table 2.1 to each of the models of study. If a characteristic corresponds to a specific phase (e.g. H and L pseudo-phases), this is reflected in the rows from Table 2.2. The abbreviation “NS” (denoting Not Specified) is used if the proposers of a particular model did not

Table 2-1. Common model assumptions. Table 2-2 shows how these assumptions apply to specific models.

General Assumptions		
Characteristic	Approach	
A) Phase division	1. Single phase (i.e. lumped, pseudo-homogeneous system)	
	2. Two phases: high density (dense, emulsion, H-phase, or discontinuous phase) and low density (bubble, dilute, void, L-phase, or continuous phase)	
	3. Three phases (i.e. bubble, cloud and emulsion)	
	4. Includes membranes for selective input/removal of species	
B) Flow regime	1. Bubbling regime	
	2. Slugging regime	
	3. Turbulent regime	
	4. Fast fluidization regime	
C) Process or reaction	1. General equations	12. Ethylene hydrogenation
	2. Ozone decomposition	13. Isomerization of cyclopropane
	3. Fluid catalytic cracking	14. Methanol to gasoline (MTG)
	4. Maleic anhydride	15. Natural gas combustion
	5. Oxychlorination	16. Ethylene synthesis
	6. Phthalic anhydride	17. Ammonia oxidation
	7. Ore roasting	18. Polyethylene production
	8. Steam reforming	19. Cracking of cumene
	9. Decomposition of nitrous oxide	20. Dehydrogenation of n-butane
	10. Cumene dealkylation	21. Polyolefin production
	11. Hydrogenation of ethylene	
D) Membranes	1. Hydrogen membranes	
	2. Oxygen membranes	
	3. Tubular	
	4. Flat	
	5. Membranes assumed to be 100% selective	
E) Regions	1. Distributor zone	
	2. Dense bed	
	3. Freeboard	
	4. Regenerator	
	5. Oxidation and reduction zones	
	6. Feed distribution along reactor	
F) Mixing characteristics	1. Stagnant phase	
	2. Perfectly mixed phase (i.e. CSTR)	
	3. Plug flow	
	4. Phase modeled as a series of perfectly mixed stages	
	5. Axially dispersed flow	
G) Chemical reaction	1. No chemical reaction	
	2. Constant catalyst activity	
	3. Catalyst deactivation accounted for	
	4. Effectiveness factor neglected	
	5. Includes catalyst effectiveness factor	
	6. Specific first order kinetic expression	

Table 2-1 (Cont'd). Common model assumptions: (b) Mole balance.

Mole Balance	
Characteristic	Approach
H) Independent variables for differential equations	1. Time (i.e. time dependent model)
	2. Axial coordinate (i.e. 1-D model)
	3. Axial and radial coordinates (i.e. 2-D model)
	4. Three spatial coordinates (i.e. 3-D model)
I) Convection	1. Continuous gas convection accounted for
	2. Accounts for species convection chemisorbed on catalyst surface
	3. Accounts for species convection chemisorbed on sorbent surface
J) Dispersion	1. Neglect gas dispersion
	2. Axial dispersion accounted for
	3. Anisotropic gas dispersion (axial and radial)
	4. Assumes perfect mixing
K) Equi-molar interphase mass transfer	1. Equi-molar mass transfer neglected
	2. Mass transfer accounted for
L) Interphase balancing mass transfer	1. Balancing mass transfer neglected
	2. Unidirectional balancing mass transfer dependent on the moles generated by chemical reaction
	3. Balancing mass transfer defined by keeping constant H-phase volumetric flow
	4. Bidirectional distributed balancing mass transfer affected the moles generated by chemical reaction, change of pressure, temperature, gas properties, membrane flux and changes in minimum fluidization velocity
	5. Balancing mass transfer significantly affects the results
	6. Balancing mass transfer does not affect the results
	7. Balancing mass transfer of solids
M) Chemical reaction	1. No chemical reaction
	2. Accounts for catalytic chemical reaction
N) Solids sorbent	1. Not considered
	2. Solids sorbent reactions (capture) accounted for
O) Species accumulation	1. Neglected (i.e. steady state equations)
	2. Accounts for gas accumulation
	3. Accounts for species accumulation due to catalyst chemisorption
	4. Accounts for species accumulation due to sorbent chemisorption
P) Gas volumetric Flow	1. Constant volumetric flow
	2. Volumetric flow affected by change in total number of moles
	3. Volumetric flow affected by changing temperature and pressure

Table 2-1 (Cont'd). Common model assumptions: (c) Energy and pressure balance.

Energy Balance	
Characteristic	Approach
Q) Overall	1. Isothermal system (No energy balance)
	2. One overall energy balance
	3. One energy balance for each phase
	4. Adiabatic system
	5. Allows for heat exchange
R) Independent variables for differential equations	1. Time (i.e. time dependent model)
	2. Axial coordinate (i.e. 1-D model)
	3. Axial and radial coordinates (i.e. 2-D model)
	4. Three coordinates (i.e. 3-D model)
S) Heat convection	1. Continuous energy transport due to gas convection accounted for
	2. Energy transport due to species convection chemisorbed on catalyst surface accounted for
	3. Energy transport due to species convection chemisorbed on sorbent surface accounted for
	4. Energy transport due to catalyst solids convection accounted for
	5. Energy transport due to solids sorbent convection accounted for
T) Heat dispersion	1. Heat dispersion neglected
	2. Axial heat dispersion
	3. Anisotropic heat dispersion (axial and radial)
	4. Assumes perfect mixing
U) Heat transfer due to equi-molar mass transfer	1. Heat transfer neglected
	2. Heat transfer accounted for
	3. Overall interphase heat transfer coefficient utilized
V) Heat transfer due to balancing mass transfer	1. Crossflow of energy neglected
	2. Bidirectional distributed crossflow of energy
	3. Overall interphase heat transfer coefficient utilized instead
W) Chemical reaction heat generation	1. Heat generation due to chemical reaction ignored
	2. Accounts for heat generation due to catalytic chemical reaction
X) Solid sorption heat generation	1. Not considered
	2. Accounts for heat generation due to solids sorption
Y) Heat accumulation	1. Neglected (i.e. steady state equations)
	2. Accounts for accumulation of energy in gas phase
	3. Accounts for accumulation of energy due to chemisorption on the catalyst surface
	4. Accounts for accumulation of energy on the chemisorbed species in due to chemisorption on the sorbent surface
	5. Accounts for accumulation of energy in catalyst solids
	6. Accounts for accumulation of energy in solid sorbent
Pressure Balance	
Z) Pressure variation	1. Isobaric system (No pressure balance)
	2. Single pressure balance accounting for catalyst gravity
	3. Single pressure balance including catalyst, sorbent and gas gravity
	4. Computational fluid dynamics calculation of pressure distribution

Table 2-2. Summary of fluidized-bed models. A to Z below refer to Table 2-1 characteristics.

Model	Phase	Approach and Assumptions																									
		General						Mole Balance										Energy Balance								P. B.	
		A	B	C	D	E	F	G	H	I	J	K	L	M	N	O	P	Q	R	S	T	U	V	W	X	Y	Z
(Shen and Johnstone, 1955)	H-Phase	2	1	1,9	NA	2	3	2,4,6	2	1	1	2	1	2	1	1	1	3,5	2	1	1	3	3	1	1	1	NS
	L-Phase	2	1	1,9	NA	2	3	1	2	1	1	2	1	1	1	1	1		2	1	1	2	3	1	1	1	
(Mathis and Watson, 1956)	H-Phase	2	NS	1,10	NA	2	3	2,4,6	2	1	1	2	1	2	1	1	1	NS	NA	NS							
	L-Phase	2	NS	1,10	NA	2	3	2,4,6	2	1	1	2	1	2	1	1	1		NA								
(Lewis <i>et al.</i> , 1959)	H-Phase	2	NS	1,11	NA	2	1 or 2	3,4,6	NA	NA	1 or 4	2	1	2	1	1	1	NS	NA	NS							
	L-Phase	2	NS	1,11	NA	2	3	3,4,6	2	1	1	2	1	2	1	1	1		NA								
Esso model (May, 1959)	H-Phase	2	NS	1,3	NA	2	5	2,4,6	2	1	2	2	1	2	1	1	1	NS	NA	NS							
	L-Phase	2	NS	1,3	NA	2	3	1	2	1	1	2	1	1	1	1	1		NA								
(Gomezplata and Shuster, 1960)	H-Phase	2	1	1,19	NA	2	3	2,4,6	2	1	1	2	1	2	1	1	1	1	NA	1							
	L-Phase	2	1	1,19	NA	2	3	1	2	1	1	2	1	1	1	1	1		NA								
(Lanneau, 1960)	H-Phase	2	1	1	NA	2	3	2,4,6	2	1	1	2	7	2	1	1	1	NS	NA	NS							
	L-Phase	2	1	1	NA	2	3	2,4,6	2	1	1	2	7	2	1	1	1		NA								
Shell model: (van Deemter, 1961)	H-Phase	2	1	1	NA	2	1	2,4,6	2	NA	2	2	1	2	1	1	NS	NS	NA	NS							
	L-Phase	2	1	1	NA	2	3	1	2	1	1	2	1	1	1	1	NS		NA								
(Orcutt <i>et al.</i> , 1962; Davidson and Harrison, 1963)	H-Phase	2	1	1,2	NA	2	2	2,4,6	NA	NA	4	2	1	2	1	1	NS	NS	NA	NS							
	L-Phase	2	1	1,2	NA	2	3	1	2	1	1	2	1	1	1	1	NS		NA								
(Mamuro and Muchi, 1965)	H-Phase	2	1	1	NA	2	4	2,4,6	NA	NA	4	2	1	2	1	1	1	NS	NA	NS							
	L-Phase	2	1	1	NA	2	4	1	NA	NA	4	2	1	1	1	1	1		NA								

*NS: Not specified, NA: Not applicable

Table 2.2 (Cont'd). Summary of fluidized-bed models. A to Z below refer to Table 2-1 characteristics.

Model	Phase	Approach and Assumptions																									
		General						Mole Balance								Energy Balance								P. B.			
		A	B	C	D	E	F	G	H	I	J	K	L	M	N	O	P	Q	R	S	T	U	V	W	X	Y	Z
(Kobayashi and Arai, 1966)	H-Phase	2	1	1	NA	2	2,3 or 5	2,4,6	2	1	1 or 2	2	1	2	1	1	1	NS	NA	NA	NA	NA	NA	NA	NA	NA	NS
	L-Phase						3	1	2	1	1	2	1	1	1	1											
(Partridge and Rowe, 1966)	H-Phase	2	1	1,2	NA	2	3	2,4,6	2	1	1	2	1	2	1	1	NS	NS	NA	NA	NA	NA	NA	NA	NA	NA	NS
	L-Phase						3	2,4,6	2	1	1	2	1	2	1	1	NS										
(Mireur and Bischoff, 1967)	H-Phase	2	1	1,2,12,13	NA	2	5	2,4,6	1,2	1	2	2	1	2	1	2	1	NS	NA	NA	NA	NA	NA	NA	NA	NA	NS
	L-Phase						3	1	1,2	1	1	2	1	1	1	2	1										
(Toor and Calderbank, 1967)	H-Phase	2	1	1	NA	2	(2,3 or 5)	2,4,6	2	1	1 or 2	2	1	2	1	1	NS	NS	NA	NA	NA	NA	NA	NA	NA	NA	NS
	L-Phase						3 or 4	2,4,6	2	1	1 or 2	2	1	2	1	1	NS										
(Hovmand and Davidson, 1968)	H-Phase	2	2	1,2,12,17	NA	2	3	2,4,6	NA	NA	4	2	1	2	1	1	1	NS	NA	NA	NA	NA	NA	NA	NA	NA	NS
	L-Phase						3	1	2	1	1	2	1	1	1	1	1										
(Kunii and Levenspiel, 1969)	Emulsion	3	1	1,2 and others	NA	2	2	2,4,6	NA	NA	4	2	1	2	1	1	NS	NS	NA	NA	NA	NA	NA	NA	NA	NA	NS
	Cloud						2	2,4,6	NA	NA	4	2	1	2	1	1	NS										
	Bubble						3	2,4,6	2	1	1	2	1	2	1	1	NS										
(Kato and Wen, 1969)	H-Phase	2	1	1,2,9	NA	1,2	4	2,4	NA	1	4	2	1	2	1	1	NS	NS	NA	NA	NA	NA	NA	NA	NA	NA	NS
	L-Phase						4	2,4	NA	1	4	2	1	2	1	1	NS										
(Fryer and Potter, 1972)	Emulsion	3	1	1,2	NA	2	3	3,4,6	2	1	1	2	1	2	1	1	NS	NS	NA	NA	NA	NA	NA	NA	NA	NA	NS
	Cloud-wake						3	3,4,6	2	1	1	2	1	2	1	1	NS										
	Bubble						3	1	2	1	1	2	1	1	1	1	NS										
(Grace and De Lasa, 1978)	H-Phase	3	1	1,2	NA	1,2	2	2,4,6	NA	NA	4	2	1	2	1	1	1	NS	NA	NA	NA	NA	NA	NA	NA	NA	NS
	Jet Phase						3	1	2	1	1	2	1	1	1	1	1										
	L-Phase						3	1	2	1	1	2	1	1	1	1	1										

*NS: Not specified, NA: Not applicable

Table 2-2 (Cont'd). Summary of fluidized-bed models. A to Z below refer to Table 2-1 characteristics.

Model	Phase	Approach and Assumptions																									
		General						Mole Balance										Energy Balance								P. B.	
		A	B	C	D	E	F	G	H	I	J	K	L	M	N	O	P	Q	R	S	T	U	V	W	X	Y	Z
(Raghuraman and Potter, 1978)	Emulsion						3	3,4,6	2	1	1	2	1	2	1	1	NS										
	Cloud-wake	3	2	1,2	NA	2	3	3,4,6	2	1	1	2	1	2	1	1	NS	NS	NA	NS							
	Bubble						3	1	2	1	1	2	1	1	1	1	NS										
(Werther, 1980)	Bulk of suspension						3	2,4,6	2	1	1	film trans	1	2	1	1	1										
	Film	3	1	1,9,12,17	NA	2	1	2,4,6	2	NA	2	film trans	1	2	1	1	1	NS	NA	NS							
	Bubble						3	1	3	1	1	film trans	1	1	1	1	1										
(Yates, 1983)	H-Phase						5	2,4,6	1,2	1	2	2	1	2	1	1 or 2	NS										
	L-Phase	2	NS	1	NA	2	5	2,4,6	1,2	1	2	2	1	1 or 2	1	1 or 2	NS	NS	NA	NS							
(Grace, 1984)	H-Phase						2	2,4,6	2	1	1	2	1	2	1	1	NS										
	L-Phase	2	1	1	NA	2	3	2,4,6	2	1	1	2	1	2	1	1	NS	NS	NA	NS							
(Mobil model (Edwards and Avidan, 1986))	One-phase	1	3	1,14	NA	2	5	NS	1,2	1	2	NA	NA	2	1	2	1	NS	NA	NS							
(Foka et al., 1994)	One-phase	1	1,3	1,15	NA	2	2,3 or 5	NS	2	1	2	NA	NA	2	1	1	NS	NS	NA	NS							
(Schoenfelder et al., 1996)	H-Phase						5	2,4,6	3	1	3	2	1	2	1	1	NS										
	L-Phase	2	4	1,2	NA	1,2,3	5	2,4,6	3	1	3	2	1	2	1	1	NS	1	NA	1							
(Adris et al., 1997)	H-Phase						3	2,4	2	1	1	2	1	2	1	1	1										
	L-Phase	2	1	1,8	1,3,5	2,3	3	2,4	2	1	1	2	1	2	1	1	1	1	NA	1							
(Thompson et al., 1999)	H-Phase						5	2,4	2	1	2	2	1	2	1	1	1										
	L-Phase	2	1,3	1,2	NA	2	5	2,4	2	1	2	2	1	2	1	1	1	1	NA	1							

*NS: Not specified, NA: Not applicable

Table 2-2 (Cont'd). Summary of fluidized-bed models. A to Z below refer to Table 2-1 characteristics.

Model	Phase	Approach and Assumptions																									
		General						Mole Balance										Energy Balance								P. B.	
		A	B	C	D	E	F	G	H	I	J	K	L	M	N	O	P	Q	R	S	T	U	V	W	X	Y	Z
(Chaouki <i>et al.</i> , 1999)	H-Phase	2	3	1,16	NA	2	5	2,4	1,2	1	2	2	1	2	1	2	1	1	NA	NA	NA	NA	NA	NA	NA	1	
	L-Phase						5	2,4	1,2	1	2	2	1	2	1	2	1	1	NA	NA	NA	NA	NA	NA	NA	1	
(Soler <i>et al.</i> , 2001)	H-Phase	2	1	1,20	NA	2,5	3	3,4	1,2	1	1	2	7	2	1	2	1	1	NA	NA	NA	NA	NA	NA	NA	1	
	L-Phase						3	3,4	1,2	1	1	2	7	2	1	2	1	1	NA	NA	NA	NA	NA	NA	NA	1	
Abba <i>et al.</i> (2002; 2003b)	H-Phase	2	1,3,4	1,2,5	NA	2,3	5	2,4	3	1	2	2	1	2	1	1	3	2,5	2	1	2	NA	NA	2	1	1	2
	L-Phase						5	2,4	3	1	2	2	1	2	1	1	3	2,5	2	1	2	NA	NA	2	1	1	2
(Abba <i>et al.</i> , 2003a)	H-Phase	2	1,3,4	1,8	1,3,5	2,3	5	2,4	2	1	2	2	3,6	2	1	1	3	2,5	2	1	2	NA	NA	2	1	1	2
	L-Phase						5	2,4	2	1	2	2	3,6	2	1	1	3	2,5	2	1	2	NA	NA	2	1	1	2
(Chen <i>et al.</i> , 2004)	One-phase	1	4	1,8	1,2,3,5	2,4	3	3,4	2	1	1	NA	NA	2	1	1	3	2,5	2	1,4	1	NA	NA	2	1	1	1
(Harshe <i>et al.</i> , 2004)	H-Phase	2	1	1,18	NA	2	4	3,4	1	1	4	2	1	2	1	2	NS	3,5	1	1,4	4	3	3	2	1	2	NS
	L-Phase						4	1	1	1	4	2	1	1	1	2	NS	3,5	1	1,4	4	3	3	1	1	2	NS
(Werther and Hartge, 2004)	H-Phase	2	1	1	NA	2	3	2,4,6	1,2	1	2	2	1	2	1	2	1	NS	NS	NA	NA	NA	NA	NA	NA	NA	NS
	L-Phase						3	1	1,2	1	2	2	1	1	1	2	1	NS	NS	NA	NA	NA	NA	NA	NA	NA	NS
(Kiashemshaki <i>et al.</i> , 2006)	H-Phase	2	NS	1,18	NA	2	4	3,4	NA	NA	4	2	1	2	1	1	NS	3,5	NA	1,4	4	2	1	2	1	1	4
	L-Phase						3	3,4	2	1	1	2	1	2	1	1	NS	3,5	2	1,4	1	2	1	2	1	1	4
(Souza-Santos, 2007, 2008)	H-Phase	2	1	1	NA	2,3	3	NS	2	1	NS	2	NS	2	NS	1	NS	3,5	2	1	NS	NS	NS	2	NS	1	NS
	L-Phase						3	NS	2	1	NS	2	NS	2	NS	1	NS	3,5	2	1	NS	NS	NS	2	NS	1	NS

*NS: Not specified, NA: Not applicable

Table 2-2 (Cont'd). Summary of fluidized-bed models. A to Z below refer to Table 2-1 characteristics.

Model	Phase	Approach and Assumptions																									
		General						Mole Balance										Energy Balance									P. B.
		A	B	C	D	E	F	G	H	I	J	K	L	M	N	O	P	Q	R	S	T	U	V	W	X	Y	Z
(Constantine au <i>et al.</i> , 2007)	H-Phase	2	12	1,7	NA	2	3	2,4,6	2	1	1	2	2	2	1	1	3	NS	NA	NA	NA	NA	NA	NA	NA	NA	NS
	L-Phase	2	12	1,7	NA	2	3	2,4,6	2	1	1	2	2	2	1	1	3										
Chen <i>et al.</i> (2003a; 2003b, c; 2008)	One-phase	1	4	1,8	1,2,3 or 4,5	2,4	3	2,4	2	1	1	NA	NA	2	2	1	3	2,5	2	1,4	1	NA	NA	2	1	1	1
(Dompazis <i>et al.</i> , 2008)	H-Phase	2	1	1,21	NA	2	4	3,5	1	1	4	2	7	2	1	2	NS	3,5	1	1,4	4	3	3	2	1	2,5	NS
	L-Phase	2	1	1,21	NA	2	4	1	1	1	4	2	7	1	1	2	NS		1	1,4	4	3	3	1	1	2,5	
Mahecha- Botero <i>et al.</i> (2006a, 2007a; 2008b; 2009b)	H-Phase	2	1,3,4	1,4,5, 6,8	1,4,5	2,3,6	5	3,5	1,(2, 3 or 4)	1,2,3	3	2	4,5	2	2	2,3,4	3	35	1,(2, 3 or 4)	1,2,3, 4,5	2 or 3	2	2	2	2	2,3,4 ,5,6	3
	L-Phase						5	3,5	1,(2, 3 or 4)	1,2,3	3	2	4,5	2	2	2,3,4	3		1,(2, 3 or 4)	1,2,3, 4,5	2 or 3	2	2	2	2	2,3,4 ,5,6	

*NS: Not specified, NA: Not applicable

explicitly address a given characteristic. “NA” is used if the characteristic is not applicable, or not available in the specific work. A brief explanation of the meaningfulness of the assumptions found in Tables 2.1 and implemented in Table 2.2 is provided in this section. In addition, the conservation equations from a few representative models (from different time periods and varying greatly in complexity) are presented in Table 2.3.

A. Phase division

In this review we focus on models that divide the reactor contents using a pseudo-phase approach. This means that the control volumes for the conservation balances may include both gas and solid particles. The term “phase” or “pseudo-phase” is utilized in this context to identify distinctive features or regions (e.g. bubbles or clusters) within the gas/solid reactor.

Defining how to divide the reactor materials in the model is a key step during model development. The simplest choice is to assume that the reactor behaves as a single-phase system. Implicitly this choice assumes that all bed properties are the same for all parts of the reactor. Even for a simple first order reaction, it is unlikely to be possible to correctly predict the overall reactant conversion using a single-phase model since the fluidized-bed reactor performance is not necessarily intermediate between single-phase perfect mixing and plug flow. Nevertheless, a single-phase approach may be a valid approximation for very slow (kinetically controlled) reacting systems whose performance is unaffected by the division of phases. Single-phase reactors may also be used for equilibrium-controlled reactors (Gibbs reactors) and may provide a reasonable approximation when fluidized-bed reactors operating well within the turbulent fluidization regime. Some single phase reactor models are presented by Edwards and Avidan (1986), Foka *et al.* (1994) and Chen *et al.* (2004).

The most common method for fluidized-bed reactor modelling utilizes a two-phase representation originated by the two-phase theory proposed by Toomey and Johnstone (1952) in which it is assumed that all or most of the gas in excess to that needed for minimum fluidization creates a low-density or L-phase (also called bubble, dilute, void or discontinuous phase). Dilutely dispersed particles may also be included in this phase. The remaining matter is assigned to a high density or H-phase (also identified as dense, particulate, emulsion or continuous phase).

Table 2-3. Summary of conservation equations for selected models.

Model	Conservation Equations	
(Orcutt <i>et al.</i> , 1962), (Davidson and Harrison, 1963)	<p>Mole balance: low-density phase: $\beta U dC_{Ab} = k_q (C_{Ad} - C_{Ab}) a_b \varepsilon_b dz$</p>	<p>high-density phase: $(1 - \beta)U(C_{Ain} - C_{Ad}) + \int_0^H (C_{Ab} - C_{Ad}) a_b \varepsilon_b dz = (1 - \varepsilon_b)(1 - \varepsilon_{mf}) H k_n C_{Ad}^n$</p>
(Partridge and Rowe, 1966)	<p>Mole balance: low-density phase: $U_c \frac{dC_{Ac}}{dz} + k_{bce} (C_{Ac} - C_{Ae}) + k_c C_{Acw}$</p>	<p>high-density phase: $U_e \frac{dC_{Ae}}{dz} + k_{bce} \frac{A_c}{A_e} (C_{Ae} - C_{Ac}) f_b + k_e C_{Ae}$</p>
(van Deemter, 1967)	<p>Mole balance: low-density phase: $\frac{\partial C_b}{\partial \xi} + N_\alpha (C_b - C_e) = 0$</p>	<p>high-density phase: $N_\alpha (C_b - C_e) - \frac{1}{N_E} \frac{\partial^2 C_b}{\partial \xi^2} + N_r C_e = 0$</p>
(Kunii and Levenspiel, 1969)	<p>Mole balance: Bubble-phase: $-U_b \frac{dC_{Ab}}{dz} = \gamma_b K_r C_{Ab} + k_{bc} (C_{Ab} - C_{Ac})$</p> <p>Emulsion-phase: $K_{ce} (C_{Ac} - C_{Ae}) = \gamma_e K_r C_{Ae}$</p>	<p>Cloud-wake-phase: $k_{bc} (C_{Ac} - C_{Ab}) = \gamma_c K_r C_{Ac} + K_{ce} (C_{Ac} - C_{Ae})$</p>
(Kato and Wen, 1969)	<p>Mole balance: low-density phase: $(AUC_{Ab})_{n-1} = [K'_0 V_b (C_{Ab} - C_{Ae})]_n + (r_b V_e)_n + (AUC_{Ab})_n$</p>	<p>high-density phase: $[K'_0 V_b (C_{Ab} - C_{Ae})]_n = (r_e V_e)_n$</p>

Table 2-3 (Cont'd). Summary of conservation equations for selected models.

Model	Conservation Equations	
(Yates, 1983)	<p>Mole balance: low-density phase:</p> $\frac{\partial C_{Ae}}{\partial t} - E \frac{\partial^2 C_{Ae}}{\partial z^2} + U_e \frac{\partial C_{Ae}}{\partial z} + k_{be}(C_{Ae} - C_{Ab}) + k_e C_{Ae} = 0$	<p>high-density phase:</p> $\frac{\partial C_{Ab}}{\partial t} - D \frac{\partial^2 C_{Ab}}{\partial z^2} + U_b \frac{\partial C_{Ab}}{\partial z} + k_{be}(C_{Ab} - C_{Ae}) + k_b C_{Ab} = 0$
(Grace, 1984)	<p>Mole balance: low-density phase:</p> $U \frac{dC_{Ab}}{dz} + k_q a_b \varepsilon_b (C_{Ab} - C_{Ad}) + k_n \phi_b C_{Ab}^n = 0$	<p>high-density phase:</p> $k_q a_b \varepsilon_b (C_{Ad} - C_{Ab}) + k_n \phi_d C_{Ad}^n = 0$
(Adris <i>et al.</i> , 1997)	<p>Mole balance: low-density phase:</p> $\frac{dn_{ib}}{dh} = k_{iq} a_b \varepsilon_b A (C_{id} - C_{ib}) + \phi_b \rho_s AR_{ib}$	<p>high-density phase:</p> $\frac{dn_{id}}{dh} = k_{iq} a_b \varepsilon_b A (C_{ib} - C_{id}) + \phi_d \rho_s AR_{id}$ <p>plus a balance for the hydrogen membranes.</p>
(Thompson <i>et al.</i> , 1999)	<p>Mole balance: low-density phase:</p> $u_L \frac{\partial C_{iL}}{\partial z} - \mathcal{D}_{z,L} \frac{\partial^2 C_{iL}}{\partial z^2} + k_q a_I \varepsilon_L (C_{iL} - C_{iH}) + \rho_L R_{iL} = 0$	<p>high-density phase:</p> $u_H \frac{\partial C_{iH}}{\partial z} - \mathcal{D}_{z,H} \frac{\partial^2 C_{iH}}{\partial z^2} - \left(\frac{\psi_L}{\psi_H} \right) k_q a_I \varepsilon_L (C_{iL} - C_{iH}) + \rho_H R_{iH} = 0$
(Abba <i>et al.</i> , 2003b)	<p>Mole balance: low-density phase:</p> $\psi_L u_L \frac{\partial C_{iL}}{\partial z} - \psi_L \mathcal{D}_{zg,L} \frac{\partial^2 C_{iL}}{\partial z^2} - \frac{\psi_L \mathcal{D}_{rg,L}}{r} \frac{\partial}{\partial r} \left(r \frac{\partial C_{iL}}{\partial r} \right) + k_{LH} a_I \psi_L (C_{iL} - C_{iH}) + \psi_L \rho_L Rate_{iL} = 0$ <p>high-density phase:</p> $\psi_H u_H \frac{\partial C_{iH}}{\partial z} - \psi_H \mathcal{D}_{zg,H} \frac{\partial^2 C_{iH}}{\partial z^2} - \frac{\psi_H \mathcal{D}_{rg,H}}{r} \frac{\partial}{\partial r} \left(r \frac{\partial C_{iH}}{\partial r} \right) + k_{LH} a_I \psi_L (C_{iH} - C_{iL}) + \psi_H \rho_H Rate_{iH} = 0$ <p>Energy balance:</p> $\frac{d}{dz} \left(k_e \frac{dT}{dz} \right) - C_{pg} \rho_g U \frac{dT}{dz} + \phi \sum_k^{N_r} (\Delta H_{k,i=basert} \times Rate_{i=basert}) - hA_s (T - T_{cool}) = 0$ <p>Pressure balance: $-\frac{dP}{dz} = \rho_p g (1 - \varepsilon)$</p>	

Table 2-3 (Cont'd). Summary of conservation equations for selected models.

Model	Conservation Equations
<p>(Chen <i>et al.</i>, 2004)</p>	<p>Mole balance: Single phase, including a balance for the hydrogen and oxygen membranes.</p> $\frac{dF_i}{dt} = \rho_c A_c (1 - \varepsilon) \sum_j \sigma_{ij} r_j + \pi N_i d_i J_i$ <p>Energy balance:</p> $\frac{dT}{dt} = \frac{\sum_j r_j (\Delta H_j) \rho_c (1 - \varepsilon) A_c + \dot{Q}}{\sum_i F_i C_{p_i}}$
<p>Mahecha-Botero <i>et al.</i> (2006a, 2007a; 2008b; 2009b). See also Section 1.2.</p>	<p>Mole balance:</p> <div style="border: 1px solid black; padding: 10px;"> <p>Gas Convection</p> $-\vec{\nabla} \cdot [\psi_\varphi \cdot \varepsilon_\varphi \cdot C_{i_\varphi} \cdot \vec{U}_{gas_\varphi}] + \left[\psi_\varphi \cdot \sum_{\substack{n=1 \\ n \neq \varphi}}^{N_\varphi} a_{I(n \rightarrow \varphi)} \cdot k_{c_{i_\varphi, (n \rightarrow \varphi)}} \cdot (C_{i_n} - C_{i_\varphi}) \right] - \left[\psi_\varphi \cdot \sum_{\substack{n=1 \\ n \neq \varphi}}^{N_\varphi} v_{Bulk(\varphi \rightarrow n)} \cdot C_{i_\varphi} \right]$ <p>Balancing M.T. to φ</p> $+ \left[\psi_n \cdot \sum_{\substack{n=1 \\ n \neq \varphi}}^{N_\varphi} v_{Bulk(n \rightarrow \varphi)} \cdot C_{i_n} \right] + \left[\psi_\varphi \cdot (1 - \varepsilon_\varphi) (1 - \alpha_\varphi) \cdot \rho_{cat} \cdot \sum_{j=1}^{N_{R_{cat}}} v_{ij_{cat, \varphi}} \cdot \Omega_{j_{cat, \varphi}} \cdot a_{j_{cat, \varphi}} \cdot r'_{j_{cat, \varphi}} \right]$ <p>Sorbent reaction generation/consumption</p> $+ \left[\psi_\varphi \cdot (1 - \varepsilon_\varphi) \alpha_\varphi \cdot \rho_{sorb} \cdot \sum_{j=1}^{N_{R_{sorb}}} v_{ij_{sorb, \varphi}} \cdot \Omega_{j_{sorb, \varphi}} \cdot a_{j_{sorb, \varphi}} \cdot r'_{j_{sorb, \varphi}} \right] - \vec{\nabla} \cdot [\psi_\varphi \cdot \varepsilon_\varphi \cdot \vec{N}_{i_\varphi}]$ <p>Convection due to catalyst chemisorption</p> $-\vec{\nabla} \cdot [\psi_\varphi \cdot (1 - \varepsilon_\varphi) (1 - \alpha_\varphi) (S_{cat_\varphi} \cdot c_{i_{cat, \varphi}}) \vec{U}_{cat_\varphi}] + \vec{\nabla} \cdot [\psi_\varphi \cdot (1 - \varepsilon_\varphi) \alpha_\varphi (S_{sorb_\varphi} \cdot c_{i_{sorb, \varphi}}) \vec{U}_{sorb_\varphi}]$ <p>Convection due to sorbent chemisorption</p> <p>Gas accumulation Accumulation due to catalyst chemisorption Accumulation due to sorbent chemisorption</p> $= \frac{\partial}{\partial t} [\psi_\varphi \cdot \varepsilon_\varphi \cdot C_{i_\varphi}] + \frac{\partial}{\partial t} [\psi_\varphi \cdot (1 - \varepsilon_\varphi) (1 - \alpha_\varphi) (S_{cat_\varphi} \cdot c_{i_{cat, \varphi}})] + \frac{\partial}{\partial t} [\psi_\varphi \cdot (1 - \varepsilon_\varphi) \alpha_\varphi (S_{sorb_\varphi} \cdot c_{i_{sorb, \varphi}})]$ </div> <p>for $i=1, 2, \dots, N_C$ and for $\varphi=1, 2, \dots, N_\varphi$</p> <p>Pressure balance:</p> <div style="border: 1px solid black; padding: 10px;"> <p>Pressure drop Catalyst gravity Sorbent gravity Gas gravity</p> $-\frac{dP_\varphi}{dz} = [(1 - \varepsilon_\varphi) \cdot (1 - \alpha_\varphi) \cdot \rho_{cat} \cdot g] + [(1 - \varepsilon_\varphi) \cdot \alpha_\varphi \cdot \rho_{sorb} \cdot g] + [\varepsilon_\varphi \cdot \rho_{gas} \cdot g]$ </div>

Table 2-3 (Cont'd). Summary of conservation equations for selected models.

Model	Conservation Equations
<p>Mahecha-Botero <i>et al.</i> (2006a, 2007a; 2008b; 2009b). See also Section 1.2.</p>	<p>Energy balance:</p> $ \begin{aligned} & -\vec{\nabla} \cdot \left[\psi_{\varphi} \cdot \varepsilon_{\varphi} \cdot \left(\sum_{i=1}^{N_C} C_{i\varphi} \cdot E_{i\varphi} \right) \overrightarrow{U}_{gas\varphi} \right] + \left[\sum_{i=1}^{N_C} \psi_{\varphi} \cdot \left(\sum_{\substack{n=1 \\ n \neq \varphi}}^{N_{\varphi}} a_{I(n \rightarrow \varphi)} \cdot k_{c_{i,(n \rightarrow \varphi)}} \cdot (C_{i_n} - C_{i\varphi}) \right) E_{i_{\varphi n}} \right] \\ & \text{E.T. from Balancing Crossflow from } \varphi \left[\sum_{i=1}^{N_C} \psi_{\varphi} \cdot \left(\sum_{\substack{n=1 \\ n \neq \varphi}}^{N_{\varphi}} v_{Bulk(\varphi \rightarrow n)} \cdot C_{i\varphi} \right) E_{i\varphi} \right] + \left[\psi_{\varphi} \cdot (1 - \varepsilon_{\varphi}) (1 - \alpha_{\varphi}) \cdot \rho_{cat} \cdot \sum_{j=1}^{N_{Rcat}} \Delta H_{jcat} \cdot \Omega_{jcat,\varphi} \cdot a_{jcat,\varphi} \cdot r'_{jcat,\varphi} \right] \\ & \text{E.T. from Balancing Crossflow to } \varphi \left[\sum_{i=1}^{N_C} \psi_n \cdot \left(\sum_{\substack{n=1 \\ n \neq \varphi}}^{N_{\varphi}} v_{Bulk(n \rightarrow \varphi)} \cdot C_{i_n} \right) E_{i_n} \right] + \left[\psi_{\varphi} \cdot (1 - \varepsilon_{\varphi}) \alpha_{\varphi} \cdot \rho_{sorb} \cdot \sum_{j=1}^{N_{R_{sorb}}} \Delta H_{jsorb} \cdot \Omega_{jsorb,\varphi} \cdot a_{jsorb,\varphi} \cdot r'_{jsorb,\varphi} \right] \\ & \text{Heat dispersion} \left[\psi_{\varphi} \cdot \overrightarrow{q}_{\varphi} \right] - \vec{\nabla} \cdot \left[\psi_{\varphi} \cdot (1 - \varepsilon_{\varphi}) (1 - \alpha_{\varphi}) \cdot \left(\sum_{i=1}^{N_C} (S_{cat,\varphi} \cdot c_{i_{cat,\varphi}}) E_{i_{cat,\varphi}} + \rho_{cat} \cdot E_{cat,\varphi} \right) \overrightarrow{U}_{cat,\varphi} \right] \\ & \text{Convection due to sorbent chemisorption and sorbent solids} \left[\psi_{\varphi} \cdot (1 - \varepsilon_{\varphi}) \alpha_{\varphi} \cdot \left(\sum_{i=1}^{N_C} (S_{sorb,\varphi} \cdot c_{i_{sorb,\varphi}}) E_{i_{sorb,\varphi}} + \rho_{sorb} \cdot E_{sorb,\varphi} \right) \overrightarrow{U}_{sorb,\varphi} \right] \\ & = \frac{\partial}{\partial t} \left[\psi_{\varphi} \cdot \varepsilon_{\varphi} \cdot \sum_{i=1}^{N_C} C_{i\varphi} \cdot E_{i\varphi} \right] + \frac{\partial}{\partial t} \left[\psi_{\varphi} \cdot (1 - \varepsilon_{\varphi}) (1 - \alpha_{\varphi}) \cdot \left(\sum_{i=1}^{N_C} (S_{cat,\varphi} \cdot c_{i_{cat,\varphi}}) E_{i_{cat,\varphi}} + \rho_{cat} \cdot E_{cat,\varphi} \right) \right] \\ & + \frac{\partial}{\partial t} \left[\psi_{\varphi} \cdot (1 - \varepsilon_{\varphi}) \alpha_{\varphi} \cdot \left(\sum_{i=1}^{N_C} (S_{sorb,\varphi} \cdot c_{i_{sorb,\varphi}}) E_{i_{sorb,\varphi}} + \rho_{sorb} \cdot E_{sorb,\varphi} \right) \right]. \end{aligned} $ <p>for $\varphi=1, 2, \dots, N_{\varphi}$</p>

In this fashion the bed contents are divided in two interacting phases subject to mass and energy transport and exchange.

Other models divide the reactor into three phases, e.g. bubble, cloud and emulsion. Some 3-phase models were presented by Fryer and Potter (1972), Raghuraman and Potter (1978) and Kunii and Levenspiel (1991). These models are less widespread since they assume that mass transfer between the cloud and emulsion plays a key role, which in general is not true (Grace, 1981). Moreover, this type of model adds complexity to the simulation process without any clear gain in accuracy (Clift, 1983).

B. Flow regime

A fluidized bed may operate in quite distinct flow regimes according to its geometry, particle and gas properties, as well as fluid velocity. Discussions on the different flow regimes are found in (Grace, 1986a; Bi and Grace, 1995; Lim *et al.*, 1995; Grace *et al.*, 1999b). Figure 2.1 graphically explains the different flow regimes for gas-solid fluidized-beds. When the flow is very small, the fluid passes through the small voids within the packed solids without causing any appreciable solids movement. When the gas flow increases, the bed reaches the minimum fluidization condition ($U \geq U_{mf}$) and for group A particles in the Geldart classification, a homogeneous expansion can be observed. If the fluid velocity is further increased beyond the minimum bubbling, most excess gas forms bubbles, corresponding to bubbling fluidization. If at some point the bubble size is physically constrained by the reactor diameter (i.e. for tall narrow vessels) the bed operates in the slugging regime. As the fluid velocity is further increased, the bubbles disappear and the turbulent fluidization flow regime is established. As solids entrainment grows, a recirculation system is needed, and the reactor is said to be in the fast fluidization regime, characterized by dilute upward-flow in the core and descending streams at the wall. A further flow regime, dense suspension upflow, can also be reached at very high solids circulation rates (Grace *et al.*, 1999b; Kim *et al.*, 2004).

Although most industrial catalytic fluidized bed reactors operate in the turbulent fluidization flow regime (Bi *et al.*, 2000), this is not reflected in the history of reactor model development, where bubbling bed models are dominant as seen in Table 2.2. Nevertheless, the models of Edwards and Avidan (1986) and Foka *et al.* (1994) deal exclusively with turbulent beds. Models for the slugging regime have been proposed by Hovmand and Davidson (1968), Raghuraman and Potter (1978), Yates and Gregoire (1980) and Constantineau *et al.* (2007).

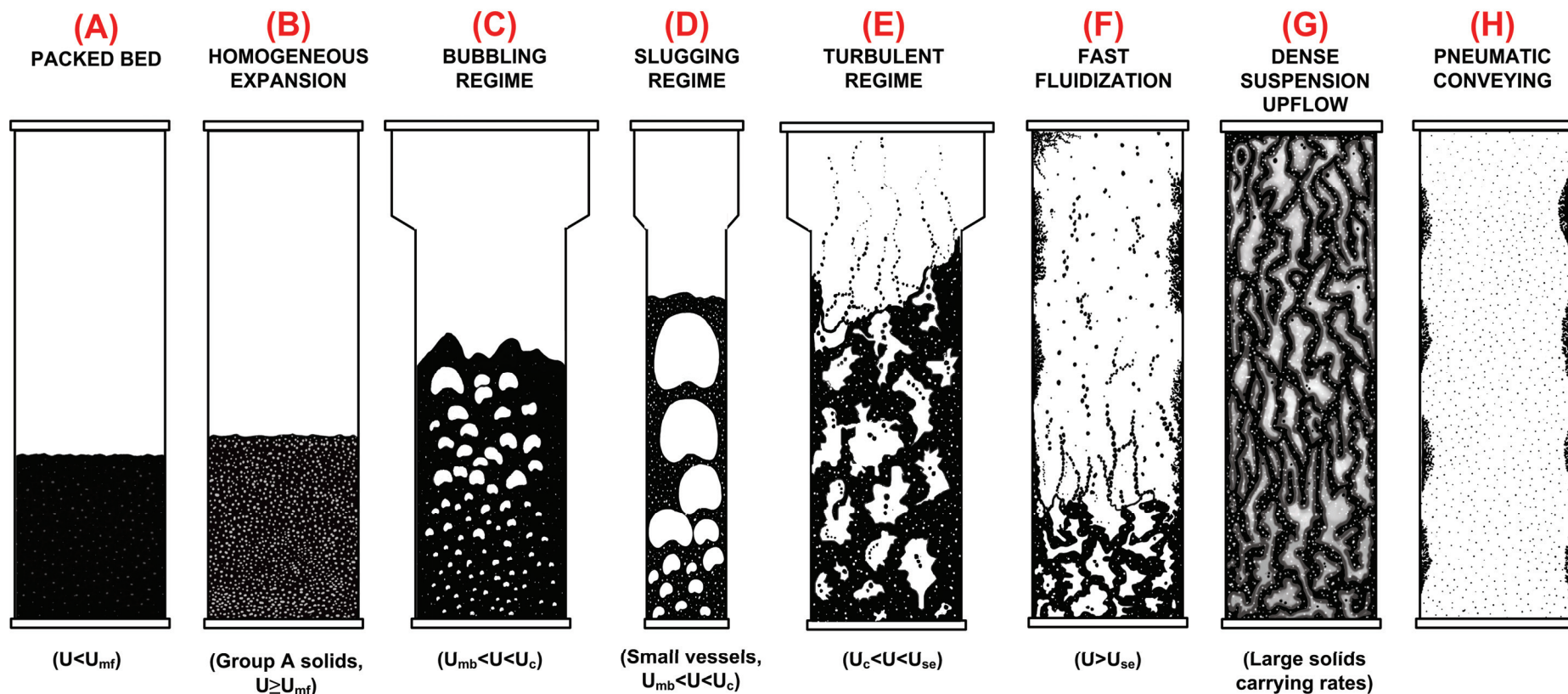


Figure 2.1. Fluidization regimes. (A) Packed bed; (B) Homogeneous / Bubble-free expansion (only for group A particles); (C) Bubbling fluidization regime; (D) Slugging fluidization regime (only in small scale vessels); (E) Turbulent fluidization regime; (F) Fast fluidization regime; (G) Dense suspension upflow (only for large solids carrying rates) (H) Pneumatic conveying. U = Superficial gas velocity; U_{mf} = Minimum fluidization velocity; U_{mb} = Minimum bubbling velocity; U_c = Velocity of transition from bubbling to turbulent fluidization regime; U_{se} = Velocity of transition from turbulent to fast fluidization regime / significant entrainment.

While most models are intended for a single flow regime, a few can deal with more than one regime, based on a probabilistic approach that allows for a continuous and smooth transition of flow regimes by means of averaging hydrodynamic and mass-transfer parameters. For instance, the model of Thompson *et al.* (1999) considers operation in both the bubbling and turbulent regimes. This was extended to a model covering bubbling, turbulent and fast fluidization regimes by Abba *et al.* (2002, 2003a; 2003b) and Mahecha-Botero *et al.* (2006a, 2007b; 2008a; 2008b; 2009b). This type of probabilistic modelling estimates a system's probability of being in a specific flow regime based on data showing regime-transition superficial velocities. These probabilities are then used as weighting factors to obtain local approximations of important fluidization parameters.

In practice, each flow regime has its own advantages and disadvantages:

- Surface-to-bed and bed-to-surface heat transfer tend to be most favourable for the turbulent fluidization flow regime and least favourable for fast fluidization.
- Axial dispersion of both gas and solids is likely to be greatest for bubbling fluidization, and least for fast fluidization.
- Losses of catalyst due to entrainment and wear of surfaces are likely to be greatest in the fast fluidization flow regime and least in the bubbling regime.
- Extra reactor volume is needed for the turbulent and bubbling flow regimes to provide a freeboard (particle disengagement) region.
- Vertical and radial temperature gradients tend to be greatest in the fast fluidization flow regime, but they also tend to be significant in the freeboard region above turbulent and bubbling fluidized beds, when unreacted gaseous species encounter particles there or when insulation is insufficient to minimize heat losses.
- The height-to-diameter ratio for the fast-fluidization flow regime tends to be much greater than for bubbling beds, with the turbulent regime case showing intermediate values. In practice, this means that fast fluidization is unlikely to be practical for small-scale systems, whereas bubbling beds are less likely to be viable for large commercial systems.

C. Process or reaction

Fluidized beds can be used to carry out many catalytic chemical reactions. The most common catalytic reactions in fluidized bed reactors are catalytic cracking, synthesis, partial oxidation, amoxidation, halogenation, reforming and polymerization processes. Many of the reactor models present general equations for reacting systems while others directly link their conservation equations with a specific chemical process. Simple first order reacting systems such as ozone decomposition have commonly been used to test reactor models (Fryer and Potter, 1972; Chavarie and Grace, 1975a, b, c), but real processes have more complex kinetics, frequently involving multiple reactions and hence selectivity/yield considerations. Section C of Table 2.2 lists some of the applications used by model developers.

D. Membranes

The introduction of membranes to fluidized bed reactor modelling has gained some attention in recent decades. Membranes are introduced to selectively add or remove chemical species. For example, chemical reactants may be added along the reactor to enhance the selectivity to a desired product, or reactor products may be selectively removed to favourably shift the equilibrium as indicated in LeChatelier's Principle (Thomsen, 2000). Membrane separation units can be installed inside the reactor to further increase process intensification. From a modeling perspective, membranes can be considered as providing an extra phase subject to mass transfer with the reactor gases.

E. Regions

A fluidized bed reactor may also be divided into a number of separate regions. For the most part, the models in the literature account for the main dense bed region which includes most of the particles, but which occupy less than half of the overall reactor volume. Models such as that suggested by Grace and De Lasa (1978) explicitly account for the behaviour at the distributor/grid region by means of a "jet-phase". Special consideration of this zone may be needed, e.g. to allow for fast reaction in the entrance region. In addition, some models account for the top (freeboard) section since it contains some solids with reduced interphase mass transfer resistance, and therefore accounts for some chemical reaction as discussed in (Souza-Santos, 2007, 2008). The solids content in the freeboard region is commonly assumed to experience an exponential decay in solids hold-up (Kunii and Levenspiel, 1991). Temperature

gradients can be significant at the top of the reactor, and this can cause reverse reaction for endothermic reactions as seen in Chapter 4. Other reactor models, such as that of Chen *et al.* (2003b, 2004), utilize a regeneration zone to refresh catalyst and burn out specific components. Specific oxidation and reduction zones are identified in the model of Soler *et al.* (2001). To treat systems with distributed reactant feed, the model of Chapter 4 simulates an input pulse that injects chemical species into the main reactor body.

F. Mixing characteristics

Different modelling techniques have been proposed to simulate the degree of mixing for each phase of a fluidized-bed reactor. In many cases the phases are modelled as being subject to axial dispersion. In some cases, the phase can be modelled as a CSTR, implying infinite dispersion (perfect mixing). At the opposite extreme, some models assume plug flow (i.e. zero dispersion). Given its high dispersion, the higher-density phase (H-phase) is more likely to be modelled as a perfectly mixed unit, whereas the lower-density phase (L-phase) is commonly simulated as plug flow. Well-mixed compartments in series provides another simple way of simulating intermediate degrees of mixing (Mamuro and Muchi, 1965; Kato and Wen, 1969; Harshe *et al.*, 2004; Kiashemshaki *et al.*, 2006).

G. Chemical reaction

The solids content of a phase determine whether chemical reaction needs to be considered in the conservation equations for that phase. Given the high solids content of the H-phase, all models covered in Table 2.2 account for chemical reaction in the H-phase, while many neglect reaction in the L-phase. In general, reaction should be considered in both phases, especially for fast reactions. If the reactions are quick enough, there can be significant conversion in the L-phase, even for very small solids concentrations within that phase.

The chemical reaction generation terms may also account for catalyst deactivation. The catalyst activity may be a function of time, site availability or the concentration of deactivation or fouling agents. For instance, as the reactions proceeds, residual carbon may be deposited on the catalyst surface reducing its catalytic activity (Chen *et al.*, 2004). If the catalyst particles are large enough, some reduction in catalytic function may be observed due to external and/or internal diffusional resistances, characterized by catalyst effectiveness factors. Table 2.2 also indicates whether the model has been solved analytically for specific (usually first order)

kinetics. For instance Grace (1984, 1986b) gave analytical expressions for simple first order consecutive ($A \rightarrow B \rightarrow C$) reactions and reversible ($A \leftrightarrow B$) reactions.

H. Independent variables for differential equations of the mole balance

The number of independent variables defines the complexity of the model equations. If time dependence is included, the model dynamic; otherwise it is steady-state. If spatial variations within the system are considered, the model is said to be distributed; otherwise it is lumped or perfectly mixed. If only one independent variable is considered, the mole balance requires the solution of ordinary differential equations, whereas more independent variables generate a system of partial differential equations. The most common independent variable is the vertical coordinate, allowing for one-dimensional distributed modeling. Some models also account for radial (or lateral) variation (e.g. Schoenfelder *et al.*, (1996)). Three-dimensional modelling is also possible, although model reduction is then desirable given the computational requirements for model solution (see Chapter 4). These independent variables define the species concentration profiles predicted by solving the model equations.

I. Mole balance convection

Most models consider gas convection in all phases in one way or another. Convection is related to the bulk movement of gas species, mostly in the axial direction (direction of flow). In the mole balance this term typically results in a first order derivative of the concentrations with respect to the axial coordinate. Convection may also occur if chemisorption of species takes place on the surface of catalyst or inert particles. In that case, there will be a net convection contribution from the movement of species attached to the solids.

J. Mole balance dispersion

Dispersion simulates the degree of mixing due to a concentration gradient. This term typically consists of a second order derivative of the concentrations with respect to the axial coordinate multiplied by an axial dispersion coefficient. This coefficient includes mixing due to several mechanisms, including molecular diffusion, solids mixing and Taylor dispersion (Li and Wu, 1991; Bi *et al.*, 2000) based on an analogy with Fick's Law of diffusion. Alternatively, diffusion could be based on Maxwell-Stephan diffusion (although this has not been the case in any of the models reviewed herein). If axial dispersion is neglected, the phase is said to be in plug-flow, a

common approximation for the L-phase. At the opposite extreme, if the dispersion coefficient tends to infinity, the phase is assumed to be perfectly mixed (sometimes adopted for the H-phase). If different coefficients are adopted for each direction (i.e. for two-dimensional and three-dimensional models) the dispersion is anisotropic. It is important to note that if dispersion is included there will be a discontinuity in concentrations at the entrance. If downflow is assumed in the H-phase (as in the model of Fryer and Potter, 1972) a split boundary condition is needed to solve the balance equations.

K. Equimolar interphase mass transfer

This term defines the conventional mass transfer between the reactor phases and is included in every multi-phase model. The mass transfer to/from the H-phase should be equal to the transfer from/to the L-phase to satisfy the overall reactor mass balance. The most widely accepted equation to estimate this mass transfer is that of Sit and Grace (1981) which includes terms for both diffusion and convection. In general a specific mass transfer coefficient must be calculated for each chemical species to account for the different mass transfer resistances encountered by molecules having different binary diffusion coefficients.

L. Interphase balancing mass transfer

This term accounts for exchange of mass between the phases required to preserve fluidization conditions in the bed. Although this balancing term has little or no effect on systems with negligible change in molar or volumetric flow, it can play an important role in systems where the molar flow changes significantly due to reaction or due to membranes. The volumetric flow is linked to change in the number of moles due to chemical reaction (Constantineau *et al.*, 2007), decrease of molar flow due to membrane removal, or changes in temperature and/or pressure (Mahecha-Botero *et al.*, 2009b). If there is a reduction of H-phase volumetric flow, the bed could de-fluidize rendering the model solution unusable. However, this is an area needing further research as it is not clear how quickly additional moles are transferred from one phase to another, or how a deficit in flow through the H-phase is made up from the L-phase.

M. Mole balance chemical reaction

This column in Table 2.2 defines whether or not the chemical reaction terms in item G are included in the mole balance equations for each phase.

N. Mole balance solids sorbent

A solid sorbent (i.e. non-catalytic) may be introduced to the fluidized bed to selectively capture chemical species. This feature is particularly useful for circulating systems coupled with a particle regenerator that allow for continuous operation. A recent example is the use of dolomite or limestone to capture carbon dioxide (Chen *et al.*, 2008) as an important step in CO₂ sequestration to reduce greenhouse gas emissions and hence grapple with global warming.

O. Mole balance species accumulation

Species accumulation can be accounted for if the model equations are time-dependent. These terms can be identified in the model equations by a derivative of the species concentrations in time. If species sorption on the catalyst surface is included, their accumulation terms should appear in the balance equations. The time-dependent behaviour of the system is defined by the start-up policy (i.e. initial conditions) implemented by the operators. Most reactor models assume steady state operation because of the added complexity of transient analysis and the tight process control of industrial applications.

P. Mole balance gas volumetric flow

The volumetric flow of gas may vary due to changes in number of moles due to reaction, feed distribution, introduction of membranes, and variations in temperature and pressure. Most pioneering models assume a constant volumetric flow and gas velocity along the reactor. This assumption is only desirable for systems with stoichiometry that do not have a net generation/consumption of moles, or for reactors operating with very dilute reactants as in the decomposition of ozone. To link all these variables with the volumetric flow, ideal gas behaviour can be assumed and, for convenience, the conservation equations may be solved in terms of molar flows.

Q. Energy balance overall assumptions

From a historic point of view, energy balances have received much less attention than mole balances during the 1955 to 2000 time period. Overall only about one literature model in five specifies some energy balance. This situation has been caused by the good heat transfer capabilities of fluidized beds coupled with the provision of external temperature control in many industrial applications. However, an energy balance is required for highly exothermic and

endothermic reactions because the temperature of operation is unknown, as well as for safety and operability reasons. Given the good internal heat transfer capabilities of fluidized-beds, a single energy balance is usually sufficient when allowance is made for energy effects coupled with mole balances.

R. Energy balance independent variables for differential equations

In Chapter 8 it is found that the heat transfer time scale is much larger than the mass-transfer/reaction time scale for a maleic anhydride reactor. This difference in time scales suggests that a pseudo-steady state assumption for the temperature profile would normally introduce very small errors to the model solution. Most models reviewed use the axial coordinate as their only independent variable in the energy balance.

S. Energy convection

Those models that consider a heat balance must estimate the energy transported due to convection. The most important term is the convection of the energy stored in the solid particles because they carry the majority of the reactor energy on a per-unit-volume basis due to the large heat capacity of the solids relative to that of the gas. A model may also account for the convection of energy associated with the gas species as well as components chemisorbed on solids surfaces.

T. Energy dispersion

A dispersion term may be included using Fourier's law of conduction. This expression ought to include the conduction coefficient of the solids/gas mixture. This parameter is a function of the solids dispersion coefficient (Matsen, 1985) which in turn is a function of the fluidization conditions, as defined by Lee and Kim, (1990) and Wei *et al.*,(1995).

U. Heat transfer due to equi-molar mass transfer

This term accounts for the energy transport associated with the mass transfer described in item K. The components that migrate from one phase to the other carry some energy depending on the local temperature, as well as a concentration gradient. This term is only needed for models that include independent phase energy balances. Some models prefer a heat transfer coefficient that accounts for items U and V in a single parameter.

V. Heat transfer due to balancing mass transfer

Bulk flow of matter from one phase, as described above in item L, results in the carrying of a certain amount of energy that should be accounted for. Clearly, large interphase mass transfer contributes temperature homogeneity across the phases.

W. Heat generation due to chemical reaction

During catalytic reactions, heat is generated/consumed as each reaction advances in proportion to the heat of reaction ($\Delta H_{j_{cat}}$). This term is key to the formulation of the overall heat input or cooling requirements for endothermic and exothermic reactions.

X. Heat generation due to solids sorption

This term accounts for the heat generation/consumption during solid sorption in the same fashion as item W. For example, carbon dioxide capture via dolomite solids is exothermic providing some heat to the bed. This term is calculated in a similar manner to item W, using the sorbent properties instead of the catalyst properties.

Y. Energy balance species accumulation

The dynamic thermal behaviour of the reactor is dominated by the heat capacity of the solid particles. Therefore the contribution from the solids energy accumulation terms is of great importance in the energy balance. Contributions from the gas phase, as well as any chemisorbed species, can also be included, although their impact on the systems dynamics is likely to be small.

Z. Pressure balance

Although some models assume isobaric behaviour, it is desirable to account for the pressure decay along the reactor height, especially for deep dense phase reactors. Various techniques have been employed to assess pressure variations within fluidized-beds. They range from an overall momentum balance where inter-particle forces, the rate of increase of momentum, the rate of momentum addition by convection and shear forces are neglected (Bird *et al.*, 2002) to linear variation of pressure with height.

2.4. Discussion and Concluding Remarks

A review of fluidized-bed catalytic reactors models is provided in this chapter with special emphasis on the implications of several mechanistic assumptions. The models are categorized according to their mole, energy and pressure balances. Other model characteristics are also studied. This work shows a clear connection between existing models and describes their key characteristics.

2.4.1. Model Comparison

A few works try to compare and analyze the results from different models. Most notable was the work of Chavarie and Grace (1975a, b, c) which compared the performance of models using as benchmark experimental results from an ozone decomposition reactor. This work concluded that none of the early model predictions was acceptable, although they provided useful insights on reactor behaviour. For the system studied, the Orcutt *et al.* (1962) and Kato and Wen (1969) models greatly under-predicted reactant conversions, whereas that of Partridge and Rowe (1966) over-predicted visible bubble flow. The model of Kunii and Levenspiel (1991) appeared to give more reasonable predictions for the ozone system investigated.

A later model comparison study was carried out by Barreteau *et al.*, (1978). This work analyzed the predictions of six classic models. The authors concluded that the Orcutt *et al.* (1962) model, with plug-flow in the dense phase gave the best predictions, while that of Partridge and Rowe (1966) gave reasonable predictions compared with experimental measurements of conversion for SO₂ sorption in a fluidized-bed. Simple homogeneous models (i.e. plug flow and perfect mixing) as well as the Kunii and Levenspiel (1991) model were found to be inadequate for their system.

Bolthrunis (1989) investigated the progress made in the modeling of phthalic anhydride reactors. The author suggests that empirical methods of scale-up are preferable to reactor modeling given the lack of availability of real industrial data for model validation. The output of the Kunii and Levenspiel (1991), Kato and Wen (1969), Grace (1984), Johnsson *et al.* (1987) and pseudo-homogeneous models were compared with industrial measurements, and limited agreement was found. This disagreement may have been caused by the over-simplified reaction kinetics scheme (DeMaria *et al.*, 1961) assumed in all of the models for this process (see also Chapter 9).

Mostoufi *et al.* (2001) compared three models for a maleic anhydride reactor. The authors concluded that a simple pseudo-homogeneous plug flow model underpredicted reactant conversions for the conditions of study. They recommended that catalyst particles should be included in the L-phase as standard two-phase models without solids in the L-phase did not give good agreement.

2.5. References

Abba, I.A., Grace, J.R. and Bi, H.T. (2002). Variable-gas-density fluidized bed reactor model for catalytic processes. *Chem. Eng. Sci.*, 57, 4797-4807.

Abba, I.A., Grace, J.R. and Bi, H.T. (2003a). Application of the generic fluidized-bed reactor model to the fluidized-bed membrane reactor process for steam methane reforming with oxygen input. *Ind. Eng. Chem. Res.*, 42, 2736-2745.

Abba, I.A., Grace, J.R., Bi, H.T. and Thompson, M.L. (2003b). Spanning the flow regimes: A generic fluidized bed reactor model. *AIChE J.*, 49, 1838-1848.

Adris, A.M., Lim, C.J. and Grace, J.R. (1997). The fluidized bed membrane reactor for steam methane reforming: Model verification and parametric study. *Chem. Eng. Sci.*, 52, 1609-1622.

Barreteau, D., Laguerie, C. and Angelino, H. (1978). An evaluation of some fluidized-bed reactor models for SO₂ sorption on copper oxide particles. in *Fluidization*. Eds. Davidson, J.F. and Keairns, D.L. pp. 297-302. Cambridge Univ. Press, Cambridge, U.K.

Bi, H.T., Ellis, N., Abba, I.A. and Grace, J.R. (2000). A state-of-the-art review of gas–solid turbulent fluidization. *Chem. Eng. Sci.*, 55, 4789–4825.

Bi, H.T. and Grace, J.R. (1995). Effect of measurement method on the velocities used to demarcate the onset of turbulent fluidization. *Chem. Eng. J.*, 57, 261-71.

Bird, R.B., Stewart, W.E. and Lightfoot, E.N. (2002). *Transport phenomena*. Wiley, New York.

Bolthrunis, C.O. (1989). An industrial perspective on fluid bed reactor models. *Chem. Eng. Prog.*, 85, 51-54.

Calderbank, P.H. and Toor, F.D. (1971). Fluidized beds as catalytic reactors. in *Fluidization*. Eds. Davidson, J.F. and Harrison, D. pp. 383-429. Academic Press, London.

Chaouki, J., Gonzalez, A., Guy, C. and Klvana, D. (1999). Two-phase model for a catalytic turbulent fluidized-bed reactor: Application to ethylene synthesis. *Chem. Eng. Sci.*, 54, 2039-2045.

Chavarie, C. and Grace, J.R. (1975a). Performance analysis of a fluidized bed reactor. I. Visible flow behaviour. *Ind. Eng. Chem. Funds.*, 14, 75-78.

Chavarie, C. and Grace, J.R. (1975b). Performance analysis of a fluidized bed reactor. II. Observed reactor behavior compared with simple two-phase models. *Ind. Eng. Chem. Funds.*, 14, 79-86.

Chavarie, C. and Grace, J.R. (1975c). Performance analysis of a fluidized bed reactor. III. Modification and extension of conventional two-phase models. *Ind. Eng. Chem. Funds.*, 14, 86-91.

Chen, Z., Po, F., Grace, J.R., Lim, C.J., Elnashaie, S.S.E.H., Mahecha-Botero, A., Rakib, M., Shirasaki, Y. and Yasuda, I. (2008). Sorbent enhanced/membrane-assisted steam methane reforming. *Chem. Eng. Sci.*, 63, 170-182.

Chen, Z., Prasad, P., Yan, Y. and Elnashaie, S.S.E.H. (2003a). Simulation for steam-reforming of natural gas with oxygen input in a novel membrane reformer. *Fuel Process. Technol.*, 83, 235-252.

Chen, Z., Yan, Y. and Elnashaie, S.S.E.H. (2003b). Modeling and optimization of a novel membrane reformer for higher hydrocarbons. *AIChE J.*, 49, 1250-1265.

Chen, Z., Yan, Y. and Elnashaie, S.S.E.H. (2003c). Novel circulating fast fluidized-bed membrane reformer for efficient production of hydrogen from steam-reforming of methane. *Chem. Eng. Sci.*, 58, 4335-4349.

Chen, Z., Yan, Y. and Elnashaie, S.S.E.H. (2004). Catalyst deactivation and engineering control for steam-reforming of higher hydrocarbons in a novel membrane reformer. *Chem. Eng. Sci.*, 59, 1965-1978.

Clift, R. (1983). An occamist view of fluidized-bed reactor modelling. *The chemical engineer*, 33, 29-31.

Constantineau, J.P., Grace, J.R., Lim, C.J. and Richards, G.G. (2007). Generalized bubbling-slugging fluidized bed reactor model. *Chem. Eng. Sci.*, 62, 70-81.

Davidson, J.F. and Harrison, D. (1963). *Fluidised particles*. Cambridge University Press, Cambridge, UK.

DeMaria, F., Longfield, J.E. and Butler, G. (1961). Catalytic reactor design. *Ind. Eng. Chem.*, 53, 259.

Dompazis, G., Kanellopoulos, V., Touloupides, V. and Kiparissides, C. (2008). Development of a multi-scale, multi-phase, multi-zone dynamic model for the prediction of particle segregation in catalytic olefin polymerization FBRs. *Chem. Eng. Sci.*, 63, 4735-4753.

Edwards, M. and Avidan, A.A. (1986). Conversion model aids scale-up of Mobil's fluid-bed MTG process. *Chem. Eng. Sci.*, 41, 839-835.

Fane, A.G. and Wen, C.Y. (1982). Fluidized-bed reactors. in Chap. 8 in *Handbook of Multiphase Systems*. Ed. Hetsroni, G. Hemisphere publishing corporation, New York.

Foka, J., Chaouki, J. and Klvana, D. (1994). Natural gas combustion in catalytic turbulent fluidized bed. *Chem. Eng. Sci.*, 49, 4269-4276.

- Fryer, C. and Potter, O.E. (1972). Countercurrent backmixing model for fluidized bed catalytic reactors. Applicability of simplified solutions. *Ind. Eng. Chem. Fundam.*, 11, 338-344.
- Gomezplata, A. and Shuster, W.W. (1960). Effect of uniformity of fluidization on catalytic cracking of cumene. *AIChE J.*, 6, 454-459.
- Grace, J.R. (1971). An evaluation of models for fluidized bed reactors. *AIChE Symp. Ser.*, 67, 159-167.
- Grace, J.R. (1981). Fluidized bed reactor modeling. An overview. in *Chemical reactors*. Ed. Fogler, H.C. 168. pp. 3-18. ACS Symp. Ser.
- Grace, J.R. (1984). Generalized models for isothermal fluidized bed reactors. in *Recent advances in engineering analysis of chemically reacting systems*. Ed. Doraiswamy, L.K. Wiley, New Delhi.
- Grace, J.R. (1986a). Contacting modes and behavior classification of gas-solid and other two-phase suspension. *Can. J. Chem. Eng.*, 64, 353-363.
- Grace, J.R. (1986b). Fluid beds as chemical reactors. in *Gas fluidization technology*. Ed. Geldart, D. Wiley, Chichester, U.K.
- Grace, J.R. (1986c). Modeling and simulation of two-phase fluidized bed reactors. in *Chemical reactor design and technology*. Ed. De Lasa, H.I. NATO ASI Series No 110. Martinus Nijhoff Publishers, Dordrecht.
- Grace, J.R. and Abba, I.A. (2005). Recent progress in the modeling of fluidized-bed reactors. in *Proc. Industrial Fluidization South Africa*, South African Inst. Mining & Metallurgy Symp. Ser. Eds. Luckos, A. and Smit, P. S42. pp. 3-22.
- Grace, J.R. and De Lasa, H.I. (1978). Reaction near the grid in fluidized beds. *AIChE J.*, 24, 364-366.
- Grace, J.R., Issangya, A.S., Bai, D. and Bi, H.T. (1999b). Situating the high-density circulating fluidized bed. *AIChE J.*, 45, 2108-2116.
- Grace, J.R. and Lim, K.S. (1997). Reactor modelling for high velocity fluidized beds. in *Circulating Fluidized Beds*. Eds. Grace, J.R., Avidan, A.A. and Knowlton, T.M. pp. 504-524. Chapman and Hall, London.
- Harshe, Y.M., Utikar, R.P. and Ranade, V.V. (2004). A computational model for predicting particle size distribution and performance of fluidized bed polypropylene reactor *Chem. Eng. Sci.*, 59, 5145-5156.
- Ho, T.C. (2003). Modeling. in Chap. 9 in *Handbook of fluidization and fluid particle systems*. Ed. Yang, W.C. pp. 239-255. Marcel Dekker, New York.
- Horio, M. and Wen, C.Y. (1977). An assessment of fluidized-bed modeling. *AIChE Symp. Ser.*, 73, 9-21.

- Hovmand, S. and Davidson, J.F. (1968). Chemical conversion in a slugging fluidised bed. *Trans. I. Chem. Engrs*, 46, T190-T203.
- Johnsson, J.E., Grace, J.R. and Graham, J.J. (1987). Fluidized-bed reactor model verification on a reactor of industrial scale. *AIChE J.*, 33, 619-627.
- Kato, K. and Wen, C.Y. (1969). Bubble assemblage model for fluidized bed catalytic reactors. *Chem. Eng. Sci.*, 24, 1351-1369.
- Kiashemshaki, A., Mostoufi, N. and Sotudeh-Gharebagh, R. (2006). Two-phase modeling of a gas phase polyethylene fluidized bed reactor. *Chem. Eng. Sci.*, 61, 3997–4006.
- Kim, S.W., Kirbas, G., Bi, H.T., Lim, C.J. and Grace, J.R. (2004). Flow behavior and regime transition in a high-density circulating fluidized bed riser. *Chem. Eng. Sci.*, 59, 3955–3963.
- Kobayashi, H. and Arai, F. (1966). Effects of several factors on catalytic reaction in a fluidized bed reactor. *Kagaku Kogaku*, 4, 166-170.
- Kunii, D. and Levenspiel, O. (1969). *Fluidization engineering*. Wiley, New York.
- Kunii, D. and Levenspiel, O. (1991). *Fluidization engineering*, 2nd ed. Butterworth-Heinemann, Boston.
- Lanneau, K.P. (1960). Gas-solids contacting in fluidized beds. *Trans. I. Chem. Engrs*, 38, 125-143.
- Lee, G.S. and Kim, S.D. (1990). Axial mixing of solids in turbulent fluidized beds. *Chem. Eng. J.*, 44, 1–9.
- Lewis, W.K., Gilliland, E.R. and Glass, W. (1959). Solid-catalyzed reaction in a fluidized bed. *AIChE J.*, 5, 419-426.
- Li, T. and Wu, P. (1991). A study on axial gas mixing in a fast fluidized-bed. in *Circulating fluidized-bed technology III*. Eds. Basu, P., Horio, M. and Hasatani, M. Pergamon, Oxford.
- Lim, K.S., Zhu, J.X. and Grace, J.R. (1995). Hydrodynamics of gas-solid fluidization. *Int. J. Multiphase Flow* 21, 141-193.
- Mahecha-Botero, A., Chen, Z., Grace, J.R., Elnashaie, S.S.E.H., Lim, C.J., Rakib, M., Yasuda, I. and Shirasaki, Y. (2008b). Comparison of fluidized bed flow regimes for steam methane reforming in membrane reactors: A simulation study. *Chem. Eng. Sci.*, In review.
- Mahecha-Botero, A., Grace, J.R., Elnashaie, S.S.E.H. and Lim, C.J. (2006a). Comprehensive modelling of gas fluidized-bed reactors allowing for transients, multiple flow regimes and selective removal of species. *Int. J. Chem. Reactor Eng.*, 4, A11.
- Mahecha-Botero, A., Grace, J.R., Elnashaie, S.S.E.H. and Lim, C.J. (2007a). A comprehensive approach to reaction engineering. *Int. J. Chem. Reactor Eng.*, 5: A17.
- Mahecha-Botero, A., Grace, J.R., Elnashaie, S.S.E.H. and Lim, C.J. (2007b). Time scale analysis of a fluidized-bed reactor based on a generalized dynamic model. in *Fluidization XII*. Eds. Bi,

X., F., B. and Pugsley, T. Harrison Hot Springs, BC, Canada., ECI Symposium Series. United Engineering Conferences, Brooklyn. http://services.bepress.com/eci/fluidization_xii/76.

Mahecha-Botero, A., Grace, J.R., Elnashaie, S.S.E.H. and Lim, C.J. (2009a). Advances in modelling of fluidized-bed catalytic reactors: A comprehensive review. Chem. Eng. Commun., in press.

Mahecha-Botero, A., Grace, J.R., Lim, C.J., Elnashaie, S.S.E.H., Boyd, T. and Gulamhusein, A. (2009b). Pure hydrogen generation in a fluidized bed membrane reactor: Application of the generalized comprehensive reactor model. Chem. Eng. Sci., in review.

Mamuro, T. and Muchi, I. (1965). A mathematical model for a fluidized bed catalytic reactor. Int. Chem. Eng., 5, 732-736.

Mathis, J.F. and Watson, C.C. (1956). Effect of fluidization on catalytic cumene dealkylation. AIChE J., 2, 518-524.

Matsen, J.M. (1985). Scale-up of chemical processes. in Fluidized beds. Eds. Bisio, A. and Kabel, R.L. pp. 347-405. Wiley, New York.

May, W.G. (1959). Fluidized-bed reactor studies. Chem. Eng. Prog., 55, 49-56.

Mireur, J.P. and Bischoff, K.B. (1967). Mixing and contacting models for fluidized beds. AIChE J., 13, 839-845.

Mostoufi, N., Cui, H. and Chaouki, J. (2001). A comparison of two- and single-phase models for fluidized-bed reactors. Ind. Eng. Chem. Res., 40, 5526-5532.

Orcutt, J.C., Davidson, J.F. and Pigford, R.L. (1962). Reaction time distributions in fluidized catalytic reactors. Chem. Eng. Prog. Symp. Ser., 58.

Partridge, B.A. and Rowe, P.N. (1966). Analysis of gas flow in a bubbling fluidized bed when cloud formation occurs. Trans. I. Chem. Engrs, 44, 335.

Pyle, D.L. (1972). Fluidized bed reactors. Review. in The first chemical reaction engineering international symposium. Advances in Chemistry Series. Ed. Bischoff, K.B. 109. pp. 106-130. American Chemical Society, Washington D.C.

Raghuraman, J. and Potter, O.E. (1978). Countercurrent backmixing model for slugging fluidized-bed reactors. AIChE J., 24, 698-704.

Schoenfelder, H., Kruse, M. and Werther, J. (1996). Two-dimensional model for circulating fluidized-bed reactors. AIChE J., 42, 1875-1888.

Shen, C.Y. and Johnstone, H.F. (1955). Gas-solid contact in fluidized beds. AIChE J., 1, 349-354.

Sit, S.P. and Grace, J.R. (1981). Effect of bubble interaction on interphase mass transfer in gas fluidized beds. Chem. Eng. Sci., 36, 327-335.

- Soler, J., Tellez, C., Herguido, J., Menendez, M. and Santamaria, J. (2001). Modelling of a two-zone fluidised bed reactor for the oxidative dehydrogenation of *n*-butane. *Powd. Technol.*, 120, 88-96.
- Souza-Santos, M.L. (2007). A new version of CSFB, comprehensive simulator for fluidised bed equipment. *Fuel*, 86, 1684-1709.
- Souza-Santos, M.L. (2008). Comprehensive simulator CSFB, applied to circulating fluidized bed equipment. *The Open Chemical Engineering Journal*, 2, 106-118.
- Thompson, M.L., Bi, H.T. and Grace, J.R. (1999). A generalized bubbling/turbulent fluidized bed reactor model. *Chem. Eng. Sci.*, 54, 2175-2185.
- Thomsen, V.B.E. (2000). LeChâtelier's principle in the sciences. *J. Chem. Educ.*, 77.
- Toomey, R.D. and Johnstone, H.F. (1952). Gaseous fluidization of solid particles. *Chem. Eng. Prog.*, 48, 220-226.
- Toor, F.D. and Calderbank, P.H. (1967). Reaction kinetics in gas-fluidized catalyst beds. Part II. Mathematical models. in *Proceedings of international symposium on fluidization*. Ed. Drinkenburg, A.A.H. University Press, Eindhoven, Netherlands.
- van Deemter, J.J. (1961). Mixing and contacting in gas-solid fluidized beds. *Chem. Eng. Sci.*, 13, 143-154.
- van Deemter, J.J. (1967). The countercurrent flow model of a gas-solids fluidized bed. in *Proc. Int. Symp. Fluidization*. Ed. Drinkenburg, A.A.H. Netherlands University Press, Amsterdam.
- Van Swaaij, W.P.M. (1985). Chemical reactors. in *Fluidization*, 2nd ed. Eds. Davidson, J.F., Clift, R. and Harrison, D. Academic Press, London.
- Wei, F., Jin, Y., Yu, Z. and Chen, W. (1995). Lateral and axial mixing of the dispersed particles in CFB. *J. Chem. Eng. Jpn.*, 28, 506-510.
- Werther, J. (1980). Modeling and scale-up of industrial fluidized-bed reactors. *Chem. Eng. Sci.*, 35, 372-379.
- Werther, J. and Hartge, E.U. (2004). Modeling of industrial fluidized-bed reactors. *Ind. Eng. Chem. Res.*, 43, 5593-5604.
- Yates, J.G. (1975). Fluidised bed reactors. *The Chemical Engineer*, 303, 671-677.
- Yates, J.G. (1983). *Fundamentals of fluidized-bed chemical processes*. Butterworth-Heinemann, London.
- Yates, J.G. and Gregoire, J.Y. (1980). Catalytic oxidation of *o*-xylene in a slugging fluidised bed. *Chem. Eng. Sci.*, 35, 380-385.

3. PURE HYDROGEN GENERATION IN FLUIDIZED-BED MEMBRANE REACTOR: EXPERIMENTAL FINDINGS³

3.1. Introduction

Hydrogen is an important commodity in several industrial processes. For example, it is required in the refining of petroleum (Shu-Ren, 1998) as well as other chemical processes such as hydrogenation of fats and oils, hydrodealkylation, hydrodesulphurization and the production of methanol and ammonia. Hydrogen is also required to implement proton exchange membrane (PEM) fuel cells. Moreover, it is expected to become an important energy carrier (Crabtree *et al.*, 2004). Interest in hydrogen as a milestone to control global warming has grown in recent years (NRC, 2004).

One of the major hurdles for the implementation of a hydrogen economy is to improve hydrogen production processes (NRC, 2004). Significant breakthroughs are required to reduce costs and improve the overall efficiency of hydrogen generation. Hydrogen may be produced by steam reforming of fossil fuels, gasification of coal/biomass, water electrolysis and high-temperature steam electrolysis. Steam reforming extracts hydrogen from hydrocarbons, as well as from water. Steam reforming of natural gas is the dominant process for hydrogen production (Koroneos *et al.*, 2004), and it is expected to play a major role during the initial stages of a hydrogen economy (Ogden, 2001). A comprehensive review on reforming technologies can be found in Ferreira-Aparicio *et al.* (2005).

Conventional steam methane reforming (SMR) occurs in large furnaces containing multiple tubes filled with fixed nickel-on-alumina catalyst pellets. The reactor contents are heated through the tube walls by heat transfer from the large surrounding furnace (Xu and Froment, 1989a, b; Nandasana *et al.*, 2003). This process, though widely used, suffers from several limitations such as low catalyst effectiveness factors, high temperature gradients and thermodynamic constraints (Elnashaie and Elshishini, 1993). Furthermore, the reactor product

³ A version of this Chapter was published as: Mahecha-Botero, A., Boyd, T., Gulamhusein, A., Comyn, N., Lim, C.J., Grace, J.R., Shirasaki, Y. and Yasuda, I. (2008). "Pure Hydrogen Generation in a Fluidized Bed Membrane Reactor: Experimental Findings". *Chemical Engineering Science*, 63, 2752-2762.

requires purification, usually via pressure swing adsorption. For example PEM fuel cells need a CO-free environment, as well as a high-purity hydrogen feed stream (Scura *et al.*, 2006). To address the above issues and to intensify the reforming process, fluidized-bed membrane reactors (FBMR) are under development for the production of hydrogen (Adris *et al.*, 1996; Grace *et al.*, 2005; Deshmukh *et al.*, 2007).

Since the steam methane reforming is endothermic and results in an increase in total molar flow, the reforming reactions are thermodynamically favoured at high temperatures and low pressures. Membranes may be introduced to reforming reactors to selectively remove hydrogen *in situ* as it is produced. This favourably shifts the equilibrium forward by LeChâtelier's principle (Thomsen, 2000). Higher natural gas conversion and hydrogen yield may then be achieved at much lower temperatures (e.g. operating temperatures of $\sim 850^{\circ}\text{C}$ for conventional reforming versus $\sim 550^{\circ}\text{C}$ for membrane reformers) if the product hydrogen is removed from the reactor (Raich and Foley, 1995; Mleczko *et al.*, 1996; Adris *et al.*, 1997). In addition, the catalyst effectiveness factor increases by several orders of magnitude when fine fluidized catalyst particles are employed instead of large catalyst pellets. Moreover, fluidized-bed operations are characterized by very low temperature gradients due to the intensive mixing of particles inside the reactor (Yates, 1983; Kunii and Levenspiel, 1991; Deshmukh *et al.*, 2005). Other advantages of FBMR include the possibility of using inexpensive metal alloys (due to the lower operating temperatures), as well as continuous/periodic catalyst replacement (Grace *et al.*, 2005). However, fluidized-bed membrane reactors present challenges such as the possibility of catalyst attrition/erosion, a more complex design/scale-up/construction process, as well as the need for reliable membranes.

Given these advantages of fluidized-bed membrane reactors, a number of theoretical and experimental studies have been performed in recent years. For example, there has been considerable modelling effort (Adris *et al.*, 1997; Grace *et al.*, 2001; Abba *et al.*, 2003a; Chen *et al.*, 2003a; Chen *et al.*, 2003b, c; Dogan *et al.*, 2003; Chen *et al.*, 2004; Prasad and Elnashaie, 2004; Patil *et al.*, 2005). Experimental studies and reactor developments have been carried out by several groups. A pilot reactor of 97 mm ID, with the provision of palladium tubes was tested by Adris (1994). Roy (1998) used high-flux membranes and heating via oxygen addition in a FBMR. A high-temperature downflow-fluidized bed with the provision of inconel-supported palladium membranes was operated by Jarosch and de Lasa (1999). Similarly, a 0.1 m ID, 2.7 m tall fluidized-bed reactor with both Pd-based H_2 perm-selective membranes and perovskite O_2

perm-selective membranes for autothermal reforming was operated under steam methane reforming conditions by Patil *et al.*, (2006). Boyd (2007) successfully operated a 0.13 m ID, 2.3 m tall internally-circulating fluidized-bed membrane reactor. More recently a 0.13 m ID, 1.6 m tall membrane reactor was operated by Chen *et al.* (2007) under ATR and SMR conditions. The FBMR process is currently being commercialized by Membrane Reactor Technologies (MRT) Limited (Adris *et al.*, 1994; Grace *et al.*, 2006; Deshmukh *et al.*, 2007).

This chapter presents new experimental results showing the influence of such parameters as reactor pressure, hydrogen permeate pressure (vacuum vs. atmospheric pressure), air top/bottom split, feed flowrate and membrane area in a novel pilot fluidized-bed membrane reactor.

3.2. Experimental Studies

3.2.1. Operation Modes

A fluidized-bed membrane reactor may be operated under different operating modes depending on how the heat required for the reforming reactions is supplied:

3.2.1.1. Steam methane reforming (SMR) with external heating: Under these conditions, the endothermic reactor heat is provided by indirect heat transfer from hot furnace gases, but for the pilot reactor, electrical heaters were used. This mode is attractive due its high hydrogen recovery, although it is subject to heat transfer constraints. The main reactions under SMR operation (Xu and Froment, 1989a, b) are:

Methane steam reforming: **(R1)**



Water-gas shift: **(R2)**



Methane overall steam reforming: **(R3)**



Note that R3 is the sum of R1 and R2.

3.2.1.2. Autothermal reforming (ATR) with addition of air or oxygen: In oxidative steam reforming, oxygen is supplied to the reactor to oxidize combustibles, thereby generating the required heat (Roy *et al.*, 1999; Hoang and Chan, 2004; Prasad, 2004). When the heat generated by the oxidation/combustion reactions balances the heat intake of the reforming reactions and heat losses, the system operates autothermally. Since heat is generated inside the fluidized-bed itself, heat transfer limitations are not an issue during ATR operation. Reforming reactions R1 to R3, as well as methane combustion R4 (Jin *et al.*, 2000) and hydrogen combustion R5 (Låte *et al.*, 2004a; Låte *et al.*, 2004b), occur simultaneously during autothermal reforming of methane. Oxygen introduction locally increases methane conversion, increases reactor temperature and reduces hydrogen yield.

Methane combustion: (R4)



Hydrogen combustion: (R5)



3.2.2. Experimental Equipment

Figure 3.1 provides a schematic of the overall experimental set-up tested in this work. Methane from the city lines was compressed and then desulphurized. Sulphur components were effectively removed to prevent catalyst deactivation. A bed of Cu-impregnated activated carbon was used for Sulphur removal (Calgon Sulfasorb-8) so that sulphur levels were small. The sulphur content of the input gas was about 13 mg S/m³. Measurements of the desulphurized methane stream indicate that its sulphur content was always below 0.28 mg S/m³. The desulphurized methane was then combined with previously deionized and compressed water. The resulting stream was then introduced into a vaporizer which raised the fluid temperature to ~550°C. The pre-heated water/methane stream was next fed to a gas distributor at the base of the FBMR. Air from gas cylinders was divided into two streams (via distributors at the bottom of the

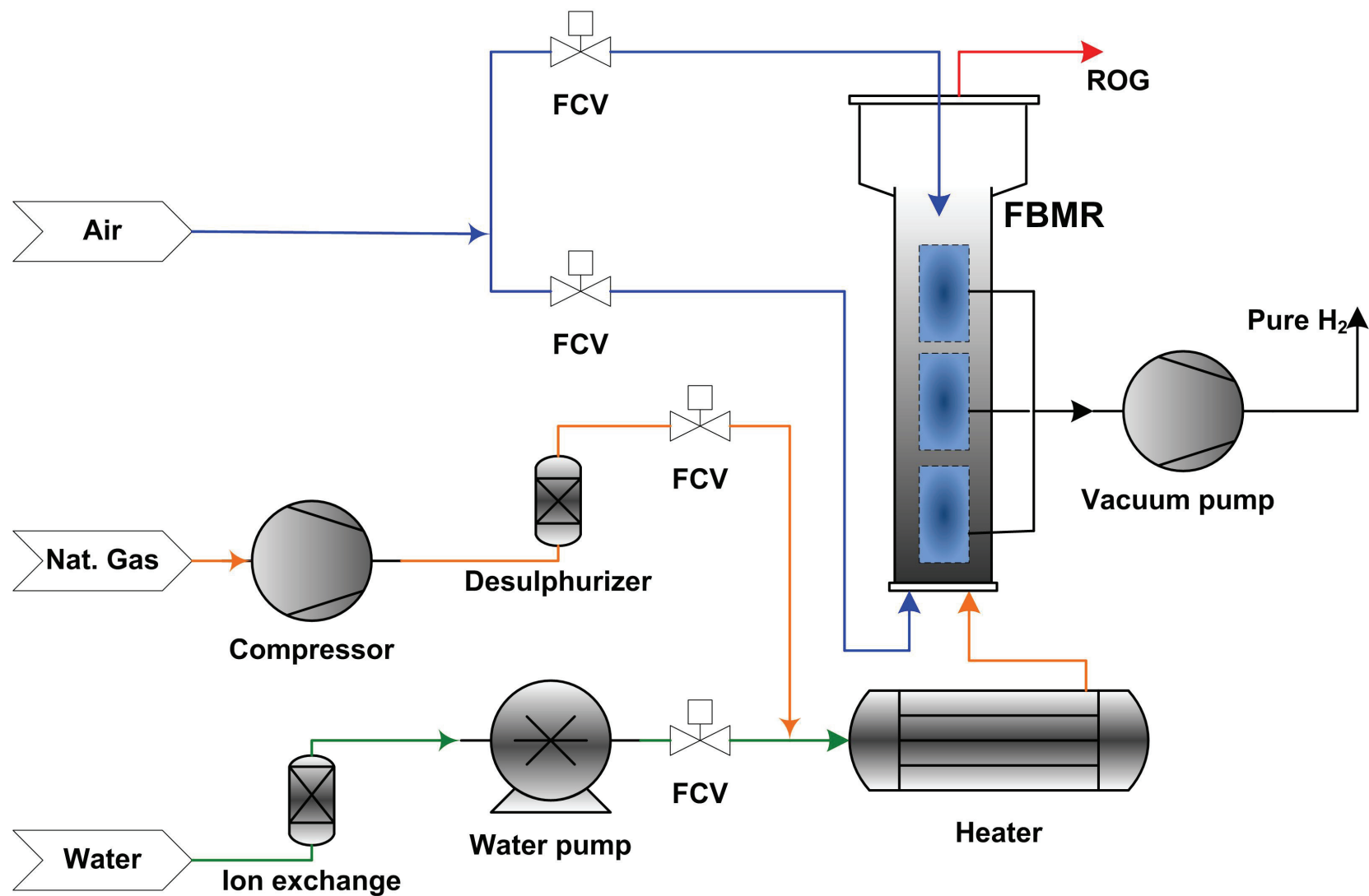


Figure 3.1. Experimental setup schematic drawing. ROG = reactor off-gas.

bed as well as 24 mm below the top expanding section). In the case of ATR operation the reactor was fed with air near both the top and bottom of the bed. The heat generated by the oxidative reactions was distributed throughout the bed by the particles depending on the top/bottom air split. Pure hydrogen product was removed via hydrogen selective membranes connected to a vacuum pump, which withdrew hydrogen at a pressure of 30 kPa(a), thus increasing the hydrogen permeation driving force. The remaining reactor gas products left the system after passing through sintered metal filters at the top of the fluidized bed freeboard to remove entrained particulates. The gas chromatograph implemented was a Shimadzu GC-8A using a thermal conductivity detector (TCD) which has an approximate detection limit for CO of 50 ppm.

The test rig allowed several process variables to be controlled accurately. The main controllable parameters for each experimental run are listed in Table 3.1.

Table 3-1. Controlled parameters for experimental program.

Controlled variables	Equipment / action
• Flowrate of methane	Flow controller action
• Flowrate of water	Modulation of water pump
• Flowrate of air (ATR operation)	Flow controller action
• Methane/water input mixture pre-heat temperature	Modulation of pre-heater output
• Split of air flow between top and bottom nozzles(ATR operation)	Flow controller action
• Pressure on permeate side	Modulation of vacuum pump speed
• Reactor pressure	Adjustment of off-gas exit valve
• Reactor temperature	Flow controller action on top/bottom air. Adjusting internal heaters output. Adjusting external heaters output.

3.2.3. Pilot Fluidized-Bed Membrane Reactor

The pilot reactor has a nominal capacity of 1.0 Nm³/h of permeate H₂ under ATR conditions, with a pressure rating of 1 MPa(g). The reactor is contained in a stainless steel vessel of height 2 m and rectangular cross-sectional area of 4840 mm². The vessel can hold up to six double-sided membrane modules (provided by Membrane Reactor Technologies Ltd.) with a nominal permeation area of 0.03 m². The membrane modules contained Pd/Ag foil of thickness 25 µm sealed onto a porous metal backing with a barrier layer to prevent interdiffusion. No sweep gas was used in any of the runs discussed here. SMR catalyst particles of average particle diameter

90 μm were introduced to the reactor. These catalyst particles have a measured minimum superficial gas velocity for fluidization of 0.0030 m/s in atmospheric air. The catalyst minimum fluidization velocity under reforming conditions was predicted to be 0.0018 m/s by the equation of Wen and Yu (1966). The fluidized-bed operated at all times within the bubbling fluidization regime. Appendix B, C and D contain other technical details of the pilot plant.

The non-permeate reactor off-gas (ROG) leaving the top of the reactor, was analyzed at the exit. In addition, reactor gas was sampled at the middle of each membrane section. These gas lines were connected to a gas chromatograph for chemical composition analysis. Reactor temperature was measured continuously at six points along the reactor. During SMR operation, internal electrical heaters at the four corners controlled the reactor temperature. The split of flow to the top/bottom air distributors was controlled during ATR operation. External electric heaters were also utilized for reactor start-up and to compensate for heat losses.

After completing the start-up process, measurements were made to characterize the reactor performance for different operating conditions. The main measured steady-state operating variables for each experimental run were:

- Temperature profile. Six points: one on each membrane panel, one embedded in the bottom distributor, one in the freeboard and one at the top air distributor.
- In-bed and ROG reactor gas samples concentration from chromatograph (H_2 , N_2 , CO , CH_4 , CO_2).
- Flowrate of pure hydrogen from membranes.
- Hydrogen purity from a gas chromatograph.
- Feed Pressure. Pressure just above distributor. Differential pressure between distributor and freeboard. Pressure drop across the filters.

3.2.4. Membranes for Hydrogen Removal

Perm-selective membranes are intended to break the thermodynamic barrier and shift the equilibrium forward to enhance hydrogen production while also purifying the product. Ceramic, metallic and composite membranes have all been proposed for hydrogen purification (Uemiya, 2004). Palladium alloy membranes are used most widely for selective hydrogen removal, having a nearly infinite selectivity since only atomic hydrogen can diffuse through the metal foil (Shu *et*

al., 1994; Shu *et al.*, 1996). The accepted mechanism for hydrogen permeation through dense metallic membranes (Paglieri and Way, 2002) is:

- 1) Transport of H₂ molecules to the surface of the metallic membrane;
- 2) Reversible chemisorption of H₂ molecules on the metal surface;
- 3) Reversible dissolution of atomic hydrogen at the membrane surface;
- 4) Diffusion of atomic hydrogen through the metal lattice (usually the rate-controlling step);
- 5) Reassociation of atomic hydrogen at the surface of the downstream metal surface;
- 6) Desorption of molecular hydrogen from the metal surface; and
- 7) H₂ transport away from the outer surface of the membrane.

The geometric configuration of the membranes inside the reactor is depicted in Figure 3.2. The membrane permeate side has a thickness of 6.3 mm. Permeate hydrogen is withdrawn from each panel via a ¼” (6.3 mm) stainless steel tube. A schematic representation of a membrane panel is depicted in Figure 3.3.

The flow of hydrogen permeating through a membrane surface can be estimated by Sieverts’ Law (Sieverts and Zapf, 1935a, b):

$$F_{H_{2\phi}} = A_M \cdot J_{H_{2\phi}} = A_M \cdot \left[\frac{k_{H_2}}{\Delta_{H_2}} \cdot e^{\left(\frac{-E_{H_2}}{R \cdot T_\phi}\right)} \cdot \left(\sqrt{P_{H_{2\phi}}} - \sqrt{P_{H_{2M}}} \right) \right], \quad (3.1)$$

where $F_{H_{2\phi}}$ is the total molar flow rate of hydrogen extracted through permselective membranes, A_M is the effective membrane surface area, $J_{H_{2\phi}}$ is the membrane flux, Δ_{H_2} is the foil thickness, T_ϕ is the membrane surface temperature, $P_{H_{2\phi}}$ is the partial pressure of hydrogen in the reactor, $P_{H_{2M}}$ is the partial pressure of hydrogen in the permeate side. Other symbols are defined in the notation section.

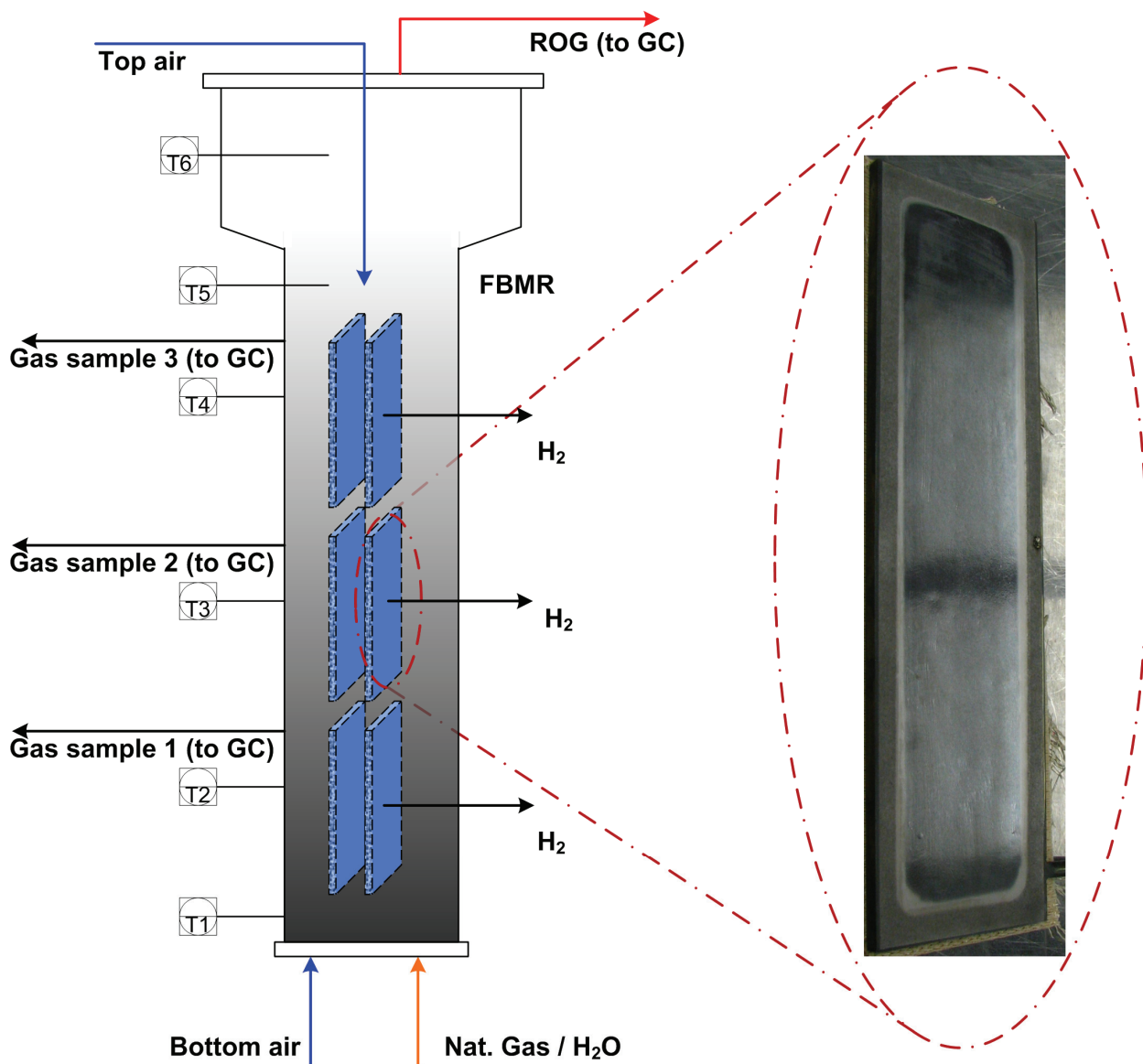


Figure 3.2. Reactor configuration.

3.2.5. Catalyst

A nickel oxide catalyst supported on alumina was utilized for all SMR experiments. A precious metal catalyst also supported on alumina (details withheld as required by the supplier) was utilized for the ATR pilot tests. The reforming reactions were quite fast, and catalyst deactivation was not expected to be an issue over the limited time of operation and given the steam-to-carbon molar ratio of 3.0 for all experimental runs. The reactor operated at low superficial gas velocities (bubbling fluidization regime with superficial gas velocities ≤ 0.08 m/s), resulting in very low catalyst attrition rates and negligible wastage of the membrane surfaces.

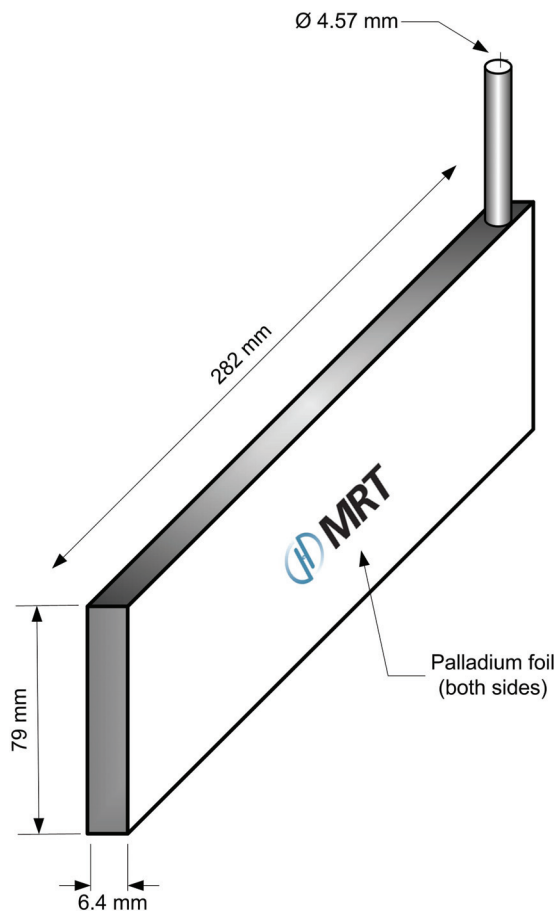


Figure 3.3. Palladium membrane details.

3.2.6. Experimental design

Several experimental runs were conducted under SMR and ATR conditions, with a total operational time of 178 hours. The performance of all reactor components and systems was tested, and the functionality of safety systems was verified. Steam reforming experiments under SMR and ATR conditions, both with and without membranes, were carried out with different numbers of active membranes. Reactor commissioning was performed without membranes (with metallic dummies replacing the membrane panels), and then reforming experiments were conducted with either half of the membrane panels (3 membrane panels, 3 dummies) or all six panels installed. All dummies were of identical area and thickness as the membrane panels.

The experimental variables are summarized in Table 3.2. Operating conditions examined, specified in Table 3.3 can be used for sensitivity analysis.

Table 3-2. Experimental conditions. (All experiments were carried out at 550°C with a steam-to-carbon molar ratio of 3.0).

Expt #	Membranes installed	O ₂ /CH ₄ ratio	Air split [% to top]	Methane feed [Nm ³ /h]	Reactor pressure [kPa(g)]	Permeate pressure [kPa(a)]
1	0	0	N/A	0.896	650	N/A
2	0	0	N/A	0.896	900	N/A
3	0	0.35	14.7	0.896	900	N/A
4	3	0	N/A	0.896	650	101
5	3	0	N/A	0.896	650	30
6	3	0	N/A	0.896	900	30
7	3	0	N/A	0.448	650	30
8	3	0	N/A	0.448	900	30
9	6	0.35	50	0.896	900	101
10	6	0.35	50	0.896	900	30
11	6	0.35	25	0.896	900	30
12	6	0.35	10.4	0.448	900	30
13	6	0.35	6.2	0.298	900	30
14	6	0	N/A	0.298	900	30

N/A: Not applicable

Table 3-3. Justification of selected operating conditions.

Experiments	Analysis
(1) vs (2)	Effect of reactor pressure without hydrogen removal
(5) vs (6) and (7) vs (8)	Effect of reactor pressure with hydrogen removal
(1) vs (4), and (2) vs (6)	Effect of area of membranes in SMR
(3) vs (9), (3) vs (10), and (3) vs (11)	Effect of area of membranes in ATR*
(4) vs (5)	Effect of permeate pressure in SMR
(9) vs (10)	Effect of permeate pressure in ATR
(2) vs (3), (6) vs (10), and (8) vs (12)	Effect of oxygen input (SMR vs ATR)
(10) vs (11)	Effect of air split in ATR
(5) vs (7), and (6) vs (8) vs (14)	Effect of reducing feed rates in SMR
(11) vs (12) vs (13)	Effect of reducing feed rates in ATR*

** Not entirely comparable due to some variation in air split*

3.2.7. Gas Sampling

Gas sampling lines were connected to the fluidized bed reactor to obtain axial concentration profiles of H₂, N₂, CO, CH₄ and CO₂ along the bed. A fine metallic mesh acted as a filter on each sampling port to exclude catalyst powder from entering the sampling tubes. Each sampling line was coiled and quenched by being submerged in a cold water bath. Sample gas was throttled with manual valves to a flowrate appropriate for the gas chromatograph sampling system. This,

combined with long sampling tubes from the reactor to the GC, caused delays in the sampling process. To address the delay issue, the following steps were followed:

- The gas residence times in the sampling lines were determined, and samples were required to exceed these times.
- Each sample was analyzed repeatedly until steady state was achieved. Typically, gas samples were analyzed until <1% variation on methane conversion was indicated.
- Only samples which satisfy the above two conditions are included in the results.
- Each sample was repeated at least three times to ensure reproducibility of the results.

For each value measured, a simple error-bar (represented by the standard error) was calculated by dividing the standard deviation by the square root of number of experimental measurements that make up the mean. In some plots, the error-bars are very small and do not appear on the figures. In some cases when the values of a measured state variable are small, the error-bars appear large due to the scale of the figures.

3.3. Results and Discussion

3.3.1. Overall Reactor Performance

Table 3.4 provides the typical composition of the natural gas from the city lines. The natural gas feed to the reactor is mainly composed of methane, which is used as model component for the subsequent calculations. Table 3.5 summarizes the performance of the reacting system. Table 3.6 contains typical gas chromatograph analyses for reactor gas samples under SMR and ATR conditions. The methane conversion at the different sampling points was calculated from an overall carbon balance, neglecting the traces of other hydrocarbons not detected by the GC, i.e.

$$X_{CH_4\varphi} = \left(\frac{Y_{CO_2\varphi} + Y_{CO\varphi}}{Y_{CO_2\varphi} + Y_{CO\varphi} + Y_{CH_4\varphi}} \right), \quad (3.2)$$

where $X_{CH_4\varphi}$ is the reactor conversion of methane and $Y_{CO_2\varphi}$, $Y_{CO\varphi}$ and $Y_{CH_4\varphi}$ are the reactor gas mole fractions of carbon dioxide, carbon monoxide and methane respectively.

Table 3-4. Typical feed natural gas analysis.

Component	Mole fraction
Methane	0.955
Ethane	0.029
Nitrogen	0.007
Propane	0.005
Carbon dioxide	0.002
n-Butane	0.001
iso-Butane	0.0005
Pentanes	0.0004
Hexanes	0.0001

Table 3-5. Experimental results.

Expt #	Maximum methane conversion	Maximum H ₂ ROG mole fraction (dry)	Permeate H ₂ flow [Nm ³ /h]	Maximum perm. H ₂ /C molar ratio	Detected permeate H ₂ purity
1	28.9 %	43.5 %	N/A	N/A	N/A
2	21.5 %	33.3 %	N/A	N/A	N/A
3	40.0 %	22.2 %	N/A	N/A	N/A
4*	ROG: 25 %	40.1 %	0.31	0.38	99.967 %
5	65.5 %	41.1 %	0.88	0.98	99.995 %
6	65.8 %	33.3 %	0.94	1.05	99.988 %
7*	ROG: 43.0%	29.4 %	0.93	2.07	99.988 %
8	66.5 %	20.6 %	0.92	2.06	99.940 %
9*	ROG: 45.9 %	22.0 %	not available	not available	not available
10	73.1 %	17.5 %	1.11	1.28	99.967 %
11	68.7 %	16.2 %	1.08	1.23	99.995 %
12	80.9 %	11.9 %	0.82	1.93	99.988 %
13*	ROG: 75.8 %	8.69 %	0.73	2.53	99.988 %
14	73.1 %	8.72 %	0.89	3.03	99.940 %

N/A: Not applicable

** in-bed gas sampling not performed*

Table 3-6. Typical reactor gas composition (dry basis). Samples taken at central membrane level.

Case	H ₂	N ₂	CO	CH ₄	CO ₂
Expt #5 (SMR)	37.4 %	6.54 %	3.63 %	19.3 %	33.1 %
Expt #12 (ATR)	12.1%	52.1 %	2.06 %	6.83 %	26.9 %

Measured reactor off-gas (ROG) methane conversions in the freeboard tended to be low due to reverse-reaction (see reactions R1 to R3) because of a drop in temperature (~100 to ~250 °C cooler than the main reactor). Samples taken directly from the reactor show much higher conversions, as the corresponding gas samples were rapidly quenched out of contact with the catalyst. In-bed gas samples were not taken during some experiments (designated by an asterisk in Table 3.5); only ROG measurements were performed for these cases, providing low methane conversions. In practice, the freeboard could be heated if it is important to obtain a reformat from the ROG, as discussed below.

Hydrogen purity was high, ~99.99%, during all experimental runs. Some trace impurities on the permeate side could be caused by residues in the gas chromatograph lines, but minor imperfections in the palladium foil are thought to be the main source of non-hydrogen gases (mainly CH₄ and some CO₂). Methane traces may appear if some methanation occurred in the sampling lines (Jorgensen *et al.*, 1995).

Methanation:

(R6)



CO could not be detected during any of the experimental runs, an important finding with respect to PEM fuel cells applications.

3.3.3. Influence of Key Operating Parameters

The continuous lines in the figures below are trend-lines through the experimental points of temperature, concentration, conversion and permeate yield. For experimental conditions see Table 3.2.

3.3.3.1. Membrane isothermality: The membrane panels are exposed to a nearly isothermal environment. Temperature variation along each membrane panel was less than 20°C. This helps to preserve membrane longevity. The ability of moving solids to circulate heat and minimize temperature gradients is a major advantage of fluidized-beds compared to conventional fixed-beds. Figure 3.4 depicts typical temperature profiles for the FBMR during SMR operation. It is clear that for all experimental runs the membrane-containing sections retained uniform temperatures, although, as noted above, there was significant cooling in the freeboard.

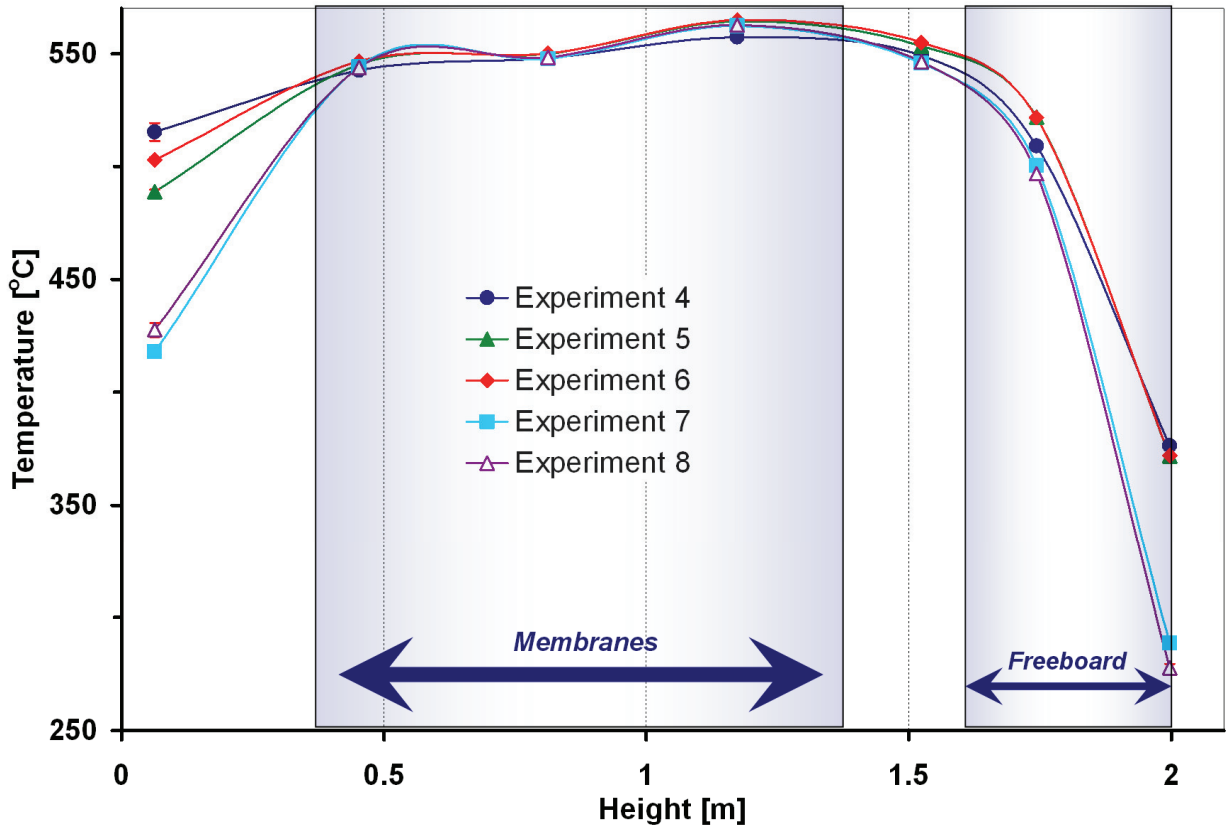


Figure 3.4. Temperature vs height for experiments 4 to 8. Membrane isothermality. For experimental conditions, see Table 3.2.

3.3.3.2. Heat effects: An axial profile of methane conversion is plotted in Figure 3.5 with its corresponding bed temperature profile. This figure shows typical behaviour of the FBMR unit under ATR conditions. Air was injected at both the top and bottom of the dense-phase portion of the reactor to provide heat for the endothermic reforming reactions. The oxidation reactions increased methane conversion and reactor temperature near the injection points. During ATR operation the system no longer relied on electrical heaters to provide the endothermic reaction heat. The bed temperature increased near the top air distributor. Nevertheless, there were no reactor hot-spots, a beneficial feature of a well-mixed fluidized-bed due to the circulation of heat by the migrating solid particles.

The temperature drop in the reactor freeboard was common to all experimental runs, leading to a decrease in reactant conversion due to reverse reactions (Adris and Grace, 1997). Note that these freeboard effects are not a problem for the intended application since they occurred beyond the upper level where product hydrogen was extracted. In addition, the exothermic reverse reactions may give some heat back to the reactor. Nevertheless, three

methods may be combined to address this issue if the non-permeate reformat product is important:

- a) **Heating the freeboard.** External heating could be provided to avoid cooling.
- b) **Rapid quenching of ROG line.** Currently the ROG line is well insulated. If the insulation were to be removed, the output gas would cool very quickly, as for the gas samples extracted from the side flanges.
- c) **Improve ROG filters/cyclones.** This may prevent small catalyst fines from entering the ROG line.

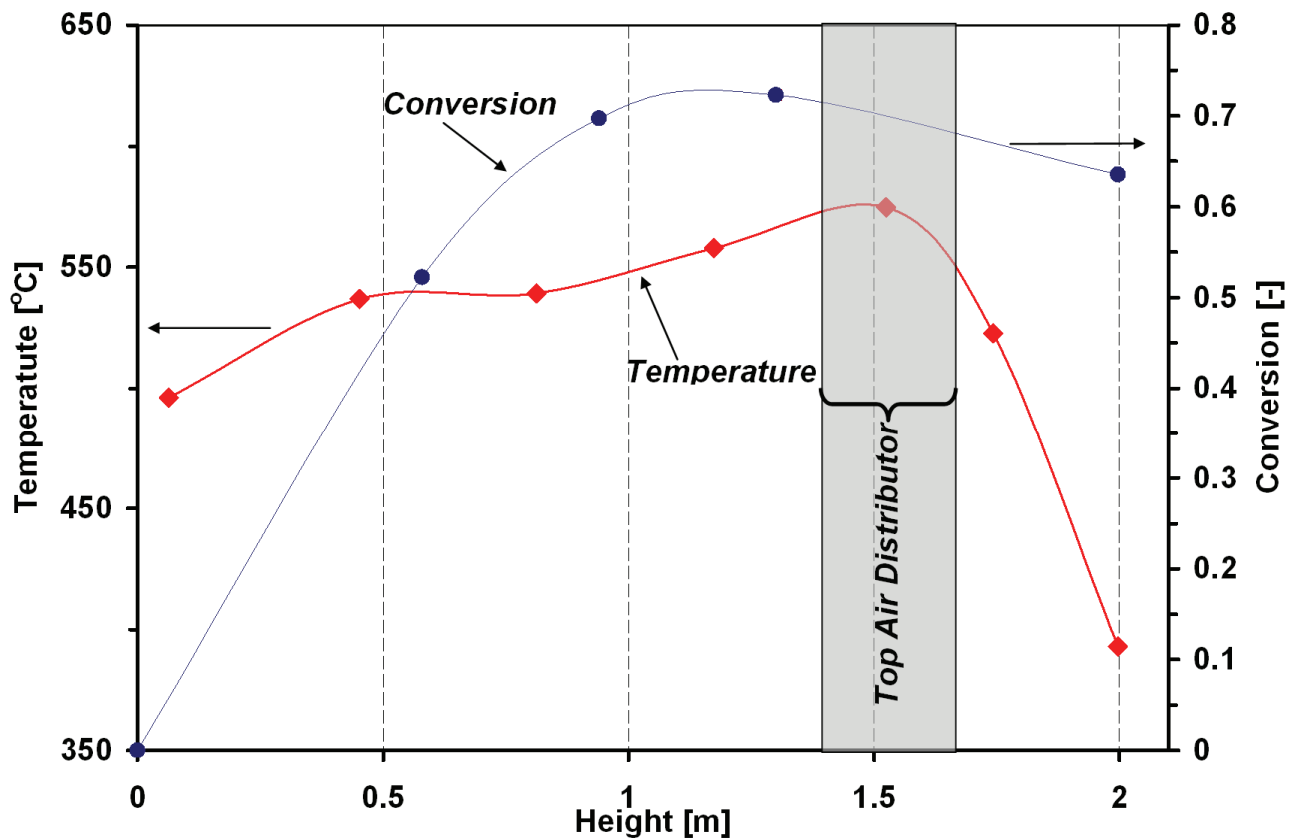


Figure 3.5. Methane conversion and temperature vs height for typical ATR operation (experiment 10). For experimental conditions, see Table 3.2.

3.3.3.3. **Thermodynamic effect of reactor pressure:** Steam methane reforming is thermodynamically enhanced by low reactor pressures. Higher equilibrium conversions are experienced at low pressures for reformers without membranes due to the increase in total molar flowrate. During reactor commissioning, the experimental set-up was operated using metallic dummy panels instead of palladium membranes. Axial conversion profiles at different reactor pressures are plotted in Figure 3.6. As expected, the system achieved a higher methane

conversion at the lower pressure. When operating with active membranes, this thermodynamic effect was offset to a significant extent by an increase in hydrogen removal, significantly offsetting the negative shift in the thermodynamic equilibrium.

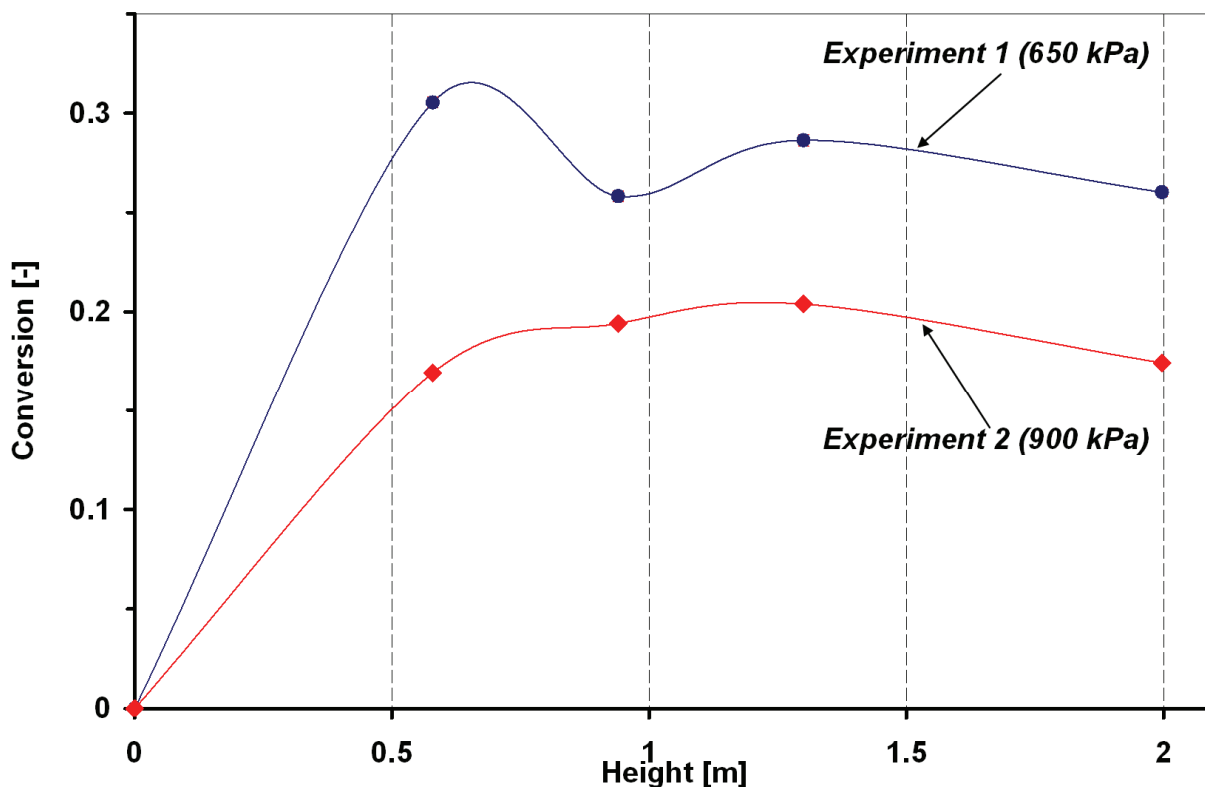


Figure 3.6. Methane conversion vs height for Experiments 1 (650 kPa) and 2 (900 kPa). Thermodynamic effect of reactor pressure. For experimental conditions, see Table 3.2.

3.3.3.4. Effect of membrane area: The FBMR is rate-controlled by membrane permeation. For the temperatures and catalyst loadings of interest, the steam reforming kinetics are fast enough that our kinetic model predicts near-equilibrium gas compositions. If hydrogen permeation could be increased, the equilibrium conversion would be further enhanced. For currently available hydrogen producing membrane reactors, the installed membrane surface area dominates reactor performance (Adris and Grace, 1997; Boyd *et al.*, 2005). It is therefore important to maximize the membrane area per unit reactor volume, as well as to minimize the membrane thickness. The first aspect depends on the reactor configuration and height, whereas the thickness requires a balance between hydrogen flux, selectivity and longevity.

The membrane permeation may be increased by increasing the pressure driving force across the membrane as described by Sieverts' Law (see equation 1). Hydrogen extraction can also be increased by installing more membrane surface area in the reactor. Figure 3.7 presents

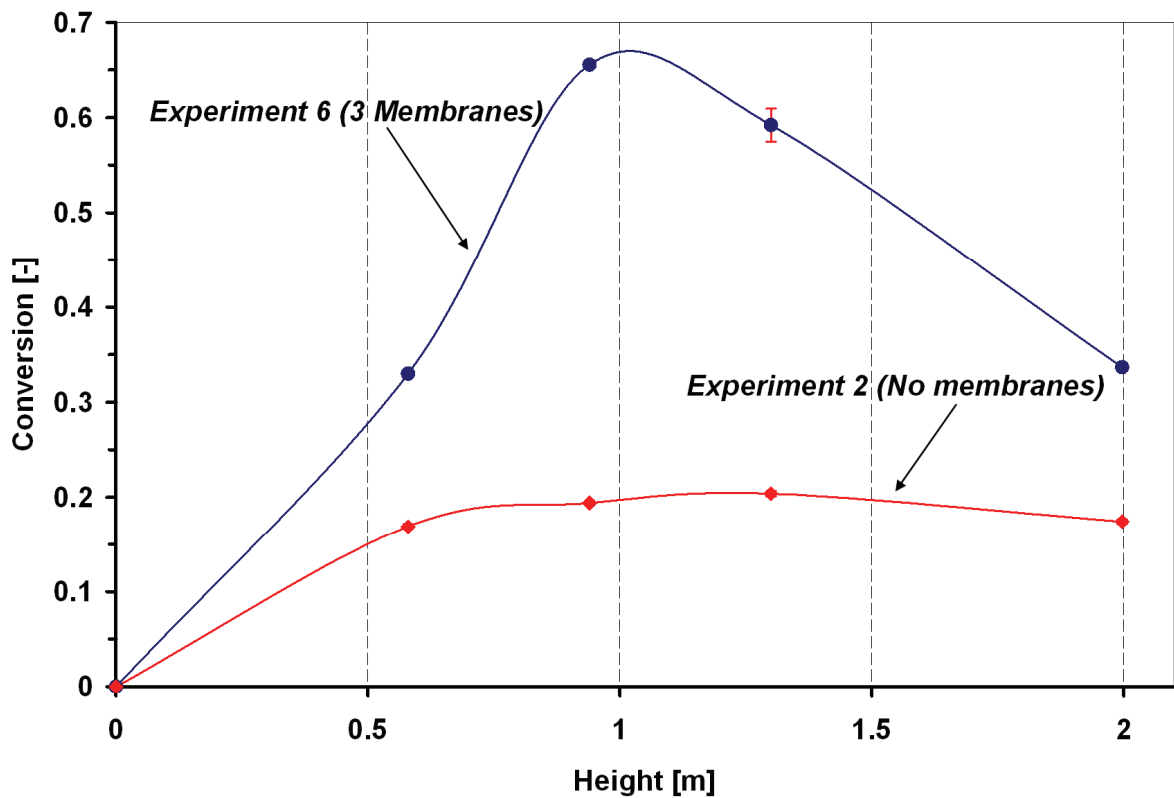


Figure 3.7. Methane conversion vs height for experiments 6 (3 membranes) and 2 (no membranes). Effect of membrane area during SMR operation. For experimental conditions, see Table 3.2.

the effect of increasing membrane area on methane conversion during SMR operation. Figure 3.8 displays the effect of increasing membrane area on methane conversion and reactor hydrogen composition over ATR operation. It is clear that a higher hydrocarbon conversion was achieved by increasing the membrane area. Furthermore, it is observed that there was a significant decrease in the concentration of hydrogen in the reactor due to the presence of membranes. For the cases with active membranes, the content of hydrogen in the reactor increased sharply in the lower section of the bed due to the rapid kinetics. This concentration decreased gradually over the middle section of the bed due to hydrogen removal, as seen in Figure 3.8. In the upper part of the bed, there was an increase in hydrogen content due to reverse reactions, as described above.

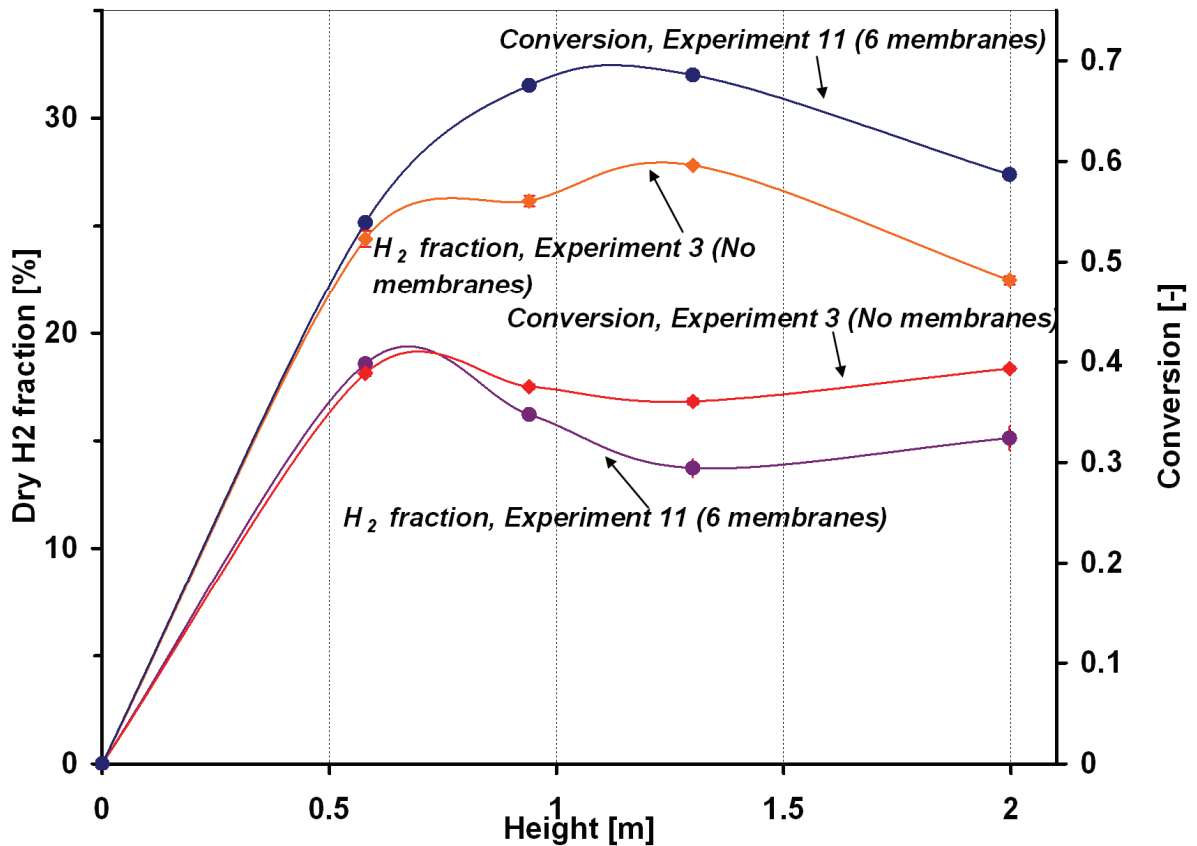


Figure 3.8. Methane conversion and dry H₂ molar fraction inside the reactor vs height for experiments 11 (6 membranes) and 3 (no membranes). Effect of membrane area during ATR operation. For experimental conditions, see Table 3.2.

3.3.3.5. Effect of pressure driving force: Hydrogen removal increased monotonically with an increase in pressure differential between the reactor and permeate. The thermodynamic advantage of operating at low reactor pressures is largely neutralized by the introduction of hydrogen removal membranes. Figure 3.9 depicts the effect of pressure differential on hydrogen production (see Equation 1). Since the driving force is dependent on the difference between the square roots of the hydrogen partial pressures, we can observe a more significant variation in driving force by adjusting the pressure in the permeate side (containing pure hydrogen so that: $P_{H_{2(M)}} = P_{(M)}$) than by varying the reactor pressure (i.e. where hydrogen partial pressure accounts for only a fraction of the total pressure as per Dalton's law of partial pressures: $P_{H_{2(\varphi)}} = Y_{H_{2(\varphi)}} \cdot P_{(\varphi)}$). Figure 3.10 portrays a small increase in conversion due to an increase in reactor pressure for Experiments 5 and 6.

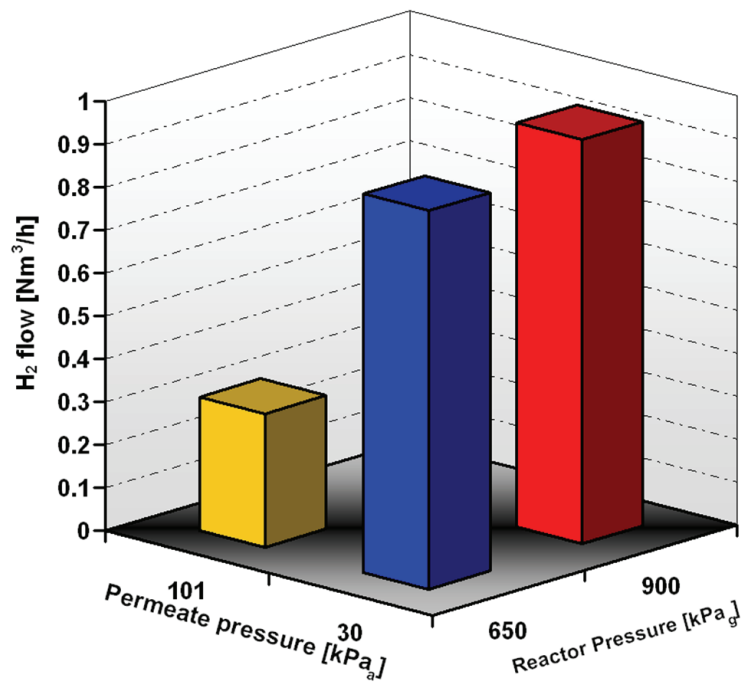


Figure 3.9. Hydrogen production vs reactor pressure and permeate pressure. (Experiments 4, 5 and 6). Effect of pressure driving force on hydrogen removal. For experimental conditions, see Table 3.2.

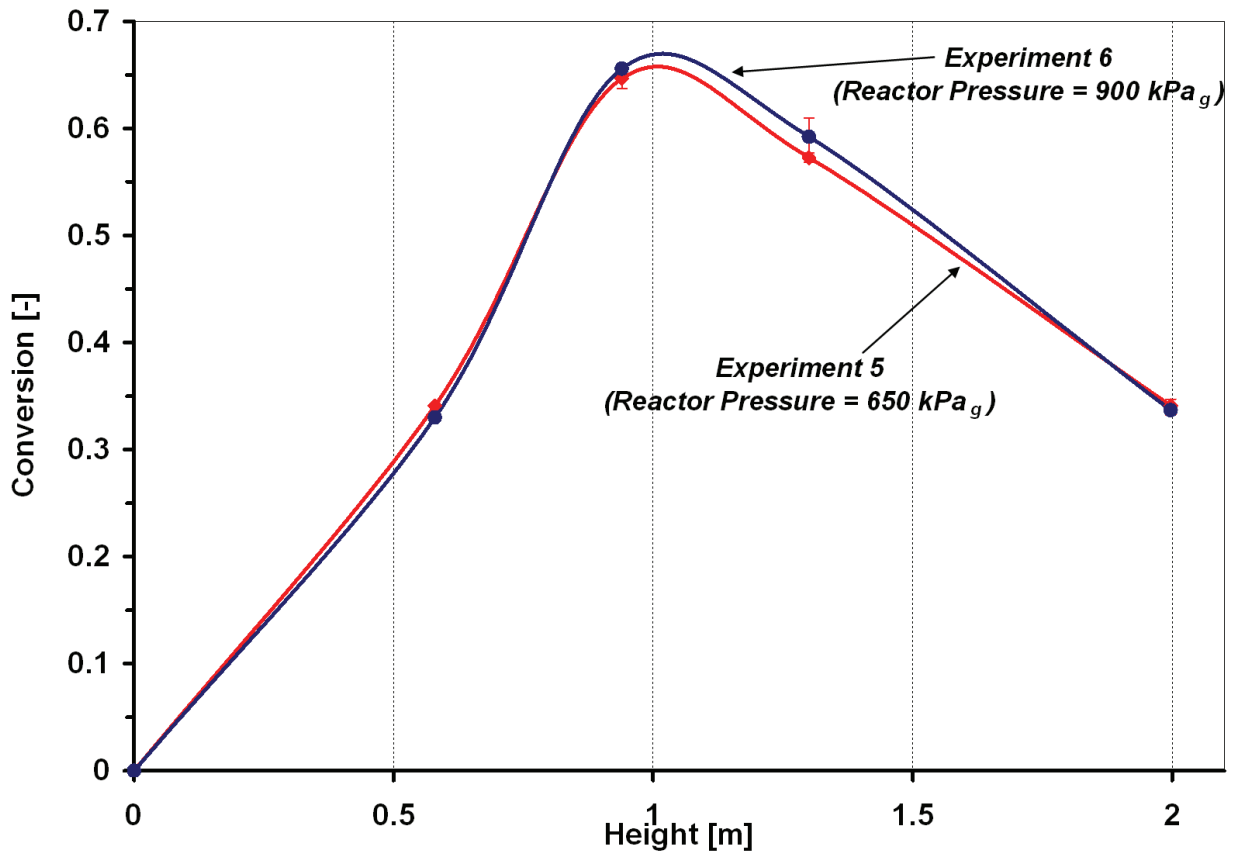


Figure 3.10. Effect of reactor pressure on methane conversion vs height. For experimental conditions, see Table 3.2, for Experiments 5 and 6.

3.3.3.6. Effect of air input (SMR vs ATR): Figure 3.11 shows the overall effect of air input. A fraction of the oxidizing air is fed at the bottom distributor converting methane almost instantaneously and therefore generating heat for the endothermic reforming reactions. A higher methane conversion is observed in the ATR cases compared to corresponding SMR cases. As discussed above, there is an increase in temperature, as well as higher methane conversion in the top distributor region due to the exothermic combustion of methane and hydrogen, as depicted in Figures 3.5 and 3.11. Reverse reactions are a little less significant during autothermal operation than during SMR. In addition, ATR runs required ~37% less electrical heating power than their SMR counterparts, a significant reduction in a small-scale prototype characterized by high heat losses due to its high shell surface area per unit volume.

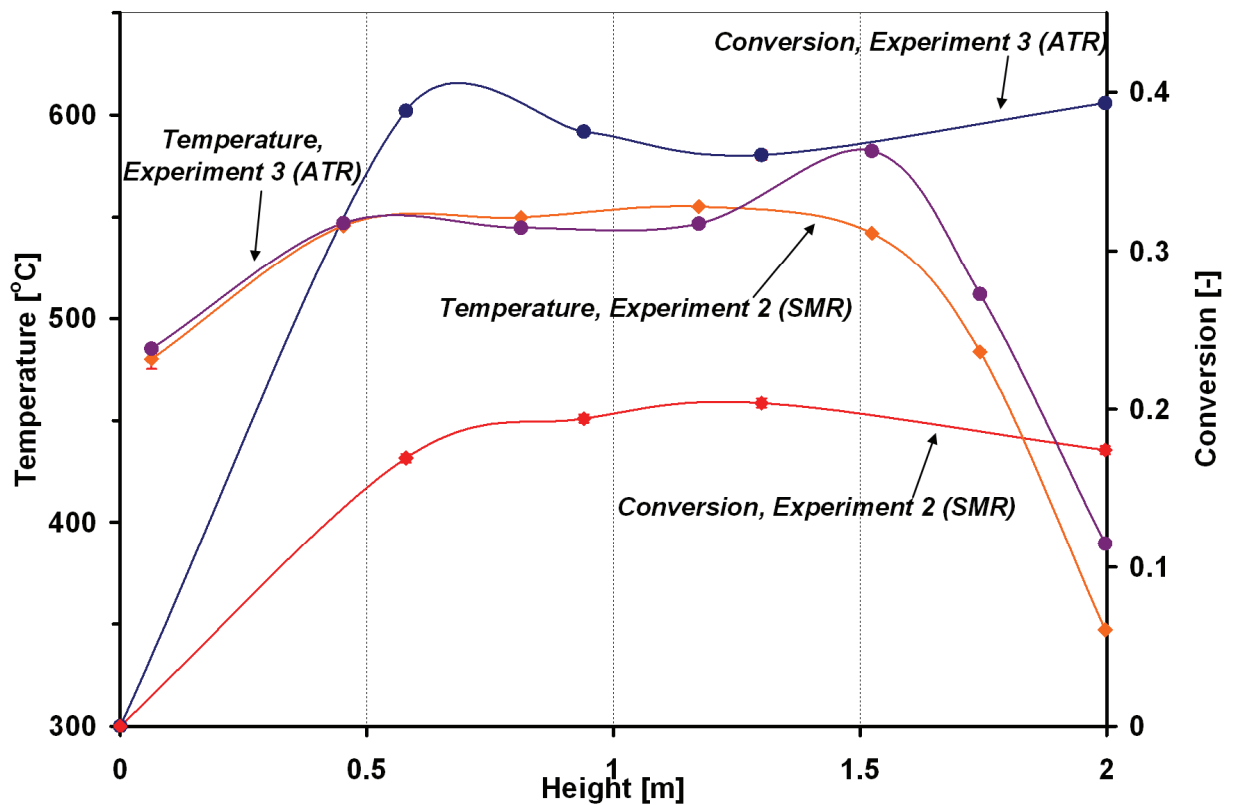


Figure 3.11. Methane conversion and temperature vs reactor height for experiments 2 (SMR) and 3 (ATR). Effect of oxygen input. For experimental conditions, see Table 3.2.

3.3.3.7. Effect of air split: Air or pure oxygen may be injected during ATR operations. Air is generally preferred for economic reasons since it does not require oxygen separation. However, nitrogen feed to the reactor in the oxidant air reduces H_2 recovery by diluting the reactor gases, thereby lowering the H_2 driving force across the membranes. This nitrogen penalty may be diminished by introducing as much air as possible at the top of the reactor, relying on catalyst

internal circulation to carry heat back to the bottom. The higher the proportion of air fed to the top of the reactor, the lower the nitrogen penalty, but at the expense of a larger axial temperature gradient.

Experiments 10 and 11 were conducted under almost identical operating conditions, the only difference being their top/bottom air split. Figure 3.12 plots the axial conversion profiles for these two experiments. As expected, Experiment 10 showed better performance, demonstrating that more air feed to the top of the reactor improves hydrogen yield because of a diminished nitrogen penalty. Appendix E provides additional information regarding the effect of the air flow division.

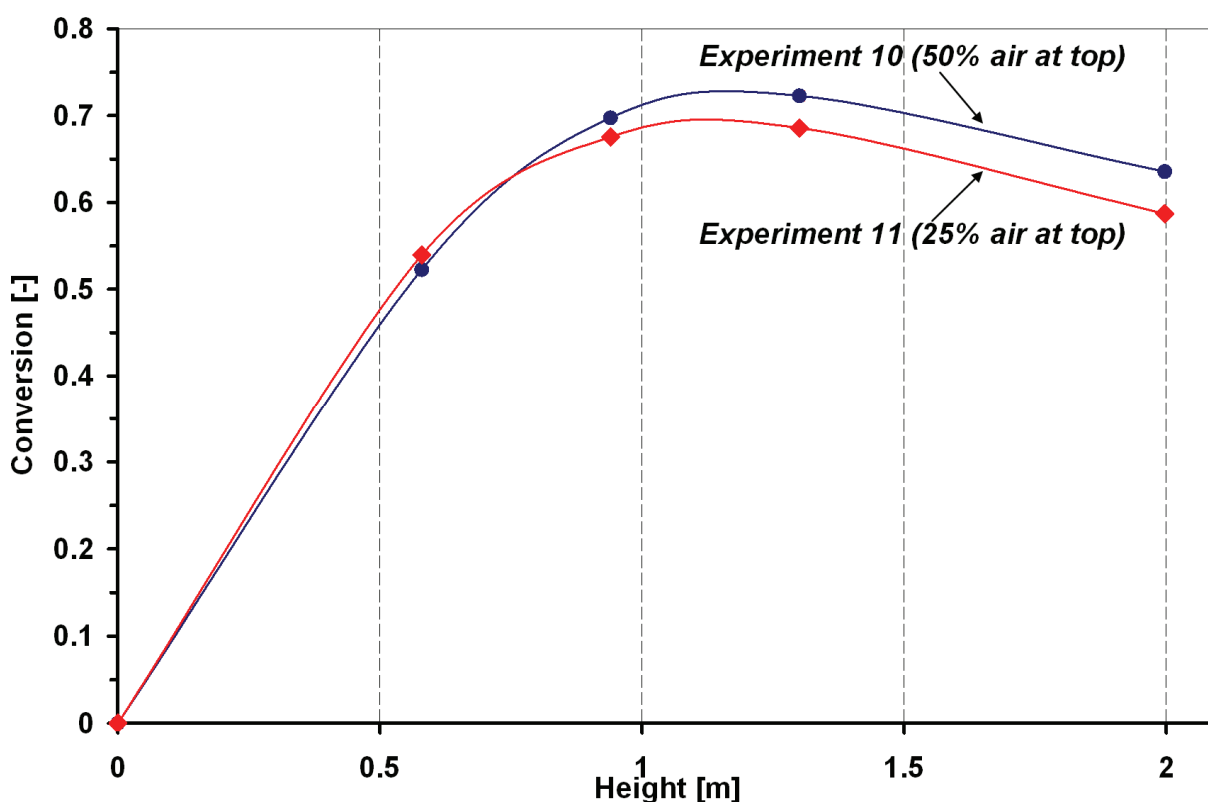


Figure 3.12. Effect of air distribution on methane conversion vs height. For experimental conditions, see Table 3.2, Experiments 10 and 11.

3.3.3.8. Gas backmixing: Downflow of particles in fluidized beds causes axial dispersion and backmixing of gas. By tracking the concentration of nitrogen along the reactor height, it is possible to establish, as in Figure 3.13, how far the oxidizing stream backmixes along the reactor. This effect is important with respect to the nitrogen penalty when air is fed at the top of the reactor. Some short-range gas backmixing was encountered in these tests. Since the total volumetric flowrate of gas varies along the reactor due to chemical reaction, species removal, as

well as temperature and pressure gradients, it is difficult to determine the dispersion of nitrogen quantitatively. Nevertheless, if changes in volumetric flowrate are ignored, the amount of N_2 backmixed from the top nozzle to the upper membrane level can be roughly estimated to be $\sim 13\%$ for Experiment 10, whereas the corresponding fractions were $\sim 43\%$ and $\sim 41\%$ for Experiments 11 and 12, respectively. The fraction of N_2 that migrated as far as the middle membrane level and below was negligible in all cases. This is a favourable result as it indicates that nitrogen entering with air at the top does not dilute the gas over most of the height, and hence its effect on hydrogen permeation is minimal.

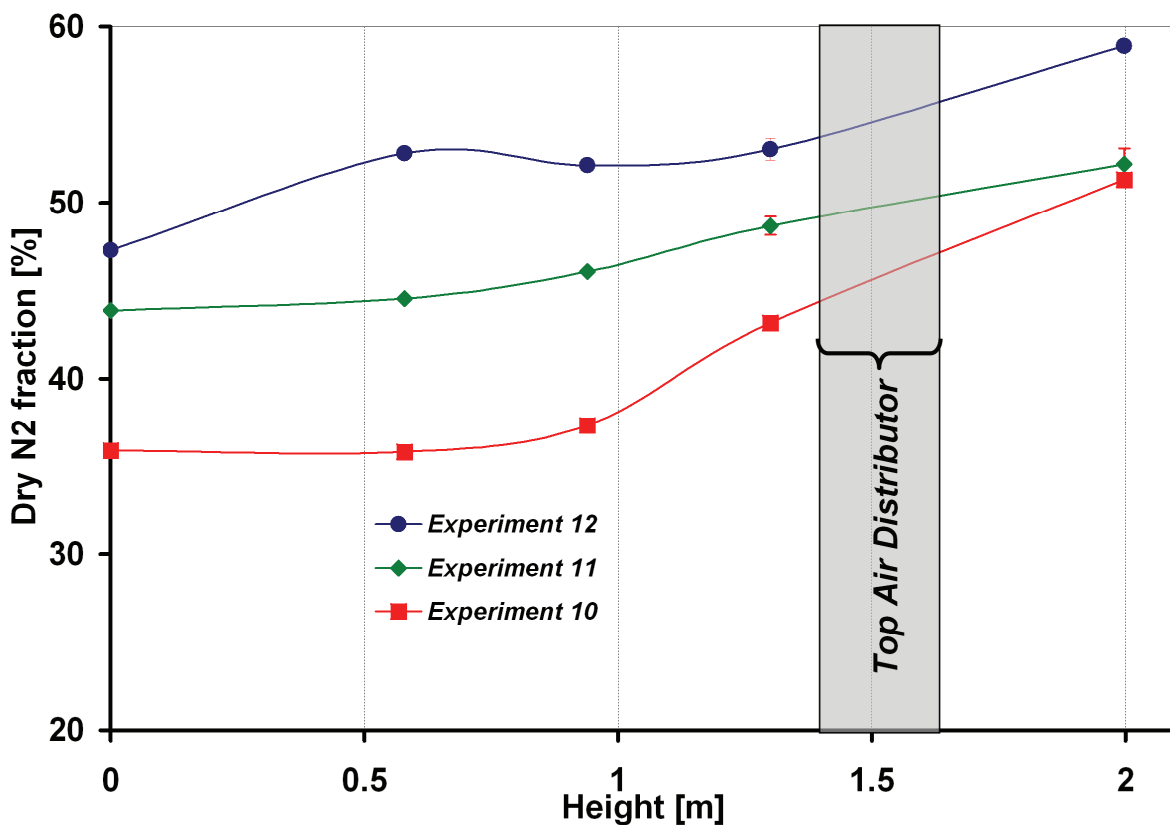


Figure 3.13. Nitrogen concentration vs height for experiments 10 (50% air at top), 11 (25% air at top) and 12 (10.4% air at top). Gas backmixing. For experimental conditions see Table 3.2.

3.3.3.9. Effect of feed rates: Figure 3.14 depicts the increase in reactor conversion when the reactant feed rate is reduced. Figure 3.15 presents the relation between the methane feed rate and the measured permeate H_2 / methane molar ratio. As can be discerned from Table 3.5, the absolute hydrogen permeate production rate during the experimental runs was very similar for the same number of membrane panels, again indicating that the membrane permeation is the controlling element for the FBMR. When the feed rates were reduced, the permeate flow was almost unchanged, so that the hydrogen recovery ratio increased, as shown in Figure 3.15.

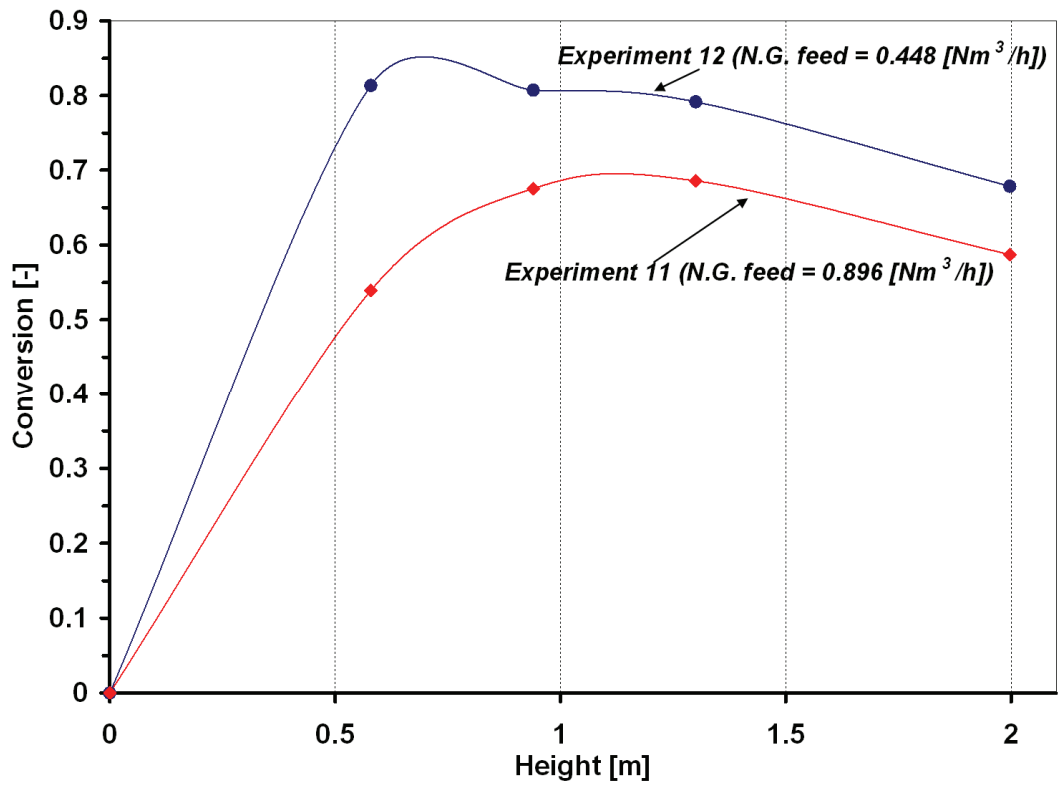


Figure 3.14. Effect of methane feed rate on axial methane conversion. For experimental conditions, see Table 3.2, Experiments 11 and 12.

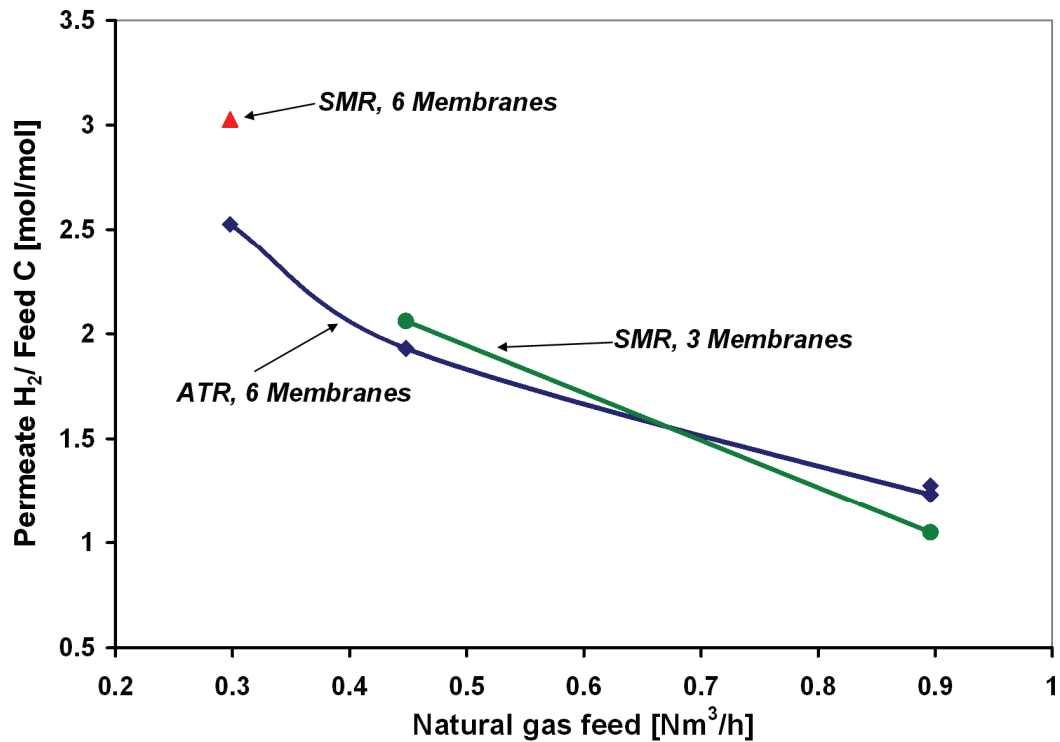


Figure 3.15. Yield of hydrogen, i.e. molar ratio of H₂ permeation rate divided by methane feed rate, as a function of methane feed rate for operation at 900 kPa(g), for 3 and 6 membranes, SMR and ATR operation. For experimental conditions see Table 3.2.

3.4. Conclusions

The performance of a novel fluidized-bed reactor containing internal vertical membrane panels was tested under steam methane reforming (SMR) and autothermal reforming (ATR) conditions, with and without active membranes. Axial temperature variations along each membrane panel were always less than 20°C, thereby enhancing membrane longevity. Some reverse reaction was observed in the reactor freeboard, thus reducing overall methane conversion. Although some minor gas backmixing was observed, provision of air from the top dense phase zone proved to be an asset since it reduced the nitrogen penalty during ATR operation, while still allowing heat to be recirculated by the catalyst particles. The effects of reactor pressure, hydrogen permeate pressure, air top/bottom split, feed flowrate and membrane load were all investigated.

Hydrogen permeate purities up to 99.995% and H₂/CH₄ yield of 2.07 were achieved with only half of the full complement of membrane panels installed under SMR conditions. The reactor produced 1.1 Nm³/h of permeate H₂ under ATR conditions. The hydrogen permeate purity was up to 99.994%, with a H₂/CH₄ yield of 3.03 with the full complement of six membrane panels under SMR conditions. The overall performance of the reactor was primarily dependent on the installed membrane area, as demonstrated by the fact that permeate hydrogen production remained almost constant when methane feed rates were varied while other conditions were unchanged.

The current chapter is the first of a series of two, dealing with a common system. The next chapter applies a generalized comprehensive reactor model accounting for a number of complex phenomena in a two pseudo-phase system, to simulate the prototype reactor described above.

3.5. References

- Abba, I.A., Grace, J.R. and Bi, H.T. (2003a). Application of the generic fluidized-bed reactor model to the fluidized-bed membrane reactor process for steam methane reforming with oxygen input. *Ind. Eng. Chem. Res.*, 42, 2736-2745.
- Adris, A.M. (1994). Fluidized-bed membrane reactor for steam-methane reforming: Experimental verification and model validation. Department of Chemical and Biological Engineering. Vancouver, University of British Columbia. Ph.D. Thesis.
- Adris, A.M. and Grace, J.R. (1997). Characteristics of fluidized-bed membrane reactors: scale-up and practical issues. *Ind. Eng. Chem. Res.*, 36, 4549-4556.

Adris, A.M., Grace, J.R., Lim, C.J. and Elnashaie, S.S.E.H. (1994). Fluidized bed reaction system for steam/hydrocarbon gas reforming to produce hydrogen. US Patent number 5326550.

Adris, A.M., Lim, C.J. and Grace, J.R. (1997). The fluidized bed membrane reactor for steam methane reforming: Model verification and parametric study. *Chem. Eng. Sci.*, 52, 1609-1622.

Adris, A.M., Pruden, B.B., Lim, C.J. and Grace, J.R. (1996). On the reported attempts to radically improve the performance of the steam methane reforming reactor. *The Canadian Journal of Chemical Engineering*, 74, 177-186.

Boyd, T. (2007). Hydrogen from an internally circulating fluidized bed membrane reactor Department of Chemical and Biological Engineering. Vancouver, University of British Columbia. Ph.D. Thesis.

Boyd, T., Grace, J.R., Lim, C.J. and Adris, A. (2005). Hydrogen from an internally circulating fluidized bed membrane reactor. *Int. J. Chem. Reactor Eng*, 3, A58.

Chen, Z., Grace, J.R., Lim, C.J. and Li, A. (2007). Experimental studies of pure hydrogen production in a commercialized fluidized-bed membrane reactor with SMR and ATR catalysts. *Int. J. Hydrogen Energy* 31, 2359-2366.

Chen, Z., Prasad, P., Yan, Y. and Elnashaie, S.S.E.H. (2003a). Simulation for steam-reforming of natural gas with oxygen input in a novel membrane reformer. *Fuel Process. Technol.*, 83, 235-252.

Chen, Z., Yan, Y. and Elnashaie, S.S.E.H. (2003b). Modeling and optimization of a novel membrane reformer for higher hydrocarbons. *AIChE J.*, 49, 1250-1265.

Chen, Z., Yan, Y. and Elnashaie, S.S.E.H. (2003c). Novel circulating fast fluidized-bed membrane reformer for efficient production of hydrogen from steam-reforming of methane. *Chem. Eng. Sci.*, 58, 4335-4349.

Chen, Z., Yan, Y. and Elnashaie, S.S.E.H. (2004). Catalyst deactivation and engineering control for steam-reforming of higher hydrocarbons in a novel membrane reformer. *Chem. Eng. Sci.*, 59, 1965-1978.

Crabtree, G.W., Dresselhaus, M.S. and Buchanan, M.V. (2004). The hydrogen economy. *Physics Today*, 57, 39-45.

Deshmukh, S.A.R.K., Heinricha, S., Mörl, L., van Sint Annaland, M. and Kuipers, J.A.M. (2007). Membrane assisted fluidized bed reactors: Potentials and hurdles. *Chem. Eng. Sci.*, 62, 416-436.

Deshmukh, S.A.R.K., Laverman, J.A., van Sint Annaland, M. and Kuipers, J.A.M. (2005). Development of a membrane-assisted fluidized bed reactor. 2. Experimental demonstration and modeling for the partial oxidation of methanol. *Ind. Eng. Chem. Res.*, 44, 5966-5976.

Dogan, M., Posarac, D., Grace, J.R., Adris, A.M. and Lim, C.J. (2003). Modeling of autothermal steam methane reforming in a fluidized bed membrane reactor. *International Journal of Chemical Reactor Engineering*, 1, A2.

- Elnashaie, S.S.E.H. and Elshishini, S.S. (1993). Modelling, simulation and optimization of industrial fixed-bed catalytic reactors. Gordon and Breach Science Publishers, Amsterdam.
- Ferreira-Aparicio, P., Benito, M.J. and Sanz, J.L. (2005). New Trends in Reforming Technologies: from Hydrogen Industrial Plants to Multifuel Microreformers. *Catalysis Reviews*, 47, 491-588.
- Grace, J.R., Elnashaie, S.S.E.H. and Lim, C.J. (2005). Hydrogen production in fluidized beds with in-situ membranes. *International Journal of Chemical Reactor Engineering*, 3, A41.
- Grace, J.R., Li, X. and Lim, C.J. (2001). Equilibrium modeling of catalytic steam reforming of methane in membrane reactors with oxygen addition. *Catalysis Today*, 64, 141-149.
- Grace, J.R., Lim, C.J., Adris, A.M., Xie, D., Boyd, T., Wolfs, W.M. and Brereton, C.M.H. (2006). Internally circulating fluidized bed membrane reactor system. U.S. Patent 7,141,231 B2.
- Hoang, D.L. and Chan, S.H. (2004). Modeling of a catalytic autothermal methane reformer for fuel cell applications *Applied Catalysis A: General*, 268, 207-216.
- Jarosch, K. and de Lasa, H.I. (1999). Novel riser simulator for methane reforming using high temperature membranes. *Chem. Eng. Sci.*, 54 1455-1460.
- Jin, W., Gu, X., Li, S., Huang, P., Xu, N. and Shi, J. (2000). Experimental and simulation study on a catalyst packed tubular dense membrane reactor for partial oxidation of methane to syngas. *Chem. Eng. Sci.*, 55, 2617-2625.
- Jorgensen, S.L., Nielsen, P.E.H. and Lehrmann, P. (1995). Steam reforming of methane in a membrane reactor. *Catalysis Today*, 25, 303-307.
- Koroneos, C., Dompros, A., Roumbas, G. and Moussiopoulos, N. (2004). Life cycle assessment of hydrogen fuel production processes. *International Journal of Hydrogen Energy*, 29, 1443-1450.
- Kunii, D. and Levenspiel, O. (1991). *Fluidization engineering*, 2nd ed. Butterworth-Heinemann, Boston.
- Låte, L., Rundereim, J.I. and Blekkan, E.A. (2004a). Selective combustion of hydrogen in the presence of hydrocarbons Part 1. Pt-based catalysts. *Applied Catalysis A: General*, 262, 53–61.
- Låte, L., Thelin, W. and Blekkan, E.A. (2004b). Selective combustion of hydrogen in the presence of hydrocarbons Part 2. Metal oxide based catalysts. *Applied Catalysis A: General*, 262, 63–68.
- Mahecha-Botero, A., Boyd, T., Gulamhusein, A., Comyn, N., Lim, C.J., Grace, J.R., Shirasaki, Y. and Yasuda, I. (2008a). Pure hydrogen generation in a fluidized bed membrane reactor: Experimental findings. *Chem. Eng. Sci.*, 63, 2752-2762.
- Mleczko, L., Ostrowski, T. and Wurzel, T. (1996). A fluidized-bed membrane reactor for the catalytic partial oxidation of methane to synthesis gas. *Chem. Eng. Sci.*, 51, 3187-3192.

Nandasana, A.D., Ray, A.K. and Gupta, S.K. (2003). Dynamic model of an industrial steam reformer and its use for multiobjective optimization. *Ind. Eng. Chem. Res.*, 42, 4028-4042.

NRC, U.S.A. (2004). The hydrogen economy: opportunities, costs, barriers, and R&D needs, Committee on alternatives and strategies for future hydrogen production and use. National Research Council, USA.

Ogden, J.M. (2001). Review of small stationary reformers for hydrogen production. A report for the International Energy Agency Agreement on the Production and Utilization of Hydrogen. Hydrogen from Carbon-Containing Materials.

Paglieri, S.N. and Way, J.D. (2002). Innovations in palladium membrane research. *Sep. Purif. Methods* 31, 1-169.

Patil, C.S., van Sint Annaland, M. and Kuipers, J.A.M. (2005). Design of a novel autothermal membrane-assisted fluidized-bed reactor for the production of ultrapure hydrogen from methane. *Ind. Eng. Chem. Res.*, 44, 9502-9512.

Patil, C.S., van Sint Annaland, M. and Kuipers, J.A.M. (2006). Experimental study of a membrane assisted fluidized bed reactor for H₂ production by steam reforming of CH₄. *Chem. Eng. Res. Des.*, 84, 399-404.

Prasad, P. (2004). Circulating fluidized bed reforming process for hydrogen production from methane. Department of Chemical Engineering. Auburn, USA, Auburn University. Ph.D. Thesis.

Prasad, P. and Elnashaie, S.S.E.H. (2004). Novel circulating fluidized-bed membrane reformer using carbon dioxide sequestration. *Ind. Eng. Chem. Res.*, 43, 494-501.

Raich, B.A. and Foley, H.C. (1995). Supra-equilibrium conversion in palladium membrane reactors: Kinetic sensitivity and time dependence. *Appl. Catal., A* 129, 167-188.

Roy, S. (1998). Fluidized-bed steam-methane reforming with high-flux membranes and oxygen input. Department of Chemical Engineering. Calgary, University of Calgary. Ph.D. Thesis.

Roy, S., Pruden, B.B., Adris, A., Grace, J.R. and Lim, C.J. (1999). Fluidized-bed steam-methane reforming with oxygen input. *Chem. Eng. Sci.*, 54, 2095-2102.

Scura, F., Barbieri, G. and Drioli, E. (2006). H₂ for PEM-FC: effect of CO in the purification by means of Pd-based membranes. *Desalination*, 200, 239-241.

Shu-Ren, H. (1998). Hydrocarbon steam-reforming process: feedstock and catalysts for hydrogen production in China. *Int. J. Hydrogen Energy*, 23, 315-319.

Shu, J., Adnot, A., Grandjean, B.P.A. and Kaliaguine, S. (1996). Structurally stable composite Pd-Ag alloy membranes: Introduction of a diffusion barrier. *Thin Solid Films*, 286, 72-79.

Shu, J., Grandjean, B.P.A. and Kaliaguine, S. (1994). Morphological study of hydrogen permeable Pd membranes. *Thin Solid Films*, 252, 26-31.

Sieverts, A. and Zapf, G. (1935a). Iron and nitrogen. *Zeitschrift für Physikalische Chemie*, 172 314-315.

Sieverts, A. and Zapf, G. (1935b). The solubility of deuterium and hydrogen in solid palladium. *Zeitschrift für Physikalische Chemie*, 174, 359-364.

Thomsen, V.B.E. (2000). LeChâtelier's principle in the sciences. *J. Chem. Educ.*, 77.

Uemiya, S. (2004). Brief review of steam reforming using a metal membrane reactor. *Top. Catal.*, 29, 79-84.

Wen, C.Y. and Yu, Y.H. (1966). A generalized method for predicting the minimum fluidization velocity. *AIChE J.*, 12, 610-612.

Xu, J. and Froment, G.F. (1989a). Methane steam reforming, methanation and water-gas shift: I. Intrinsic kinetics. *AIChE J.*, 35, 88-96.

Xu, J. and Froment, G.F. (1989b). Methane steam reforming: II. Diffusional limitations and reactor simulation. *AIChE J.*, 35, 97-103.

Yates, J.G. (1983). *Fundamentals of fluidized-bed chemical processes*. Butterworth-Heinemann, London.

4. PURE HYDROGEN GENERATION IN FLUIDIZED-BED MEMBRANE REACTOR: APPLICATION OF GENERALIZED COMPREHENSIVE MODEL ⁴

4.1. Introduction

In this work, a simplified version of the conservation equations described in Section 1.2 (Equations 1.9, 1.18 and 1.21) is used to simulate a fluidized-bed membrane reactor, modeled as two interacting phases, utilizing an extension of the two-phase theory of fluidization (Toomey and Johnstone, 1952) to set the flow distribution. The characteristics of the reactor were those of the experimental equipment used to obtain the experimental data reported and discussed in Chapter 3. Table 4.1 explains the steps followed for the utilization of the conservation equations.

All the features not covered in Table 4.1 are maintained equal to those of the general conservation equations above of Section 1.2.

4.2. Model Implementation

After the reduction steps described, the model is applied to simulate the fluidized-bed membrane reactor. The reactor is divided into two phases which contain gas and solids, as well as a membrane phase (i.e. $N_\phi=3$). The high-density and low-density phases occupy ψ_H and ψ_L fractions of the non-membrane reactor volume respectively.

⁴ *A version of this Chapter is under review for publication as: Mahecha-Botero, A., Grace, J.R., Lim, C.J., Elnashaie, S.S.E.H., Boyd, T. and Gulamhusein, A. (2009). "Pure Hydrogen Generation in a Fluidized Bed Membrane Reactor: Application of the Generalized Comprehensive Reactor Model"*.

Table 4-1. Model reduction and simplification of conservation equations.

System characteristic	Measured experimental data in Chapter 3	Modeling approach
Distributed system with large variations in concentrations along the reactor's height.	Measured in-bed concentration profile along the reactor's height. Gas chromatograph detection at five different heights. At each level the samples were taken at a single horizontal position.	A one-dimensional distributed model was implemented to simulate the concentration variation with height in the two phases (Sections 4.2.1 and 4.4).
Selective hydrogen removal using Palladium membranes.	Membrane parameters were experimental. The overall hydrogen production as well as distributed conversion along the bed were measured.	Membrane removal simulated implementing Sieverts' Law. Mole balance included for the hydrogen membranes divided into stages according to reactor geometry (Section 4.2.4).
Steady state operation.	Gas sampling and data recording performed with system stabilized; <1% variations in methane conversion.	System assumed to be at steady state.
Pilot plant reactor with distributed internal and external heaters. Heat losses difficult to characterize. Very large internal heat dispersion and virtually uniform in-bed temperature profile.	Temperature profile measured along reactor at eight levels. Heat loss characterization outside the scope of this work.	Two different models were tested. In Section 4.2.2.1 a 2-D distributed model accounting for heat dispersion was implemented. This model concluded that for SMR runs the temperature variation is expected to be less than 2°C. Therefore subsequent modeling was performed using a simple spline interpolation of the experimental data points which are clearly affected by external heat effects as discussed in Section 4.2.2.2.
Air fed at top and bottom for autothermal operation.	Top/bottom air split measured experimentally.	Model in Section 4.2.8 allows for introduction of an air pulse at top of the reactor.
No sorbent added to the reactor solids.	No carbonation studies were done.	All sorbent terms in the model equations were neglected. Chen <i>et al.</i> (2008) showed that for an equal number of moles of H ₂ or CO ₂ removed, membranes are more effective in pushing the equilibrium forward, although hydrogen yield also benefits significantly from both membranes or sorbents.
Catalyst chemisorption is expected to be small.	No measurements of catalyst chemisorption.	All chemisorption terms in the model equations were neglected.
Reforming occurs over entire surface of catalyst particles.	Catalyst particles of average diameter 90 μm were introduced to the reactor. These small particles have high effectiveness.	Catalyst overall effectiveness factor assumed to be 1.0.
Catalyst deactivation may occur during SMR.	Catalyst deactivation was not expected to be an issue over the limited time of operation given the constant steam-to-carbon molar ratio of 3.0.	Catalyst activity assumed to be 1.0.

4.2.1. Mole Balance Equations for the Two Phases

By simplifying Equation 1.9, the resulting mole balances for the two phases and hydrogen membranes are:

High-density phase (emulsion):

$$\begin{aligned}
 & -\frac{1}{A} \cdot \frac{d}{dz} (v_H \cdot C_{i_H}) + \psi_H \cdot a_{I_{HL}} \cdot k_{c_{iHL}} \cdot (C_{i_L} - C_{i_H}) - \psi_H \cdot v_{Bulk_{HL}} \cdot C_{i_H} + \psi_L \cdot v_{Bulk_{LH}} \cdot C_{i_L} \\
 & + \psi_H \cdot (1 - \varepsilon_H) \cdot \rho_{cat} \cdot \sum_{j=1}^{N_R} v_{ij} \cdot \Omega_{j_H} \cdot a_{j_H} \cdot r'_{j_H} - \psi_H \cdot p_M \cdot J_{i_H} + (Split_{top} \cdot v_{f_H} \cdot C_{if_H}) \delta(z - z_{Top}) = 0
 \end{aligned} \tag{4.1}$$

$i = 1, 2, \dots, N_C$

Low-density phase (bubble):

$$\begin{aligned}
 & -\frac{1}{A} \cdot \frac{d}{dz} (v_L \cdot C_{i_L}) + \psi_L \cdot a_{I_{LH}} \cdot k_{c_{iLH}} \cdot (C_{i_H} - C_{i_L}) - \psi_L \cdot v_{Bulk_{LH}} \cdot C_{i_L} + \psi_H \cdot v_{Bulk_{HL}} \cdot C_{i_H} \\
 & + \psi_L \cdot (1 - \varepsilon_L) \cdot \rho_{cat} \cdot \sum_{j=1}^{N_R} v_{ij} \cdot \Omega_{j_L} \cdot a_{j_L} \cdot r'_{j_L} - \psi_L \cdot p_M \cdot J_{i_L} + (Split_{top} \cdot v_{f_L} \cdot C_{if_L}) \delta(z - z_{Top}) = 0
 \end{aligned} \tag{4.2}$$

$i = 1, 2, \dots, N_C$

Membranes:

$$-\frac{1}{A_M} \cdot \frac{d}{dz} (v_M \cdot C_{i_M}) + \psi_H \cdot p_M \cdot J_{i_H} + \psi_L \cdot p_M \cdot J_{i_L} = 0 \tag{4.3}$$

$i = 1, 2, \dots, N_{CM}$

where the phase's volumetric flow is $v_\varphi = \psi_\varphi \cdot \varepsilon_\varphi \cdot U_{gas_\varphi} \cdot A$, p_M is the membrane perimeter per unit area of reactor cross section, J_{i_φ} the species membrane flux and N_{CM} the number of chemical species in the membrane ($N_{CM}=2$ if sweep nitrogen or steam is used to reduce the partial pressure of hydrogen, or $N_{CM}=1$ if there is no sweep gas). Likewise v_{f_φ} and C_{if_φ} are the feed volumetric flowrate and feed concentration of species i in phase φ . $Split_{top}$ is the fraction of the feed gas that is injected from the top of the reactor, whereas δ is the Dirac delta function which simulates top air feed pulse, as explained in Section 4.2.8.

The bed volume fractions add up to unity:

$$\psi_H + \psi_L = 1 \quad (4.4)$$

The molar flow-rate of each species in the reactor is divided between the two phases, i.e.

$$F_i = v_H \cdot C_{i_H} + v_L \cdot C_{i_L} \quad (4.5)$$

4.2.2. Energy Balance

Two steps were followed to simulate the temperature variations in the pilot FBMR. **(1)** Initially a 2-D distributed model accounting for heat dispersion was implemented to verify the heat dispersion in the system and to identify the best strategy for further simulations. This model demonstrated that the temperature variation is expected to be less than 2°C. **(2)** Subsequent modeling used a simple spline interpolation of the experimental temperature data points which are clearly affected by external heat effects such as heat losses for a reactor of small volume and large surface area.

4.2.2.1. Preliminary heat studies:

Fluidized-beds provide excellent interphase internal heat transfer (Grace, 1982; Howard, 1989). Consequently including both phases within a single overall heat balance does not introduce significant error. This implies that the three interphase heat transfer terms from Equation 1.18 cancel in the overall balance. Table 4.1 explains some of the terms reduced from Equation 1.18. Including these assumptions we obtain:

$$\begin{aligned} & -\vec{\nabla} \cdot \left[\varepsilon_T \cdot \sum_{i=1}^{NC} (C_{i_T} \cdot E_{i_T}) \overrightarrow{U_{gas_T}} \right] - \vec{\nabla} \cdot \left[(1 - \varepsilon_T) \cdot \rho_{cat} \cdot E_{cat_T} \cdot \overrightarrow{U_{cat_T}} \right] - \vec{\nabla} \cdot (\overrightarrow{q_T}) \\ & + \left[(1 - \varepsilon_T) \rho_{cat} \cdot \sum_{j=1}^{N_{Rcat}} \Delta H_{j_{cat}} \cdot \Omega_{j_{cat,T}} \cdot a_{j_{cat,T}} \cdot r'_{j_{cat,T}} \right] = 0 \end{aligned} \quad (4.6)$$

Mean values are used for physical properties such as the heat capacity and density. The overall heat balance used in the simulations is:

$$\begin{aligned} & -\vec{\nabla} \cdot \left[\left(\varepsilon_T \cdot \langle \rho_{gas_T} \rangle \cdot \langle C_{p_{gas,T}} \rangle + (1 - \varepsilon_T) \cdot \rho_{cat} \cdot C_{p_{cat,T}} \right) T_T \cdot \overrightarrow{U_{gas_T}} \right] - \vec{\nabla} \cdot \left[-\langle K_T \rangle \vec{\nabla} \cdot (T_T) \right] \\ & + \left[(1 - \varepsilon_T) \rho_{cat} \cdot \sum_{j=1}^{N_{Rcat}} \Delta H_{j_{cat}} \cdot \Omega_{j_{cat,T}} \cdot a_{j_{cat,T}} \cdot r'_{j_{cat,T}} \right] = 0 \end{aligned} \quad (4.7)$$

where the thermal dispersion coefficient is a function of the flow regime, gas velocity, and gas properties as described in Section 4.2.10.6. The temperature variation predicted by the model in the absence of heat losses are considered to be small (typically less than 2°C as depicted in Figure 4.1). The temperature deviations from the experimental data of Chapter 3 are related to the means of external heating, as well as external heat losses in a vessel of small volume.

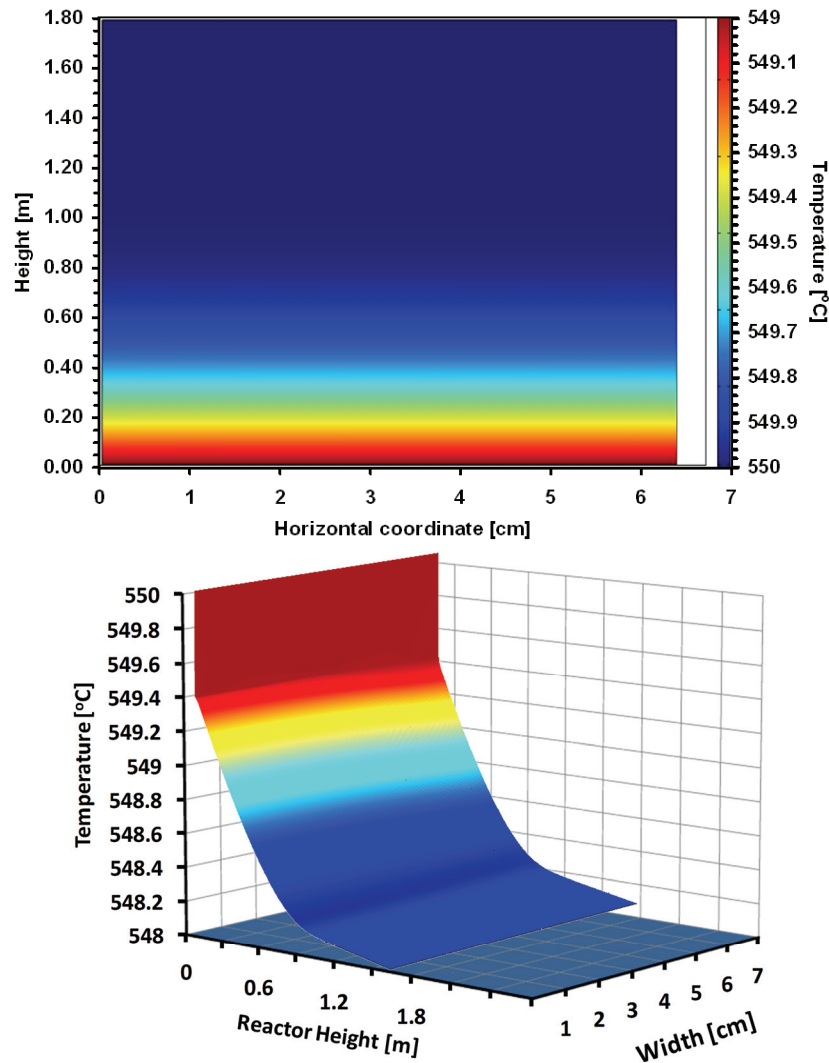


Figure 4.1. Simulated 2-D adiabatic temperature profile.

4.2.2.2. Simplified temperature profiles:

In view of the preliminary heat dispersion studies from Section 4.2.2.1, it was decided that the most practical way to study the fluidization characteristics of the prototype reactor was to implement a simple interpolation routine through the experimental temperature data points. In this fashion, the more complex fluidization issues could be studied without introducing errors caused by the characterization of the reactor insulation and heating characteristics. Typical

reactor temperature profiles are presented in Figures 3.4, 3.5 and 3.11 of Chapter 3. Figure D.2 depicts the actual insulation implemented in the experimental program.

4.2.3. Pressure Balance

With average properties for the H and L phases, Equation 1.21 gives:

$$-\frac{dP_T}{dz} = [(1 - \varepsilon_T) \cdot \rho_{cat} \cdot g] + [\varepsilon_T \cdot \rho_{gas} \cdot g] \quad (4.8)$$

Figure 4.2 shows a typical pressure profile. It is seen that the pressure decays almost linearly along the dense phase. Above the expanded bed surface, the pressure decays much more gradually in the freeboard region. The total bed pressure drop was very small (less than 20 kPa) in all experimental runs.

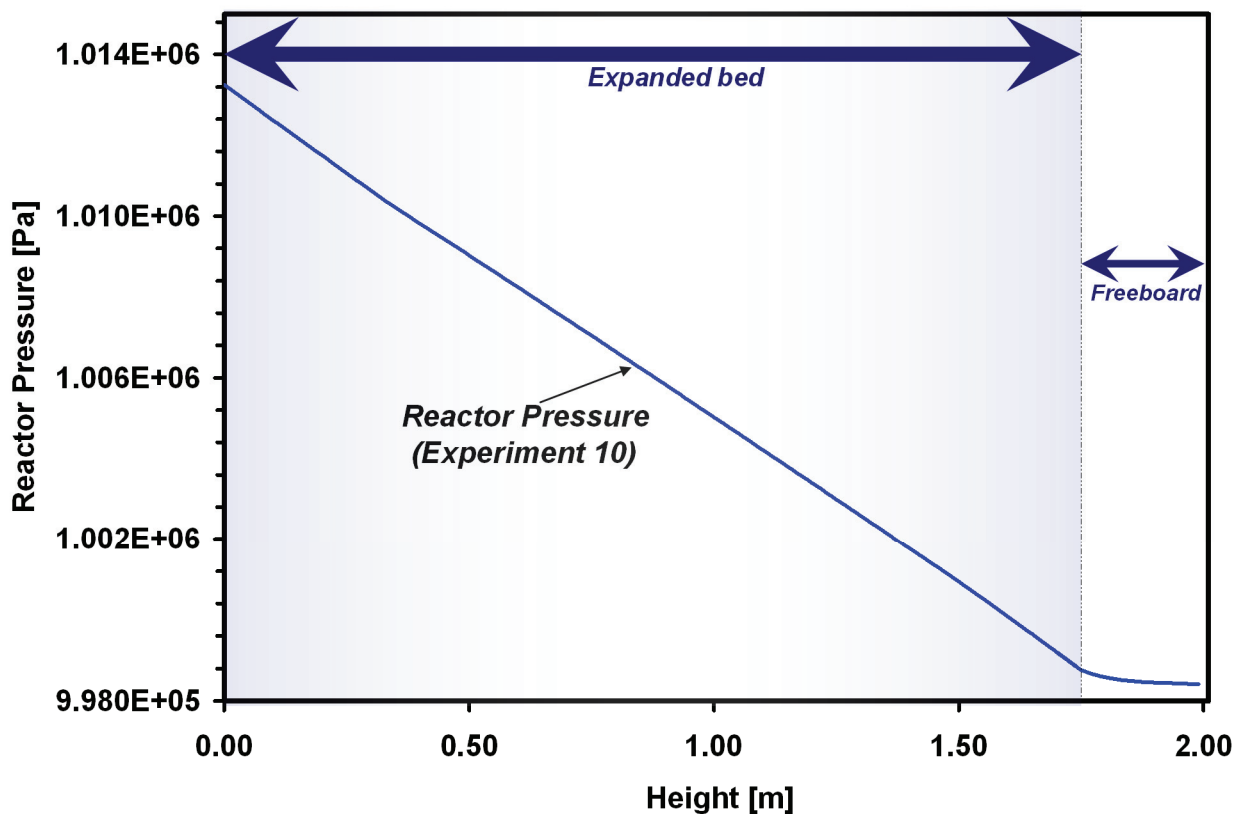


Figure 4.2. Simulated reactor pressure drop vs height (Experiment 10). For experimental/simulation parameters see Table 3.2.

4.2.4. Selective Removal of Species via Membranes

Hydrogen permeation through a membrane surface is estimated by Sieverts' Law (Sieverts and Zapf, 1935a, b):

$$J_{H_{2,\phi}} = \frac{k_{H_2}}{\Delta_{H_2}} \cdot e^{\left(\frac{-E_{H_2}}{R \cdot T_\phi}\right)} \cdot \left(\sqrt{P_{H_{2,\phi}}} - \sqrt{P_{H_{2,M}}}\right) \quad (4.9)$$

$$J_{i_\phi} = 0 \quad i \neq H_2 \quad (4.10)$$

where Δ_{H_2} is the Palladium foil thickness, T_ϕ the membrane surface temperature, and $P_{H_{2,\phi}}$ the partial pressure of hydrogen. In the actual reactor the membrane perimeter per unit area of reactor cross section, p_M'' , varies with height, and this is reflected in the model. The total flow of hydrogen permeating through a membrane panel of height $(z_2 - z_1)$ is estimated by

$$F_{H_{2,\phi}} = A_{Panel} \cdot \frac{\int_{z_1}^{z_2} J_{H_{2,\phi}} \cdot dz}{(z_2 - z_1)}, \text{ where } A_{Panel} \text{ is the corresponding effective membrane surface area.}$$

Section 6.3 discusses the effect of different membrane removal policies such as the use of vacuum and sweep gas.

4.2.5. Equi-molar Interphase Mass Transfer

Mass transferred due to a concentration gradient to/from the *H-phase* should be equal to that transferred from/to the *(L)-phase* to satisfy the overall reactor mass balance. Therefore:

$$\psi_H \cdot a_{I(H \rightarrow L)} \cdot k_{c_{i,(H \rightarrow L)}} \cdot (C_{i_L} - C_{i_H}) = -\psi_L \cdot a_{I(L \rightarrow H)} \cdot k_{c_{i,(L \rightarrow H)}} \cdot (C_{i_H} - C_{i_L}) \quad (4.11)$$

Since literature mass transfer correlations are usually presented on a “per unit volume of bubbles” basis, the mass transfer coefficients are calculated in terms of the *L-phase*. Although this term is expressed in terms of a concentration gradient, it accounts for both, diffusive and convective mass transfer (Sit and Grace, 1981).

4.2.6. Interphase Balancing Mass Transfer

In a bubbling fluidized-bed, the *H-phase* occupies most of the volume, and therefore has greater contact with membranes, compared with the *L-phase*. Most of the reaction occurs in the *H-phase*, whereas most flow is through the *L-phase*. These factors can lead to significant changes in flow in the *H-phase*; for example causing defluidization there, if there is no balancing flow to maintain a more appropriate flow distribution.

Estimating the balancing gas cross-flow is a critical step in reactor modelling where there is significant variation in the total molar flows due to reaction and/or membrane flux. In this work, accounting for interphase cross-flow proved to be very important. If interphase cross-flow were to be ignored, the bed could de-fluidize due to the reduction in gas flow in the H-phase caused by membrane removal. To calculate the interphase crossflow between the fluidizing phases, it is imperative to impose a flow division.

For bubbling beds, Toomey and Johnstone (1952) defined what is commonly now referred to as the two-phase theory of fluidization, giving a “visible” bubble flow of.:

$$v_{VB} = (U - U_{mf})A \quad (4.12)$$

There is considerable evidence (Turner, 1966; Rowe and Yacono, 1976; Yacono *et al.*, 1979) that this standard two-phase theory overestimates the visible gas flow. This may be due to increased flow in the *H-phase* or increased throughflow in the *L-phase*. Grace and Clift (1974) summarized the results from experimental studies dealing with the gas flow division in fluidized-beds. They showed that if one writes:

$$v_{VB} = (U - m.U_{mf})A \quad (4.13)$$

then m , based on experimental data, varied over a wide range (1.0 to ~18).

Other research has adopted an alternative modification of the standard two-phase theory:

$$v_{VB} = Y.(U - U_{mf})A \quad (4.14)$$

where Y is a constant smaller than unity, with experimental values between 0.67 and 0.8 (Werther, 1974). This constant may be predicted using the dimensional correlation proposed by Peters *et al.* (1982) applicable only for $U - U_{mf} \leq 0.233m.s^{-1}$ (Clift and Grace, 1985):

$$Y = 0.7585 - 0.13.(U - U_{mf}) + 5.(U - U_{mf})^2 \quad (4.15)$$

Although this issue has never been resolved, some earlier works treat it as follows:

- Adris (1994) tested the possibility of fixing the volumetric flow of the H -phase. However, Adris reported that the model is insensitive to changes in this value for a membrane reformer operating at low fluidization velocity with very low flux through the membrane surfaces.
- Abba (2001) assumed bulk transfer proportional to the difference between the H -phase volumetric flow and its entry value. However, Abba reported little influence of this term in an oxychlorination reactor operating near the turbulent/bubbling boundary and no effect was investigated for a reforming case study (Abba *et al.*, 2003a).
- Constantineau *et al.* (2007) accounted for bulk transfer of the extra moles generated by chemical reaction. In that case there were no membranes, and effects of temperature and pressure were ignored. Furthermore, Constantineau *et al.* (2007) assumed bulk flow to go only from the L -phase to the H -phase.

In the present work inter-phase convective mass transfer is introduced to the model equations to account for bulk migration of fluid between the phases. This phenomenon is not caused by a concentration gradient. Instead, gas is distributed between the phases depending on the increase/decrease of total volumetric flow, which may change due to chemical reaction, membrane permeation, changes in temperature or pressure, or a combination of the above. All of these variations are included in the current model. It is important to note that the composition of the flow leaving one phase will match that of the source phase.

The convective flow leaving the H -phase is given by:

$$\psi_H \cdot v_{Bulk(H \rightarrow L)} \cdot C_{i_H} \quad i = 1, 2, \dots, N_C \quad (4.16)$$

while that leaving the L - phase is:

$$\psi_L \cdot v_{Bulk(L \rightarrow H)} \cdot C_{i_L} \quad i = 1, 2, \dots, N_C \quad (4.17)$$

It is assumed that in order to maintain fluidization conditions throughout the bed, it is crucial to define what amount of gas flow is required in the high-density phase to prevent collapse. This amount of gas is defined according to the modified two-phase theory as $v_H = m \cdot U_{mf} \cdot A$ where m is taken as 1.0 by default (i.e. corresponding to the standard two-phase

theory). Although there is no consensus about the value of m (Grace and Clift, 1974; Fan and Zhu, 2005), it could be adjusted in the future depending on experimental measurements. The calculation algorithm at any integration point to maintain fluidizing conditions is:

<p>a) If $v_H < m.U_{mf}.A$ Gas flows to the H- phase to avoid de-fluidization.</p>	$v_{Bulk_{(H \rightarrow L)}}''' = 0,$ $v_{Bulk_{(L \rightarrow H)}}''' = \frac{(m.U_{mf}.A - v_H)}{\psi_H.A.\Delta z}.$
<p>b) If $v_H = m.U_{mf}.A$ There is no cross-flow.</p>	$v_{Bulk_{(H \rightarrow L)}}''' = 0,$ $v_{Bulk_{(L \rightarrow H)}}''' = 0.$
<p>c) If $v_H > m.U_{mf}.A$ Excess gas in the <i>H-phase</i> flows out to the <i>L-phase</i> (e.g. in the bubbling flow regime, this will form bubbles).</p>	$v_{Bulk_{(H \rightarrow L)}}''' = \frac{(v_H - m.U_{mf}.A)}{\psi_H.A.\Delta z},$ $v_{Bulk_{(L \rightarrow H)}}''' = 0.$

4.2.7. Variation in Volumetric Flowrate Due to Expansion/Compression and Changes in Total Molar Flows

Based on the ideal gas law, the total volumetric flow rate is given by:

$$v_\varphi = \frac{R.T_\varphi}{P} \cdot \sum_{i=1}^{N_C} F_{i\varphi} \quad (4.18)$$

The most convenient way to account for this change in volumetric flow is to solve the conservation equations in terms of molar flows instead of species concentrations, using the relation: $F_{i\varphi} = v_\varphi \cdot C_{i\varphi} = \psi_\varphi \cdot \varepsilon_\varphi \cdot U_{gas\varphi} \cdot A \cdot C_{i\varphi}$. Figure 4.3 depicts a typical variation of gas-flow as reaction proceeds and hydrogen is withdrawn through membranes, accompanied by axial variations in pressure and temperature. This figure also shows how the balancing interphase crossflow modulates the phase volumetric flows by changing the slopes of the curves after ~0.5 m of height. In this section, significant flow from the L-phase is transferred to the H-phase to compensate for hydrogen removal and to maintain fluidization in the H-phase.

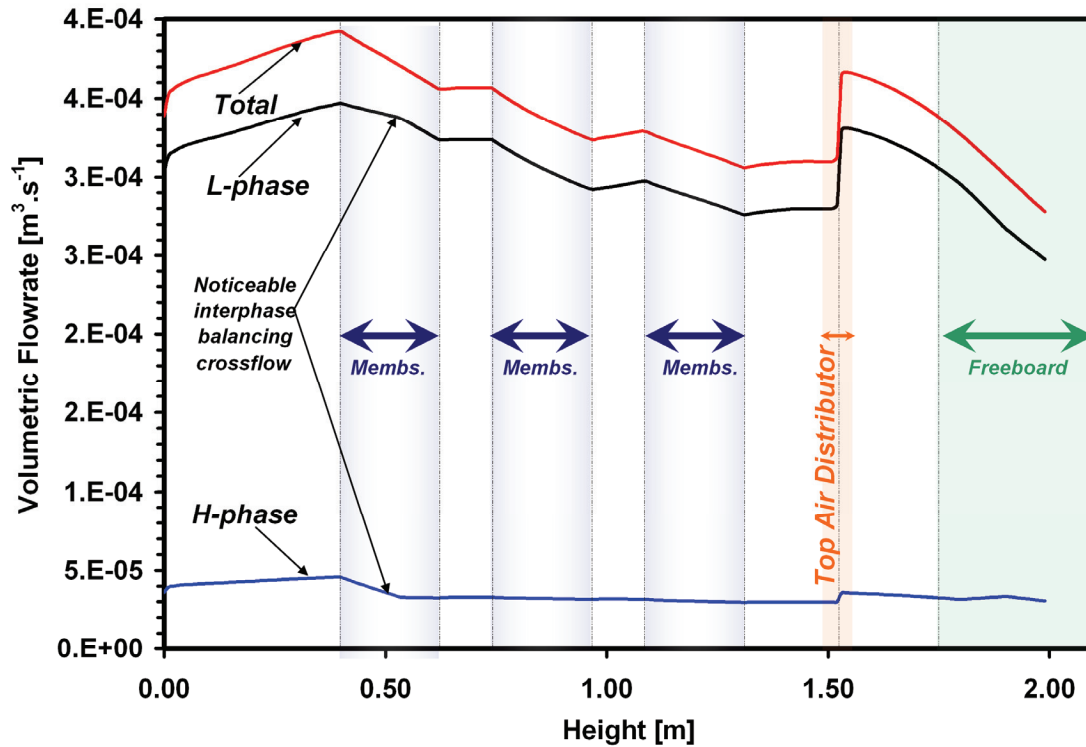


Figure 4.3. Simulated volumetric flow rates vs height (Experiment 10). For experimental/simulation parameters see Table 3.2.

4.2.8. Feed Distribution along the Reactor

Air is introduced into the pilot-scale fluidized-bed reactor to provide some of the heat required for the endothermic reforming reactions. Li *et al.* (2008) predicted that the performance advantage of pure oxygen over regular air is small. Therefore air is preferred due to the cost associated with oxygen generation and the greater likelihood of hot spots if pure oxygen were to be used. Relative to SMR, air introduction enhances methane conversion, increases reactor temperature and reduces hydrogen yield. It is desirable to introduce some of the air near the top of the dense bed (above the membrane sections) to reduce the membrane-flux dilution penalty caused by nitrogen.

To simulate introduction of air at the top, a pulse function is added to the mole balance by means of a Dirac delta function, which transforms into a unit pulse (Heaviside step function, also called the unit step function) after integration. As a result the added molar flow in the differential equations for species i in phase φ is equal to: $(Split_{top} \cdot v_{f\varphi} \cdot C_{if\varphi}) \delta(z - z_{Top})$.

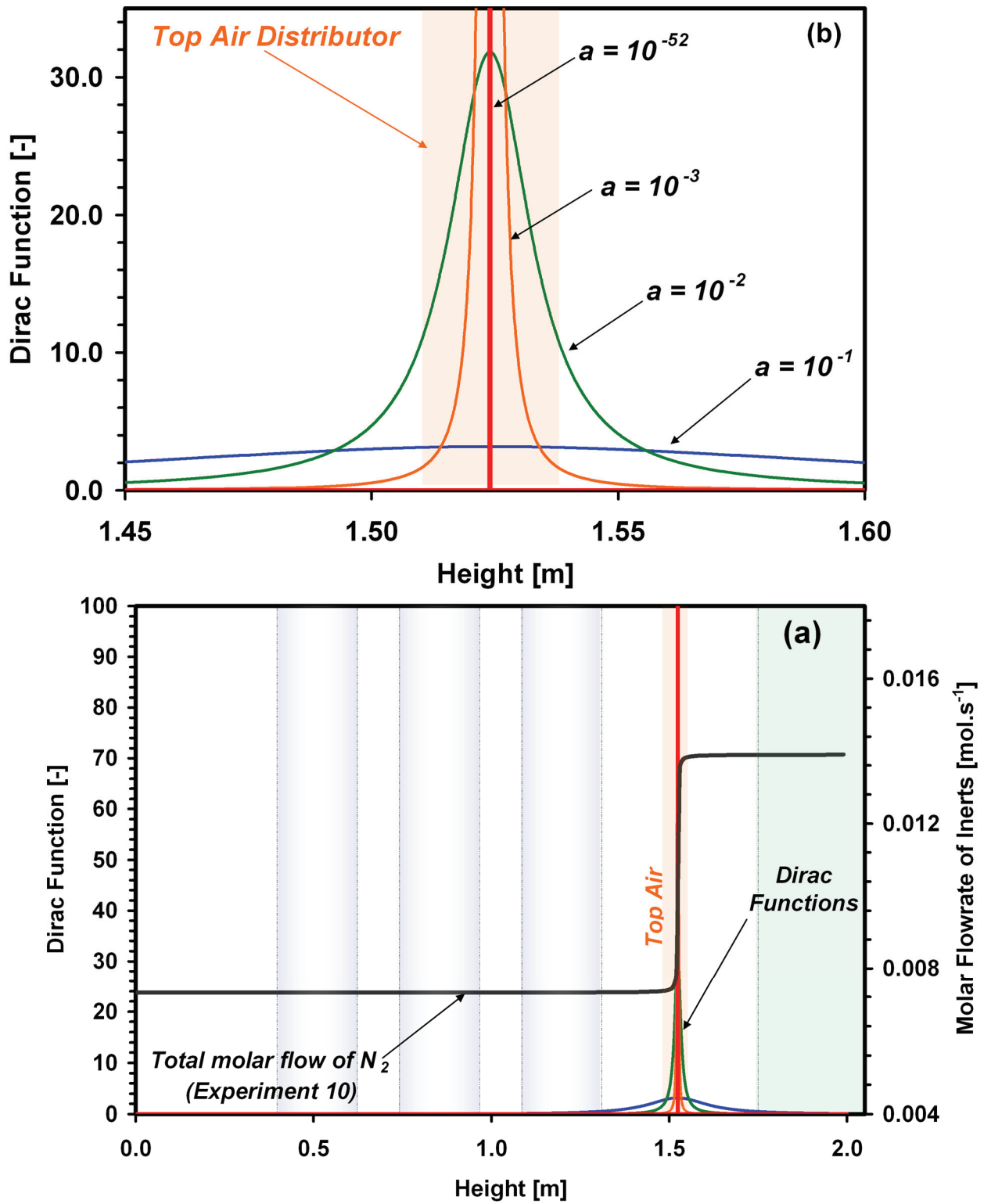


Figure 4.4. a) Simulated impulse Dirac function and molar flow rate of inerts vs height (Experiment 10, 50% air at top). b) Enlargement of a) at the top air distributor section ($z=1.45$ to $z=1.6$). For experimental/simulation parameters see Table 3.2.

This leads to a step increase in the flowrate of nitrogen and superficial gas velocity at the upper injection level. Numerically the Dirac delta function may be conveniently defined as:

$$\delta(z - z_{Top}) = \lim_{a \rightarrow 0} \left[\frac{1}{\pi} \cdot \left(\frac{a}{(z - z_{Top})^2 + a^2} \right) \right] \quad (4.19)$$

where “ a ” is a very small number carefully chosen during the numerical solution of the model. The effect of varying “ a ” on the Dirac function is depicted on Figure 4.4a and 4.4b. This parameter is chosen to be very small so that the Dirac function reaches values several orders of magnitude higher at the top distributor than anywhere else on the bed. The numerical solver has to be tweaked in order to deal with large changes in the state variables in this section of the bed (i.e. by reducing the integration step-size at the top air distributor to correctly integrate the Dirac function). It was found empirically that “ a ” should be smaller than 10^{-3} m to represent the top feed.

4.2.9. Boundary Conditions

The superficial gas velocity at the distributor plate is calculated from the ideal gas law:

$$\text{At } z=0: U_{in} = \frac{R.T_{in}}{A.P_{in}} \cdot \sum_{i=1}^{N_C} F_{i,in} \quad (4.20)$$

where the subscript “ in ” identifies entry conditions. This gas flow is divided into the two phases making use of a split factor:

$$\text{At } z=0: F_{iH,in} = Split_H \cdot F_{i,in}; F_{iL,in} = F_{i,in} - F_{iH,in} \quad (4.21)$$

with the split factor calculated using:

$$Split_H = (m.U_{mf} \cdot A.C_{t,in}) / F_{t,in} \quad (4.22)$$

where the minimum fluidization velocity is calculated by the correlation of Wen and Yu (1966).

$$U_{mf} = \frac{Re_{mf} \cdot \mu}{\rho_{gas} \cdot d_p} \quad (4.23)$$

$$Re_{mf} = (33.7^2 + 0.0408 \cdot Ar)^{0.5} - 33.7 \quad (4.24)$$

$$Ar = \frac{(\rho_{gas} \cdot (\rho_{cat} - \rho_{gas}) \cdot g \cdot d_p^3)}{\mu^2} \quad (4.25)$$

4.2.10. Calculation of Reactor Parameters

Fluidized-bed reactors may operate in different flow regimes (bubbling, turbulent and fast fluidization). Each has its advantages and shortcomings as seen in Chapter 5. In the experimental work, the prototype fluidized-bed operated at all times predominantly within the bubbling fluidization regime. However, the modeling accounts for minor contributions from the other regimes. Hydrodynamic parameters are calculated from the general probabilistic approach (Abba *et al.*, 2003b) covering the three most common fluidization flow regimes. The probabilities of being above or below the regime transition boundaries are estimated by means of probability density functions, using the U_c and U_{se} regime boundary correlations. These probabilities are then used to calculate weighting factors on the key terms of regime-specific models for the different individual flow regimes.

The probabilities of being in each of the three flow regimes are expressed as:

$$P_{bubb} = 1 - P(U^* > U_c^*) = \left(1 + e^{-\beta v_c^*}\right)^{-1}, \quad (4.26)$$

$$P_{fast} = P(U^* > U_{se}^*) = \left(1 + e^{-\beta v_{se}^*}\right)^{-1}, \quad (4.27)$$

The fluidized-bed system generally shows characteristics found in more than one flow regime following the summation rule:

$$P_{turb} = 1 - P_{fast} - P_{bubb}, \quad (4.28)$$

where:

$$v_c^* = \frac{(U^* - U_{\min}^*) - U_c^*}{\sigma_c^*}, \quad v_{se}^* = \frac{U^* - U_{se}^*}{\sigma_{se}^*},$$

$$U^* = \frac{Re}{Ar^{1/3}}, \quad U_{\min}^* = \frac{Re_{\min}}{Ar^{1/3}}, \quad U_c^* = \frac{Re_c}{Ar^{1/3}}, \quad U_{se}^* = \frac{Re_{se}}{Ar^{1/3}},$$

$$Re_c = 0.74 \cdot Ar^{0.426}, \quad Re_{se} = 1.68 \cdot Ar^{0.469},$$

$$\sigma_{se}^{*2} = \frac{1}{n-1} \sum_{j=1}^n (U_{se,exp,j}^* - U_{se}^*(Ar)_j)^2, \quad \sigma_c^{*2} = \frac{1}{n-1} \sum_{j=1}^n (U_{c,exp,j}^* - U_c^*(Ar)_j)^2.$$

Using the fitted parameters: $\beta = 1.7$, $\sigma_c^* = 0.292$, $\sigma_{se}^* = 0.448$ (Abba *et al.*, 2002; Abba *et al.*, 2003b). Figure 4.5 depicts the probability distribution for the three flow regimes as a function of the superficial gas velocity. Figure 4.5 would be different for other systems with different fluidization conditions. This plot can also be constructed in terms of the dimensionless variable U^* which takes into account gas and particle properties. The current simulations for the prototype reactor were executed under “mostly bubbling” conditions where bubbling parameters dominate in the weighting process since P_{bubb} was typically above 0.97.

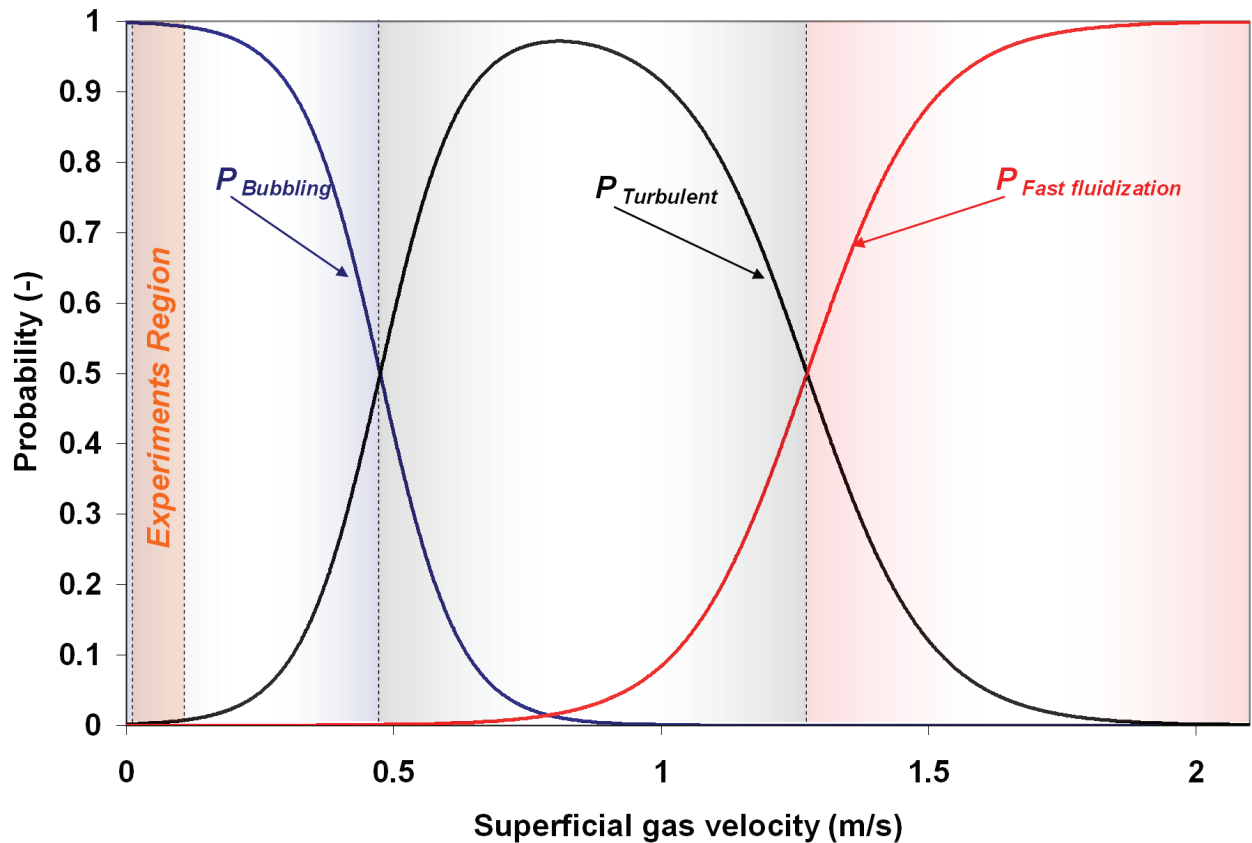


Figure 4.5. Regime mapping for the FBMR experiments. Simulated probability distribution for bubbling, turbulent and fast fluidization flow regimes vs superficial gas velocity.

Once the probabilities of being in each flow regime have been estimated, the next key step is to employ these probabilities as weighting factors to obtain point approximations of the hydrodynamic parameters. The model parameters (coefficients in the mole and energy balance equations for each separate fluidization regime), are then weighted according to:

$$\hat{\theta} = \sum_{r=1}^3 \theta_r P_r, \quad (4.29)$$

where θ_r is the value of θ for regime r , and P_r is the probability of being in regime r , with bubbling fluidization corresponding to $r = 1$, whereas $r = 2$ for turbulent fluidization (Bi *et al.*, 2000) and $r = 3$ for fast fluidization.

The major assumptions for the probabilistic averaging procedure (Abba *et al.*, 2003b) are:

- $U > U_{mb}$, i.e. the gas velocity is at least sufficient to initiate bubbling;
- Large or shallow enough column and/or small enough particles that slug flow conditions are avoided over the entire range of interest;
- $U < U_{DSU}$ to ensure that the system is not operating in the dense suspension upflow regime (Grace *et al.*, 1999a). The boundary between fast fluidization and dense suspension upflow

is estimated using the correlation: $\frac{(U_{DSU}/\varepsilon)}{v_t} = 22.8 \left(\frac{G_S}{\rho_p(1-\langle\varepsilon\rangle)v_t} \right)^{0.59} .Ar^{-0.20}$, proposed

by Kim *et al.* (2004).

4.2.10.1. Mass transfer coefficients

A specific mass transfer coefficient is calculated for each species, i.e.:

$$a_{I(H \rightarrow L)} . k_{c_i(H \rightarrow L)} = \left(a_{I(H \rightarrow L)} . k_{c_i(H \rightarrow L)} \right)_{bubb} . P_{bubb} + \left(a_{I(H \rightarrow L)} . k_{c_i(H \rightarrow L)} \right)_{turb} . P_{turb} + \left(a_{I(H \rightarrow L)} . k_{c_i(H \rightarrow L)} \right)_{fast} . P_{fast} \quad (4.30)$$

The regime specific contributions to mass transfer are:

Bubbling regime	Turbulent regime	Fast fluidization regime
$\left(a_I . k_{c_i} \right)_{bubb} = \left(\frac{U_{mf}}{3} + 2 \left(\frac{D_i . \varepsilon_{mf} . U_H}{\pi . d_b} \right)^{1/2} \right) \cdot \frac{6}{d_b}$ <p>(Sit and Grace, 1981)</p>	$\left(a_I . k_{c_i} \right)_{turb} = 1.631 . Sc_i^{0.37} . U$ <p>(Foka <i>et al.</i>, 1996)</p>	$\left(a_I . k_{c_i} \right)_{fast} = \left[\frac{4 . D_i . \varepsilon_H . U}{\pi . L_t} \right]^{1/2} \cdot \frac{2}{r_C}$ <p>(Pugsley <i>et al.</i>, 1992)</p>

where $a_{I(H \rightarrow L)} = 6/d_b$, and $Sc_i = \mu/(\rho_{gas} . D_i)$.

In the current modeling, these values are calculated for each species using its own diffusion coefficient, while in their original literature references the diffusion coefficient of the “gas mixture” was implemented instead. Our treatment generates mass transfer coefficients that are unique to each species, thus accounting for variations among the different molecules. For the reforming reactor, it is clear from Figure 4.6 that hydrogen molecules migrate more easily than the other molecules due to their higher diffusion coefficient. In this figure it is seen how the diffusion coefficients change along the bed due to variations in species concentrations, temperature and pressure. Also it is observed a change in diffusivities near the top air distributor due to dilution and temperature increase.

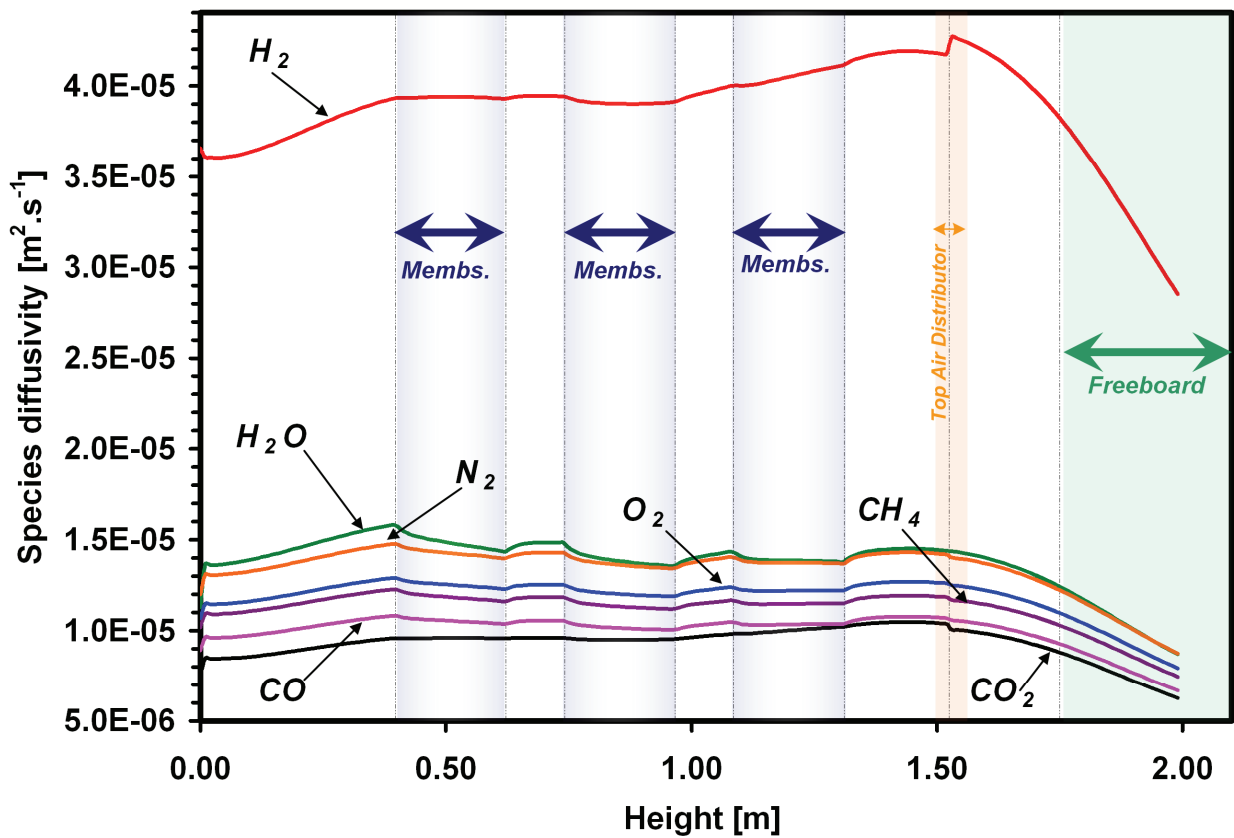


Figure 4.6. Simulated species diffusivity vs height. (Experiment 10). For experimental/simulation parameters see Table 3.2.

The diffusion coefficient of each species is calculated from the method of Wilke (1950).

$$D_i = (1 - y_i) / \sum_{\substack{j=1 \\ j \neq i}}^{N_C} \left(\frac{y_j}{D_{ij}} \right) \quad (4.31)$$

where y_i is the overall mole fraction of component i , and D_{ij} is the binary diffusion coefficient between species i and j calculated from:

$$D_{ij} = \frac{0.00143.T^{1.75}}{P \cdot \sqrt{\frac{2}{\frac{1}{Mw_i} + \frac{1}{Mw_j}} \cdot ((\Sigma_v)_i^{1/3} + (\Sigma_v)_j^{1/3})^2}} \quad (4.32)$$

here Σ_v denotes summation of atomic diffusion volume increments calculated from Fuller and Giddings (1965) and Fuller *et al.* (1965).

4.2.10.2. Bed volume fractions profiles

The volume fraction of each phase is calculated by averaging the three contributions:

$$\psi_L = \psi_{L_{bubb}} \cdot P_{bubb} + \psi_{L_{turb}} \cdot P_{turb} + \psi_{L_{fast}} \cdot P_{fast} \quad (4.33)$$

Bubbling regime	Turbulent regime	Fast fluidization regime
$\psi_{L_{bubb}} = \psi_{L_{turb}} = (\varepsilon - \varepsilon_{mf}) / (\varepsilon_{L0} - \varepsilon_{mf})$ (Abba <i>et al.</i> , 2002; Abba <i>et al.</i> , 2003b)		$\psi_{L_{fast}} = r_C^2 / \left(\frac{D_t}{2}\right)^2$ (Abba <i>et al.</i> , 2002; Abba <i>et al.</i> , 2003b)

where core radius is calculated by: $r_C = \frac{D_t}{2} - \frac{D_t}{2} \cdot \left(1 - \left(1.34 - 1.3 \cdot (1 - \varepsilon_{fast})^{0.2} + (1 - \varepsilon_{fast})^{1.4}\right)^{0.5}\right)$,

(Bi *et al.*, 1996).

The voidage at minimum fluidization is obtained from experimental measurements, with a small increase to 0.55 to account for the elevated pressure (King and Harrison, 1982; Weimer and Quarderer, 1985).

The void fraction of bubbles is very important because it determines the amount of reaction in the L - phase (bubbles). Although the value of this parameter has never been resolved, many models in the literature assume $\varepsilon_{L0} = 1$ which is a poor approximation for systems with fast chemical reactions. This value of voidage is expected to be between 0.97 (Abba, 2001) to 0.999 or even higher (Grace, 1986b), likely smaller for systems with wide particle size distributions (Grace and Sun, 1990). Below we take by default $\varepsilon_{L0} = 0.97$. For more information on voidage studies see (Sun and Grace, 1994; Yates *et al.*, 1994).

4.2.10.3. Velocity profiles

It is important to differentiate the diverse velocities encountered in the model, which have a unique physical meaning. The intrinsic gas velocities of the phases are given by:

$$U_{gas_\varphi} = v_\varphi / (\psi_\varphi \cdot \varepsilon_\varphi \cdot A) \quad (4.34)$$

The bed superficial gas velocity is given by:

$$U = (v_H + v_L) / A \quad (4.35)$$

The bubble rise velocity is calculated from the equation of Davidson and Harrison (1963). However, the maximum bubble size is constrained by the internal reactor layout, including any internals (planar membranes here). Also when bubbles are squeezed between flat surfaces (membrane panels), they deform into two-dimensional bubbles. To account for this we take:

Bubbling regime	
if $d_b \leq \tau$	$(u_{br})_{bubb} = (U - U_{mf}) + 0.711 \cdot (g \cdot d_b)^{0.5}$ (Davidson and Harrison, 1963; Sit and Grace, 1981)
if $d_b > \tau$	$(u_{br})_{bubb} = (U - U_{mf}) + 0.51 \cdot (g \cdot d_b)^{0.5}$ (Davidson and Harrison, 1963; Sit and Grace, 1981)

where τ is the gap between membrane surfaces and the bubble diameter calculated from the correlation of Mori and Wen (1975):

$$db = db_m - (db_m - db_0) \cdot e^{\left(\frac{-0.3 \cdot z}{D_t}\right)} \quad (4.36)$$

$$db_m = 1.64 \cdot \left(A \cdot (U_{in} - U_{mf})\right)^{0.4} \quad (4.37)$$

$$db_0 = \frac{1.38}{g^{0.2}} \cdot \left(\frac{A \cdot (U_{in} - U_{mf})}{N_{or}}\right)^{0.4} \quad (4.38)$$

4.2.10.4. Bed expansion and freeboard

It is important to estimate the bed expansion to simulate the system. The fluidized bed is divided into two sections: a dense bed extending from the distributor at $z = 0$ to the top of the dense bed at $z = z_d$, and a freeboard from $z = z_d$ to the top of the reactor, $z = z_R$.

The total solids inventory is:

$$M_{solids} = \rho_{solids} \cdot \left[\langle A \rangle \cdot (z_d - 0) \cdot (1 - \langle \varepsilon_T \rangle) \right] + \rho_{solids} \cdot \left[\langle A_f \rangle \cdot (z_R - z_d) \cdot (1 - \langle \varepsilon_f \rangle) \right] \quad (4.39)$$

This can be solved iteratively after estimating the bed voidage profile (see below) along the reactor and then numerically calculating the mean value of the bed voidages by integration:

$$M_{solids} = \rho_{solids} \cdot \left[\langle A \rangle \cdot (z_d - 0) \cdot \left(1 - \frac{\int_0^{z_d} \varepsilon_T \cdot dz}{(z_d - 0)} \right) \right] + \rho_{solids} \cdot \left[\langle A_f \rangle \cdot (z_R - z_d) \cdot \left(1 - \frac{\int_{z_d}^{z_R} \varepsilon_f \cdot dz}{(z_R - z_d)} \right) \right] \quad (4.40)$$

The bed expansion can then be obtained by solving Equation (4.40) for z_d .

4.2.10.5. Voidage profiles

The bed voidage profile is calculated from:

Voidage Profile		
Dense bed	if $0 \leq z \leq z_d$:	$\varepsilon_T = \varepsilon_{bubb} \cdot P_{bubb} + \varepsilon_{turb} \cdot P_{turb} + \varepsilon_{fast} \cdot P_{fast}$
Freeboard (if existing)	if $z_d \leq z \leq z_R$:	$\varepsilon_f = \varepsilon^* + (\langle \varepsilon_T \rangle - \varepsilon^*) \cdot e^{-\left(\frac{3}{U - U_{mf}}\right) \cdot z}$ (Kunii and Levenspiel, 1991)

where ε^* and U_{mb} are obtained from the correlations of Morikawa *et al.* (2001) and Abrahamsen and Geldart (1980), respectively:

$$\varepsilon^* = 1 - 0.022(U - U_{mb})^{3.64} \quad (41)$$

$$U_{mb} = \frac{U_{mf} \cdot 2300 \cdot \rho_{gas}^{0.126} \cdot \mu_{gas}^{0.523} \cdot e^{(0.176 \cdot \text{Fines})}}{d_p^{0.8} \cdot g^{0.934} (\rho_{solid} - \rho_{gas})^{0.934}} \quad (42)$$

The regime contributions for the dense bed section are given by:

Bubbling regime	Turbulent regime	Fast fluidization regime
$\varepsilon_{bubb} = 1 - \frac{(1 - \varepsilon_{mf})}{\left(1 + \frac{U - U_{mf}}{0.711\sqrt{g \cdot db}}\right)}$ <p>(Clift and Grace, 1985)</p>	$\varepsilon_{turb} = \frac{U + 1}{U + 2}$ <p>(King, 1989)</p>	$\varepsilon_{fast} = \left[1 + \frac{G_{so} \Psi_{slip}}{\rho_p U}\right]^{-1}$ <p>(Patience <i>et al.</i>, 1992)</p>

For the L -Phase:

$$\varepsilon_L = \varepsilon_{Lbubb} \cdot P_{bubb} + \varepsilon_{Lturb} \cdot P_{turb} + \varepsilon_{Lfast} \cdot P_{fast} \quad (4.43)$$

Bubbling regime	Turbulent regime	Fast fluidization regime
$\varepsilon_{Lbubb} = \varepsilon_{L0}$ <p>(Abba, 2001)</p>	$\varepsilon_{Lturb} = \varepsilon$	$\varepsilon_{Lfast} = \varepsilon_{fast}$

For the H -Phase:

$$\varepsilon_H = (\varepsilon - \psi_L \cdot \varepsilon_L) / \psi_H \quad (4.44)$$

4.2.10.6. Heat dispersion:

Heat is dispersed within the reactor due to continuous particle mixing. Heat is transported from the hot to the cold zones of the reactor, thus preventing hot spots. Heat dispersion was modelled as described in Section 4.2.2.1. The overall axial heat dispersion can be obtained from:

$$K_\varphi = K_{\varphi_{Bubb}} \cdot P_{Bubb} + K_{\varphi_{Turb}} \cdot P_{Turb} + K_{\varphi_{Fast}} \cdot P_{Fast} \quad (4.45)$$

with the thermal conductivity for each regime estimated from an analogy proposed by Matsen (1985):

$$K_\varphi = (1 - \varepsilon_\varphi) \left[\rho_{solid} \cdot C_{p_{solid}} \cdot D_{solid} \right] \quad (4.46)$$

The axial dispersion coefficients for the solid particles is then estimated by:

Bubbling regime	Turbulent regime	Fast fluidization regime
$D_{solid_{Bubb}} = D_{solid_{Turb}}$ $= 1.058 \cdot (U - U_{mf}) \cdot D \cdot \left(\frac{g \cdot D}{U - U_{mf}} \right)^{0.653} \cdot Ar^{-0.368}$ <p>(Lee and Kim, 1990)</p>		$D_{Solid_{Fast}} = 0.0139 \cdot \frac{L}{D} \cdot \frac{\mu_\varphi}{\rho_\varphi} \cdot (1 - \varepsilon_\varphi)^{-0.67}$ <p>(Wei <i>et al.</i>, 1995)</p>

The overall horizontal heat dispersion coefficient is assumed to be equal to the volume average thermal conductivity coefficient as an approximation (i.e. in practice this value is larger due to solids mixing in the horizontal direction).

4.2.10.7. Gas dispersion:

The overall gas dispersion is obtained from:

$$D_{i\varphi} = D_{i\varphi_{Bubb}} \cdot P_{Bubb} + D_{i\varphi_{Turb}} \cdot P_{Turb} + D_{i\varphi_{Fast}} \cdot P_{Fast} \quad (4.47)$$

The regime specific correlations are:

Bubbling regime	Turbulent regime	Fast fluidization regime
$D_{iL_{Bubb}} = D_{iL}$	$D_{iL_{Turb}} = \frac{U \cdot H_t}{Pe_{turb}}$ (Bi <i>et al.</i> , 2000)	$D_{iL_{Fast}} = 0.184 \cdot \varepsilon_{fast}^{-4.445}$ (Li and Wu, 1991)
$D_{iH_{Bubb}} = \frac{U \cdot H_t}{Pe_{bubb}}$	$D_{iH_{Turb}} = \frac{U \cdot H_t}{Pe_{turb}}$ (Bi <i>et al.</i> , 2000)	$D_{iH_{Fast}} = 0.184 \cdot \varepsilon_{fast}^{-4.445}$ (Li and Wu, 1991)

where: $Pe_{bubb} = Pe_{turb} = 3.472 \cdot Ar^{0.149} \cdot Re^{0.0234} \cdot Sc^{-0.231} \left(\frac{H_t}{D_t} \right)$

The dispersion coefficients suggested here are calculated for each species using its own diffusion coefficient. The horizontal diffusion coefficient is assumed to be equal to the molecular diffusion coefficient for each species as a lower limit, and it is expected to be larger due to horizontal solids mixing.

4.3. Reacting System and Kinetics

The prototype reactor can operate under steam methane reforming (SMR) or autothermal reforming (ATR) conditions depending on the heat source. The reactions considered in the model and the kinetic expressions are given in Table 4.2 which implement the kinetic expressions for reforming from Xu and Froment (1989a, b) and for oxidation from (Jin *et al.*, 2000). The equilibrium and rate constants are listed in Table 4.3. The partial pressure of each component can be calculated assuming ideal gas behaviour, i.e.:

$$P_{i\varphi} = P_T \cdot F_{i\varphi} / F_{T\varphi} \quad (4.48)$$

The reforming kinetics developed by Xu and Froment originate from experiments executed at temperatures above 500°C. The pilot FBMR operated at an average temperature of 550°C, but during some runs exit temperatures dropped below 500°C due to freeboard cooling. In this work, Xu and Froment kinetics are assumed to be valid in these colder regions, although they may not be accurate. Since conventional steam reforming is operated at much higher temperatures (typically above 800°C (Rostrup-Nielsen, 1984)), low-temperature reforming kinetics are lacking in the literature. Further work is needed on low-temperature reforming kinetics.

Table 4-2. Reaction and kinetics for methane steam reforming/oxidative reforming. See Table 4-3 for parameter values.

Reaction/Equation number	Kinetic rate equation	Reference
(R1) Methane steam reforming: $CH_4 + H_2O \leftrightarrow CO + 3H_2$ $(\Delta H_{298}^0 = 206.2 \text{ kJ.mol}^{-1})$	$r_1 = \frac{k_1 \cdot \left(\frac{P_{CH_4} \cdot P_{H_2O}}{P_{H_2}^{2.5}} - \frac{P_{CO} \cdot P_{H_2}^{2.5}}{K_1} \right)}{DEN^2}$	(Xu and Froment, 1989a, b)
(R2) Water-gas shift: $CO + H_2O \leftrightarrow CO_2 + H_2$ $(\Delta H_{298}^0 = -41.2 \text{ kJ.mol}^{-1})$	$r_2 = \frac{k_2 \cdot \left(\frac{P_{CO} \cdot P_{H_2O}}{P_{H_2}} - \frac{P_{CO_2}}{K_2} \right)}{DEN^2}$	(Xu and Froment, 1989a, b)
(R3) Methane overall steam reforming: $CH_4 + 2H_2O \leftrightarrow CO_2 + 4H_2$ $(\Delta H_{298}^0 = 165.0 \text{ kJ.mol}^{-1})$	$r_3 = \frac{k_3 \cdot \left(\frac{P_{CH_4} \cdot P_{H_2O}^2}{P_{H_2}^{3.5}} - \frac{P_{CO_2} \cdot P_{H_2}^{0.5}}{K_2 \cdot K_1} \right)}{DEN^2}$	(Xu and Froment, 1989a, b)
(R4) Methane combustion: $CH_4 + 2O_2 \leftrightarrow CO_2 + 2H_2O$ $(\Delta H_{298}^0 = -802.7 \text{ kJ.mol}^{-1})$	$r_4 = k_4 \cdot P_{CH_4} \cdot P_{O_2}$	(Jin <i>et al.</i> , 2000)
(R5) Methane dry reforming: $CH_4 + CO_2 \leftrightarrow 2CO + 2H_2$ $(\Delta H_{298}^0 = 246.9 \text{ kJ.mol}^{-1})$	$r_5 = k_5 \cdot P_{CH_4} \cdot P_{H_2O} \cdot \left(1 - \frac{P_{CO}^2 \cdot P_{H_2}^2}{K_5 \cdot P_{CH_4} \cdot P_{CO_2}} \right)$	(Jin <i>et al.</i> , 2000)
where $DEN = \left(\frac{1 + K_{CO} \cdot P_{CO} + K_{H_2} \cdot P_{H_2} + K_{CH_4} \cdot P_{CH_4} + K_{H_2O} \cdot P_{H_2O}}{P_{H_2}} \right)$		

Table 4-3. List of kinetic parameters.

Reaction parameters for steam reforming of methane (Xu & Froment, 1989) (reactions rates in kmol.kg⁻¹.h⁻¹)	
k_1 (kmol.kPa ^{0.5} .kgcat ⁻¹ .h ⁻¹)	$9.49 \times 10^{16} .e^{\left(\frac{-28879}{T_\phi}\right)}$
k_2 (kmol.kgcat ⁻¹ .h ⁻¹ .kPa ⁻¹)	$4.39 \times 10^4 .e^{\left(\frac{-8074.3}{T_\phi}\right)}$
k_3 (kmol.kPa ^{0.5} .kgcat ⁻¹ .h ⁻¹)	$2.29 \times 10^{16} .e^{\left(\frac{-29336}{T_\phi}\right)}$
K_{CH_4} (kPa ⁻¹)	$6.65 \times 10^{-6} .e^{\left(\frac{4604.28}{T_\phi}\right)}$
K_{CO} (kPa ⁻¹)	$8.23 \times 10^{-7} .e^{\left(\frac{8497.71}{T_\phi}\right)}$
K_{H_2O} (kPa ⁻¹)	$1.77 \times 10^5 .e^{\left(\frac{-10666.35}{T_\phi}\right)}$
K_{H_2} (kPa ⁻¹)	$6.12 \times 10^{-11} .e^{\left(\frac{9971.13}{T_\phi}\right)}$
K_1 (kPa ²)	$10266.76 .e^{\left(\frac{-26830}{T_\phi} + 30.11\right)}$
K_2 (dimensionless)	$e^{\left(\frac{4400}{T_\phi} - 4.036\right)}$
K_3 (kPa ²)	$K_1 . K_2$
Reaction kinetics and parameters for oxidative reforming of methane (Jin et al., 2000) (reactions rates in kmol.kg⁻¹.h⁻¹)	
k_4 (kmol.kgcat ⁻¹ .h ⁻¹ .kPa ⁻²)	$3.96 \times 10^7 .e^{\left(\frac{-166000}{R.T_\phi}\right)}$
k_5 (kmol.kgcat ⁻¹ .h ⁻¹ .kPa ⁻²)	$8.71 \times 10^{-2} .e^{\left(\frac{-23700}{R.T_\phi}\right)}$
K_5 (kPa ²)	$e^{\left(\frac{-30782}{T} + 42.97\right)}$

4.4. Concentration Profiles and Reactor Performance

The above-derived model is utilized to simulate all experimental runs covered in Chapter 3. Figures 4.7 to 4.14 compare simulation predictions (represented by continuous lines) with experimental data (represented by right angled trapeziums). Shaded sections in all figures

indicate the locations of the three membrane levels, air distributor and freeboard region. Each membrane interval may contain either one or two membrane panels.

Figures 4.7 and 4.8 present the simulation results from Experiments 1 and 3 where there were no membrane surfaces in the reactor, and the model output is clearly defined by thermodynamic equilibrium constraints. The variations along the reactor height are then primarily due to variations in temperature and pressure. The difference between the predicted reactor conversion and the experimental values for the dense-phase region was less than 19% for all points with the experimental values consistently slightly lower than the model predictions as seen in Figure 4.7a and 4.8a. This slight overprediction is likely due to reverse reaction during sampling. Although the sampling lines quickly quenched the reactor gases, some reverse reaction may also have occurred at the sampling ports in contact with the reactor surface. Differences at the top of the freeboard region may be due to the use of higher temperature kinetics. The predicted species concentrations in the two phases are very similar to the experimental values in the middle of the reactor where the system is very close to equilibrium. At the reactor entry, it is seen that a sharper decrease in methane conversion is predicted for the H-phase since it contains most of the catalyst and is characterized by more favourable reaction conditions (Figure 4.7c and 4.8c). Above roughly half a meter of height, the concentrations in the two phases equalize due to interphase mass transfer, as well as to reaction in the L-phase.

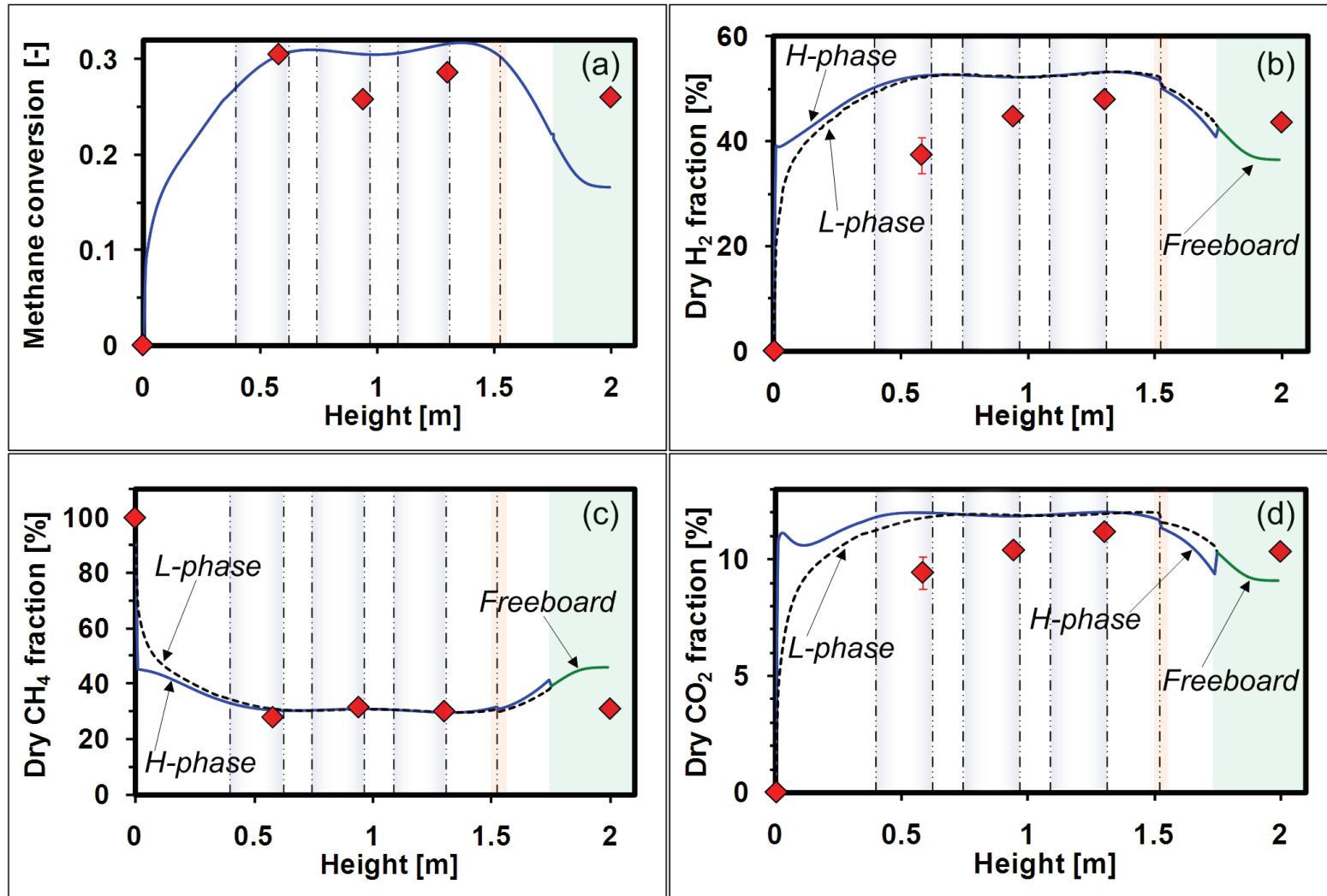


Figure 4.7. Methane conversion and two-phase species concentrations vs height. (Experiment 1). a) Overall methane conversion. b) Dry hydrogen concentration. c) Dry methane concentration. d) Dry carbon dioxide concentration. Points indicate experimental measurements. Lines show model predictions. For experimental/simulation parameters see Table 3.2.

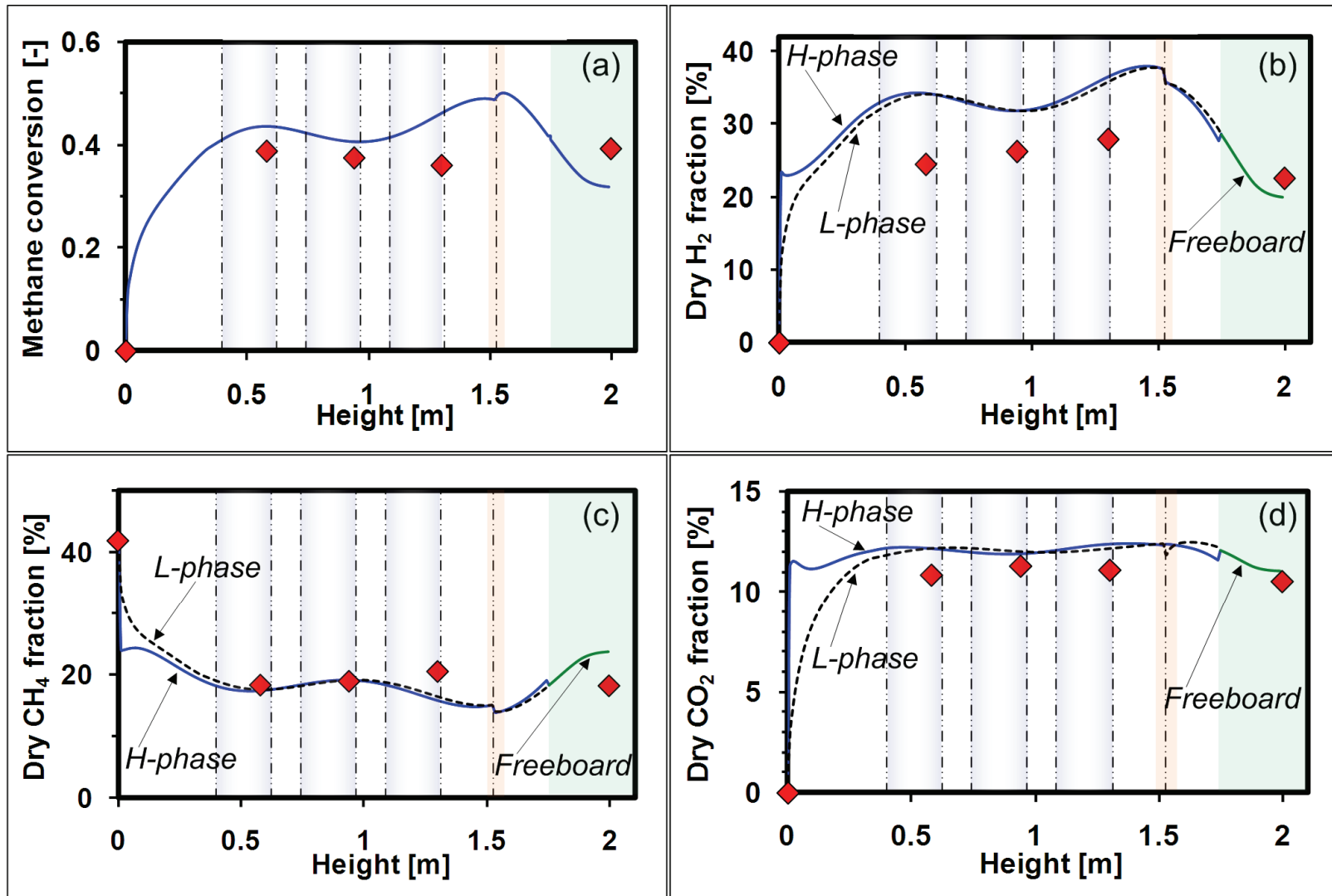


Figure 4.8. Methane conversion and two-phase species concentrations vs height. (Experiment 3). a) Overall methane conversion. b) Dry hydrogen concentration. c) Dry methane concentration. d) Dry carbon dioxide concentration. Points indicate experimental measurements. Lines show model predictions. For experimental/simulation parameters see Table 3.2.

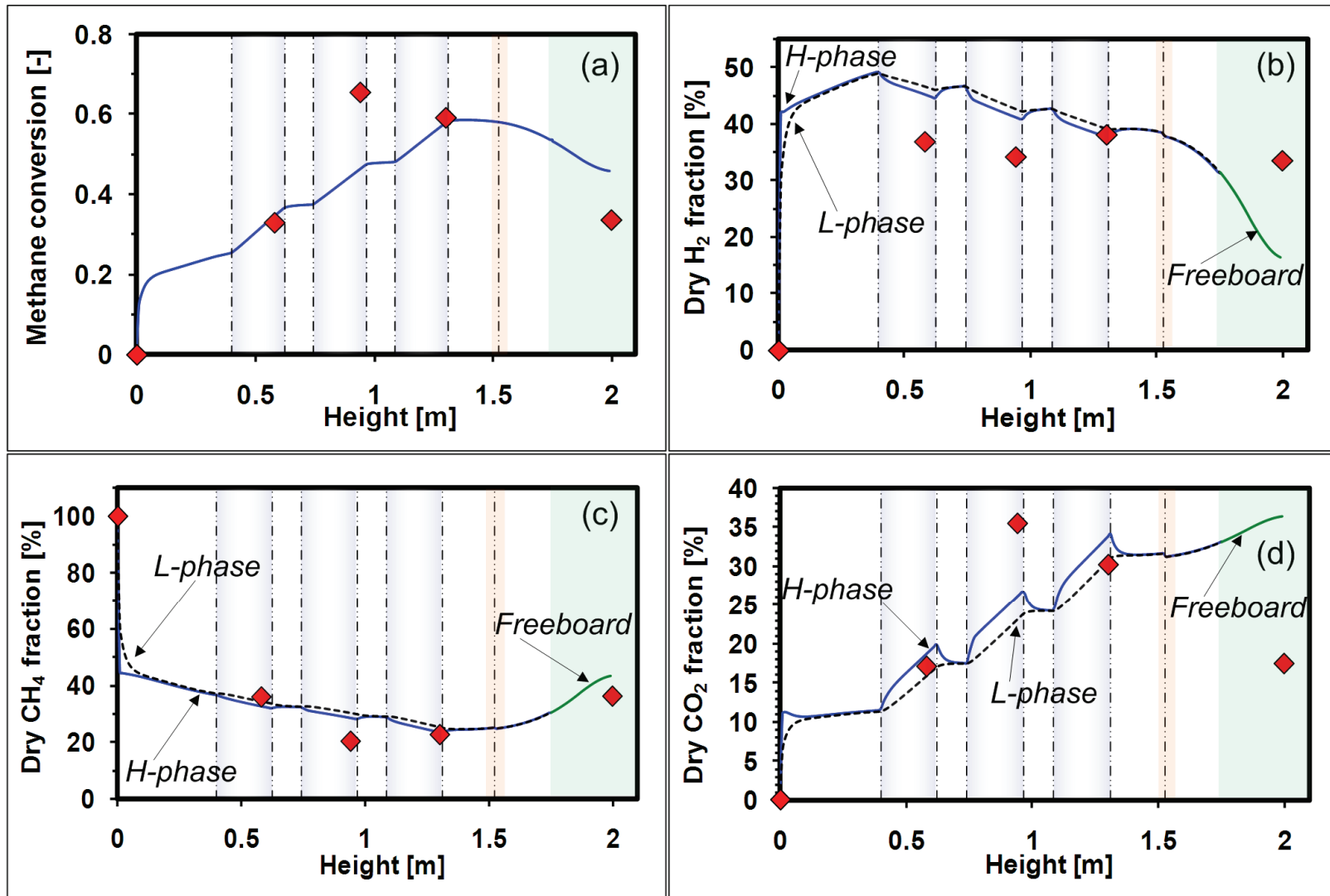


Figure 4.9. Methane conversion and two-phase species concentrations vs height. (Experiment 6). a) Overall methane conversion. b) Dry hydrogen concentration. c) Dry methane concentration. d) Dry carbon dioxide concentration. Points indicate experimental measurements. Lines show model predictions. For experimental/simulation parameters see Table 3.2.

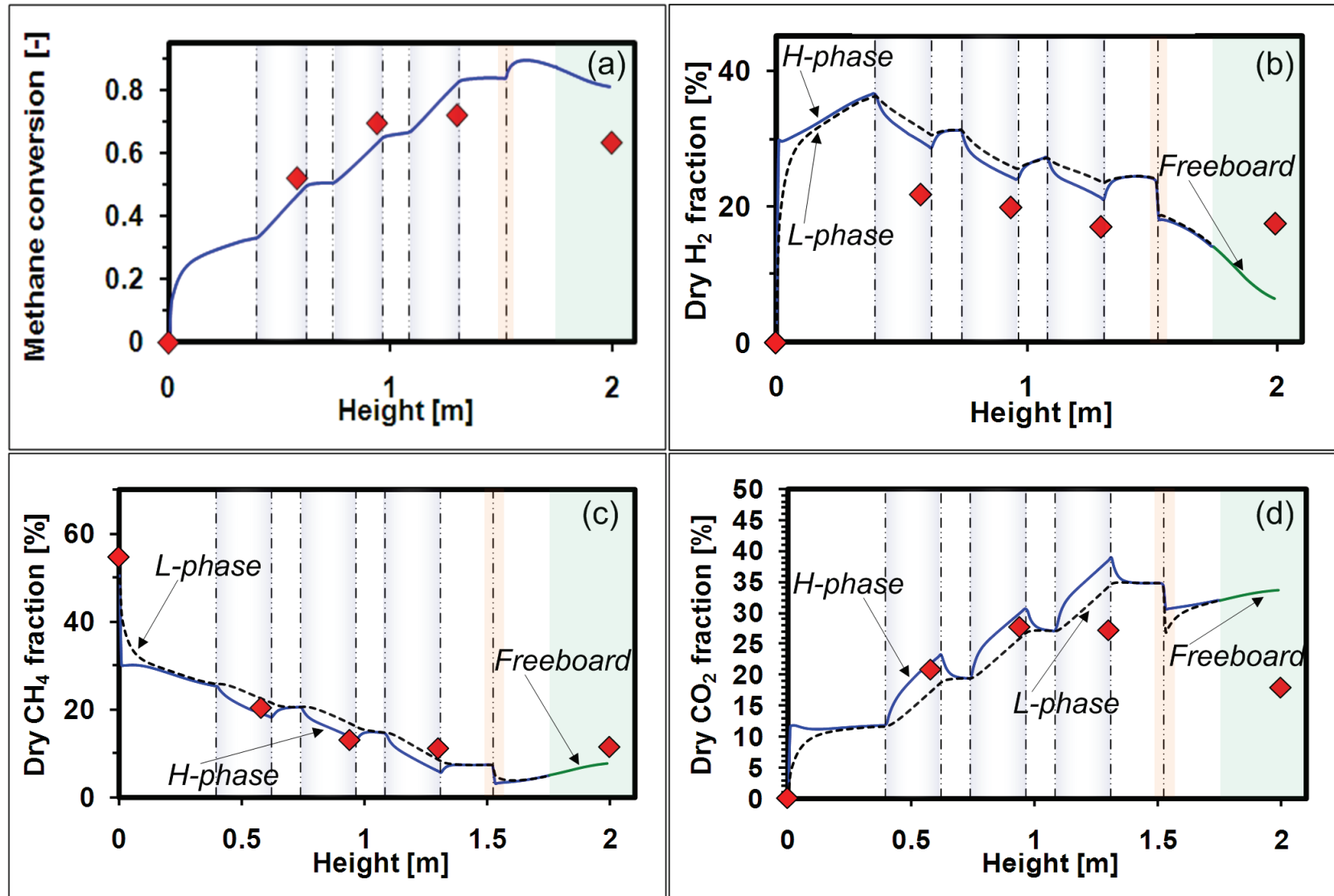


Figure 4.10. Methane conversion and two-phase species concentrations vs height. (Experiment 10). a) Overall methane conversion. b) Dry hydrogen concentration. c) Dry methane concentration. d) Dry carbon dioxide concentration. Points indicate experimental measurements. Lines show model predictions. For experimental/simulation parameters see Table 3.2.

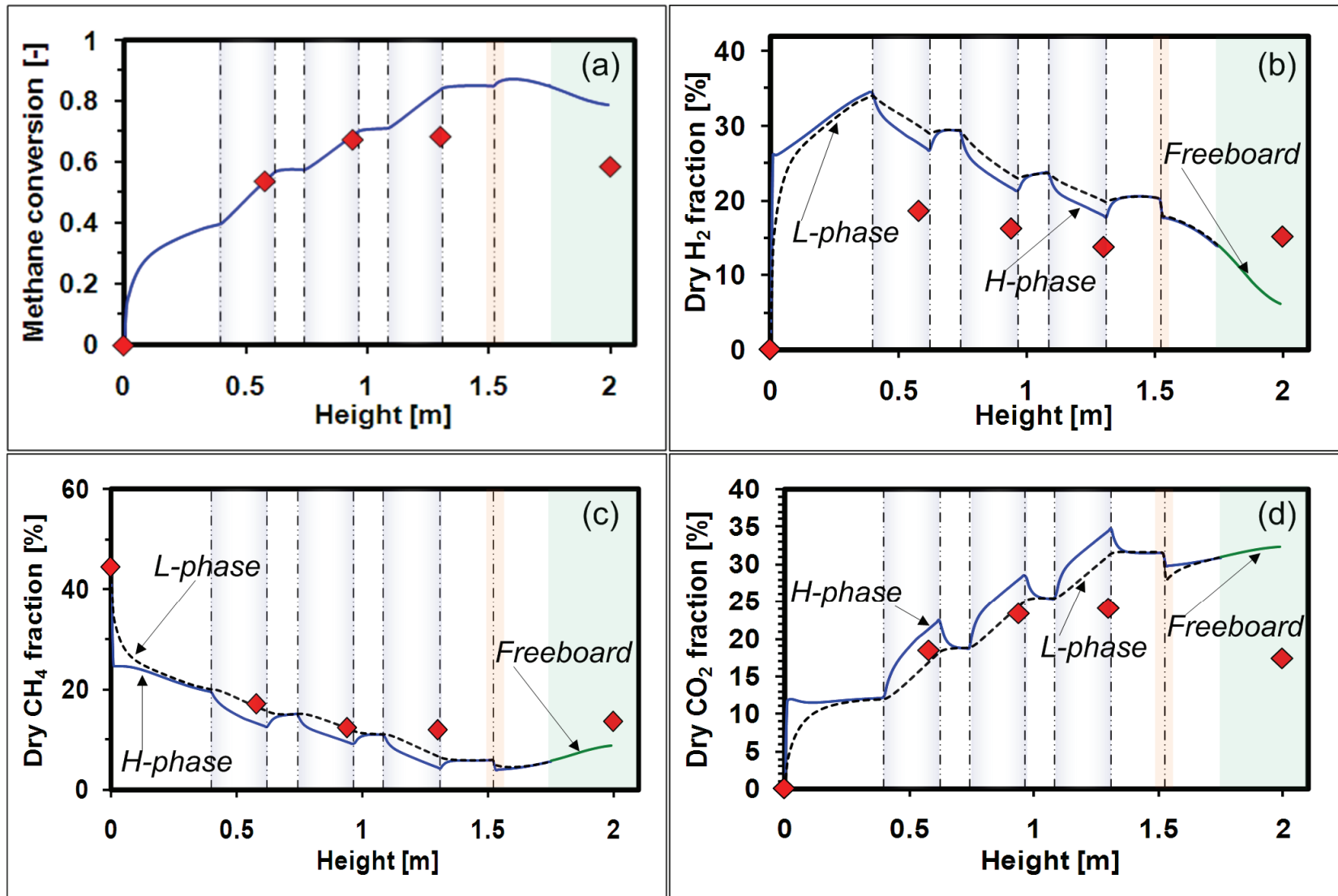


Figure 4.11. Methane conversion and two-phase species concentrations vs height. (Experiment 11). a) Overall methane conversion. b) Dry hydrogen concentration. c) Dry methane concentration. d) Dry carbon dioxide concentration. Points indicate experimental measurements. Lines show model predictions. For experimental/simulation parameters see Table 3.2.

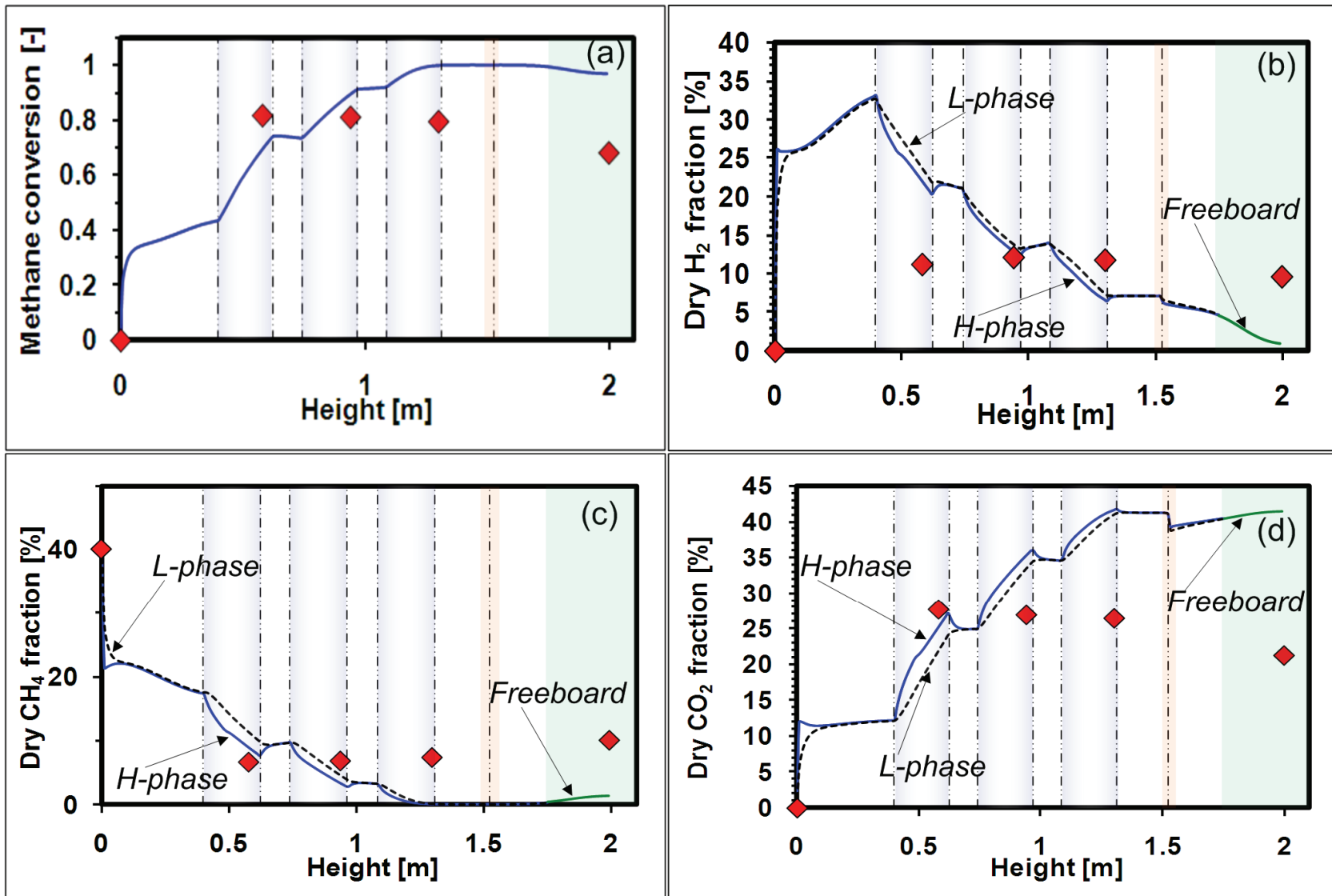


Figure 4.12. Methane conversion and two-phase species concentrations vs height. (Experiment 12). a) Overall methane conversion. b) Dry hydrogen concentration. c) Dry methane concentration. d) Dry carbon dioxide concentration. Points indicate experimental measurements. Lines show model predictions. For experimental/simulation parameters see Table 3.2.

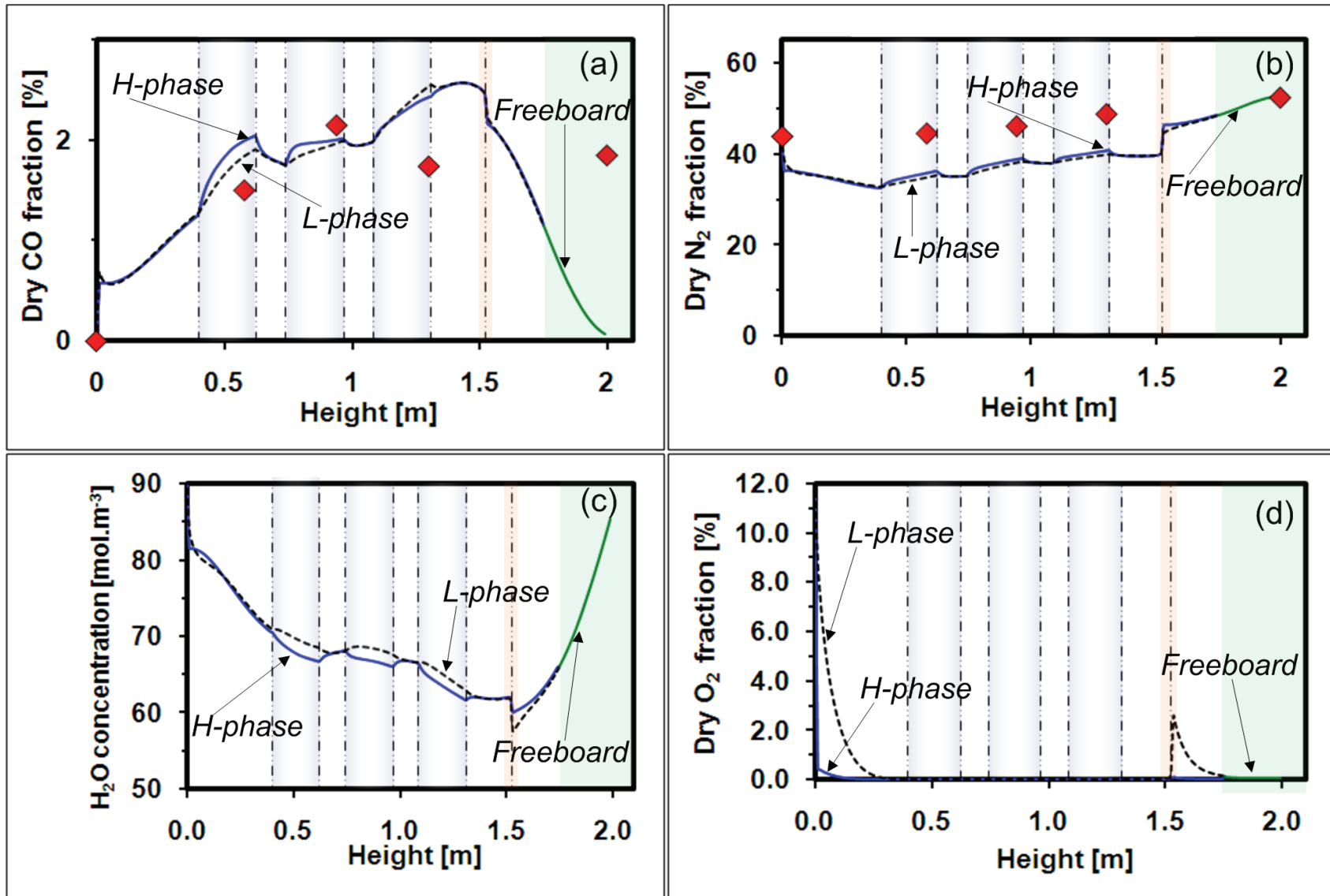


Figure 4.13. Two-phase species concentrations vs height. (Experiment 11). a) Dry carbon monoxide. b) Dry nitrogen. c) Dry oxygen. d) Steam concentration. Points indicate experimental measurements. For experimental/simulation parameters see Table 3.2.

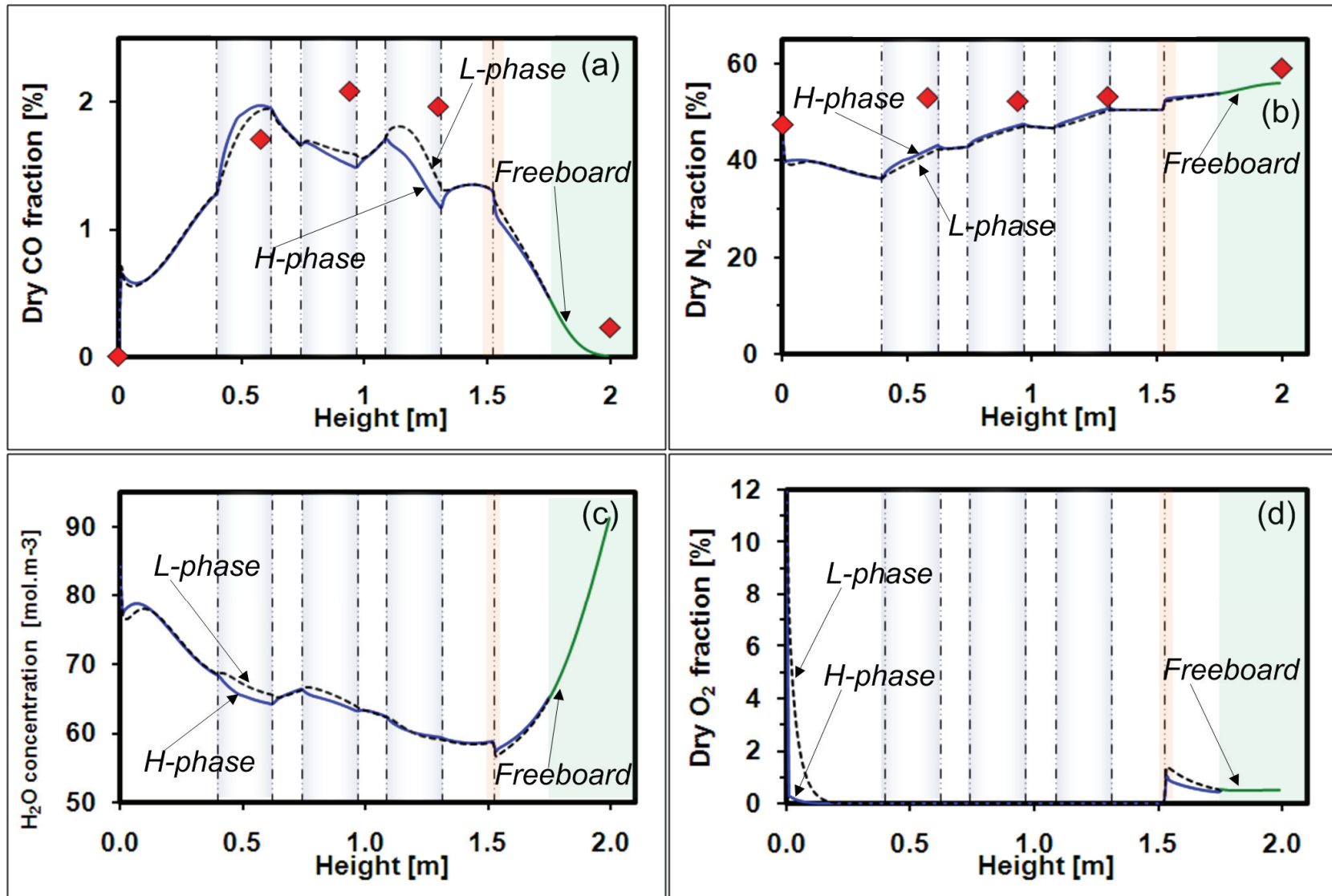


Figure 4.14. Two-phase species concentrations vs height. (Experiment 12). a) Dry carbon monoxide. b) Dry nitrogen. c) Dry oxygen. d) Steam concentration. Points indicate experimental measurements. For experimental/simulation parameters see Table 3.2.

When membranes come into play, five stages can be observed for the reforming system: **(1)** A very quick increase in conversion due to very fast reforming kinetics over the initial ~0.2 m of reactor depending on the shape of the temperature profile. **(2)** A gradual increase in conversion due to the staged hydrogen removal that shifts the equilibrium forward due to selective removal of the product hydrogen. Figures 4.9a, 4.10a, 4.11a, and 4.12a show the strong impact of hydrogen membranes on overall methane conversion. Since the membranes occur in stages, one can observe how each membrane section pulls the thermodynamic equilibrium forward step-wise in conversion and hydrogen yield. **(3)** If air is added at the top of the reactor, a local increase in methane conversion and total flow is observed. **(4)** If the reactor approaches complete methane conversion (~0.999+%) the conversion profiles become flat. This is only achieved for very large hydrogen removal and very small feed rates as seen in Figure 4.11. **(5)** The reactor gases reach the freeboard where they are in contact with exponentially decaying amounts of catalysts and low temperatures. Some reverse conversion is seen in this zone.

The species concentrations in the two phases are predicted to differ significantly in the zones in contact with active membrane surfaces as seen in Figures 4.9b-d, 4.10b-d, 4.11b-d, and 4.12b-d,. This is a direct consequence of the relative differences in membrane exposure to the two phases as noted above. Since the H-phase is in contact with a larger fraction of the total membrane area than the L-phase while it contains a smaller fraction of the total gas flow as indicated by Figure 4.3, the equilibrium is pushed further in the H-phase as observed in the methane and carbon dioxide profiles of Figures 4.9-4.12 and the water concentration profiles of Figures 4.13-4.14 (i.e. lower concentration of reforming reactants and larger concentration of products). The opposite appearance is detected in the hydrogen profiles from Figures 4.9-4.12 where the hydrogen (reforming product) concentration is lower in the H-phase due to membrane removal of hydrogen. These differences in the two phases appear to be greater where there was more membrane area per unit volume, causing the impact of hydrogen removal to be bigger (e.g. compare Experiments 6 and 10).

A clearer representation of membrane withdrawal is depicted in Figure 4.15. This figure shows how the total hydrogen removal is taking place and how each membrane panel contributes to the enhancement of performance. Figure 4.15 also indicates which membrane sections are more productive and which are not being utilized to their full potential. For instance, during Experiment 5 all three membrane levels (each containing a single panel) produced roughly the same amount of ultra-pure hydrogen, $\sim 3 \times (0.4) \text{ Nm}^3 \cdot \text{h}^{-1}$. On the other hand, Experiments 14 and

13 produced most of their hydrogen from the two lower membrane sections (each containing two panels), while poorly utilizing the top two membranes, an undesirable situation. A number of factors may determine this variation in membrane performance, the most important being hydrogen availability and local reactor pressure. The former is determined by the total hydrogen flow adjacent to each membrane, which is lower in regions where high conversion is achieved by hydrogen removal. Since the membrane flux is determined by the partial pressure of hydrogen, modulated by the local pressure on the reactor side, this flux is reduced at the top of the reactor due to pressure decay as illustrated in Figure 4.2.

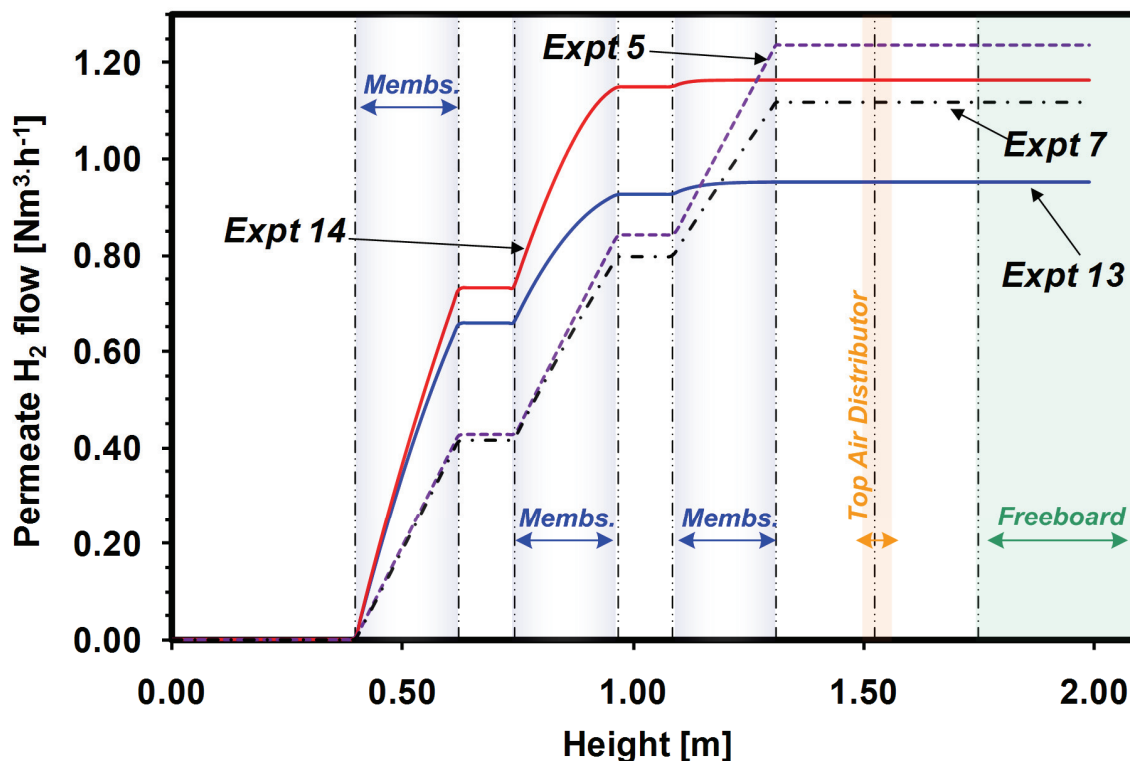


Figure 4.15. Pure hydrogen production vs height. (Experiments 5, 7, 13 and 14). For experimental/simulation parameters see Table 3.2.

Other reactor profiles are presented in Figures 4.13 and 4.14. Figures 4.13a and 4.14a show interesting non-monotonic behaviour of carbon monoxide concentrations. CO is the only chemical species that switches the location of its maximum concentration in the two phases due to hydrogen removal. Within the two lower membrane sections for Experiment 11 and bottom membrane section for Experiment 12, the carbon monoxide concentration was larger in the H-phase, but the opposite occurred at higher levels. This may be caused by the rapid CO production near the bottom of the reactor, followed by CO consumption due to the water-gas shift reaction, promoted by withdrawal of hydrogen.

Figures 4.13d and 4.14d show the quick decrease in oxygen concentration due to the fast oxidation kinetics. At the top air distributor, the additional oxygen is again rapidly consumed within a few centimetres of the nozzle feed. Figure 4.14d indicates that for that run, not all oxygen molecules were consumed due to virtually complete conversion of methane and nearly complete removal of hydrogen (see Figures 4.12b-c).

4.4.1. Differences between Model Predictions and Experimental Measurements

Although the model correctly captures many details of the experimental FBMR, there are some differences between the model estimates and the experimental data. It is possible that some reverse reaction (methanation) occurred in the hot sections of the sampling lines connected to the reactor, explaining model over-prediction of methane conversion.

In addition, difficulties in membrane characterization under reforming conditions likely account for some error. The palladium membranes in the experimental study were characterized in a cold pressurized vessel which did not contain catalyst. Issues such as membrane blockage, impurity absorption at surfaces and permeate-side pressure resistances may reduce membrane fluxes in the reactor. Furthermore, the measured permeate flow is believed to be under-represented by the gas flow meter from the experimental rig. Later recalibration of this hydrogen flow meter suggests that the actual hydrogen produced during the experimental runs may have been up to 15% higher than reported in Chapter 3.

Fluctuations in the input process variables due to proportional, integral and derivative controllers may also have contributed to variations in output variables. Other factors could include particle segregation and horizontal pressure fluctuations.

4.5. Conclusions

A comprehensive reactor model was developed which accounts for diverse phenomena encountered in fluidized-bed reactors. The model was applied to simulate a prototype fluidized-bed membrane reactor for the production of ultra-pure hydrogen at fourteen different operating conditions. The model successfully simulated key reactor characteristics and proved to be able to advance the fundamental understanding of this unusual type of reactor.

Two phases (high- and low-density) in two regions (dense bed and freeboard) are considered in the model, which also accounts for local variations of species concentrations, volumetric flow, solids content, pressure, mass transfer parameters, crossflow, reactor geometry, membrane permeation and distributed feed. It is shown that heat dispersion dominates the temperature distribution inside the reactor if heat losses are neglected. For small volume vessels with high external surface area, the temperature profile is dominated by external heat losses. It is also shown that equilibrium conversion is affected by local temperature variations.

The solids distribution among the phases and regions affected the local pressure and rates of reaction. Reactor pressure is predicted to decrease nearly linearly along the dense region, but it declines more gradually in the freeboard where the solids content is reduced exponentially. Larger catalyst content generates quicker reaction kinetics, forward or reverse, depending on the difference from chemical equilibrium. Also increasing the local pressure difference between the reactor and the membranes favourably affects membrane hydrogen flow.

A simple method for distributing flow between the H- and L-phases was developed and simulated successfully. A numerically generated pulse was introduced to account for injection of air at high level in the bed. This method gave predictions consistent with inerts profiles which showed an increase at the injection level. The effect of oxygen addition was also investigated demonstrating how it locally increases conversion and lowers hydrogen yield. In addition, it was shown that introducing some of the air above the membranes successfully reduces the nitrogen dilution penalty, with a positive impact on reactor performance.

The model shows the interaction between kinetics, chemical equilibrium and membrane removal. The simulation also provides a means of determining the optimal number and location of membranes. In addition, it is seen that interphase crossflow is required to avoid defluidization. If this crossflow is ignored, the gas content in the H-phase may reach smaller values than required to support fluidization. The model does not use any adjustable parameters and its predictions result from fundamental derivations, two-phase theory analysis and the choice of the most appropriate correlations. Given the scatter in the experimental data, the predictions are reasonably good. The model predicts membrane efficiencies (i.e. measured hydrogen production divided by the predicted hydrogen production) ranging from ~60% to ~95% with an average efficiency of ~76%. It is likely that the accuracy of the model could be further improved by introducing more realistic membrane parameters for fluidization conditions.

4.6. References

- Abba, I.A. (2001). A generalized fluidized bed reactor model across the flow regimes. Department of Chemical and Biological Engineering. Vancouver, Canada, University of British Columbia. Ph.D. Thesis.
- Abba, I.A., Grace, J.R. and Bi, H.T. (2002). Variable-gas-density fluidized bed reactor model for catalytic processes. *Chem. Eng. Sci.*, 57, 4797-4807.
- Abba, I.A., Grace, J.R. and Bi, H.T. (2003a). Application of the generic fluidized-bed reactor model to the fluidized-bed membrane reactor process for steam methane reforming with oxygen input. *Ind. Eng. Chem. Res.*, 42, 2736-2745.
- Abba, I.A., Grace, J.R., Bi, H.T. and Thompson, M.L. (2003b). Spanning the flow regimes: A generic fluidized bed reactor model. *AIChE J.*, 49, 1838-1848.
- Abrahamsen, A.R. and Geldart, D. (1980). Behavior of gas-fluidized beds of fine powders. *Powder Technol.*, 26, 35-46.
- Adris, A.M. (1994). Fluidized-bed membrane reactor for steam-methane reforming: Experimental verification and model validation. Department of Chemical and Biological Engineering. Vancouver, University of British Columbia. Ph.D. Thesis.
- Bi, H.T., Ellis, N., Abba, I.A. and Grace, J.R. (2000). A state-of-the-art review of gas–solid turbulent fluidization. *Chem. Eng. Sci.*, 55, 4789–4825.
- Bi, H.T., Zhu, J.X., Qin, J. and Grace, J.R. (1996). Annular wall thickness in CFB risers. *Can. J. Chem. Eng.*, 74, 811-814.
- Chen, Z., Po, F., Grace, J.R., Lim, C.J., Elnashaie, S.S.E.H., Mahecha-Botero, A., Rakib, M., Shirasaki, Y. and Yasuda, I. (2008). Sorbent enhanced/membrane-assisted steam methane reforming. *Chem. Eng. Sci.*, 63, 170-182.
- Clift, R. and Grace, J.R. (1985). Continuous bubbling and slugging. in *Fluidization*. Eds. Davidson, J.F., Clift, R. and Harrison, D. pp. 73-132. Academic Press, London.
- Constantineau, J.P., Grace, J.R., Lim, C.J. and Richards, G.G. (2007). Generalized bubbling–slugging fluidized bed reactor model. *Chem. Eng. Sci.*, 62, 70-81.
- Davidson, J.F. and Harrison, D. (1963). *Fluidised particles*. Cambridge University Press, Cambridge, UK.
- Fan, L.S. and Zhu, C. (2005). *Principles of gas-solid flows*. Cambridge University Press, New York.
- Foka, J., Chaouki, J. and Guy, D.K. (1996). Gas phase hydrodynamics of gas-solid turbulent fluidized-bed reactors. *Chem. Eng. Sci.*, 55, 713-723.
- Fuller, E.N. and Giddings, J.C. (1965). A comparison of methods for predicting gaseous diffusion coefficients. *Journal of Gas Chromatography*, 3 222-227.

Grace, J.R. (1982). Fluidized-bed heat transfer. in Handbook of Multiphase Systems. Ed. Hetsroni, G. Hemisphere, New York.

Grace, J.R. (1986b). Fluid beds as chemical reactors. in Gas fluidization technology. Ed. Geldart, D. Willey, Chichester, New York.

Grace, J.R., Abba, I.A., Bi, H.T. and Thompson, M.L. (1999a). Fluidized bed catalytic reactor modeling across the flow regimes. *Can. J. Chem. Eng.*, 77, 305-311.

Grace, J.R. and Clift, R. (1974). On the two-phase theory of fluidization. *Chem. Eng. Sci.*, 29, 327-334.

Grace, J.R. and Sun, G. (1990). Fines concentration in voids in fluidized beds. *Powder Technol.*, 62, 203-205.

Howard, J.R. (1989). Fluidized bed technology. Principles and applications. Adam Hilger, New York.

Jin, W., Gu, X., Li, S., Huang, P., Xu, N. and Shi, J. (2000). Experimental and simulation study on a catalyst packed tubular dense membrane reactor for partial oxidation of methane to syngas. *Chem. Eng. Sci.*, 55, 2617-2625.

Kim, S.W., Kirbas, G., Bi, H.T., Lim, C.J. and Grace, J.R. (2004). Flow behavior and regime transition in a high-density circulating fluidized bed riser. *Chem. Eng. Sci.*, 59, 3955–3963.

King, D.F. (1989). Estimation of dense bed voidage in fast and slow fluidized beds of FCC catalyst. in Fluidization VI. Eds. Grace, J.R., Schemilt, L.W. and Bergougnou, M.A. pp. 1-8. Engineering Foundation, New York.

King, D.F. and Harrison, D. (1982). The dense phase of a fluidised bed at elevated pressures. *Trans. I. Chem. Engrs*, 60, 26-30.

Kunii, D. and Levenspiel, O. (1991). Fluidization engineering, 2nd ed. Butterworth-Heinemann, Boston.

Lee, G.S. and Kim, S.D. (1990). Axial mixing of solids in turbulent fluidized beds. *Chem. Eng. J.*, 44, 1–9.

Li, A., Lim, C.J., Boyd, T. and Grace, J.R. (2008). Simulation of autothermal reforming in a staged-separation membrane reactor for pure hydrogen production. *Can. J. Chem. Eng.*, 86, 387-394.

Li, T. and Wu, P. (1991). A study on axial gas mixing in a fast fluidized-bed. in Circulating fluidized-bed technology III. Eds. Basu, P., Horio, M. and Hasatani, M. Pergamon, Oxford.

Mahecha-Botero, A., Grace, J.R., Lim, C.J., Elnashaie, S.S.E.H., Boyd, T. and Gulamhusein, A. (2009b). Pure hydrogen generation in a fluidized bed membrane reactor: Application of the generalized comprehensive reactor model. *Chem. Eng. Sci.*, in review.

Matsen, J.M. (1985). Scale-up of chemical processes. in Fluidized beds. Eds. Bisio, A. and Kabel, R.L. pp. 347-405. Wiley, New York.

Mori, S. and Wen, C.Y. (1975). Estimation of bubble diameter in gaseous fluidized beds. *AIChE Journal*, 21.

Morikawa, H., Bi, H.T., Lim, C.J. and Grace, J.R. (2001). Entrainment from pilot scale turbulent fluidized beds of FCC particles. in *Fluidization X*. Eds. Kwauk, M., Li, J. and Yang, W.C. pp. 181-188. Engineering Foundation, New York.

Patience, G.S., Chaouki, J., Berruti, F. and Wong, R. (1992). Scaling considerations for circulating fluidized bed risers. *Powder Technol.*, 72, 31-37.

Peters, M.H., Fan, L.S. and Sweeney, T.L. (1982). Reactant dynamics in catalytic fluidized bed reactors with flow reversal of gas in the emulsion phase. *Chem. Eng. Sci.*, 37, 553-565.

Pugsley, T.S., Patience, G.S., Berruti, F. and Chaouki, J. (1992). Modeling the catalytic oxidation of n-butane to maleic anhydride using a circulating fluidized bed reactor. *Ind. Eng. Chem. Res.*, 31, 2652-2660.

Rostrup-Nielsen, J.R. (1984). Catalytic steam reforming. in *Catalysis: Science and Technology*. Eds. Anderson, J.R. and Boudart, M. 5. Springer, Berlin.

Rowe, P.N. and Yacono, C. (1976). The bubbling behaviour of fine powders when fluidised. *Chem. Eng. Sci.*, 31, 1179-1192.

Sieverts, A. and Zapf, G. (1935a). Iron and nitrogen. *Zeitschrift für Physikalische Chemie*, 172 314-315.

Sieverts, A. and Zapf, G. (1935b). The solubility of deuterium and hydrogen in solid palladium. *Zeitschrift für Physikalische Chemie*, 174, 359-364.

Sit, S.P. and Grace, J.R. (1981). Effect of bubble interaction on interphase mass transfer in gas fluidized beds. *Chem. Eng. Sci.*, 36, 327-335.

Sun, G. and Grace, J.R. (1994). Experimental determination of particle dispersion in voids in a fluidized bed. *Powd. Technol.*, 80, 29-34.

Toomey, R.D. and Johnstone, H.F. (1952). Gaseous fluidization of solid particles. *Chem. Eng. Prog.*, 48, 220-226.

Turner, J.C.R. (1966). On bubble flow in liquids and fluidised beds. *Chem. Eng. Sci.*, 21, 971-974.

Wei, F., Jin, Y., Yu, Z. and Chen, W. (1995). Lateral and axial mixing of the dispersed particles in CFB. *J. Chem. Eng. Jpn.*, 28, 506-510.

Weimer, A.W. and Quarderer, G.J. (1985). On dense phase voidage and bubble size in high pressure fluidized beds of fine powders. *AIChE J.*, 31, 1019-1028.

Wen, C.Y. and Yu, Y.H. (1966). A generalized method for predicting the minimum fluidization velocity. *AIChE J.*, 12, 610-612.

- Werther, J. (1974). Influence of bed diameter on the hydrodynamics of gas fluidized beds. *AIChE Symp. Ser.*, 141, 53-62.
- Wilke, C.R. (1950). Diffusional properties of multicomponent gases. *Chem. Eng. Prog.*, 46 95-104.
- Xu, J. and Froment, G.F. (1989a). Methane steam reforming, methanation and water-gas shift: I. Intrinsic kinetics. *AIChE J.*, 35, 88-96.
- Xu, J. and Froment, G.F. (1989b). Methane steam reforming: II. Diffusional limitations and reactor simulation. *AIChE J.*, 35, 97-103.
- Yacono, C., Rowe, P.N. and Angelino, H. (1979). An analysis of the distribution of flow between phases in a gas fluidised bed. *Chem. Eng. Sci.*, 34, 789-800.
- Yates, J.G., Cheesman, D.J. and Sergeev, Y.A. (1994). Experimental observations of voidage distribution around bubbles in a fluidized bed. *Chem. Eng. Sci.*, 49, 1885-1895.

5. COMPARISON OF FLUIDIZED-BED FLOW REGIMES FOR STEAM METHANE REFORMING IN MEMBRANE REACTORS⁵

5.1. Introduction

An important decision in the design of fluidized bed reactors is which of several flow regimes to choose. Almost all fluidized bed reactor models are restricted to a single flow regime, making comparison difficult, especially near the regime boundaries. This chapter examines the performance of fluidized bed methane reformers with three models - a simple equilibrium model and two kinetic distributed models, based on different assumptions of varying sophistication. Membranes are incorporated to improve reactor performance. Eighteen cases are simulated for different flow regimes and membrane configurations. Predictions for the fast fluidization and turbulent flow regimes show that the rate-controlling step is permeation through the membranes (i.e. linked to developments in material science/engineering). Bubbling regime simulations predict somewhat less hydrogen production than for turbulent and fast fluidization calculations, due to the effects of interphase crossflow and mass transfer. Overall reactor performance is found to be best under turbulent fluidization operation. Practical considerations also affect the advantages, shortcomings and ultimate choice of flow regime.

Hydrogen is one of the most important industrial chemicals, required for example in petroleum refining (Shu-Ren, 1998), as well as in other chemical processes such as hydrogenation of fats and oils, hydro-cracking, hydrodealkylation, hydrodesulphurization and the production of methanol and ammonia. Moreover it could become an important energy carrier (Crabtree *et al.*, 2004). World production is currently $\sim 5 \times 10^{11}$ Nm³ per annum (Ewan and Allen, 2005), and demand is increasing rapidly. Pure hydrogen is required for fuel cells (e.g.

⁵ *A version of this Chapter is under review for publication as: Mahecha-Botero, A., Chen, Z., Grace, J.R., Elnashaie, S.S.E.H., Lim, C.J., Rakib, M., Yasuda, I. and Shirasaki, Y. (2008b). "Comparison of fluidized bed flow regimes for steam methane reforming in membrane reactors"*.

proton exchange fuel cells) to produce electricity with an efficiency of 45-55% and with reduced acid gas emissions (Borroni-Bird, 1996; Brown, 2001).

5.1.1. Steam Methane Reforming

Steam methane reforming (SMR) is the dominant process for hydrogen production (Twigg, 1989; Scholz, 1993; Koroneos *et al.*, 2004), and it is expected to play a major role during the initial stages of a hydrogen economy (Ogden, 2001). For a comprehensive review on reforming technologies, see Ferreira-Aparicio *et al.* (2005). SMR is a reversible, endothermic process, usually carried out in fixed bed reactors at 700-900°C and 15-30×10⁵ Pa, using nickel-on-alumina catalyst pellets. Despite its industrial importance, conventional SMR, carried out in parallel vertical fixed-bed catalyst tubes suspended within huge high-temperature furnaces, coupled with purification by pressure swing adsorption (PSA), suffers from several significant limitations:

- The reversibility of the reforming reactions constrains hydrogen production to thermodynamic equilibrium values (Twigg, 1989; Elnashaie and Elshishini, 1993).
- In fixed bed reformers the flow rate is high enough that external diffusional resistances can be neglected. However, intra-particle resistances are high, giving rise to low catalyst effectiveness factors (typically 10⁻³ to 10⁻²) (Rostrup-Nielsen, 1977; De Deken *et al.*, 1982; Soliman *et al.*, 1988).
- Carbon formation can deactivate reforming catalysts leading to low efficiency (Twigg, 1989; Bartholomew, 2001; Sehested, 2006).
- Because of the endothermic nature of steam reforming, conventional SMR is operated at high temperature with a large demand for external heat. Only ~50% of the heat of combustion is used directly for the steam reforming reactions (Armor, 1999). In addition, temperature gradients are large in the fixed beds and expensive materials of construction are needed to cope with the high wall temperatures in the presence of hydrogen.
- NO_x is generated during the burning of fuels in the furnaces. In addition, CO₂ is produced both in the furnace and due to the reforming process, limiting the environmental advantages of hydrogen as a fuel.

5.1.2. Fluidized-Bed Membrane Reformers

The internal diffusion limitation can be removed if catalyst pellets are replaced by fine fluidized catalyst powder. Moreover, fluidized-bed operations generally experience low temperature gradients due to intensive mixing of particles inside the reactor (Yates, 1983; Deshmukh *et al.*, 2005). Other advantages of FBMR include the possibility of using inexpensive metal alloys for the reactor vessel (due to its lower operating temperatures) as well as continuous or periodic catalyst replacement (Grace *et al.*, 2005). In addition, membranes may be introduced into reforming reactors to selectively remove hydrogen *in situ* as it is produced. This favourably shifts the equilibrium forward by LeChâtelier's principle (Thomsen, 2000). Higher hydrogen yield and natural gas conversion may then be achieved at much lower temperatures if hydrogen is extracted from the reactor (Raich and Foley, 1995; Mleczko *et al.*, 1996; Adris *et al.*, 1997). However, fluidized-bed membrane reactors present challenges, such as the possibility of catalyst attrition/erosion, a more complex design/scale-up/construction process, as well as the need for reliable and durable membranes.

To achieve the above advantages, different reforming configurations have been modelled in efforts to improve the process, e.g. bubbling fluidized-bed membrane reformers (FBMR) (Adris *et al.*, 1997; Abba *et al.*, 2003a; Dogan *et al.*, 2003; Patil *et al.*, 2005; Dehkordi and Memari, 2009; Mahecha-Botero *et al.*, 2009b) and fast fluidized-bed membrane reformers Chen *et al.* (2003a; 2003b, c, 2004). Furthermore several experimental studies and reactor developments for FBMRs have been carried out (Adris *et al.*, 1994; Roy *et al.*, 1999; Jarosch and de Lasa, 1999 ; Boyd *et al.*, 2005; Patil *et al.*, 2006; Chen *et al.*, 2007; Mahecha-Botero *et al.*, 2008a), and the FBMR process is currently being commercialized (Adris *et al.*, 1994; Grace *et al.*, 2006; Deshmukh *et al.*, 2007).

A fluidized-bed membrane reactor may operate under different conditions depending on how the heat required for the reforming reactions is supplied. The main reactions for SMR are then (Xu and Froment, 1989a, b):

Methane steam reforming:

(R1)



Methane overall steam reforming: **(R2)**



Water-gas shift: **(R3)**



Note that R2 is the sum of reactions R1 and R3.

For *autothermal reforming (ATR)* conditions, oxygen is supplied to the reactor to oxidize combustibles, thereby generating the required heat (Roy *et al.*, 1999; Hoang and Chan, 2004). Reforming reactions R1 to R3, as well as methane combustion, occur simultaneously during autothermal reforming of methane.

FBMRs can be operated in several different flow regimes. In this chapter we investigate the relative merits of different fluidization hydrodynamic regimes – bubbling, turbulent and fast fluidization. In addition, we study the influence of operating variables, such as reactor pressure and temperature, and of key equipment variables, such as the palladium alloy coating membrane thickness and membrane surface area per unit volume of reactor.

5.2. Description of Reactor Models

Gas-fluidized bed reactors may operate in several different flow regimes - bubbling, slugging, turbulent, fast fluidization, or dense suspension upflow. Choosing the flow regime is a key question in the design of the reactors. While there have been many attempts to model gas-fluidized bed reactors addressing the essential inherent two-phase flow issues, almost all of these models are specific to one of these flow regimes (Abba *et al.*, 2003b). This makes it very difficult to compare the flow regimes, especially near the regime boundaries, where the regime-specific models predict abrupt changes at the regime boundaries, whereas experimental evidence (Sun and Grace, 1990) show that the transitions are smooth and gradual.

In this chapter, three reactor models are developed to investigate the performance of fluidized-bed membrane methane reformers. The simplest, Model 1, is a single-stage Gibbs reactor model which, after removing the desired hydrogen generation from the abundances of the various species, assumes that the remaining mixture reaches chemical equilibrium, given the

rapid kinetics. Model 2 incorporates the chemical kinetics of the reforming and water-gas shift reactions, as well as, when applicable, the oxidation reactions caused by addition of air to provide autothermal reforming. It adopts a very simple plug flow, no-slip representation of the hydrodynamics and mixing, as a first approximation to what might occur in a riser (fast-fluidized bed) reactor. The model accounts for possible regeneration of catalyst by burning in the return loop any coke formed on the catalyst surface during reforming. Model 3 is the most sophisticated of the models. It implements the two-phase theory of fluidization, as well as probabilistic averaging of hydrodynamic parameters, so that the various flow regimes of fluidization can be compared. It also accounts for such factors as the increase in volumetric flow due to the change in the number of moles due to reaction, interphase crossflow, withdrawal of hydrogen through membrane surfaces, and mass and heat transfer resistances. The key features of the three models are compared in Table 5.1.

Simulations were carried out both for steam methane reforming with external heat transfer (SMR) and for autothermal reforming (ATR) with air introduced to provide the endothermic heat absorbed by the reforming reactions. For comparison, some cases are considered without permselective membranes. Thermodynamic equilibrium analyses were carried out for the base case with and without membranes using Model 1. The different models gave very similar results when applied to the same operating and equipment conditions, demonstrating the compatibility and consistency of this set of models.

Mechanistic simulations are carried out using two kinetic models, Models 2 and 3, to test the influence of fluidization flow regime on the reactor performance. The three most common flow regimes of fluidization – bubbling, turbulent fluidization and fast fluidization – are compared. The superficial gas velocity is first chosen to maximize the probability of being in the turbulent flow regime according to Model 3, with probabilities estimated as outlined by Abba *et al.* (2003b). Conditions for the bubbling and fast fluidization flow regimes are then chosen to match that (high) probability (0.971) of being in turn in each of these flow regimes. Simplifications introduced to the kinetic models for ease of direct comparison are:

Table 5-1. Summary of reactor models.

Model Characteristic	(1) Single-Stage Model	(2) Plug-Flow Reactor Model with Complete Conversion Regenerator	(3) Generic Reactor Model
Software used	Microsoft Excel	Fortran	Matlab 7.5
Number of independent variables (lumped or distributed model)	Lumped	One independent variable (1-D distributed model)	One independent variable (1-D distributed model)
Number of pseudo-phases	One pseudo-phase	One pseudo-phase	Two pseudo-phases (i.e. high and low density)
Kinetic or Equilibrium model	Equilibrium model	Kinetic model	Kinetic model
Accounts for change in number of moles	Yes	Yes	Yes
Can account for the heat capacity of the gases and solids	N/A (Isothermal)	Yes	Yes
Includes a pressure balance	No	No	Yes
Accounts for hydrodynamics	No	Yes (fast fluidization only)	Yes (i.e. for bubbling, turbulent and fast fluidization)
Accounts for voidage profiles	No	No	Yes
Accounts for mass transfer between phases	N/A	N/A	Yes
Uses probabilistic averaging of hydrodynamic parameters	No	No	Yes (i.e. for bubbling, turbulent and fast fluidization)
Includes hydrogen removal	Yes (Net H ₂ removal)	Yes (Differential H ₂ removal)	Yes (Differential H ₂ removal)
Allows for carbon formation	No	Yes	No
Allows for catalyst recirculation	No	Yes (external)	No
Assumes ideal regeneration	N/A	Yes	N/A
Numerical technique adopted for model solution	Empirical iterations	<i>DGEAR</i> subroutines for solving stiff differential equations. <i>fom</i> algorithm for two point boundary value problem	<i>ODE15s</i> routine for accurately solving stiff differential equations

Table 5-1. (Cont'd). Summary of reactor models.

Model Characteristic	(1) Single-Stage Model	(2) Plug-Flow Reactor Model	(3) Generic Reactor Model
Design/operating parameters	Reactor input conditions: mole fractions, temperature, pressure, gas velocity; Membrane characteristics and input conditions; Reactor dimensions	Reactor input conditions: mole fractions, temperature, pressure, gas velocity; Membrane characteristics and input conditions; Reactor dimensions	Reactor input conditions: mole fractions, temperature, pressure, gas velocity; Membrane characteristics and input conditions; Reactor dimensions
Required chemical kinetics	N/A	SMR Kinetics from Xu and Froment (1989); Coking Kinetics from Tottrup (1976) and Snoeck et al. (1997); Coke Gasification from Chen et al. (2000)	SMR Kinetics from Xu and Froment (1989); Oxidation kinetics from Jin et al. (2000)
Physico-chemical parameters	Equilibrium constants from Xu and Froment (1989); van't Hoff equation for heats of reaction	Heat capacity correlations and parameters; Heats of reaction; Catalyst properties: particle size and density; Species properties: molecular weight	Regime correlations; Heats of reaction; Catalyst properties: particle size and density; Species properties: Heat capacity, viscosity and diffusivity correlations and parameters; molecular weight.
Equations of state	Ideal	Ideal	Ideal
Model output	Exit Molar flows, Temperature, Conversion and H ₂ Yield	Molar flows, Temperature, Velocity, Conversion and H ₂ Yield profiles along the reactor length	Profiles along reactor length for: Molar flows of all species in both phases; Phase volumetric flowrates; Flow regime probabilities; Effective mass transfer coefficients for all species; Gas density; Minimum fluidization velocity; Hydrogen removal from each pseudo-phase; Volumetric crossflow between phases, Bubble diameter; Phase voidage; Temperature; Velocity; Pressure; Conversion and H ₂ Yield. Hydrodynamic parameters show the weighted contribution from each flow regime.
Suitable applications of the model	Reactors not controlled by kinetics	Coking environments, fast fluidization, reactor-regenerator systems	Bubbling, turbulent and fast fluidized beds

- (1) Steady-state operation (i.e. dynamic terms turned off for Model 3).
- (2) The palladium-based membranes are 100% selective for the permeation of hydrogen.
- (3) The performance of the membranes is unaffected by carbon deposition.
- (4) The membrane permeation flux is calculated with a membrane efficiency factor of 0.7 (i.e. the membrane permeability is taken as 70% of that measured in the permeation rig without particles and only gas present).
- (5) The membranes are assumed to begin at the bottom and extend without interruption to the top of the reactor.
- (6) Isothermal operation (i.e. energy balance turned off for Models 2 and 3).

5.2.1. Single-Stage Equilibrium Model (Model 1)

For operating conditions of interest (i.e., temperature 550 to 900°C and absolute pressure 5×10^5 to 30×10^5 Pa), the steam reforming and water gas shift reactions in the presence of a catalyst are fast enough that the production of hydrogen closely approaches the equilibrium values. As a result, thermodynamic equilibrium analysis provides a simple and direct basis for practical applications. At the equilibrium state, the second steam methane reforming reaction (R2) is just the summation of reactions R1 and R3. Hence it is sufficient to include any two of the above three reactions in the thermodynamic equilibrium analysis.

When air is introduced into the reformer, its oxygen is considered to be used up rapidly and irreversibly, supplying the exothermic heat of reaction balancing the endothermic steam reforming. For example, partial oxidation of methane can be represented by the irreversible reaction:

Methane partial oxidation:

(R4)



Equilibrium constants for the reversible steam methane reforming reaction R1 and water-gas-shift reaction R3 are calculated (Elnashaie and Elshishini, 1993) by:

$$K_1 = \frac{P_{H_2}^3 P_{CO}}{P_{CH_4} P_{H_2O}} = 10000e^{\frac{26830}{T} - 30.114} \quad (\text{kPa}^2) \quad (5.1)$$

$$K_2 = \frac{P_{CO_2} P_{H_2}}{P_{CO} P_{H_2O}} = e^{\frac{4400}{T} - 4.036} \quad (5.2)$$

A Microsoft Excel spreadsheet program has been developed for the thermodynamic equilibrium analysis. Details are summarized in Table 5.1 in comparison with the other three models.

5.2.2. Plug Flow Reactor Model with Complete Conversion Regenerator (Model 2)

This model considers a circulating fluidized bed membrane reactor modeled as a plug flow reactor with a constant solid fraction and slip between the solid and gas neglected, because fine catalyst particles (mean diameter of $\sim 100 \mu\text{m}$) are used (Patience *et al.*, 1992). Steam methane reforming, partial oxidation of methane, carbon formation and gasification are considered in the kinetic model. Table 5.2 summarizes the main reactions and assumed kinetics.

The non-permeate reformer off-gas (ROG) is composed of some unreacted methane, by-product carbon monoxide and un-permeated hydrogen. Their heats of combustion are used to preheat the cold feeds of water, methane and air. Carbon deposited on the catalyst is assumed to be burned-off in the catalyst regenerator with excess air. Kinetics of carbon deposition on the catalyst surface are described in Table 5.2.

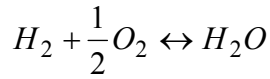
Thus, the following four reactions are assumed to take place in the catalyst regenerator, with excess air for complete conversion:

Methane combustion: (R5)

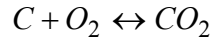


CO oxidation: (R6)



Hydrogen combustion:**(R7)**

$$(\Delta H_{298}^0 = -241.8 \text{ kJ.mol}^{-1})$$

Carbon combustion:**(R8)**

$$(\Delta H_{298}^0 = -393.5 \text{ kJ.mol}^{-1})$$

Table 5-2. Reaction kinetics applied to membrane reformer.

Reaction	Reaction Heat (kJ/mol)	Kinetic rate equation	Reference
$CH_4 + H_2O \leftrightarrow CO + 3H_2$	-206.2	$r_1 = k_1 \left(\frac{P_{CH_4} P_{H_2O}}{P_{H_2}^{2.5}} - \frac{P_{CO} P_{H_2}^{0.5}}{K_2} \right) / DEN^2$	(Xu and Froment, 1989a, b)
$CO + H_2O \leftrightarrow CO_2 + H_2$	-41.2	$r_2 = k_2 \left(\frac{P_{CO} P_{H_2O}}{P_{H_2}} - \frac{P_{CO_2}}{K_3} \right) / DEN^2$	
$CH_4 + 2H_2O \leftrightarrow CO_2 + 4H_2$	165.0	$r_3 = k_3 \left(\frac{P_{CH_4} P_{H_2O}^2}{P_{H_2}^{3.5}} - \frac{P_{CO_2} P_{H_2}^{0.5}}{K_2 \cdot K_3} \right) / DEN^2$	
$CH_4 + 2O_2 \rightarrow CO_2 + 2H_2O$	-802.6	$r_4 = k_4 P_{CH_4} P_{O_2}$	(Jin <i>et al.</i> , 2000)
$CH_4 + CO_2 \leftrightarrow 2CO + 2H_2$	247.05	$r_5 = k_5 P_{CH_4} P_{CO_2} \left(1 - \frac{P_{CO}^2 P_{H_2}^2}{K_5 P_{CH_4} P_{CO_2}} \right)$	
$CH_4 \leftrightarrow C + 2H_2$	74.6	$r_6 = \frac{k_6 K_{CH_4} \left(P_{CH_4} - \frac{P_{H_2}^2}{K_{6a}} \right)}{\left(1 + \frac{P_{H_2}^{1.5}}{K_{6b}} + K_{CH_4} P_{CH_4} \right)^2}$	(Snoeck <i>et al.</i> , 1997)
$2CO \rightarrow C + CO_2$	-172.45	$r_7 = \frac{k_7 P_{CO}}{\left(1 + K_{7a} P_{CO} + K_{7b} \frac{P_{CO_2}}{P_{CO}} \right)^2}$	(Tottrup, 1976)
$C + H_2O \rightarrow CO + H_2$	131.296	$r_8 = k_8 P_{H_2O}^{0.5}$	(Chen <i>et al.</i> , 2000)
$C + 0.5O_2 \rightarrow CO$	-110.53	$r_9 = k_9 P_{O_2}^{0.5}$	
$C + CO_2 \rightarrow 2CO$	172.45	$r_{10} = k_{10} P_{CO_2}^{0.5}$	
$DEN = 1 + K_{CO} P_{CO} + K_{H_2} P_{H_2} + K_{CH_4} P_{CH_4} + K_{H_2O} P_{H_2O} / P_{H_2}$			

The steady state model equations for the membrane reformer are summarized in Table 5.3. The product hydrogen yield is defined as the total moles of hydrogen permeated through

membranes per mole of methane fed. Methane conversion is defined as the total number of moles of methane converted per mole of methane fed. The catalyst activity in Table 5.3 is the ratio of the catalytic reaction rate to the initial reaction rate with fresh catalyst (no carbon deposited). Key features of this model are compared with those of the other models in Table 5.1.

Table 5-3. Steady state equations for Model 2.

Mole Balance on Riser Reformer Reaction Side	
Component i	$\frac{dF_i}{dz} = \rho_C(1-\varepsilon)A \sum_{j=1}^{10} \nu_{i,j} r_j - a_{H_2} t p_{H_2}$ $\begin{cases} a = 1 & i = H_2 \\ a = 0 & i \neq H_2 \end{cases}$ <p>(i = CH₄, CO₂, CO, H₂, H₂O, O₂, N₂ and C)</p>
Boundary condition	at z = 0, F _i = F _{i0}
Mole Balance on Hydrogen Permselective Membrane Modules	
Hydrogen	$\frac{dF_{H_2,P}}{dz} = J_{H_2} t p_{H_2}$
Boundary condition	at z = 0, F _{H₂,P} = F _{H₂,P0} = 0
Hydrogen permeation flux	$J_{H_2} = \frac{Q_{H_2}}{\delta_{H_2}} \exp\left(\frac{-E_{H_2}}{RT}\right) (\sqrt{p_{H_2,r}} - \sqrt{p_{H_2,p}})$
Energy Balance for Riser Reformer and Membrane Modules	
Temperature profile	$\frac{dT}{dz} = \frac{\sum_{j=1}^{10} r_j (-\Delta H_j) \rho_C (1-\varepsilon) A + \dot{Q}}{\sum F_i C_{p_i}}$
Boundary condition	at z = 0, T = T ₀
Catalyst Deactivation and Modified Reaction Kinetics (Chen <i>et al.</i>, 2004)	
Specific catalyst activity	$\phi_j = \begin{cases} \exp(-\alpha_C C_k) & \text{Reaction } j \text{ is affected by carbon deposition} \\ 1.0 & \text{Reaction } j \text{ is not affected by carbon deposition} \end{cases}$
Reaction rate	r _j = r _{j0} · φ _j
Energy Balance for Catalyst Regenerator	
Heat generation rate	$Q_g = \sum_{j=1}^{14} F_{ii} (-\Delta H_j) \quad (ii = CH_4, CO, H_2 \text{ and } C)$
Preheating rate	$Q_p = \sum F_k [(T_{k,b} - T_{room}) C_{p_{k(l)}} + \Delta H_{k,vap} + (T' - T_{k,b}) C_{p_{k,b(g)}}] + G_{cat} C_{p_{cat}} (T' - T_{exit})$ (k=feed water and methane, air)
Autothermal Reactor-Regenerator System	
Autothermal system	T ₀ = T' and Q _g = Q _p

5.2.4. Generic Reactor Model (Model 3)

Model 3 corresponds to the model discussed previously in Section 1.2 of this thesis. It is implemented using the same simplifications as in Chapter 4, for the unique conditions of this chapter.

5.3. Flow Regimes of Fluidization

5.3.1. Introduction

The FBMR process could be operated in several different flow regimes. In this section, we consider which flow regime is most appropriate for the FBMR SMR process. Both kinetic models (Models 2 and 3 described in Section 5.2) are developed, assuming isothermal conditions for identical inputs in order to compare the reactor volumes required to achieve a specified hydrogen yield. The results are then compared, and other factors are also factored into a discussion of which flow regime is most appropriate.

5.3.2. Simulations and Discussion

Table 5.4 summarizes the parameters chosen for reactor configuration comparison. A specific membrane perimeter-to-free-cross-sectional area of reactor (i.e., membrane permeation area per unit volume of reactor, which determines how intensively packed the membranes are inside the reformer) of $200 \text{ m}^2/\text{m}^3$ is chosen as a practical upper limit.

Table 5-4. Base values for reactor comparison.

Variable	Value	Units
Reactor operating absolute pressure	10	bar
Reactor operating temperature	823	K
Steam:methane molar feed ratio	3.0	mol/mol
Oxygen:methane molar feed ratio	0.35	mol/mol
Permeate pressure	0.3	bar
Membrane area per unit reactor volume	200	m^2/m^3
Membrane Pd/Ag layer thickness	2.5E-05	m
Feed rate of methane	4.465	kmol/h
Catalyst particle diameter	1.00E-04	m
Catalyst particle density	2270	kg/m^3

To verify the correctness of the models, this case was simulated with and without membranes by all three models (i.e. Model 2 and Model 3 under fast fluidization conditions). Table 5.5 summarizes the overall simulation results, indicating that different models give very similar results when run independently for a common non-membrane case. The simulations for the base case without membranes appear to be governed by chemical thermodynamics due to the fast reforming kinetics. These simulations typically differ from model to model by ~1 to ~2% in conversion values. For the cases without hydrogen removal, the differences in equilibrium values are caused by the variation in model parameters. In addition, since under fast fluidization with membranes, reactor performance is limited by hydrogen removal, the results are reasonably similar as well for Models 2 and 3, with differences in performance of less than 5%.

Table 5-5. Comparison of simulation results for base case (as specified in Table 5.4) for different models.

		Without H2 membranes			With H2 membranes		
		Model 1	Model 2	Model 3	Model 1	Model 2	Model 3
Fluidization regime		N.A.	Fast	Fast	N.A.	Fast	Fast
ROG dry composition							
CH4	mol%	16.3%	16.1%	16.8%	11.4%	11.5%	11.2%
H2O	-	-	-	-	-	-	-
CO	mol%	1.2%	1.2%	1.3%	1.6%	1.6%	1.8%
H2	mol%	31.6%	31.8%	33.0%	24.7%	24.0%	25.2%
CO2	mol%	12.1%	12.2%	12.6%	19.6%	19.8%	21.3%
O2	mol%	0.0%	0.0%	0.0%	0.0%	0.0%	0.0%
N2	mol%	38.7%	38.7%	36.3%	42.6%	43.1%	40.5%
Total	mol%	100.0%	100.0%	100.0%	100.0%	100.0%	100.0%
CH4 conversion	-	45.0%	45.8%	43.6%	65.1%	65.2%	65.1%
Total H2 yield	mol H ₂ /mol CH ₄	1.1	1.0	1.0	1.9	1.8	1.9
Pure H2 yield	mol H ₂ /mol CH ₄	N.A.	N.A.	N.A.	1.1	1.1	1.1
Thickness of membrane	μm	N.A.	N.A.	N.A.	25.0	25.0	25.0
Membrane effectiveness factor	-	N.A.	N.A.	N.A.	0.7	0.7	0.7
Superficial gas velocity	(m/s)	1.7	1.7	1.7	1.7	1.7	1.7

The generic model (Model 3) was next used to find the flow regime probability distributions for the reactor conditions given in Table 5.4 and different input superficial gas velocities. Probability distribution curves for the conditions of interest are depicted in Figure 5.1. The probability of being in the turbulent regime, P_{turb} , reached a maximum “ $P_{turb,max}$ ” of 0.971 at a superficial gas velocity of 0.82 m/s, representing the condition where the system is “most turbulent”. We next found the gas velocities where $P_{bubb} = P_{turb,max}$ and $P_{fast} = P_{turb,max}$, these being 0.21 m/s and 1.68 m/s, respectively. The corresponding probabilities for the different fluidization flow regimes are listed in Table 5.6. These three superficial gas velocities are chosen to assure that we compare operation where each of the flow regimes is equally dominant.

Note that the probability curves shift somewhat along the reactor as the molar flow varies due to the reactions and hydrogen removal. Input conditions are therefore utilized for this calculation procedure. The curves are also sensitive to changes in the average gas density, which is affected by the temperature and pressure variation along the reactor, as well as by the gas composition. The fluidization velocities for the different dominant fluidization regimes from Table 5.6 are also used in conjunction with Model 2 for the fast fluidization regime. A comprehensive set of fluidization correlations is implemented to estimate the solids distribution along the fluidized bed. In order to provide Model 2 with an estimated bed voidage, height averages are calculated by integration from Model 3. The resulting average values are included in Table 5.6.

Table 5-6. Parameters for different fluidization flow regimes.

Flow regime	Model	Gas velocity (m/s)	P_{bubb} (-)	P_{turb} (-)	P_{fast} (-)	Voidage (-)	Free cross-sectional area (m²)	Reactor height (m)
Bubbling	Model 3	0.21	0.971	0.028	9.2*10 ⁻⁵	0.587	0.206	0.549*
Turbulent	Model 3	0.82	0.0096	0.971	0.019	0.721	0.0579	1.954*
Fast fluidization	Models 2 and 3	1.68	9.71*10 ⁻⁸	0.028	0.971	0.95	0.0279	4.056

*Dense bed height

In order to cover a variety of membrane reactor designs, six different combinations of palladium layer thickness of the membrane and membrane specific surface area are simulated with the kinetic models, as summarized in Table 5.7.

Table 5-7. Configurations for reactor simulations.

Configuration	Membrane palladium layer thickness	Specific membrane surface area
(1)	50 μm	200 m ² /m ³
(2), Base Case	25 μm	200 m ² /m ³
(3)	15 μm	200 m ² /m ³
(4)	5 μm	200 m ² /m ³
(5)	1 μm	200 m ² /m ³
(6)	25 μm	1000 m ² /m ³

5.3.2.1. Plug flow reactor model with complete conversion regenerator (Model 2)

The plug-flow reactor model (Model 2: see Section 5.2.2 for details) is next used to simulate the six cases of interest. Given its simple approach to hydrodynamics, intended only for fast fluidization, this model gives very similar results when used to simulate reforming in different flow regimes. Since Model 2 does not allow for regime specific correlations and assumes single-phase plug-flow, it is used exclusively for fast fluidization simulations. Furthermore, the results from Model 2 are compared to those from Model 3 under fast fluidization conditions resulting in very small differences (typically ~2% to ~5%), suggesting correctness in the model implementation. It is shown that hydrogen permeation is the rate-limiting step in the membrane reformer operations for fast fluidization. Decreasing membrane thickness and/or increasing the membrane permeation area per unit volume of reactor enhance the hydrogen production.

Figures 5.2a and 5.2b show the predicted pure hydrogen production rate and methane conversion respectively as a function of reactor volume for the different configurations outlined in Table 5.7. The pure hydrogen production rate increases significantly with decreasing membrane thickness, resulting in quick increases followed by levelling off, specifically for thinner membranes. A similar trend is found for the methane conversion, where we observe how the reformer could achieve complete conversion for very thin membranes. Therefore, for thinner membranes, the reactor height could be significantly decreased, or less surface area could be included. Increasing the membrane permeation area per unit volume of reactor could in principle increase the hydrogen production rate. For current membranes, a more compact reformer with a higher density of membranes could, if this were possible, also increase the pure hydrogen production capacity. The results for cases 4 and 6 in Figure 5.2 also indicate that for the same ratio of membrane permeation area per unit volume of reactor to the membrane thickness, the reactor performance is virtually the same since the hydrogen permeation flux would be virtually the same. For comparison, detailed reformer simulation results are shown in Figures 5.3 and 5.4 below. The products of the reactor height and free cross-sectional area, listed in Table 5.6, give the corresponding reactor volumes.

As shown in Figure 5.3, methane conversion is predicted to increase quickly at first in the base case ($25\mu\text{m}$, $200\text{m}^2/\text{m}^3$ configuration), and then more slowly as the resistance to permeation becomes rate-controlling. More hydrogen is generated as hydrogen is withdrawn through the membranes. The total flowrate of hydrogen (i.e. inside the membranes plus inside the reactor) is

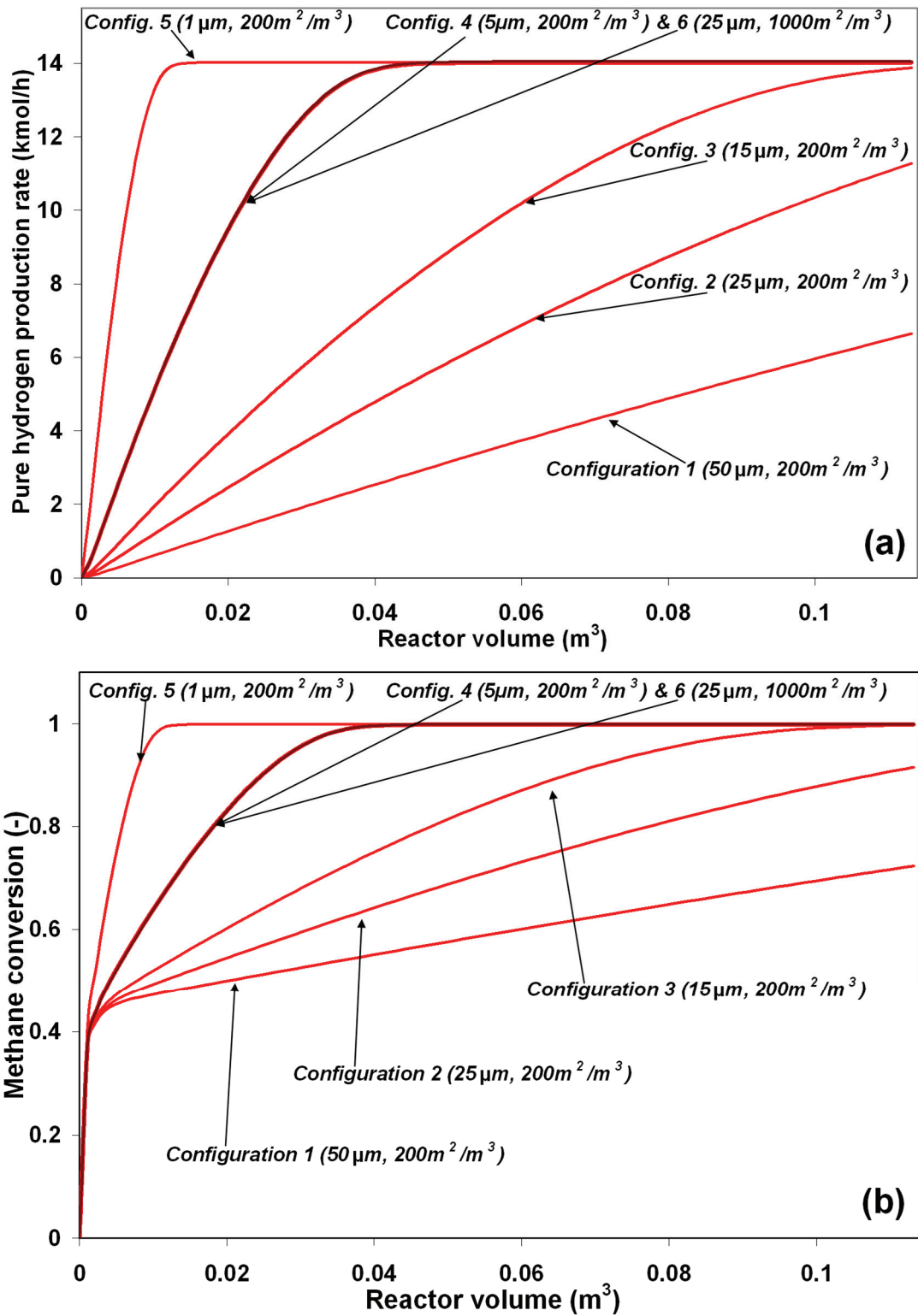


Figure 5.1. a) Comparison of pure hydrogen production rates and b) methane conversion for different membrane thicknesses, different permeation area per unit volume of reactor and for different fluidization flow regimes based on Model 2 for fast fluidization. For conditions see Tables 5.6 and 5.7.

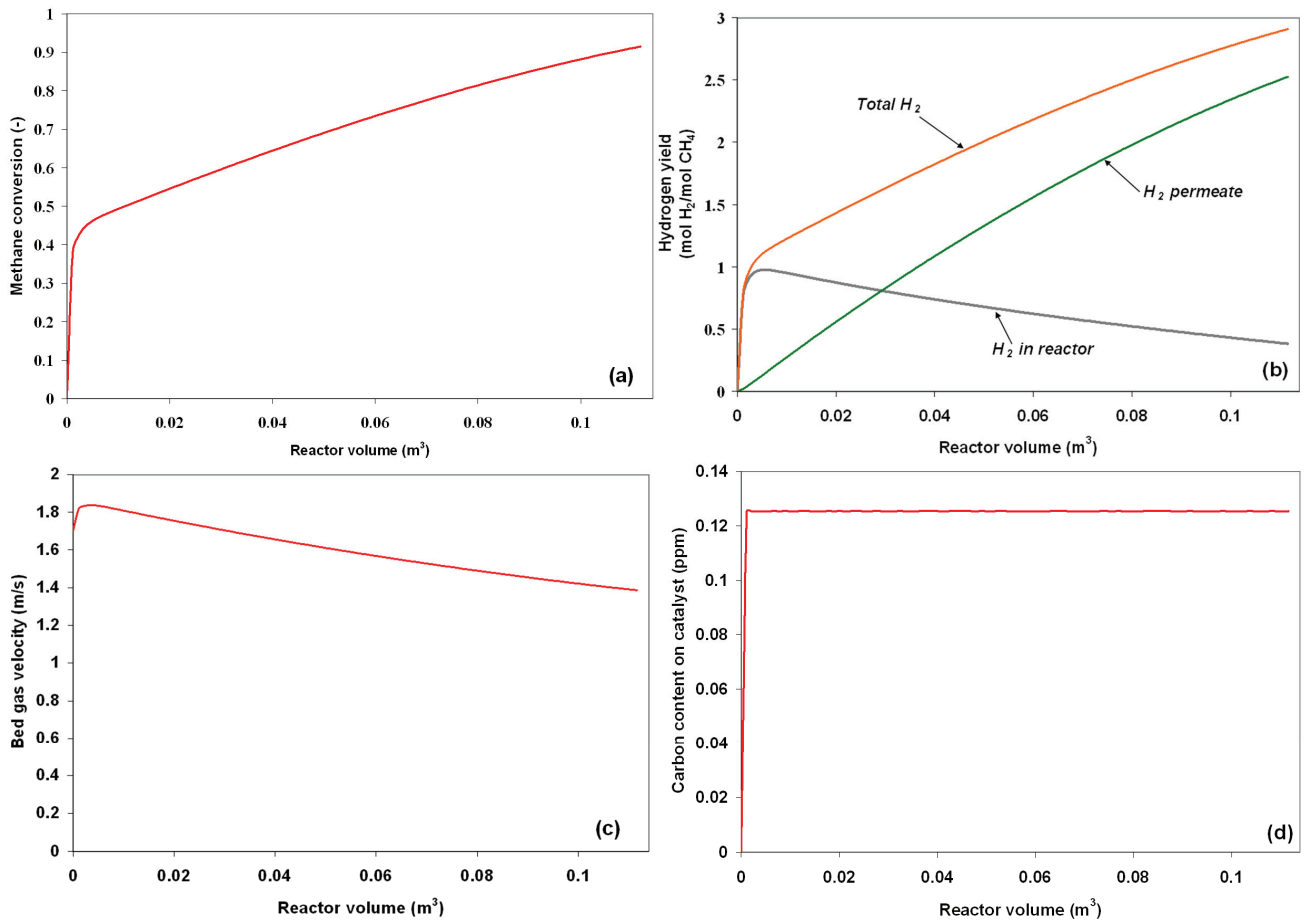


Figure 5.2. Predicted profiles of key variables for base case (i.e. configuration 2). Simulations using Model 2 for fast fluidization. For conditions see Tables 5.6 and 5.7.

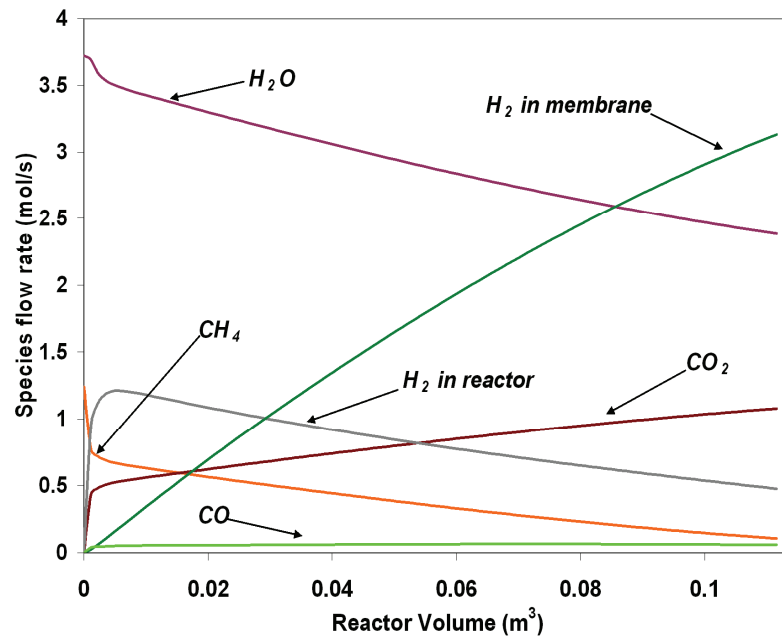


Figure 5.3. Predicted profiles of species molar flow-rates for base case (i.e. configuration 2). Simulations using Model 2 under fast fluidization. For conditions see Tables 5.6 and 5.7.

seen to increase monotonically over the reactor height. Reactor (non-permeate) hydrogen flowrate reaches a maximum after quick initial reaction and then decreases due to membrane removal. The superficial gas velocity in the reactor increases at first because of the increase in molar flowrate (via reactions R1 and R3), but then declines gradually as hydrogen is withdrawn. Based on the model, the carbon content of the catalyst (via reactions in Table 5.2) grows quickly and then maintains a constant value.

When thinner membranes are simulated, the hydrogen production rate and methane conversion increase much more quickly than for the base case (Figure 5.2). Thinner membranes allow the concentrations of CH₄ and H₂O to drop considerably more quickly. The CO₂ concentration rises more steeply with the thinner membranes but, because of the promotion of the water-gas shift reaction by H₂ removal, the CO concentration remains very low along the entire reactor. The oxygen profiles are not shown in these figures, as the oxygen partial pressure falls very quickly to essentially zero since the oxidation reactions proceed even faster than the reforming reactions.

5.3.2.3 Generic reactor model (Model 3)

Model 3 was employed to address other issues of the multiphase behaviour. With the parameters in Tables 5.4 and 5.6, six reactor configurations (see Table 5.7) were simulated for all three flow regimes, giving a total of eighteen cases (Figures 5.5 to 5.10).

Figures 5.5a, 5.5b and 5.5c depict the pure hydrogen production rate for the six configurations in Table 5.7 for the bubbling, turbulent and fast fluidization regimes respectively. Although the turbulent regime has a very small edge in performance (less than 1%) in the simulations, they show very similar results to fast fluidization simulations, resulting in almost the same overall production of pure hydrogen for all configurations. The bubbling regime is predicted to produce 22 to 24% less hydrogen than for the turbulent regime for all configurations where the membrane area is limiting (i.e. for cases where not all of the available hydrogen is removed).

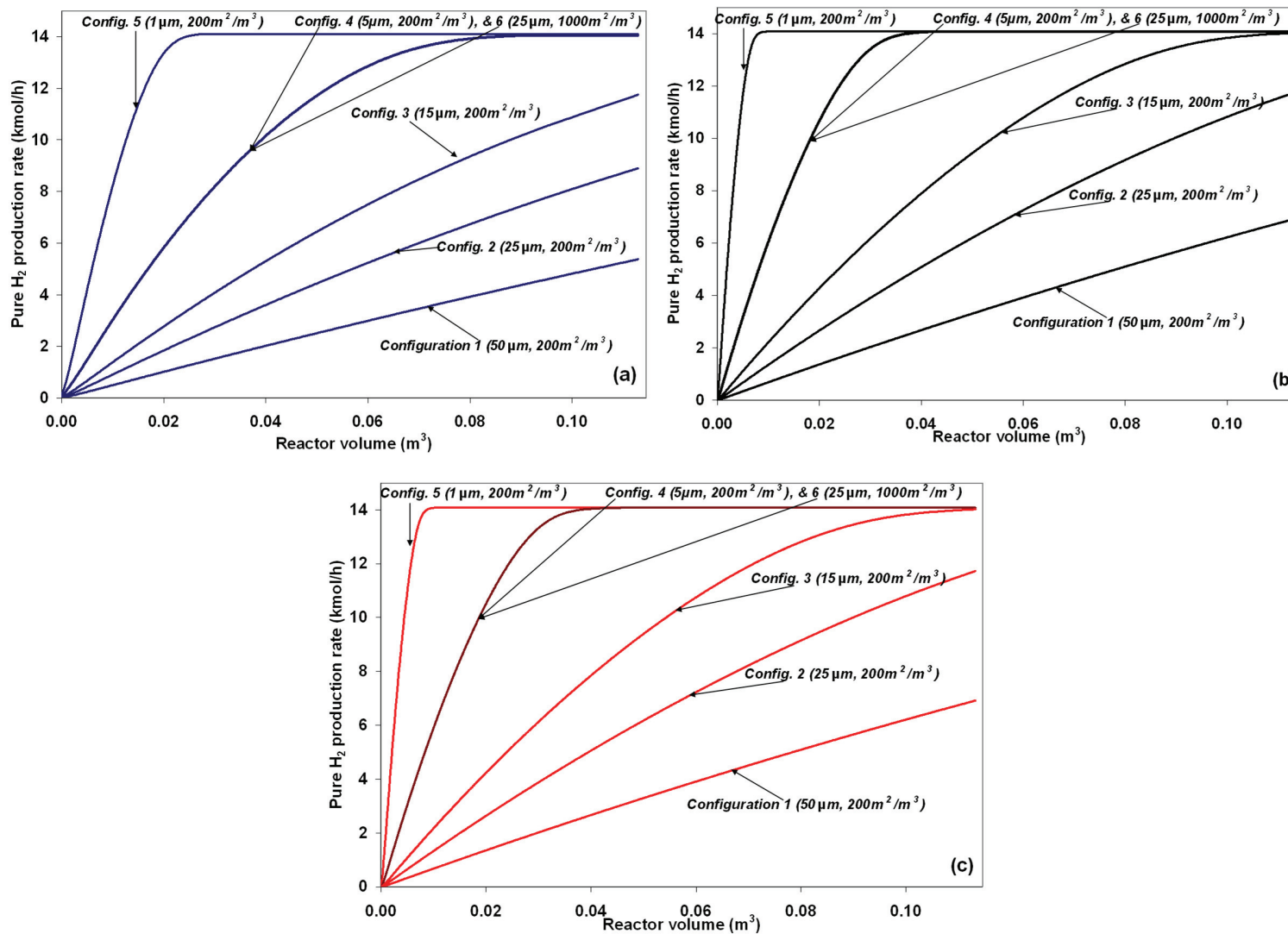


Figure 5.4. Comparison of pure hydrogen production rates for different membrane thicknesses and different permeation area per unit volume of reactor. (a) Bubbling fluidization regime, (b) Turbulent fluidization regime, (c) Fast fluidization regime. Simulations using Model 3. For conditions see Tables 5.6 and 5.7.

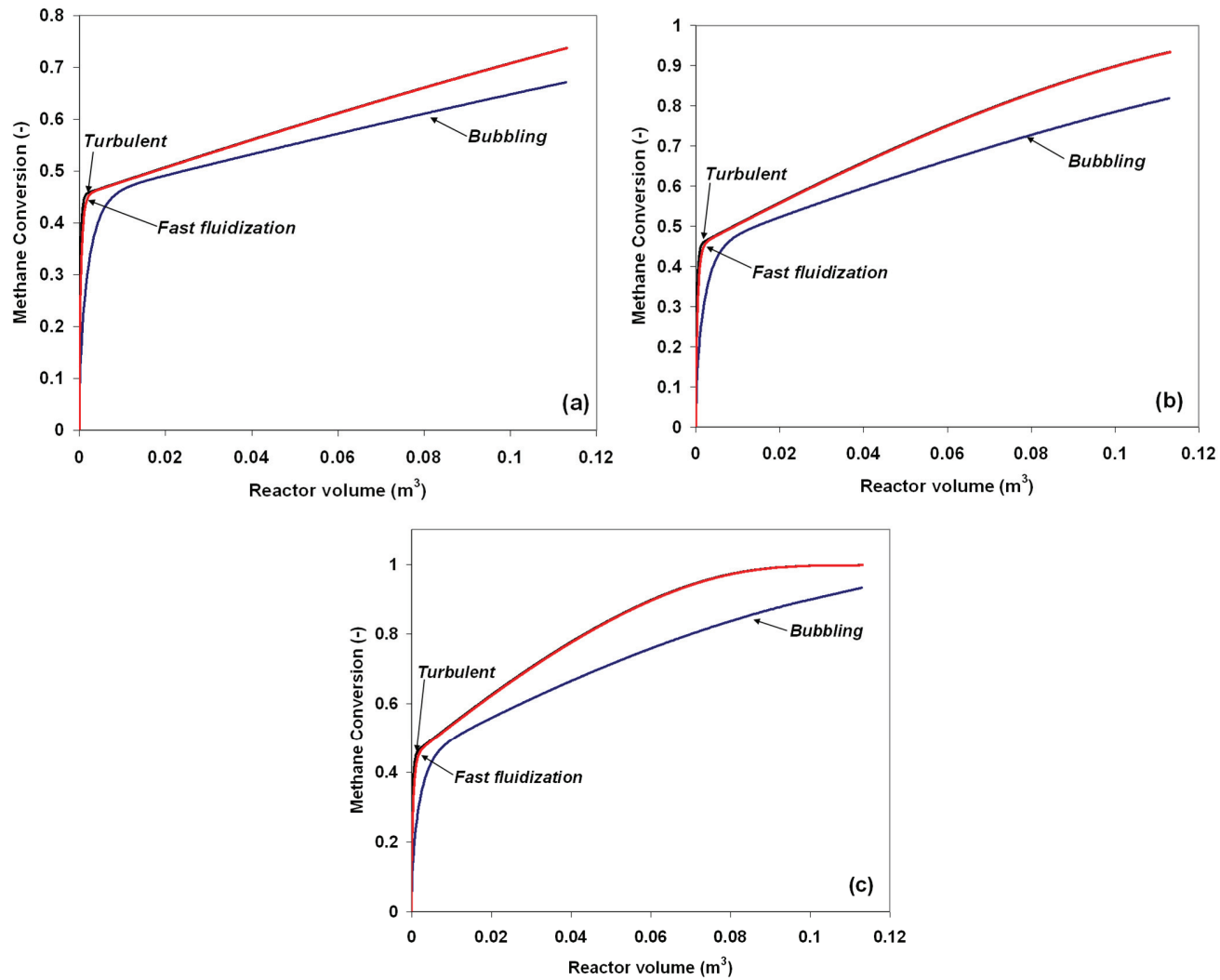


Figure 5.5. Comparison of methane conversion for different flow regimes: bubbling (blue), turbulent (black) and fast fluidization (red). (a) Configuration 1 (50 μm , 200m²/m³), (b) Configuration 2 (25 μm , 200m²/m³), (c) Configuration 3 (3 μm , 200m²/m³). Simulations using Model 3. For conditions see Tables 5.6 and 5.7.

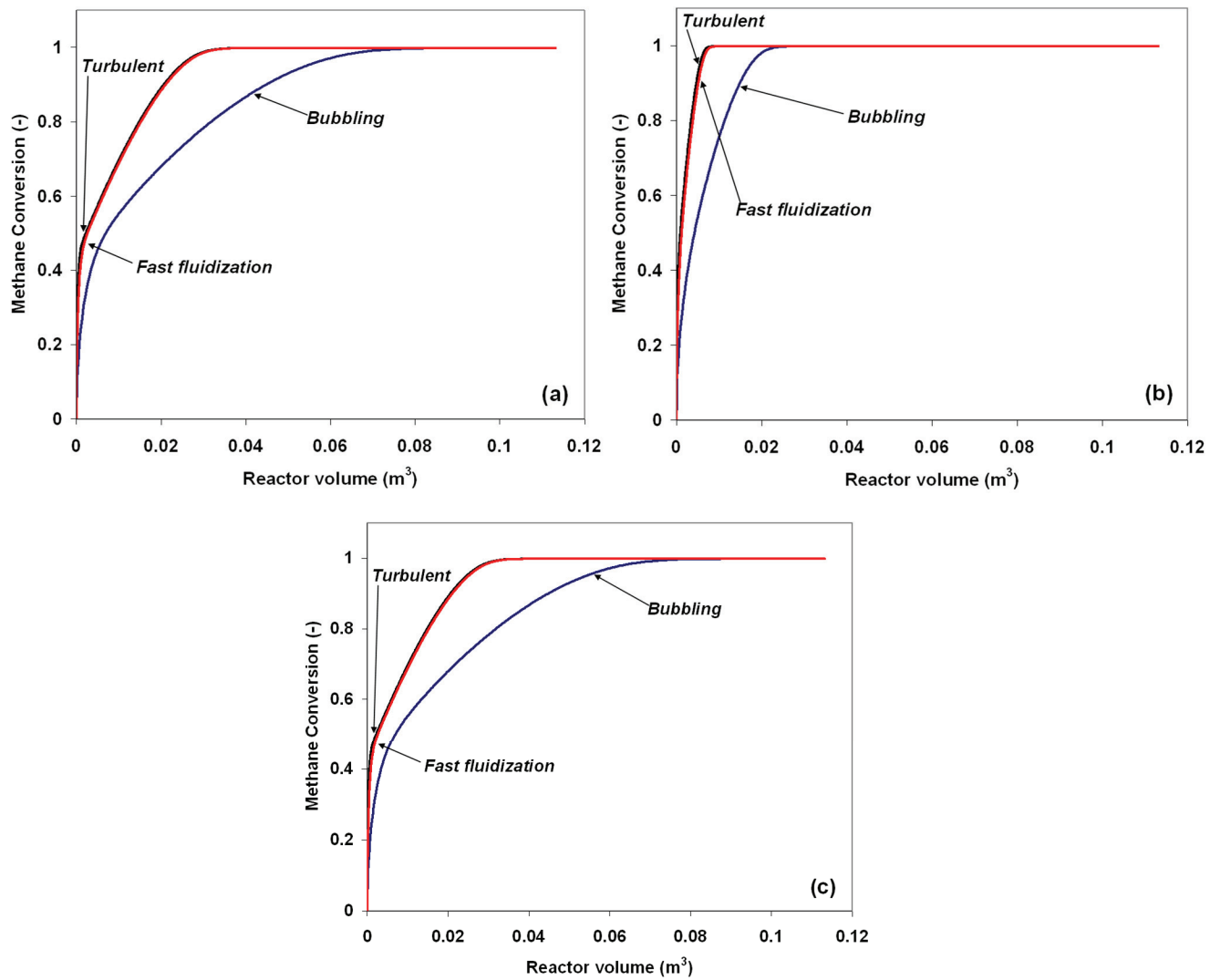


Figure 5.6. Comparison of methane conversion for different flow regimes: bubbling (blue), turbulent (black) and fast fluidization (red). (a) Configuration 4 (5 μm, 200 m²/m³), (b) Configuration 5 (1 μm, 200 m²/m³), (c) Configuration 6 (25 μm, 1000 m²/m³). Simulations using Model 3. For conditions see Tables 5.6 and 5.7.

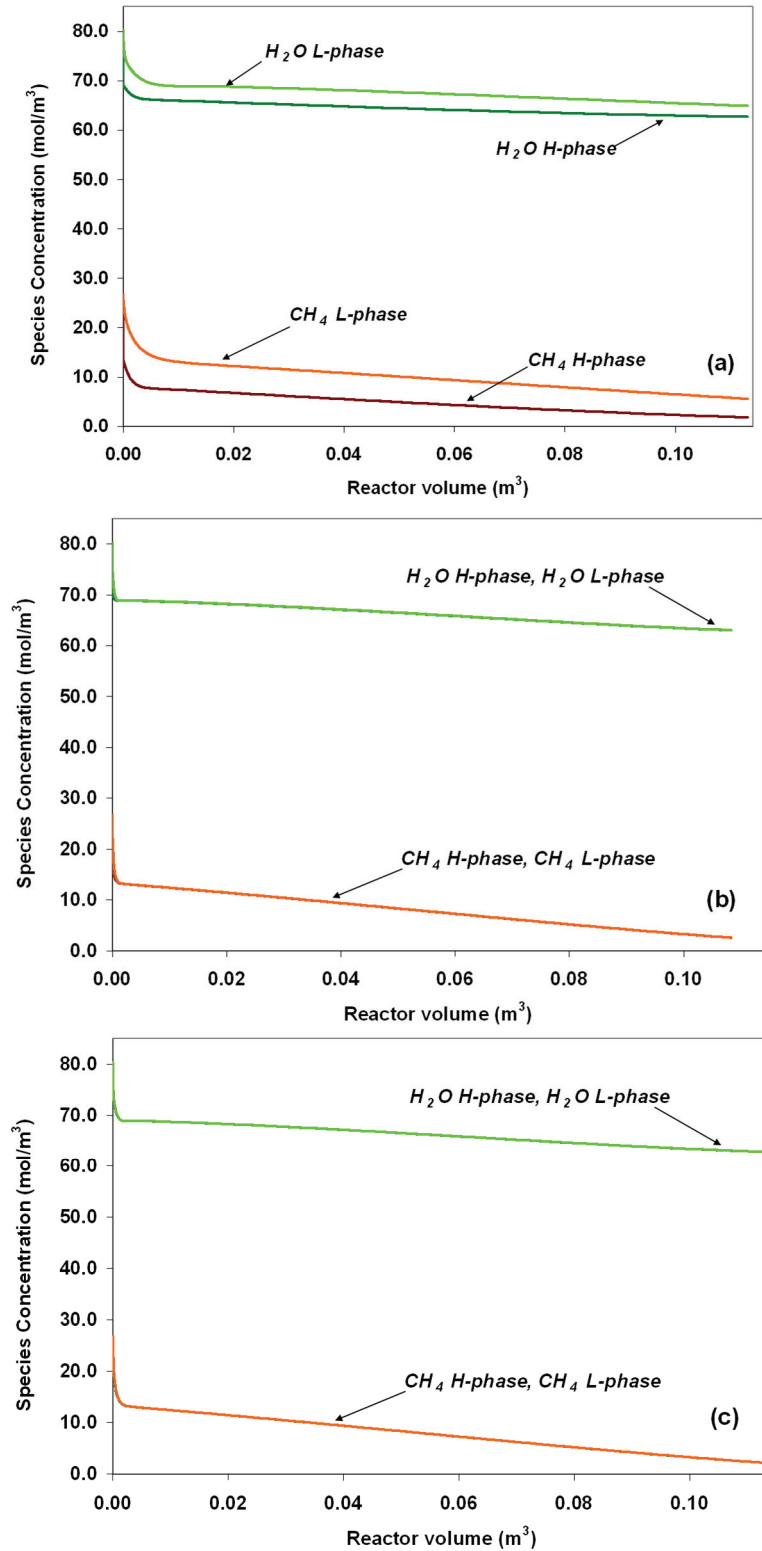


Figure 5.7. Comparison of CH₄ and H₂O concentrations in the high and low density pseudo-phases for different flow regimes (base case). (a) bubbling regime, (b) turbulent regime, (c) fast fluidization regime. Simulations using Model 3. For conditions see Tables 5.6 and 5.7.

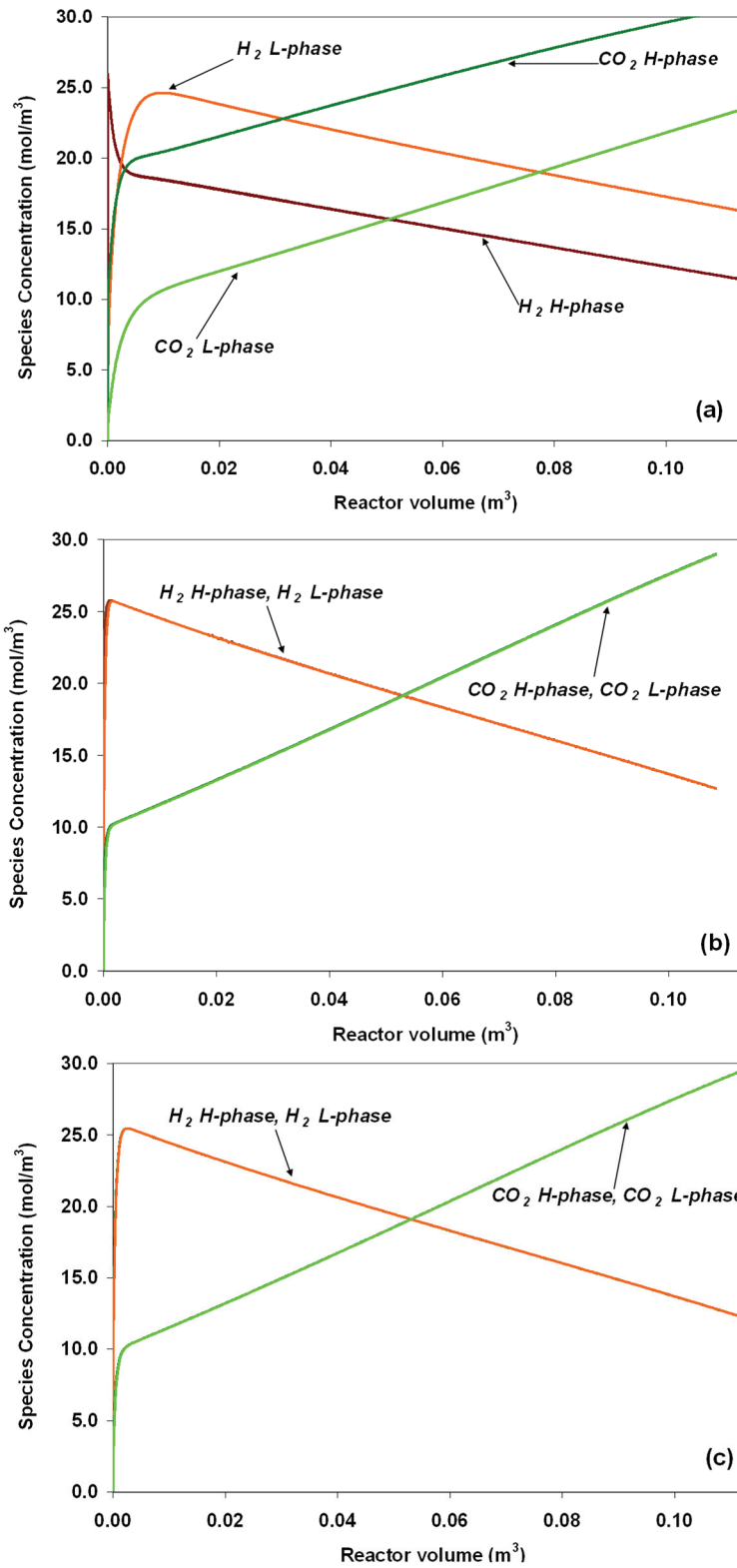


Figure 5.8. Comparison of H₂ and CO₂ concentrations in the high and low density pseudo-phases for different flow regimes (base case). (a) bubbling regime, (b) turbulent regime, (c) fast fluidization regime. Simulations using Model 3. For conditions see Tables 5.6 and 5.7.

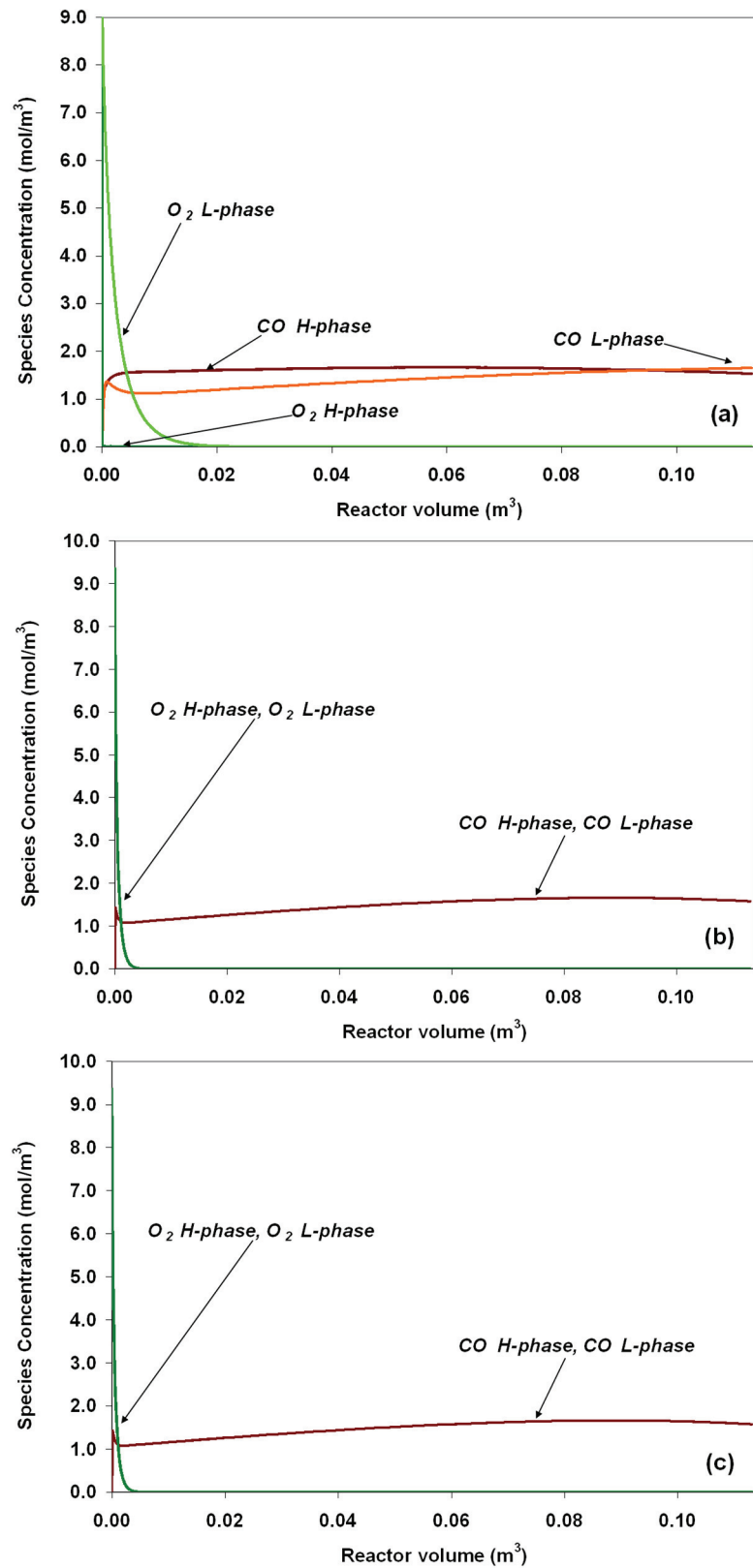


Figure 5.9. Comparison of CO and O₂ concentrations in the high and low density pseudo-phases for different flow regimes (base case). (a) bubbling regime, (b) turbulent regime, (c) fast fluidization regime. Simulations using Model 3. For conditions see Tables 5.6 and 5.7.

Configurations 1 and 2 show that the pure hydrogen (permeate) production rate increases almost linearly with reactor volume (or height) for all three flow regimes. Comparison between the different configurations shows that thinner membranes greatly accelerate the production of hydrogen. For instance, Configurations 4, 5 and 6 achieve complete hydrogen removal before the exit. After a quick increase in permeate hydrogen, hydrogen production stops. Clearly for the operating conditions considered, those configurations are over-designed, since a shorter reactor would lead to virtually the same overall performance. From a reactor design point of view for the reforming conditions under scrutiny, Configuration 3 appears to use the installed membrane area in a more optimal way. The results for Configurations 4 and 6 are indistinguishable as already shown in Figure 5.2 based on Model 2.

Figures 5.6 and 5.7 compare the methane conversion for the different flow regimes. It is observed that the turbulent regime results in the fastest conversion in the region directly above the distributor. The methane conversion curves for turbulent and fast fluidization simulations then overlap over most of the reactor height. Again the bubbling regime simulations achieve smaller conversion values for each case. The positive impact of reducing membrane thickness on reactor performance is again demonstrated. Three stages can be observed for the reforming system: 1) A very quick increase in conversion due to very fast chemical kinetics. This stage occurs during the initial $\sim 0.005 \text{ m}^3$ of reactor for turbulent/fast fluidization and $\sim 0.01 \text{ m}^3$ for bubbling fluidization (with these values depending on the gas residence time inside the reactor). 2) A gradual increase in conversion due to the continuous hydrogen removal that shifts the equilibrium forward. 3) The reactor achieves complete conversion (i.e. $\sim 0.999+\%$) and the conversion profiles become flat. This latter stage is only achieved for very thin membranes (e.g. Configurations 4, 5 and 6) in Table 5.7.

Figures 5.8 to 5.10 plot concentration profiles of the different species in the high-density and low-density phases for the three flow regimes and the base case. An important finding is that the concentrations in both the H- and L-phases are predicted to be very similar for the high-velocity flow regimes (turbulent and fast fluidization), as shown in Figures 5.8b-c, 5.9b-c and 5.10b-c. For these two flow regimes the concentration profiles in the high- and low-density pseudo-phases are virtually indistinguishable, due to fast mass transfer between the high- and low-density phases. Furthermore, since the SMR kinetics are fast and the low-density phase contains significant proportions of catalyst particles by volume, significant conversion is

predicted to occur in the low-density phase, yielding similar concentrations to the high-density phase.

Figures 5.8a, 5.9a and 5.10a show the predicted species concentrations in the bubbling regime. The CO concentration profile in Figure 5.10a shows non-monotonic behaviour, passing through a maximum as it is produced during the initial rapid kinetically-controlled reaction near the bottom of the reactor, and then being consumed due to the water-gas shift reaction, promoted by withdrawal of hydrogen. Reactants in the high-density phase achieve lower concentrations (Figures 5.8a, 5.9a, 5.10a) than in the low-density phase, whereas reaction products attain higher concentrations in the high-density phase. These differences reflect the better conditions for reaction (more catalyst particles) in the high-density phase. In this flow regime interphase mass transfer is limited. Moreover, most of the membrane surface area is in contact with the high-density phase, while it only accounts for a very small fraction of the total amount of gas flow, thus allowing more equilibrium shift due to hydrogen removal. For the configurations that achieve complete conversion before the reactor exit (e.g. configuration 4, 5 and 6), it is observed that after complete conversion is reached (Figure 5.7), the concentrations in the two phases become almost the same due to interphase mass transfer.

5.4. Other Factors Affecting Choice of Flow Regime

The comparison of flow regimes above is solely in terms of the reactor volume needed to achieve a given hydrogen production. The simulations above suggest that the turbulent regime would give superior performance compared to the other two fluidization regimes considered. However, other factors are also important in practice when considering which flow regime to use in a given case:

- a) Surface-to-bed heat transfer tends to be most favourable for the turbulent fluidization flow regime and least favourable for fast fluidization. The same order of merit is likely to apply to bed-to-surface mass transfer (at the membrane surfaces).
- b) In practice, axial dispersion of both gas and solids is likely to be greatest for bubbling fluidization, and least for fast fluidization.
- c) Wear of surfaces tends to be greatest in the fast fluidization flow regime given the higher particle velocities.

- d) Losses of catalyst due to entrainment are likely to be greatest in the fast fluidization flow regime and least in the bubbling regime.
- e) Extra reactor volume will be needed for the turbulent and bubbling flow regimes to provide a freeboard region. The disadvantage of having a freeboard could be offset, at least in part, by extending the membrane surfaces into the freeboard region.
- f) Vertical and radial temperature gradients tend to be greatest in the fast fluidization flow regime, but they can also be significant in the freeboard region above turbulent and bubbling fluidized beds. This is an important consideration for the SMR process as the reforming reactions will reverse in the presence of catalyst if the temperature drops.
- g) The height-to-diameter ratio for fast-fluidization tends to be much greater than for bubbling beds, with the turbulent regime case showing intermediate values. In practice, this means that fast fluidization is unlikely to be practical for small-scale systems, whereas bubbling beds are less likely to be viable for large commercial systems.

Given these factors, it is impossible to unambiguously choose a single flow regime for all cases. In each case in practice, it is necessary to weigh the competing factors. It is also important to remember that experimental FBMR results have so far been obtained only for the bubbling flow regime, whereas most industrial catalytic fluidized bed reactors operate in the turbulent fluidization flow regime.

5.5. Conclusions

Incorporation of perm-selective membranes provides an innovative possible means of overcoming the equilibrium barrier in the production of hydrogen, while also decreasing the adverse effect of pressure and providing *in situ* hydrogen purification. However, with currently available membranes, the removal of hydrogen via permeation is relatively slow, requiring tall membranes and high reactors, or a very congested arrangement of membrane surfaces in the reformer. The resistance to permeation through the membrane surfaces is the rate-controlling factor for currently available membranes. The overriding importance of the membrane permeability means that the future of membrane reactor technology is critically dependent on developing thinner pinhole-free membrane foil or coatings, which are also robust.

An important issue which has received little previous attention is the choice of the flow regime in which the reactor operates. The simulation predictions for the three flow regimes show that the turbulent regime is capable of yielding higher hydrogen production for a given configuration, compared to the bubbling and fast fluidization regimes. Two kinetic reactor models are used to simulate the conditions of an isothermal fluidized bed membrane reactor for steam methane reforming. Model 1, an equilibrium model is a useful tool for overall estimation. A simple reactor model (Model 2) gives predictions very similar to those for a more comprehensive probabilistic Model 3 for the fast fluidization regime. The latter is especially useful for setting the conditions where the three flow regime can be compared and to provide insights on reactor characteristics such as mass transfer and phase concentration. For turbulent and fast fluidization, Model 3, the comprehensive model derived from Chapters 1 and 4, estimated virtually the same volume requirement for a given production rate of pure hydrogen, and almost the same retentate (non-permeate stream) gas composition for a given reactor volume when the same membranes and membrane packing density are available. From a practical point of view, low-velocity fluidization is likely to be the flow regime of choice for at least the next few years because of the gentler environment it provides for the membranes, in addition to decreased entrainment.

Overall, modelling is shown to be a useful tool for the simulation of complex processes like FBMR steam methane reforming. The modelling demonstrates the considerable promise of the technology and the pre-eminent need for material science to provide thin robust pinhole-free membranes to make the process economically viable.

5.6. References

Abba, I.A., Grace, J.R. and Bi, H.T. (2003a). Application of the generic fluidized-bed reactor model to the fluidized-bed membrane reactor process for steam methane reforming with oxygen input. *Ind. Eng. Chem. Res.*, 42, 2736-2745.

Abba, I.A., Grace, J.R., Bi, H.T. and Thompson, M.L. (2003b). Spanning the flow regimes: A generic fluidized bed reactor model. *AIChE J.*, 49, 1838-1848.

Adris, A.M., Grace, J.R., Lim, C.J. and Elnashaie, S.S.E.H. (1994). Fluidized bed reaction system for steam/hydrocarbon gas reforming to produce hydrogen. US Patent number 5326550.

Adris, A.M., Lim, C.J. and Grace, J.R. (1997). The fluidized bed membrane reactor for steam methane reforming: Model verification and parametric study. *Chem. Eng. Sci.*, 52, 1609-1622.

- Armor, J.N. (1999). Review: The multiple roles for catalysis in the production of H₂. *Applied Catalysis A: General*, 176, 159-176.
- Bartholomew, C.H. (2001). Mechanisms of catalyst deactivation. *Applied Catalysis A: General*, 212, 17-60.
- Borrioni-Bird, C.E. (1996). Fuel cell commercialization issues for light-duty vehicle applications. *J Power Sources* 61, 33–48.
- Boyd, T., Grace, J.R., Lim, C.J. and Adris, A. (2005). Hydrogen from an internally circulating fluidized bed membrane reactor. *Int. J. Chem. Reactor Eng.* 3, A58.
- Brown, L.F. (2001). A Comparative Study of Fuels for Onboard Hydrogen Production for Fuel Cell Powered Automobiles. *Int. J of Hydrogen Energy*, 26, 381-397.
- Chen, C.X., Horio, M. and Kojima, T. (2000). Numerical simulation of entrained flow coal gasifiers. Part I: Modeling of coal gasification in an entrained flow gasifier. *Chem. Eng. Sci.*, 55, 3861-3874.
- Chen, Z., Grace, J.R., Lim, C.J. and Li, A. (2007). Experimental studies of pure hydrogen production in a commercialized fluidized-bed membrane reactor with SMR and ATR catalysts. *Int. J. Hydrogen Energy* 31, 2359-2366.
- Chen, Z., Po, F., Grace, J.R., Lim, C.J., Elnashaie, S.S.E.H., Mahecha-Botero, A., Rakib, M., Shirasaki, Y. and Yasuda, I. (2008). Sorbent enhanced/membrane-assisted steam methane reforming. *Chem. Eng. Sci.*, 63, 170-182.
- Chen, Z., Prasad, P., Yan, Y. and Elnashaie, S.S.E.H. (2003a). Simulation for steam-reforming of natural gas with oxygen input in a novel membrane reformer. *Fuel Process. Technol.*, 83, 235-252.
- Chen, Z., Yan, Y. and Elnashaie, S.S.E.H. (2003b). Modeling and optimization of a novel membrane reformer for higher hydrocarbons. *AIChE J.*, 49, 1250-1265.
- Chen, Z., Yan, Y. and Elnashaie, S.S.E.H. (2003c). Novel circulating fast fluidized-bed membrane reformer for efficient production of hydrogen from steam-reforming of methane. *Chem. Eng. Sci.*, 58, 4335-4349.
- Chen, Z., Yan, Y. and Elnashaie, S.S.E.H. (2004). Catalyst deactivation and engineering control for steam-reforming of higher hydrocarbons in a novel membrane reformer. *Chem. Eng. Sci.*, 59, 1965-1978.
- Crabtree, G.W., Dresselhaus, M.S. and Buchanan, M.V. (2004). The hydrogen economy. *Physics Today*, 57, 39-45.
- De Deken, J.C., Devos, E.F. and Froment, G.F. (1982). Steam reforming of natural gas. *Chemical Reaction Engineering, Am. Chem. Soc. Symp. Ser.*, Washington DC, 181-197.

- Dehkordi, A.M. and Memari, M. (2009). Compartment model for steam reforming of methane in a membrane-assisted bubbling fluidized-bed reactor. *Int. J of Hydrogen Energy*, 34, 1275-1291.
- Deshmukh, S.A.R.K., Heinricha, S., Mörl, L., van Sint Annaland, M. and Kuipers, J.A.M. (2007). Membrane assisted fluidized bed reactors: Potentials and hurdles. *Chem. Eng. Sci.*, 62, 416-436.
- Deshmukh, S.A.R.K., Laverman, J.A., van Sint Annaland, M. and Kuipers, J.A.M. (2005). Development of a membrane-assisted fluidized bed reactor. 2. Experimental demonstration and modeling for the partial oxidation of methanol. *Ind. Eng. Chem. Res.*, 44, 5966-5976.
- Dogan, M., Posarac, D., Grace, J.R., Adris, A.M. and Lim, C.J. (2003). Modeling of autothermal steam methane reforming in a fluidized bed membrane reactor. *International Journal of Chemical Reactor Engineering*, 1, A2.
- Elnashaie, S.S.E.H. and Elshishini, S.S. (1993). Modelling, simulation and optimization of industrial fixed-bed catalytic reactors. Gordon and Breach Science Publishers, Amsterdam.
- Ewan, B.C.R. and Allen, R.W.K. (2005). A figure of merit assessment of the routes to hydrogen. *International Journal of Hydrogen Energy*, 30, 809-819.
- Ferreira-Aparicio, P., Benito, M.J. and Sanz, J.L. (2005). New Trends in Reforming Technologies: from Hydrogen Industrial Plants to Multifuel Microreformers. *Catalysis Reviews*, 47, 491-588.
- Grace, J.R., Elnashaie, S.S.E.H. and Lim, C.J. (2005). Hydrogen production in fluidized beds with in-situ membranes. *International Journal of Chemical Reactor Engineering*, 3, A41.
- Grace, J.R., Lim, C.J., Adris, A.M., Xie, D., Boyd, T., Wolfs, W.M. and Brereton, C.M.H. (2006). Internally circulating fluidized bed membrane reactor system. U.S. Patent 7,141,231 B2.
- Hoang, D.L. and Chan, S.H. (2004). Modeling of a catalytic autothermal methane reformer for fuel cell applications *Applied Catalysis A: General*, 268, 207-216.
- Jarosch, K. and de Lasa, H.I. (1999). Novel riser simulator for methane reforming using high temperature membranes. *Chem. Eng. Sci.*, 54 1455-1460.
- Jin, W., Gu, X., Li, S., Huang, P., Xu, N. and Shi, J. (2000). Experimental and simulation study on a catalyst packed tubular dense membrane reactor for partial oxidation of methane to syngas. *Chem. Eng. Sci.*, 55, 2617-2625.
- Koroneos, C., Dompros, A., Roumbas, G. and Moussiopoulos, N. (2004). Life cycle assessment of hydrogen fuel production processes. *International Journal of Hydrogen Energy*, 29, 1443-1450.
- Mahecha-Botero, A., Boyd, T., Gulamhusein, A., Comyn, N., Lim, C.J., Grace, J.R., Shirasaki, Y. and Yasuda, I. (2008a). Pure hydrogen generation in a fluidized bed membrane reactor: Experimental findings. *Chem. Eng. Sci.*, 63, 2752-2762.

Mahecha-Botero, A., Chen, Z., Grace, J.R., Elnashaie, S.S.E.H., Lim, C.J., Rakib, M., Yasuda, I. and Shirasaki, Y. (2008b). Comparison of fluidized bed flow regimes for steam methane reforming in membrane reactors: A simulation study. *Chem. Eng. Sci.*, In review.

Mahecha-Botero, A., Grace, J.R., Lim, C.J., Elnashaie, S.S.E.H., Boyd, T. and Gulamhusein, A. (2009b). Pure hydrogen generation in a fluidized bed membrane reactor: Application of the generalized comprehensive reactor model. *Chem. Eng. Sci.*, In Review.

Mleczko, L., Ostrowski, T. and Wurzel, T. (1996). A fluidized-bed membrane reactor for the catalytic partial oxidation of methane to synthesis gas. *Chem. Eng. Sci.*, 51, 3187-3192.

Ogden, J.M. (2001). Review of small stationary reformers for hydrogen production. A report for the International Energy Agency Agreement on the Production and Utilization of Hydrogen. *Hydrogen from Carbon-Containing Materials*.

Patience, G.S., Chaouki, J., Berruti, F. and Wong, R. (1992). Scaling considerations for circulating fluidized bed risers. *Powder Technol.*, 72, 31-37.

Patil, C.S., van Sint Annaland, M. and Kuipers, J.A.M. (2005). Design of a novel autothermal membrane-assisted fluidized-bed reactor for the production of ultrapure hydrogen from methane. *Ind. Eng. Chem. Res.*, 44, 9502-9512.

Patil, C.S., van Sint Annaland, M. and Kuipers, J.A.M. (2006). Experimental study of a membrane assisted fluidized bed reactor for H₂ production by steam reforming of CH₄. *Chem. Eng. Res. Des.*, 84, 399-404.

Raich, B.A. and Foley, H.C. (1995). Supra-equilibrium conversion in palladium membrane reactors: Kinetic sensitivity and time dependence. *Appl. Catal.*, A 129, 167-188.

Rostrup-Nielsen, J.R. (1977). Hydrogen via steam reforming of naphtha. *Chemical Engineering Progress*, 9, 87.

Roy, S., Pruden, B.B., Adris, A., Grace, J.R. and Lim, C.J. (1999). Fluidized-bed steam-methane reforming with oxygen input. *Chem. Eng. Sci.*, 54, 2095-2102.

Scholz, W.H. (1993). Processes for industrial production of hydrogen and associated environmental effects. *Gas Sep. Purif.*, 7, 131-139.

Sehested, J. (2006). Four challenges for nickel steam-reforming catalysts. *Catalysis Today*, 111, 103-110.

Shu-Ren, H. (1998). Hydrocarbon steam-reforming process: feedstock and catalysts for hydrogen production in China. *Int. J. Hydrogen Energy*, 23, 315 - 319.

Snoeck, J.W., Froment, G.F. and Fowlest, M. (1997). Kinetic Study of the Carbon Filament Formation by Methane Cracking on a Nickel Catalyst. *J. Catalysis*, 169, 250-262.

Soliman, M.A., Elnashaie, S.S.E.H., Al-Ubaid, A.S. and Adris, A. (1988). Simulation of steam reformers for methane. *Chem. Eng. Sci.*, 43, 1801-1806.

Sun, G. and Grace, J.R. (1990). Effect of particle size distribution on the performance of fluidized bed reactors. *Chem. Eng. Sci.*, 45, 2187-2194.

Thomsen, V.B.E. (2000). LeChâtelier's principle in the sciences. *J. Chem. Educ.*, 77.

Tottrup, P.B. (1976). Kinetics of decomposition of carbon monoxide on a supported nickel catalyst. *Journal of Catalysis*, 42, 29–36.

Twigg, M.V. (1989). *Catalyst Handbook*, 2nd Edition. Wolfe Publishing Ltd, London, England.

Xu, J. and Froment, G.F. (1989a). Methane steam reforming, methanation and water-gas shift: I. Intrinsic kinetics. *AIChE J.*, 35, 88-96.

Xu, J. and Froment, G.F. (1989b). Methane steam reforming: II. Diffusional limitations and reactor simulation. *AIChE J.*, 35, 97-103.

Yates, J.G. (1983). *Fundamentals of fluidized-bed chemical processes*. Butterworth-Heinemann, London.

6. OTHER CONFIGURATIONS FOR STEAM REFORMING⁶

6.1. Introduction

In Chapters 3, 4 and 5 axially distributed analysis is performed for fluidized-bed membrane reformers. In this Chapter, studies on several other fluidized-bed configurations are presented to extend the possible applications of steam methane reforming.

In Section 6.2 an alternative steam reforming reactor configuration is summarized. Since hydrogen and carbon dioxide are the two major products of reforming, their removal drives the equilibrium forward as indicated by LeChatelier's Principle. The effect of hydrogen removal on chemical equilibrium is theoretically larger than removal of carbon dioxide because of the different stoichiometric coefficients. If enough carbon dioxide could be removed, however, a significant increase in equilibrium methane conversion is expected as demonstrated by Prasad and Elnashaie, (2004) and Johnsen *et al.*, (2006). Here a membrane reformer is simulated with a solid sorbent (CaO) mixed with the catalyst particles to capture some carbon dioxide, thereby improving reactor performance. Details about this modelling study not found below are provided elsewhere (Chen *et al.*, 2008). Additional details about the practical implementation of this sorbent-enhanced reforming technology, such as the design of a solids circulation loop in an experimental reactor, are described in Appendix F.

The membrane reformers tested in Chapters 3 to 5 use a vacuum pump in the permeate side to reduce the partial pressure of hydrogen. A different strategy is to introduce a sweep gas such as steam or nitrogen on the permeate side to dilute the hydrogen molecules inside the membranes keeping the total permeate pressure constant. Section 6.3 examines the effect of these two hydrogen removal strategies in a two-dimensional fast fluidized bed. The simulations were two-dimensional to find cases where horizontal variation can be neglected.

⁶ *An extended version of Section 6.2 was published as: Chen, Z., Po, F., Grace, J.R., Lim, C.J., Elnashaie, S.S.E.H., Mahecha-Botero, A., Rakib, M., Shirasaki, Y. and Yasuda, I. (2008). "Sorbent enhanced/membrane-assisted steam methane reforming". *Chemical Engineering Science*, 63, 170-182.*

6.2. Sorbent-Enhanced/Membrane-Assisted Steam-Methane Reforming

This section considers a circulating fluidized bed membrane reformer coupled with a catalyst/sorbent regenerator. Sorbent enhancement combined with membranes provides high hydrogen yields. In addition, since carbonation is exothermic, with its heat of reaction similar in magnitude to that of the endothermic heat of reaction of the net reforming reactions, CO₂ capture could provide much of the heat needed in the reformer. The parameter values used in these simulations are listed in Table 6.1. The model presented in section 5.2.2 is utilized in this section. Some of its assumptions are:

- Unidirectional flow.
- Single pseudo-phase in fast fluidization regime.
- Terms such as feed distribution, sorption of species and solid chemisorption are not considered. Effectiveness factors and catalyst activity are assumed to be 100%, i.e. $\Omega_{j_{cat,\phi}} \cdot a_{j_{cat,\phi}} = 1.0$. Reaction kinetics are listed in Table 5.2.
- Steady state operation.

The overall heat needed for the process would then be provided in a separate calciner, acting as a sorbent regenerator. The reaction between CO₂ and CaO sorbent in the CO₂ carbonator is:

Carbonation (CO₂ capture): **(R1)**



The other reforming reactions are explained in Table 5.2. The chemical kinetics and parameters of the carbonation reaction can be obtained (Bhatia and Perlmutter, 1989; Chen, 2004) from:

$$r_1 = k_1 (1 - X_{\text{CaO}})^{0.67} (C_{\text{CO}_2} - C_{\text{eq,CO}_2}) \quad \text{(6.1)}$$

where $k_1 = 1.6752 \times 10^{-2} \cdot e^{\left(\frac{-1748.3}{R.T}\right)} (\text{m}^3 \cdot \text{mol}^{-1} \cdot \text{s}^{-1})$.

Table 6-1. Basis for kinetic reactor simulation

Operating parameter and conditions	Value	Unit
Reactor operating absolute pressure	1000	kPa
Reactor feed temperature	823	K
Steam-to-carbon feed ratio	3.0	mol/mol
Oxygen-to-carbon feed ratio	0.35	mol/mol
Permeate pressure	30	kPa
Specific membrane area per unit reactor volume	200	m ² /m ³
Membrane thickness	25	μm
Feed rate of methane	4.465	kmol/h
Mean catalyst particle diameter	100	μm
Catalyst particle density	2270	kg/m ³
Superficial gas velocity (based on free cross-sectional area)	1.7	m/s
Total volumetric solid fraction in reformer	0.05	v/v
Volumetric feed ratio of CaO sorbent to total solids	0.1	v/v
Free cross-sectional area	0.028	m ²
CaO sorbent mean particle diameter	100	μm
CaO particle density (porous)	1568	kg/m ³

6.2.1. Predictions and Discussion

Isothermal Simulation

The effects of CO₂ removal by CaO sorbent and hydrogen removal via membranes on reformer performance are compared under isothermal conditions based on four cases:

- No membranes and no sorbent;
- Sorbent-enhancement, but no membranes;
- Membranes present without sorbent;
- Both sorbent enhancement and membranes present.

When neither hydrogen membranes nor CaO sorbent are present, after a short entrance region, the methane conversion reaches a level controlled by thermodynamic equilibrium, as shown in Figure 6.1a, with a constant carbon dioxide yield as seen in Figure 6.1b. When CaO sorbent is present, the CO₂ yield in the reformer first increases and then decreases, passing through a maximum yield near the reactor entrance, as shown in Figure 6.1b. This is due to the fast reforming and oxidation reactions, leading to rapid generation of CO₂ near the entrance, followed by slower continuous CO₂ capture by CaO sorbent. With CaO sorbent present, the methane conversion increases, since the removal of CO₂ from the reversible steam reforming

system “breaks” the thermodynamic equilibrium barrier, allowing the reactions to advance further to produce more hydrogen and CO₂. When coupled with hydrogen membranes, hydrogen production is predicted to be significantly enhanced. As a result, both pure hydrogen production in Figure 6.2a and the fraction of hydrogen removed by membranes (defined as the pure hydrogen permeation rate divided by the total hydrogen production rate) are increased in Figure 6.2b.

When both CaO sorbent and hydrogen membranes are employed, the exit methane conversion can reach 100% (Figure 6.1a), while the exit CO₂ yield in the reformer approaches zero (Figure 6.1b) because almost all of the CO₂ is converted to CaCO₃, resulting in a higher CO₂ yield in the catalyst regenerator (Figure 6.1c). This suggests that by-product CO₂ in the regenerator could be produced with high purity, improving the economics and enhancing the environmental benefits of the process.

With hydrogen membranes present, CO₂ capture by CaO sorbent is enhanced, as shown in Figures 6.1c and d, because more CO₂ is generated via the shift of the reversible reforming reactions. However, due to the large mass ratio of CaO sorbent to gas feed in the reformer, the conversion of CaO is low after a single sorbent circuit (between the reformer and regenerator). Note that in the kinetic reactor model simulations, both the catalyst and CaO sorbent are assumed to be fully regenerated before being recycled to the reformer.

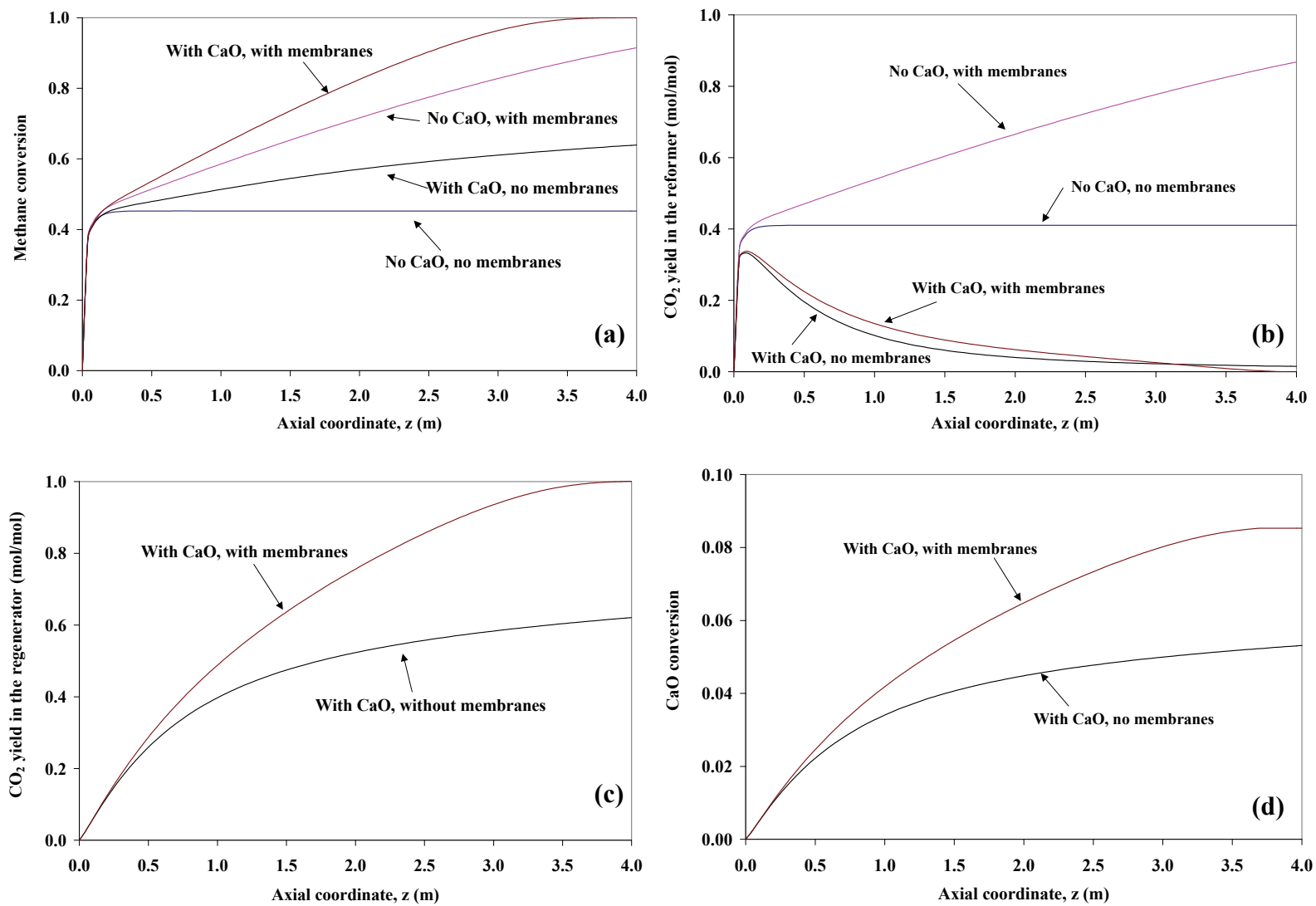


Figure 6.1. Effect of CO₂ capture on reformer performance. For conditions, see Table 6.1. (a) Isothermal methane conversion; (b) Isothermal CO₂ yield in the reformer; (c) Isothermal CO₂ yield in the regenerator; (d) Isothermal CaO conversion.

Non-Isothermal Simulation

In this section, the effect of CO₂ capture on the reformer performance is investigated to predict the thermal effect of the exothermic carbonation reaction on the reactor temperature. The effect of CaO sorbent feed ratio on the reformer performance is also studied by varying the volumetric ratio of CaO sorbent to total solids (catalyst plus sorbent), (parameter *b* in Figure 6.2 and 6.3) from 0 to 0.1 v/v. Figures 6.2c, 6.2d and 6.3 show the predictions for the non-isothermal cases (adiabatic reforming) with hydrogen membranes and different CaO feed ratios.

Figure 6.2c shows that the temperature in the reformer increases quickly near the entrance of the reformer because of fast exothermic carbonation. However, for low feed ratios of CaO to total solids, e.g., *b*=0 or 0.01 v/v, the reformer temperature decreases along the rest of reactor length due to endothermic steam reforming, promoted by continuous removal of hydrogen.

If the CaO sorbent volumetric feed ratio is high, e.g., 0.05 or 0.1 v/v, the reformer temperature is predicted to resume its increase along the reformer after initial oxidation and reforming due to the *in situ* supply of heat by the exothermic carbonation reaction, as shown in Figure 6.2d. The heat supply increases along the reactor length and also with increasing CaO sorbent feed ratio. When the CaO sorbent feed ratio is 0.1 v/v or higher, there is no further increase of heat supply from the carbonation of CaO because the methane conversion has already reached 100% (see Figure 6.3a), and essentially all the CO₂ has already been removed by the CaO (Figure 6.3b).

With increasing ratio of calcium sorbent to total solids, the reformer temperature (Figure 6.2c), methane conversion (Figure 6.3a), CO₂ yield in the regenerator and fraction of pure hydrogen removed by membranes (Figure 6.3d) all increase, whereas the CO₂ yield in the reformer (Figure 6.3b) and the CaO conversion (Figure 10.3c) are both predicted to decrease.

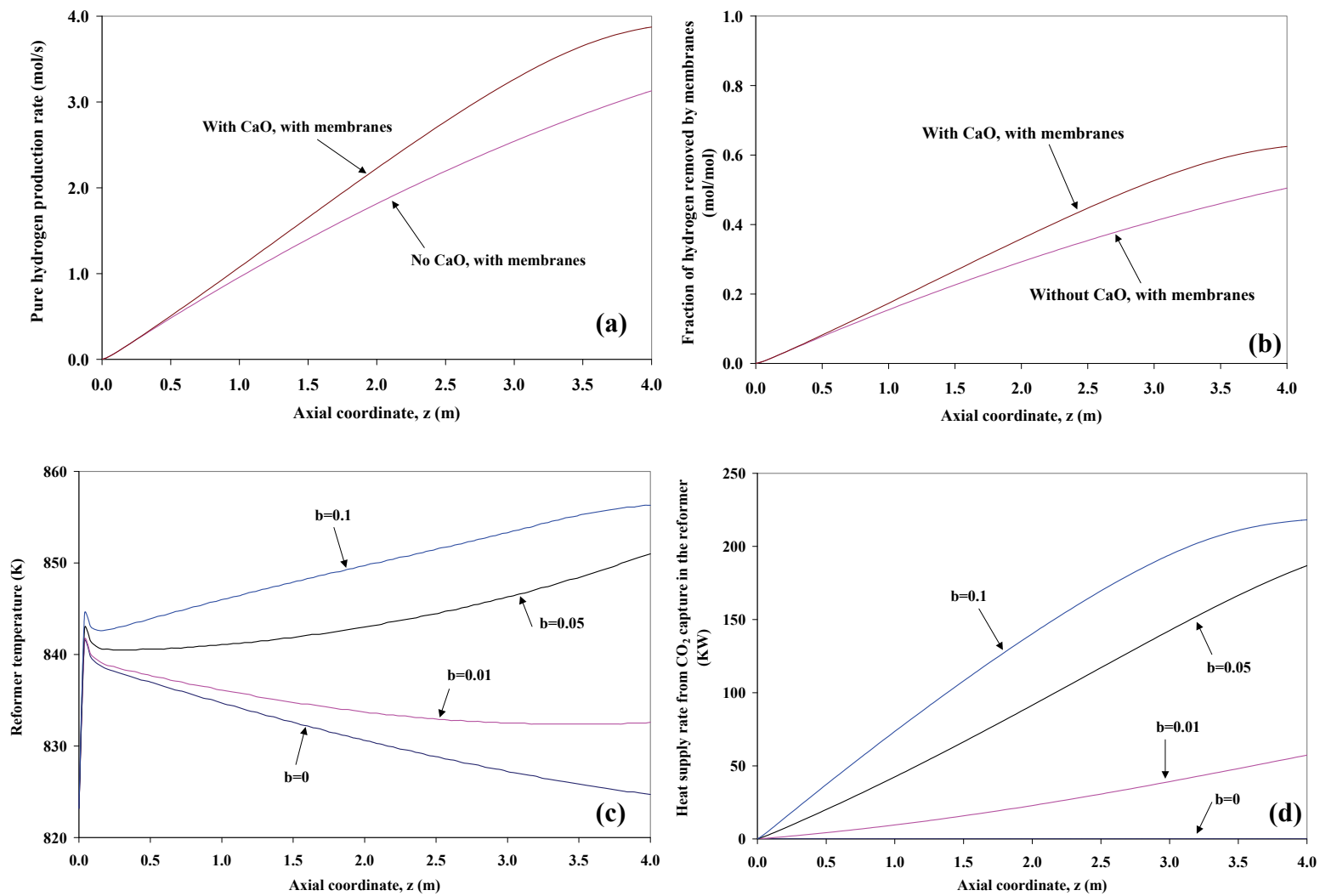


Figure 6.2. Effect of CO₂ capture on reformer performance. For conditions, see Table 6.1. (a.) Isothermal pure hydrogen production rate; (b.) Isothermal fraction of hydrogen removed by membranes; (c.) Non-isothermal reformer temperature. (d.) Non-isothermal heat supply rate from CO₂ capture. The parameter “ b ” is the ratio of CaO sorbent to total solids.

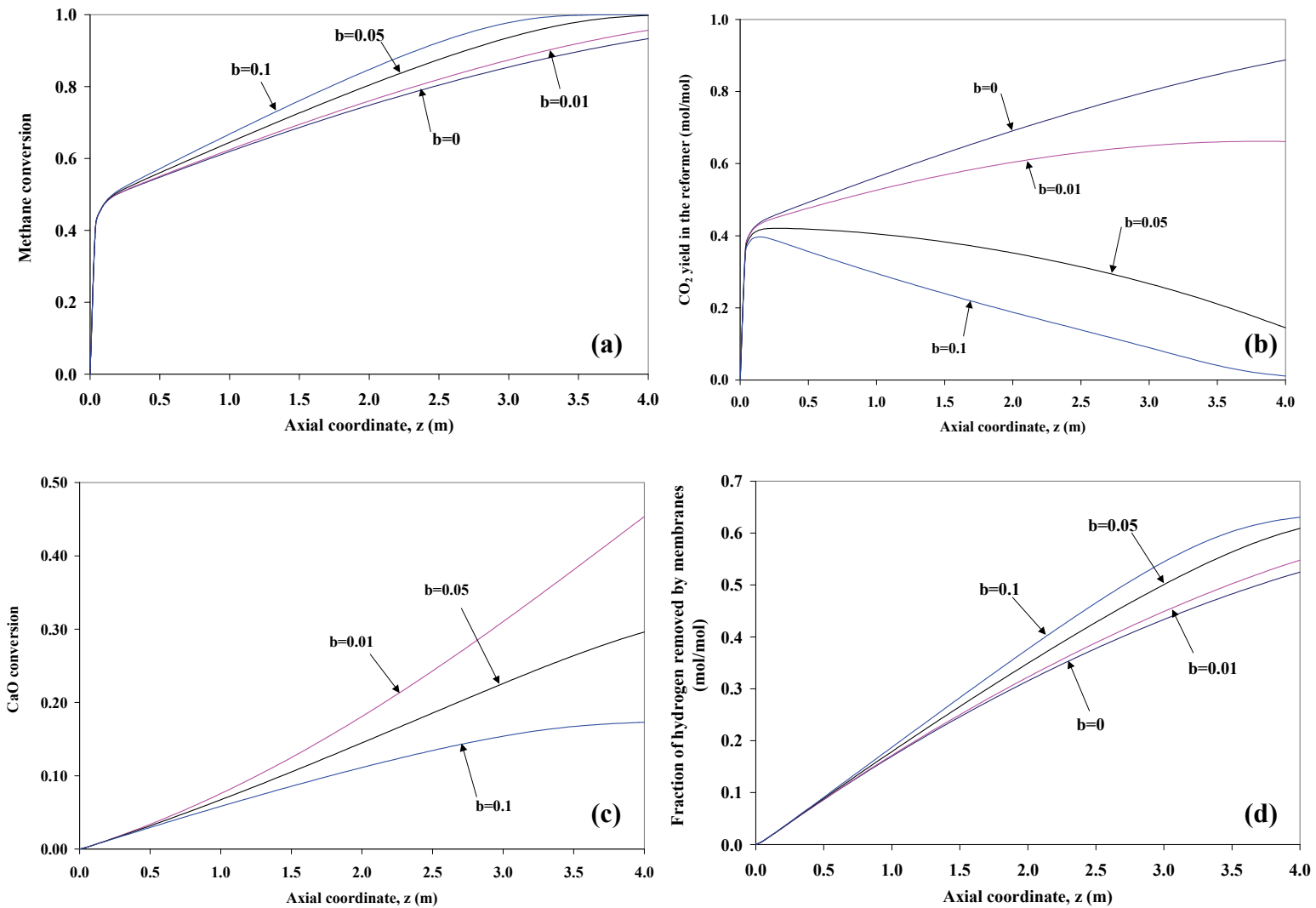


Figure 6.3. Effect of CO₂ capture on reformer performance. For conditions, see Table 6.1. (a.) Non-isothermal methane conversion; (b.) Non-isothermal CO₂ yield in the reformer; (c.) Non-isothermal CaO conversion. (d.) Non-isothermal fraction of hydrogen removed by membranes. The parameter “ b ” is the ratio of CaO sorbent to total solids.

6.3. 2-D Modelling of a Fast Fluidization Reactor

Chen *et al.* (2003a, b, c; 2004) and Prasad and Elnashaie (2004) proposed a novel configuration of a fluidized-bed membrane reactor for the production of hydrogen which included a fast fluidized bed membrane reformer. In this section, a 3 m tall reactor with a $4 \times 10^{-4} \text{ m}^2$ rectangular channel is simulated under fast fluidization conditions. The reactor is fed with a mixture of hydrocarbon and steam with a steam-to-carbon ratio of 3.0 at 600°C and a superficial gas velocity of 3 m/s. The reactor pressure is 0.5 MPa, and the permeate side of the membranes is at 0.06 MPa. The reactor is assumed to include a panel of stacked flat palladium alloy membranes to remove hydrogen and break the thermodynamic barrier to enhance the efficiency of the process (see Figure 6.4). The catalyst is composed of 15% Ni, 85% Alumina with an average particle size of 100 microns and a 2270 kg/m^3 of density. The steam-to-carbon molar feed ratio is maintained at 3.0. A solids circulation rate of $226 \text{ Kg.m}^{-2}.\text{s}^{-1}$ is calculated implementing the methodology of Pugsley and Berruti (1996). A two-dimensional model is used to investigate the horizontal variation of the state variables.

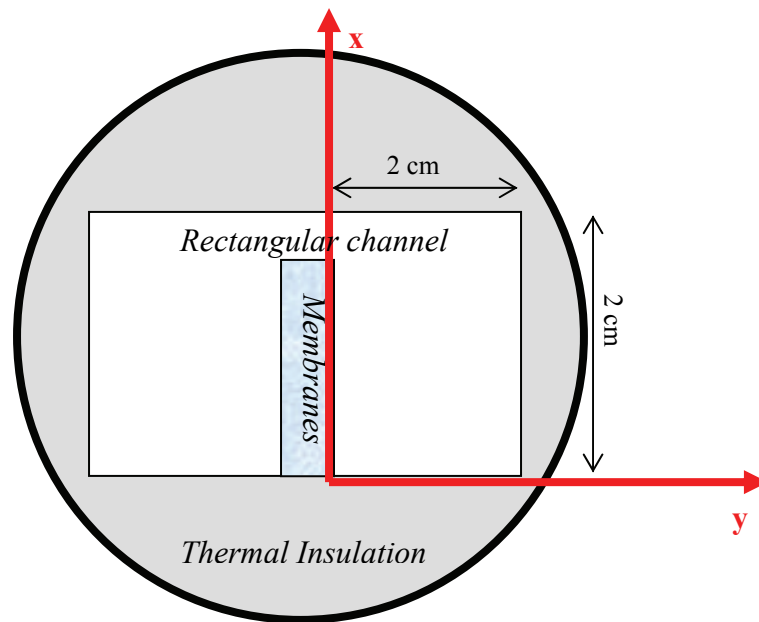


Figure 6.4. Reactor cross-section (Not to scale).

6.3.1. Model Implementation

The model developed in Section 1.2 is simplified to a single phase configuration, and it is coded in *COMSOL Multiphysics* coupled with *Matlab*, with *Matlab scripting* and *COMSOL* routines.

The model uses a conservative *diffusion-reaction mole balance* accounting for the change in number of moles and 2-D species diffusion. All 2-D plots correspond to the zy-plane. It also adopts a conservative *conduction-convection energy balance* accounting for the heat capacity of the solids and 2-D heat conduction. Selective membrane diffusion of H₂ is considered in the boundary conditions. Danckwerts boundary conditions (Danckwerts, 1953) are employed at the bottom and top of the channel. The model developed in Section 1.2 and Chapter 4 is simplified based on:

- Two-dimensional geometry with membranes on the left side.
- Single pseudo-phase in fast fluidization regime.
- Terms such as feed distribution, sorption of species and solid chemisorption are not considered. Effectiveness factors and catalyst activity are assumed to be 100%, i.e. $\Omega_{j_{cat,\phi}} \cdot a_{j_{cat,\phi}} = 1.0$. Steam reforming kinetics are as given in Tables 4.2 and 4.3.
- Steady state operation.

Axial symmetry is assumed to simulate the square geometry in two dimensions (see Figures 6.4 and 6.5). The model simulates “half” the reactor starting from the membrane surface up to the reactor wall. Note that the zx-plane is adopted as the plane of symmetry. In all two-dimensional figures of this section, the left side corresponds to the membrane surface, whereas the right side corresponds to the reactor wall.

Iterative numerical stabilization techniques were used to solve the model. Three parametric solvers were employed to achieve convergence:

- The program gradually increases the reaction rates (based on the steam reforming kinetics from Tables 4.2 and 4.3). A simulation is performed with all reaction rates zero, and the solution is stored. Then, the model is solved with increasing reaction rates (by increasing the catalyst activity) using the previous solution as an initial guess. This process is automatically repeated until the program reaches the desired values of the kinetic parameters.

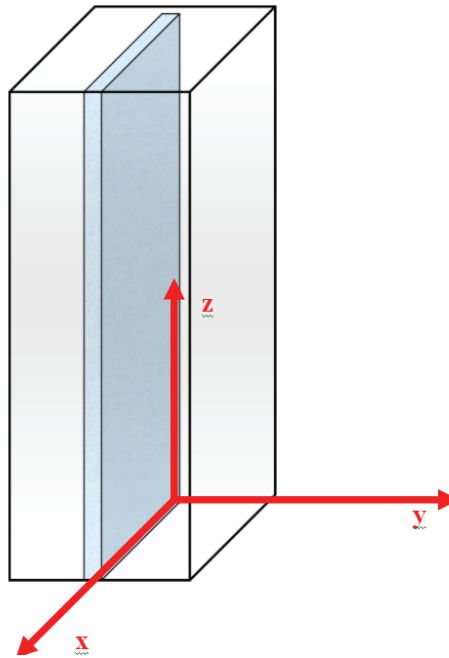


Figure 6.5. Membrane reactor (Not to scale). Note that the zx -plane is adopted as the plane of symmetry.

- The program gradually increases the superficial gas velocity to improve program convergence as described above.
- The program gradually increases the reactor pressure (i.e. set in a momentum balance boundary condition) to improve program convergence as described above.

The gas velocity profile was estimated based on the ideal gas law accounting for changes in number of moles, temperature and pressure. The possibility of utilizing the *COMSOL* Navier-Stokes based *non-isothermal flow momentum balance* was also explored, but the predicted parabolic velocity profiles were not considered because they appear unrealistic since they ignore turbulence and the effect of solid particles on the flow behaviour.

6.3.2. Discussion

Two cases were investigated with this model to determine the effect of different membrane fluxes on the reactor performance:

6.3.2.1. Membrane gas removal via sweep gas.

The first case is presented in Figures 6.6 to 6.9 corresponding to membrane hydrogen removal

using sweep-gas. In this case nitrogen is used on the membrane permeate side to significantly reduce the partial pressure of hydrogen (0.1 MPa total membrane pressure). Figure 6.6 depicts the two-dimensional variation in hydrogen concentration inside the reactor. One-dimensional traces are presented in Figure 6.8. Hydrogen is quickly produced at the bottom of the bed, reaching $\sim 27 \text{ mol/m}^3$ within the initial 0.2 meters of height. Hydrogen is continuously removed from the left side, and a drop in its concentration to below 17 mol/m^3 is predicted at the top-left. Given the high membrane flux, some radial variation is observed. The methane overall conversion reaches $\sim 63\%$ as seen in Figures 6.7 and 6.9.

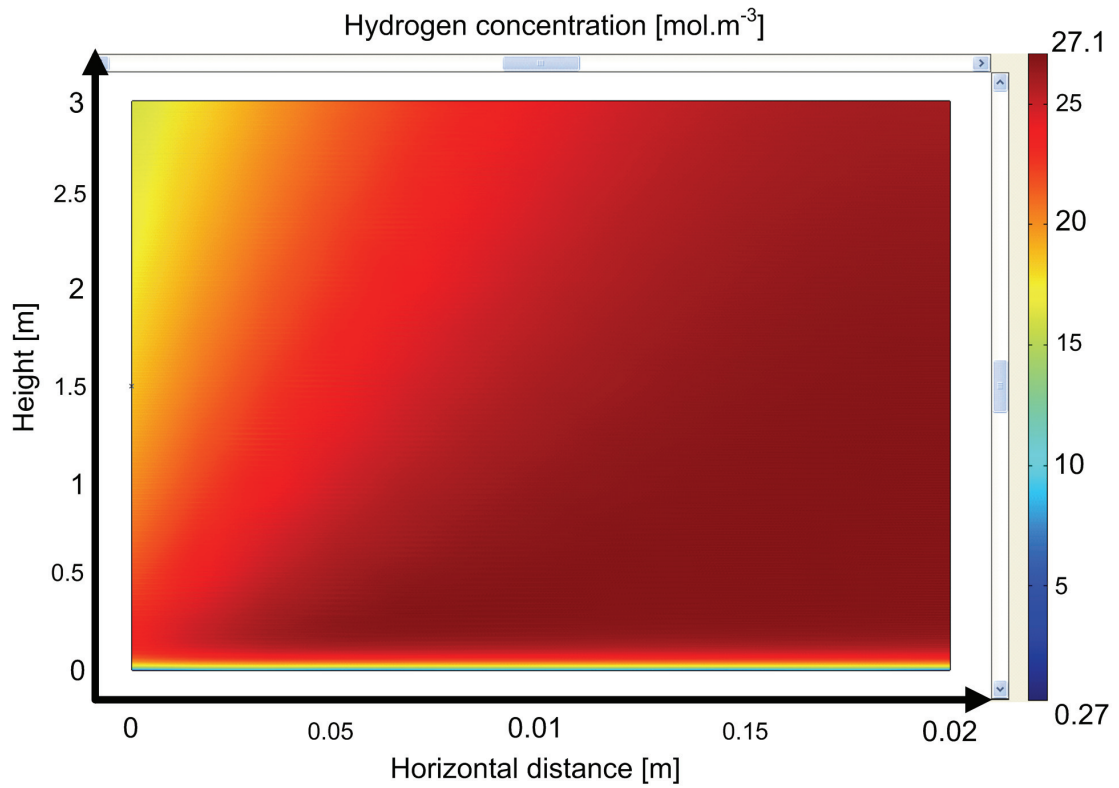


Figure 6.6. 2-D H₂ concentration profile using sweep gas (Geometry not to scale).

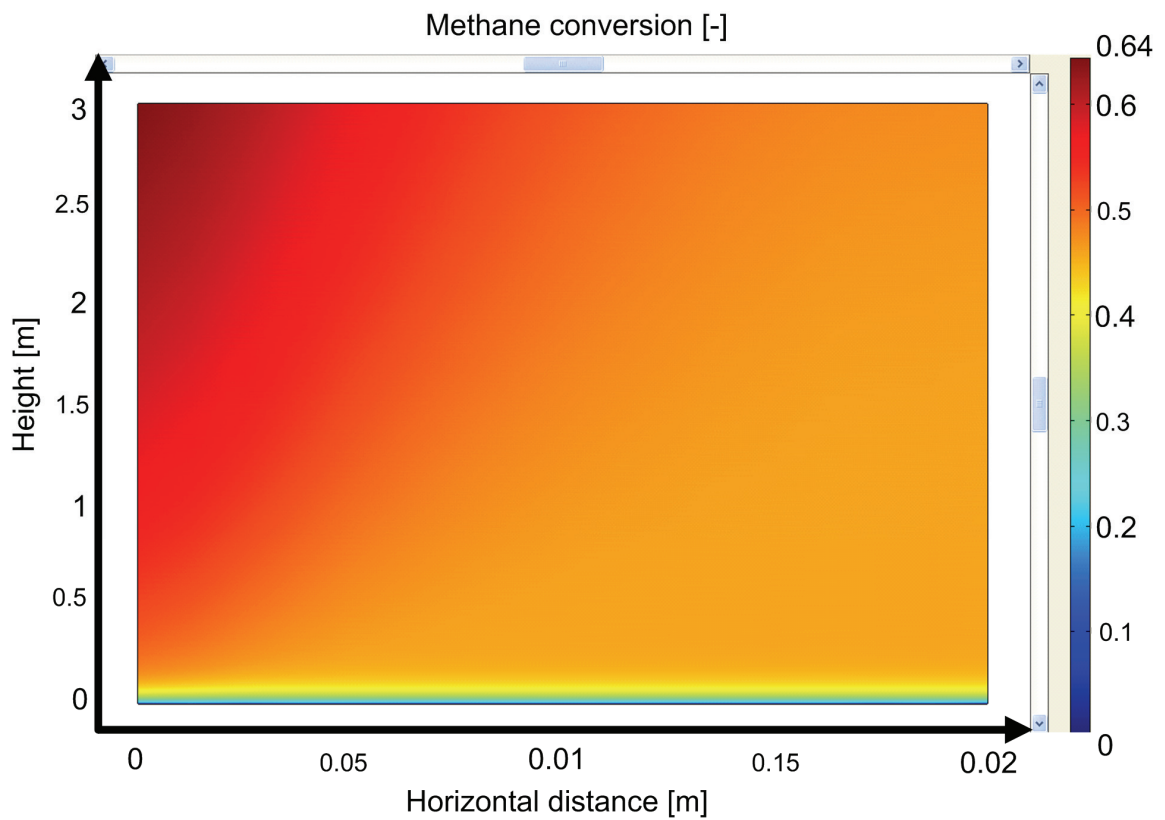


Figure 6.7. 2-D local conversion profile using sweep gas (Geometry not to scale).

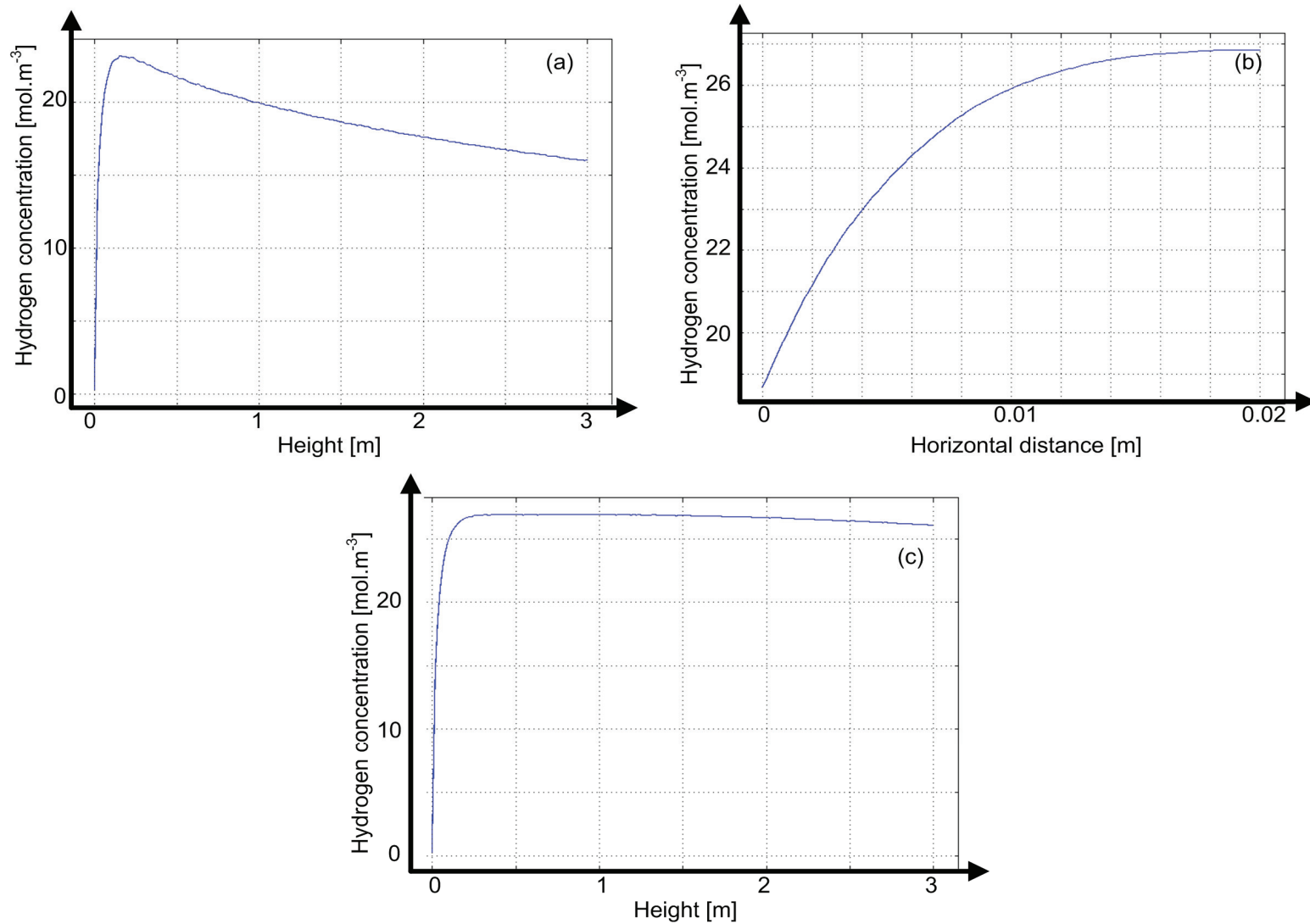


Figure 6.8. Predicted local axial and radial H₂ concentration profiles using sweep gas. (a.) Axial H₂ concentration profile. H₂ concentration vs height (at y = 0 m). (b.) Horizontal H₂ concentration profile. H₂ concentration vs horizontal distance (at z = 1.5 m). (c.) Axial H₂ concentration profile. H₂ concentration vs height (at y = 20 mm).

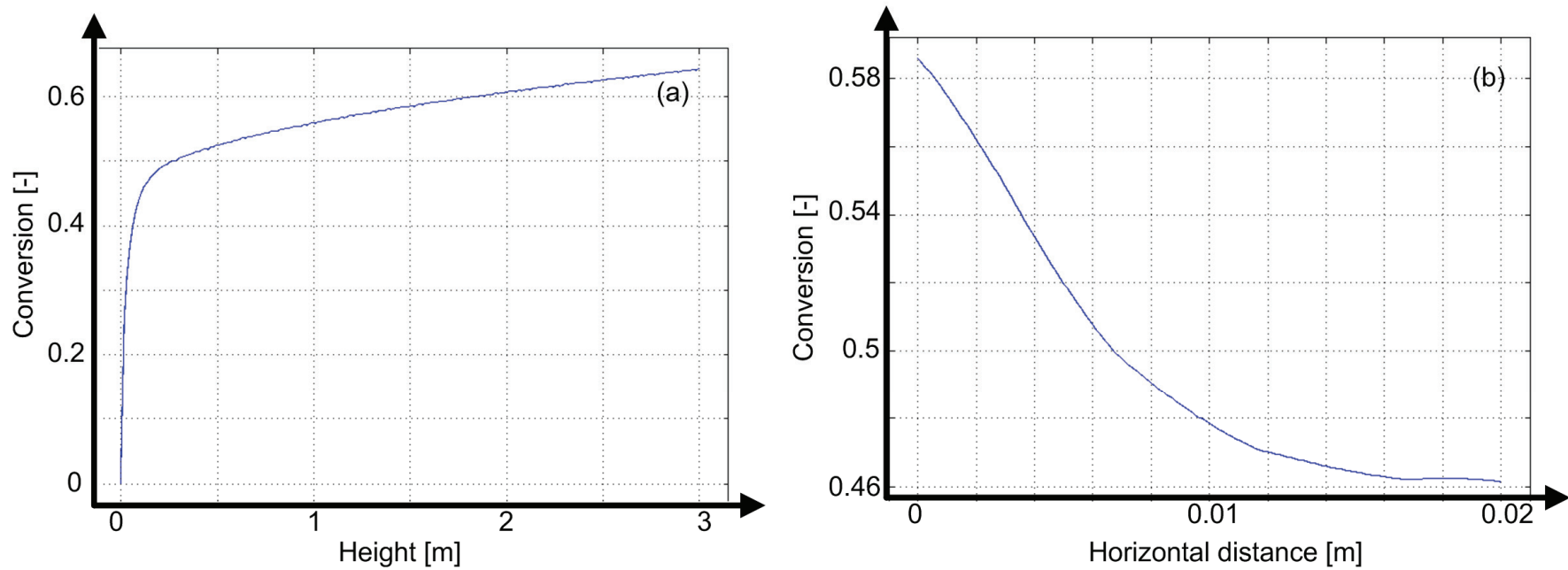


Figure 6.9. Predicted local axial and radial conversion profiles using sweep gas. (a.) Axial conversion profile. Conversion vs height (at $y = 0$ m). (b.) Horizontal conversion profile. Conversion vs horizontal distance (at $z = 1.5$ m).

6.3.2.2. Membrane removal via vacuum.

Figures 6.10 to 6.13 present simulation results with vacuum instead of sweep gas applied to the membranes. In this case the total membrane pressure is equal to the hydrogen partial pressure since it is the sole species found inside the membranes. The total pressure on the membrane permeate side is 60 kPa. Some reduction in membrane removal is predicted compared to sweep gas simulations. The overall methane conversion drops to ~52% as seen in Figures 6.11 and 6.13. Furthermore, the radial variation practically disappears compared to what was found previously when sweep gas was included. The model ignores the mass transfer resistance on the membrane side. In practice, the flow in the permeate side is likely to be laminar, and the mass transfer resistance significant (i.e. reducing the membrane flux).

6.4. Conclusions

In **Section 6.2** it is demonstrated that sorbent-enhancement and membrane-hydrogen-withdrawal can complement each other to further improve the performance of fluidized bed membrane reactors for hydrogen production. Membranes are shown to be somewhat more effective for an equal molar removal rate of H₂ or CO₂, but hydrogen yield can benefit significantly from either membranes or sorbents. The most favourable results would occur if sorption enhancement could be coupled with membranes. Since carbonation is exothermic, the sorbents could also assist with supplying the heat needed for the endothermic reforming. In addition to improving the yield of hydrogen, the process heat could then be supplied to a sorbent regenerator. Moreover, this option could facilitate sequestration of CO₂, the main greenhouse gas.

Section 6.3 presents two-dimensional simulations for a fast fluidized membrane reactor. It is predicted that reactor performance increases when sweep gas is utilized instead of vacuum. Furthermore, it is predicted that horizontal variation is very small for vacuum membrane hydrogen removal due to the limited membrane flux. It can be concluded that for the narrow geometry considered and low membrane permeation, a one-dimensional model is appropriate. In reality, the horizontal variation is expected to be even smaller than predicted due to horizontal solids mixing. Although sweep gas allows for lower partial pressure of permeate hydrogen and higher predicted methane conversions, it is associated with the large extra cost of generating/purifying the sweep gas.

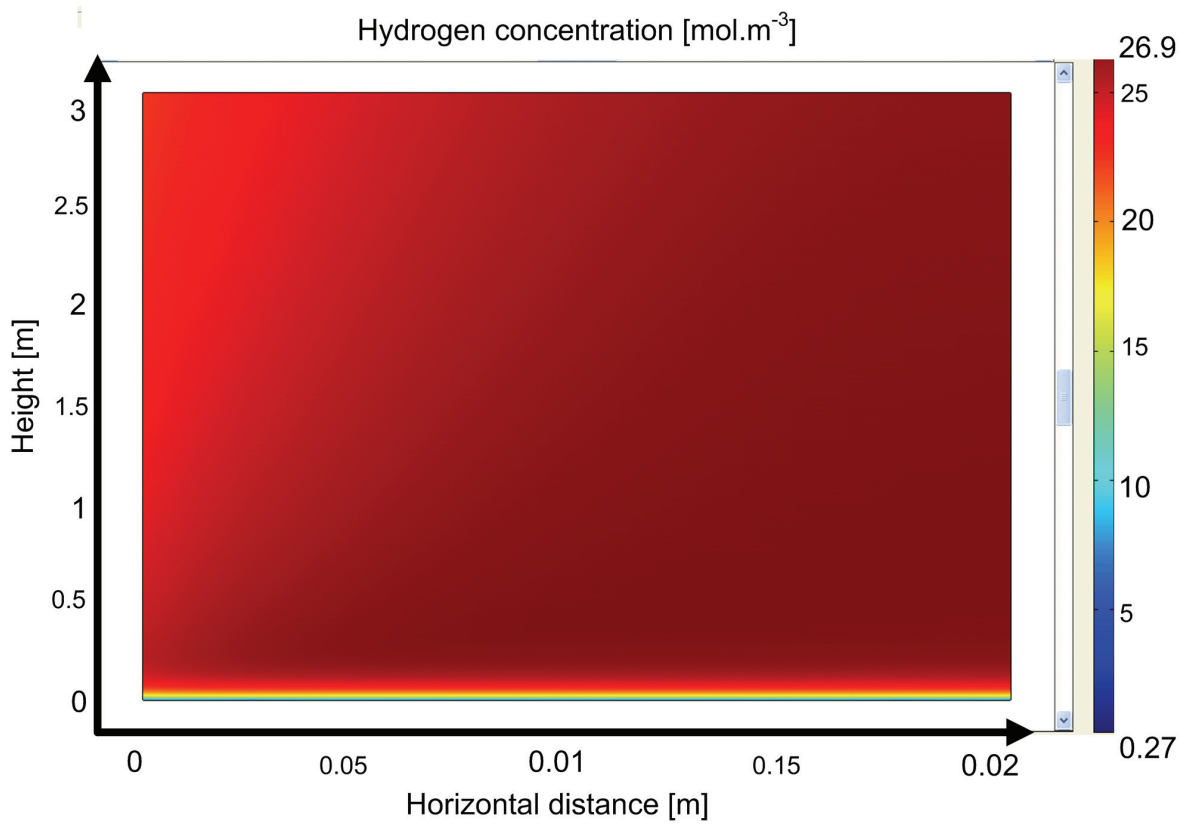


Figure 6.10. 2-D H₂ concentration profile using vacuum (Geometry not to scale).

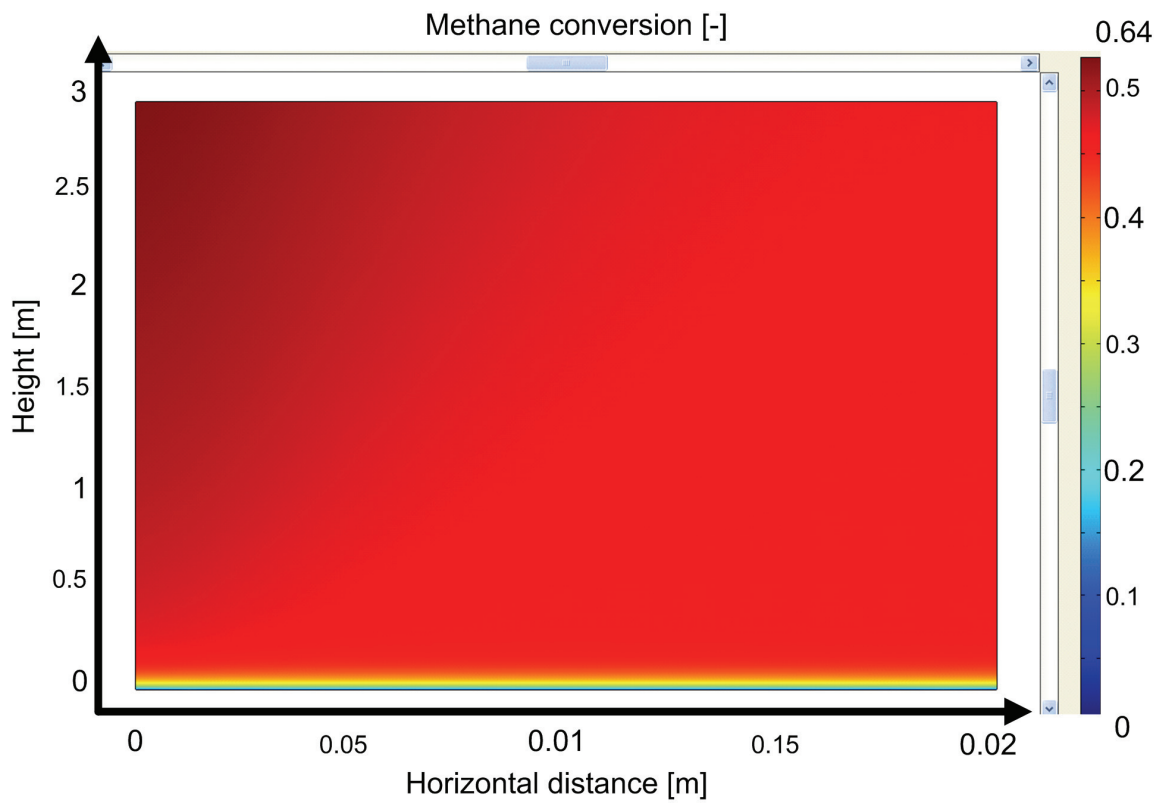


Figure 6.11. 2-D local conversion profile using vacuum (Geometry not to scale).

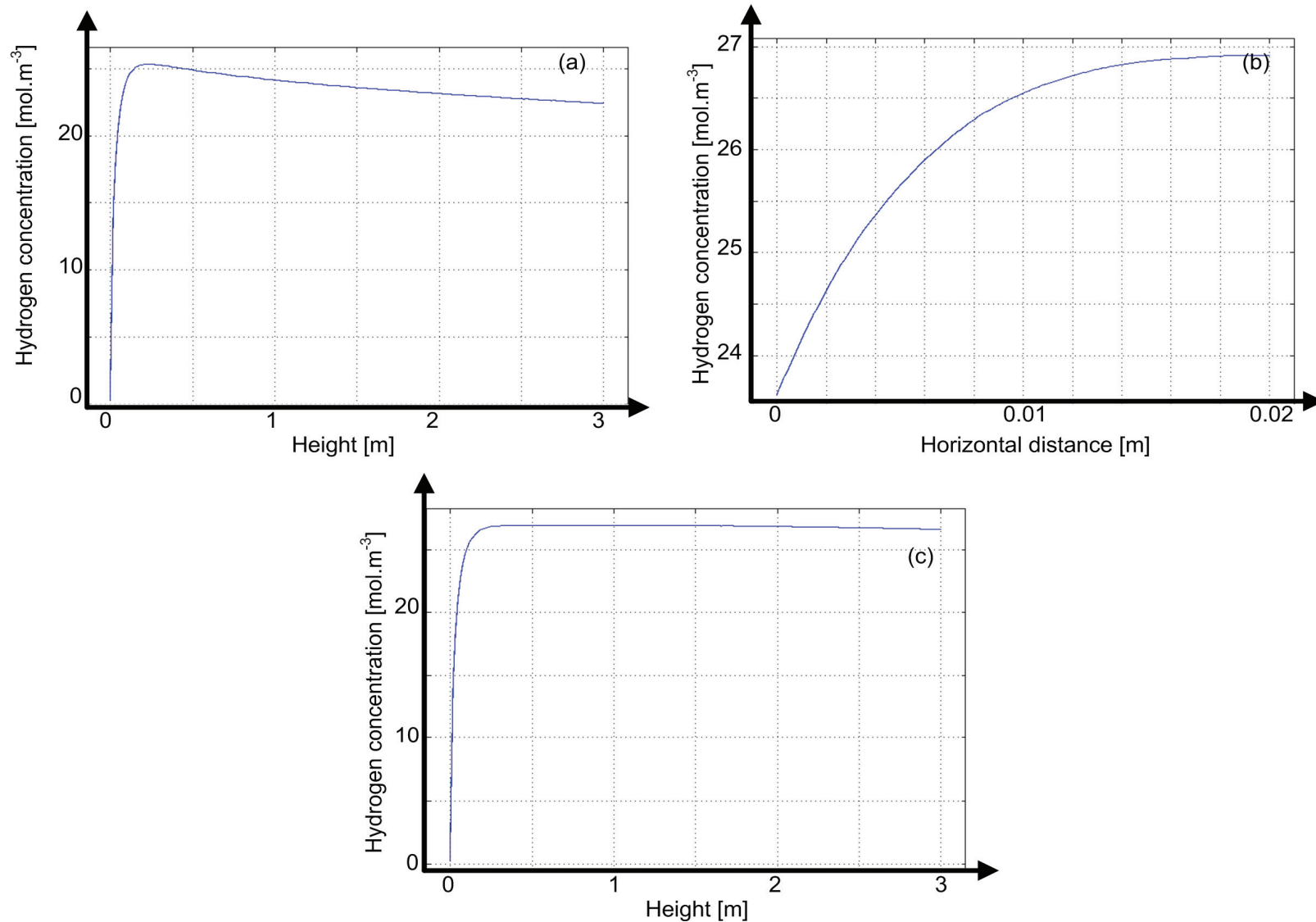


Figure 6.12. Predicted local axial and radial H₂ concentration profiles using vacuum. (a.) Axial H₂ concentration profile. H₂ concentration vs height (at y = 0 m). (b.) Horizontal H₂ concentration profile. H₂ concentration vs horizontal distance (at z = 1.5 m). (c.) Axial H₂ concentration profile. H₂ concentration vs height (at y = 20 mm).

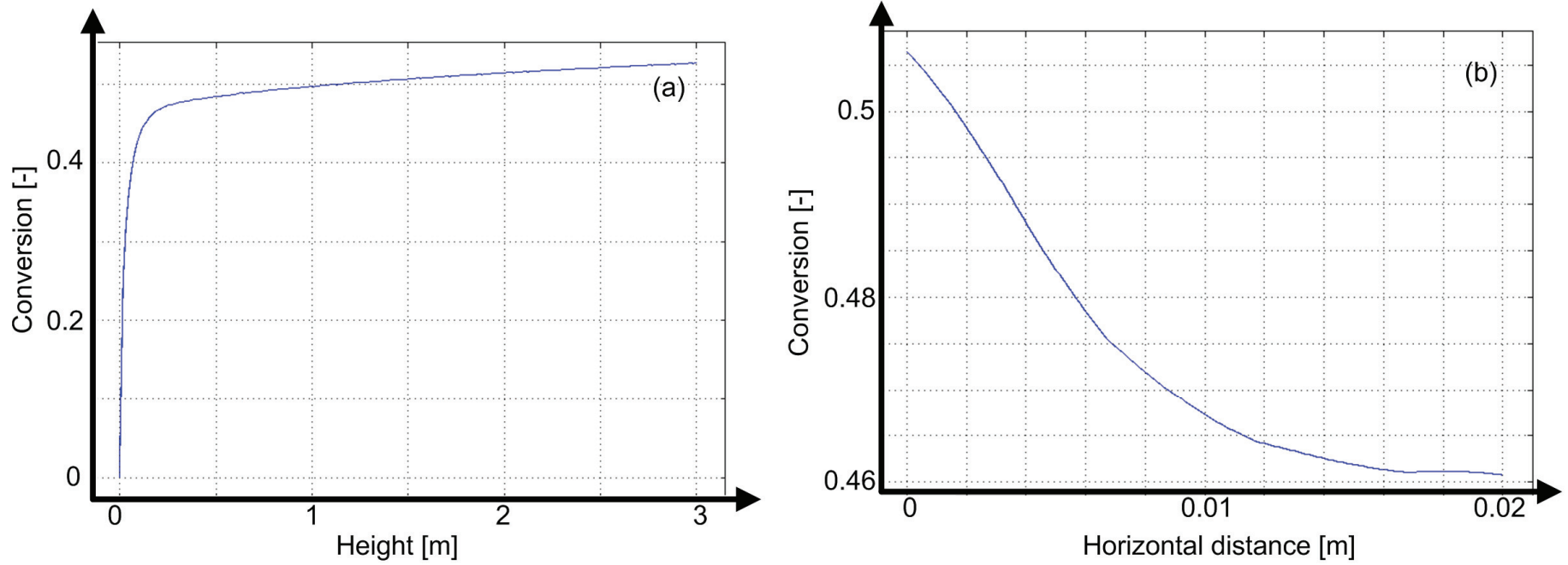


Figure 6.13. Predicted local axial and radial conversion profiles using vacuum. (a.) Axial conversion profile. Conversion vs height (at $y = 0$ m). (b.) Horizontal conversion profile. Conversion vs horizontal distance (at $z = 1.5$ m).

6.5. References

- Bhatia, S.K. and Perlmutter, D.D. (1989). Effect of the Product Layer on the Kinetics of the CO₂-Lime Reaction. *AIChE J.*, 35, 88.
- Chen, Z. (2004). A novel circulating fluidized bed membrane reformer for efficient pure hydrogen production for fuel cells from higher hydrocarbons. Auburn, Ph.D. Thesis, Auburn University.
- Chen, Z., Po, F., Grace, J.R., Lim, C.J., Elnashaie, S.S.E.H., Mahecha-Botero, A., Rakib, M., Shirasaki, Y. and Yasuda, I. (2008). Sorbent enhanced/membrane-assisted steam methane reforming. *Chem. Eng. Sci.*, 63, 170-182.
- Chen, Z., Prasad, P., Yan, Y. and Elnashaie, S.S.E.H. (2003a). Simulation for steam-reforming of natural gas with oxygen input in a novel membrane reformer. *Fuel Process. Technol.*, 83, 235-252.
- Chen, Z., Yan, Y. and Elnashaie, S.S.E.H. (2003b). Modeling and optimization of a novel membrane reformer for higher hydrocarbons. *AIChE J.*, 49, 1250-1265.
- Chen, Z., Yan, Y. and Elnashaie, S.S.E.H. (2003c). Novel circulating fast fluidized-bed membrane reformer for efficient production of hydrogen from steam-reforming of methane. *Chem. Eng. Sci.*, 58, 4335-4349.
- Chen, Z., Yan, Y. and Elnashaie, S.S.E.H. (2004). Catalyst deactivation and engineering control for steam-reforming of higher hydrocarbons in a novel membrane reformer. *Chem. Eng. Sci.*, 59, 1965-1978.
- Danckwerts, P.V. (1953). Continuous flow systems: Distribution of residence times. *Chem. Eng. Sci.*, 2, 1-13.
- Johnsen, K., Ryu, H.J., Grace, J.R. and Lim, C.J. (2006). Sorption-enhanced steam reforming of methane in a fluidized bed reactor with dolomite as CO₂-acceptor. *Chem. Eng. Sci.*, 61, 1195-1202
- Prasad, P. and Elnashaie, S.S.E.H. (2004). Novel circulating fluidized-bed membrane reformer using carbon dioxide sequestration. *Ind. Eng. Chem. Res.*, 43, 494-501.
- Pugsley, T. and Berruti, F. (1996). A predictive hydrodynamic model for circulating fluidized bed risers. *Powd. Technol.*, 89, 57-69.

7. MODELLING OF OXY-CHLORINATION FLUIDIZED-BED REACTOR FOR PRODUCTION OF ETHYLENE DICHLORIDE ⁷

7.1. Introduction

Oxychlorination of hydrocarbons designates a set of chemical transformations in which oxygen and hydrogen chloride react with a hydrocarbon in the vapour phase to produce a chlorinated hydrocarbon and water (Magistro and Cowfer, 1986). Oxychlorination is one of the most industrially important partial oxidation processes. Other partial oxidation processes which have led to fluidized bed processes include the oxidation of n-butane to maleic anhydride, propylene to acrylonitrile, and o-xylene to phthalic anhydride (Allen and Butner, 2002). The oxychlorination process plays a vital role in the synthesis of polyvinyl chloride (PVC).

In this chapter a case study for the application of the comprehensive model is presented. An industrial scale fluidized-bed reactor simulated based on the model described in Section 1.2 using the simplifications indicated in Section 7.3.1.

7.2 Overview of the PVC Production Process

PVC is one of the largest commodity chemicals produced worldwide (Lakshmanan *et al.*, 1999). Its monomer (vinyl chloride) was at an earlier stage produced by reacting hydrogen chloride and acetylene using a mercuric chloride catalyst (Chanania and Austin, 1999; Lakshmanan *et al.*, 1999). Currently PVC is produced by dehydrohalogenation of ethylene dichloride (EDC) (Magistro, 1976). Eighty-five percent of total EDC production is used for the production of PVC (Al-Zahrani *et al.*, 2001). EDC can be produced by direct chlorination or oxychlorination of ethylene, but usually it is manufactured by a combination of the two processes. Chlorine is extracted from an aqueous solution of sea salt via electrolysis (Allen and Clark, 1971), and ethylene is derived from hydrocarbon raw materials. Then, ethylene is directly chlorinated to

⁷ A version of this Chapter was published as: Mahecha-Botero, A., Grace, J.R., Elnashaie, S.S.E.H. and Lim, C.J. (2006). "Comprehensive modelling of gas fluidized-bed reactors allowing for transients, multiple flow regimes and selective removal of species". International Journal of Chemical Reactor Engineering, 4, A11.

produce EDC in reactors such as gas-liquid bubble column reactors as described by (Orejas, 1999, 2001) or liquid phase reactors (Lakshmanan *et al.*, 1999):



Although half of the chlorine yields the desired product, the excess hydrogen chloride is fed to the oxychlorination reactor to complete what is usually called the “balance process” (Lakshmanan and Biegler, 1997; Lakshmanan *et al.*, 1999). The overall oxychlorination reaction can be written:



By utilizing both the oxychlorination pathway and the direct chlorination pathway, the waste hydrogen chloride can be used as a raw material, and essentially all of the molecular chlorine originally reacted with ethylene is incorporated in the desired vinyl chloride (Allen and Butner, 2002). Although this is a good example of process integration using industrial ecology principles, treatment of wastewater generated in the purification stages remains a major concern (Chanania and Austin, 1999). Secondary products include trichloroethane and hydrogen chloride. Then, EDC undergoes pyrolytic decomposition to yield the vinyl chloride monomer. This is normally carried out in tubular reactors at temperatures of 480-530°C and reactor gauge pressures of 0.6-3.5 MPa (Lakshmanan *et al.*, 1999). The main reaction is:



In the final stage, the vinyl chloride is fed to a polymerization reactor to produce PVC:



Commercially, this final reaction step follows suspension, emulsion or solution polymerization schemes (Naqvi, 2004).

7.2.1. Byproducts

Aside from the main products, a variety of byproducts are also produced in the oxychlorination process. Several of these byproducts are classified as hazardous, and treatment and disposal may be expensive (Lakshmanan *et al.*, 1999). Some of the most significant byproducts are 1,1,2-trichloroethane, chloral (trichloroacetaldehyde), cis and trans-1,2 dichloroethylenes, mono-, di-,

tri- and tetra-chloromethanes and carbon oxides. Recent studies have indicated how some of the byproducts can bioaccumulate and have toxic effects on humans (Hansson *et al.*, 1997).

Developing flowsheets and processes which minimize wastes is a major objective in the synthesis of a chemical plant. This can be best addressed by maximizing the product yield and avoiding the generation of wasteful products in the reaction network (Lakshmanan and Biegler, 1997; Lakshmanan *et al.*, 1999).

7.2.2. PVC

PVC polymer is utilized commercially in a wide spectrum of vinyl plastic products. It could appear in both rigid and flexible (plasticized forms). One of the main features of PVC is its composition (Dana *et al.*, 1927). It consists of 57% by weight chlorine making it less sensitive to variations in the costs of hydrocarbon raw materials than competing polymers (Magistro and Cowfer, 1986).

PVC also has inherent flame retardant properties making it a very competitive product for a variety of applications. Flame retardants are compounds added to polymeric materials to enhance their flame retardancy (Alaee and Wenning, 2002). They can be divided into four families: inorganic flame retardants, nitrogen-based organic flame retardants, organophosphorus flame retardants, and halogenated flame retardants, (e.g. polychlorinated naphthalenes). The latter category includes chlorine inside the polymer structures.

7.3. Application of Model to an Oxychlorination Fluidized-Bed Reactor

7.3.1. Model Implementation

The ethylene oxychlorination process involves complex reactions with non-linear temperature dependence (Abba *et al.*, 2002). Despite the great industrial impact of oxychlorination reactions, few studies are available in the literature (Carrubba and Spencer, 1970) and detailed studies (e.g. (Ellis *et al.*, 2000) are proprietary.

The general model described in Section 1.2 is simulated in both *Matlab* and *COMSOL Multiphysics* by introducing the following assumptions:

- Unidirectional flow.

- Interphase balancing mass-transfer is neglected*.
- Terms such as feed distribution, sorption of species and solid chemisorption are not considered. Effectiveness factors and catalyst activity are assumed to be 100%, i.e. $\Omega_{j_{cat,\phi}} \cdot a_{j_{cat,\phi}} = 1.0$.
- Reaction pathways are the same as in Abba et al. (2002). Reaction kinetics are obtained from a proprietary study for LG Chem.
- Steady state operation (Dynamic simulations were also conducted, but the results are in the form of Videos, not presented here).

7.3.2. Reaction Pathways and Kinetics

The reaction network was simplified as suggested by Abba et al. (2002). We assume that the main product is EDC. Byproduct impurities (IMP) include a few percent of carbon oxides (CO_x) and less than one percent chlorinated hydrocarbons that exclude EDC.



The reactor parameters are listed in Table 7.1.

Table 7-1. Reactor parameters.

Parameter	Value
Inlet Temperature	430 K
Inlet Pressure	5*10 ⁵ Pa
Expanded bed height	12 m
Inlet superficial gas velocity	0.4 m/s
Average particle diameter	50 μm
Catalyst density	1600 kg/m ³
Internal diameter	4 m

* Our interest in this chapter is in the turbulent flow regime, where this term plays a minor role due to small concentration differences in the two phases. The importance of this term was studied later in the project (i.e. in the chapters dealing with steam methane reforming).

7.3.2.1. Estimation of proprietary kinetic parameters

A kinetic study was conducted based on data provided by Sud-Chemie that included composition, temperature and pressure values for a number of pilot plant experimental runs. We proceeded to do the parameter estimation using the available data, although the numerical estimates can suffer from systematic errors since the number of conversion values and experimental runs was quite limited. To reduce possible errors and improve the likelihood of reasonable results, we ultimately decided to use the form of the equations employed in the previous work of Abba et al. (2002), with the constants least-squares-fitted to the new data from Sud-Chemie. Experimental data (concentration versus time) with all reactants in excess except for one, and with each reactant in turn being the rate-limiting species, would be required to obtain kinetic expressions without having to make use of the previous kinetic expressions. In order for the oxygen dependence to be included, levels of oxygen would need to be varied and reported. The kinetic parameters were estimated for each experimental run and then averaged for a given temperature.

Using the available pilot plant data, a separate steady-state model is created based on the catalyst mass:

$$\frac{dF_i}{dW} = \sum_{j=1}^{N_R} \nu_{ij} \cdot r'_j \quad \text{for } i=1,2,\dots,N_C \quad (7.1)$$

Constant pressure and isothermal conditions are assumed for each experimental run, given the lack of detailed information. It is important to bear in mind that the reaction kinetics assume that oxygen is present in considerable excess. A Gauss-Newton method was used to obtain the k_0 and E_a parameters that best fit the experimental data. The software EASY-FIT was used to fit the experimental results to the model equations. This software is available commercially, and it is based on Schittkowski (2004).

7.4. Results and Discussion

Profiles are depicted in normalized form due to the proprietary nature of the results. Axial profiles of molar flow rates predicted for each chemical species and obtained from the *Matlab* program are plotted in Figures 7.1 to 7.7. As ETY, HCl and O₂ are consumed, EDC and H₂O are

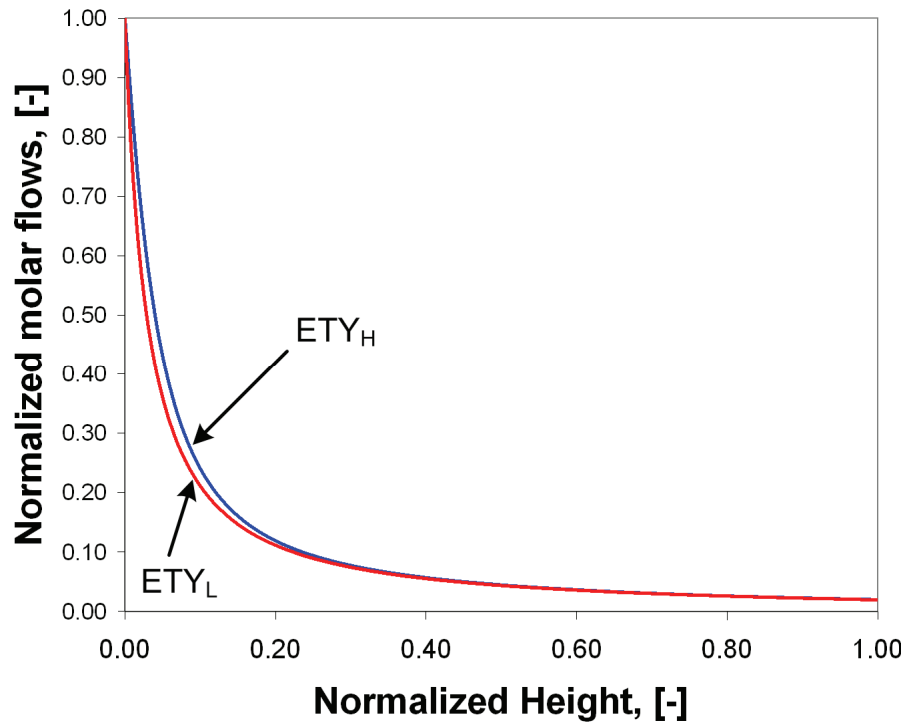


Figure 7.1. Predicted steady-state ETY molar flows in the high- and low-density pseudo-phases vs height in the reactor. For operating conditions see Table 7.1. Values are normalized by their maximum value.

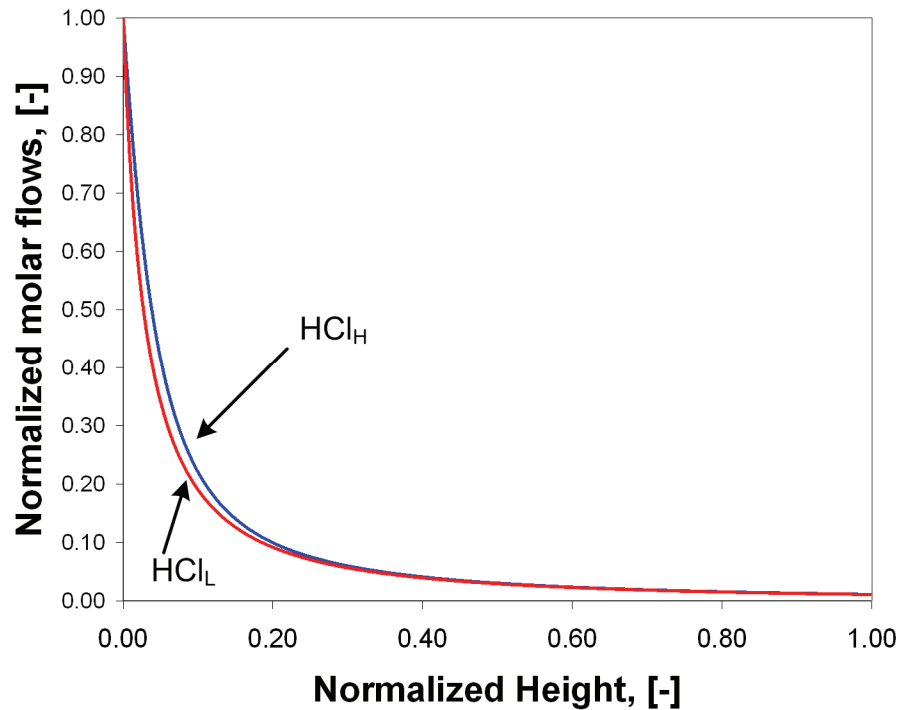


Figure 7.2. Predicted steady-state HCl molar flows in the high- and low-density pseudo-phases vs height. For conditions see Table 7.1. Values are normalized by their maximum value.

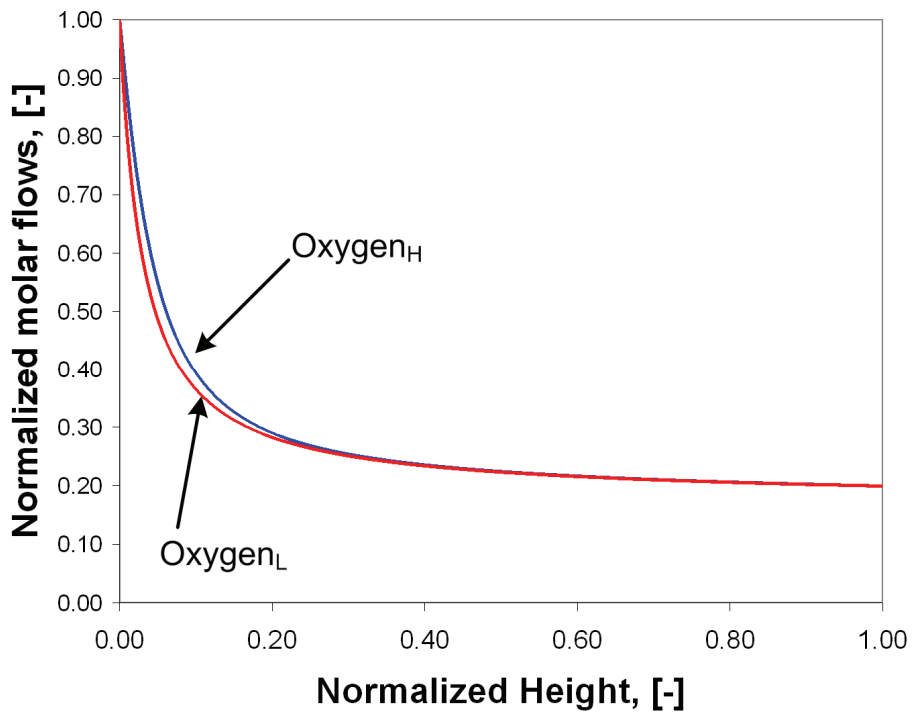


Figure 7.3. Predicted steady-state oxygen molar flows in the high- and low-density pseudo-phases vs height. For operating conditions see Table 7.1. Values are normalized by their maximum value.

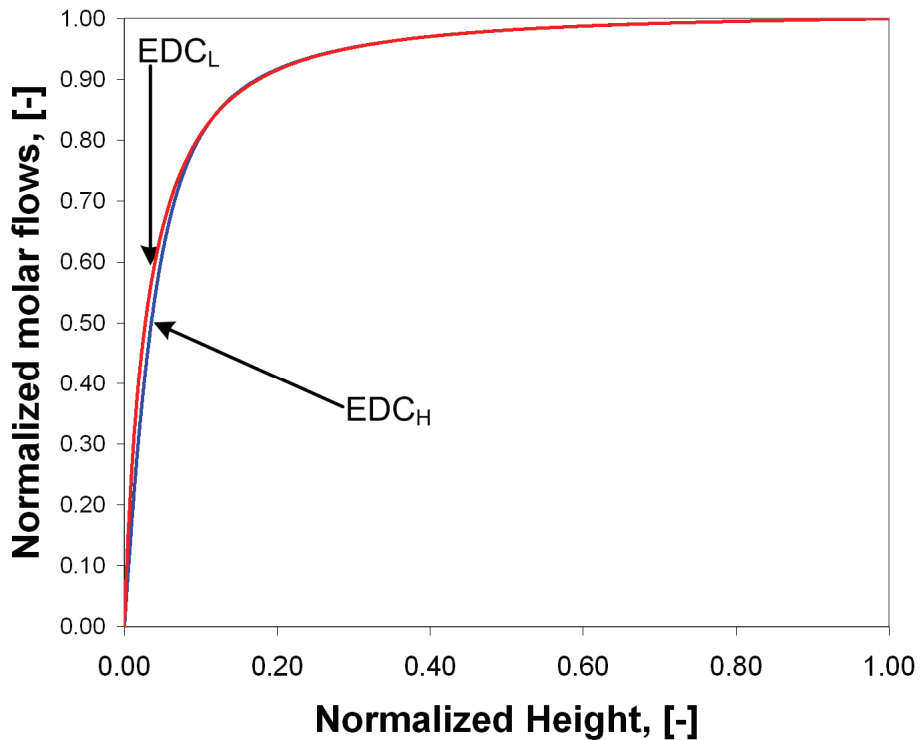


Figure 7.4. Predicted steady-state EDC molar flows in the high- and low-density pseudo-phases vs height. For operating conditions see Table 7.1. Values are normalized by their maximum value.

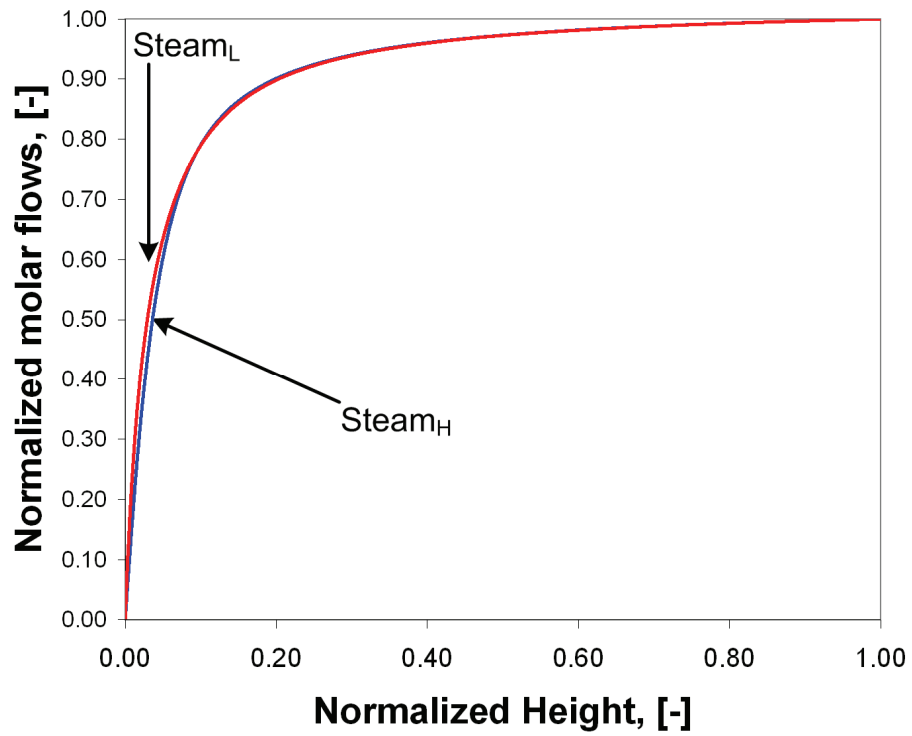


Figure 7.5. Predicted steady-state H₂O molar flows in the high- and low-density pseudo-phases vs height. For operating conditions see Table 7.1. Values are normalized by their maximum value.

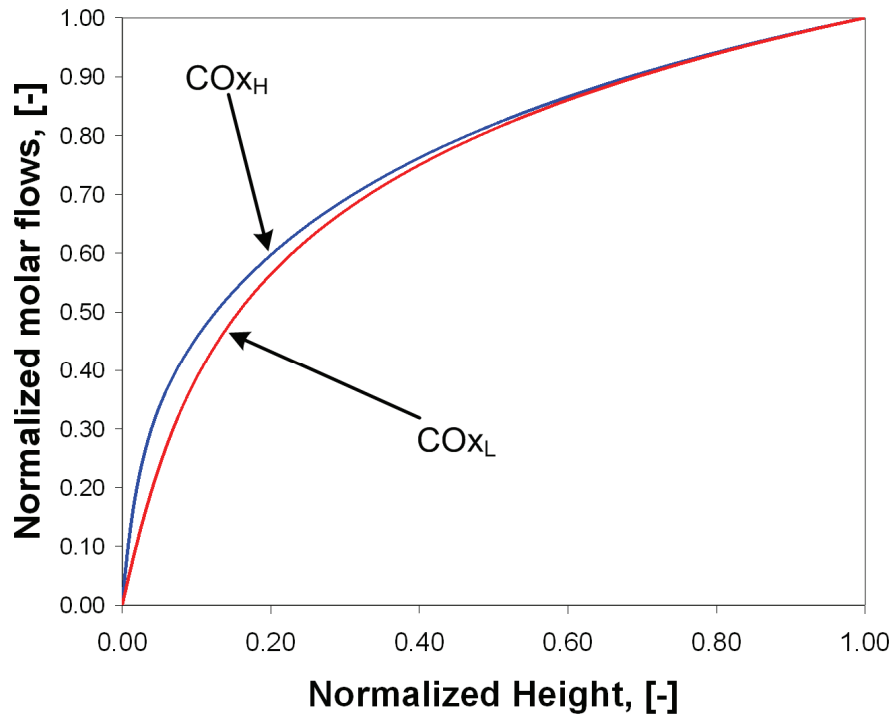


Figure 7.6. Predicted steady-state CO_x molar flows in the high- and low-density pseudo-phases vs height. For operating conditions see Table 7.1. Values are normalized by their maximum value.

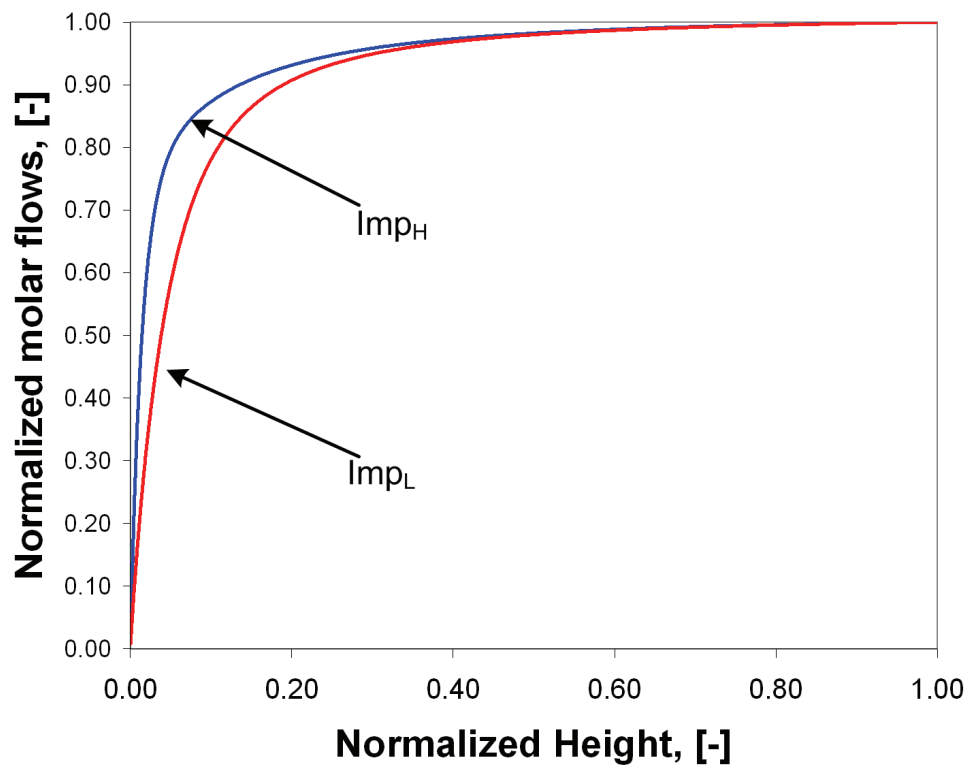


Figure 7.7. Predicted steady-state impurity molar flows in the high- and low-density pseudo-phases vs height. For operating conditions see Table 7.1. Values are normalized by their maximum value.

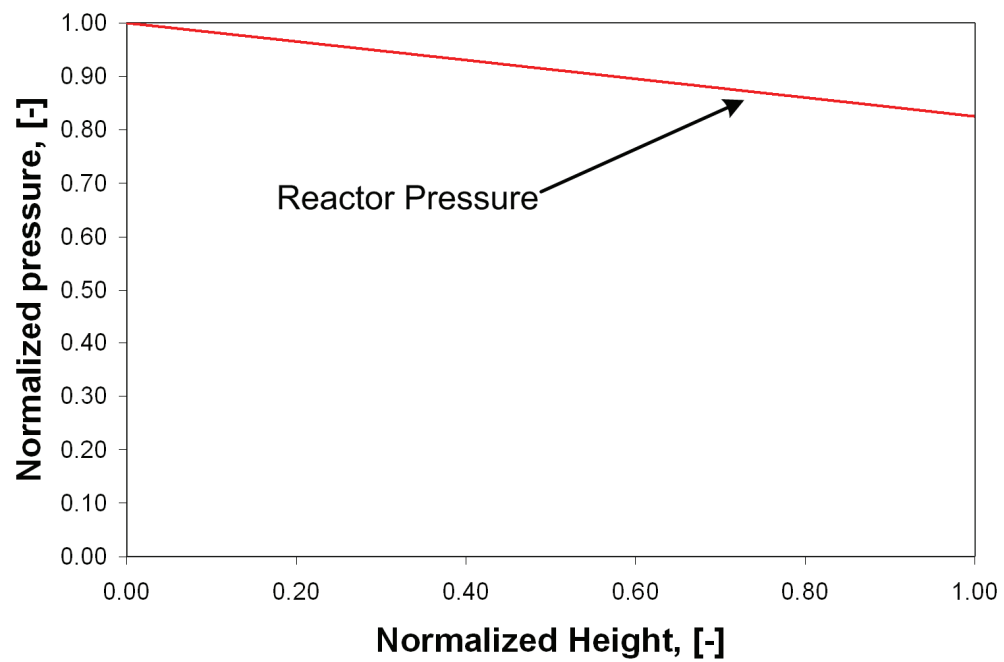


Figure 7.8. Pressure vs reactor height. For conditions see Table 7.1. Values are normalized by their maximum value.

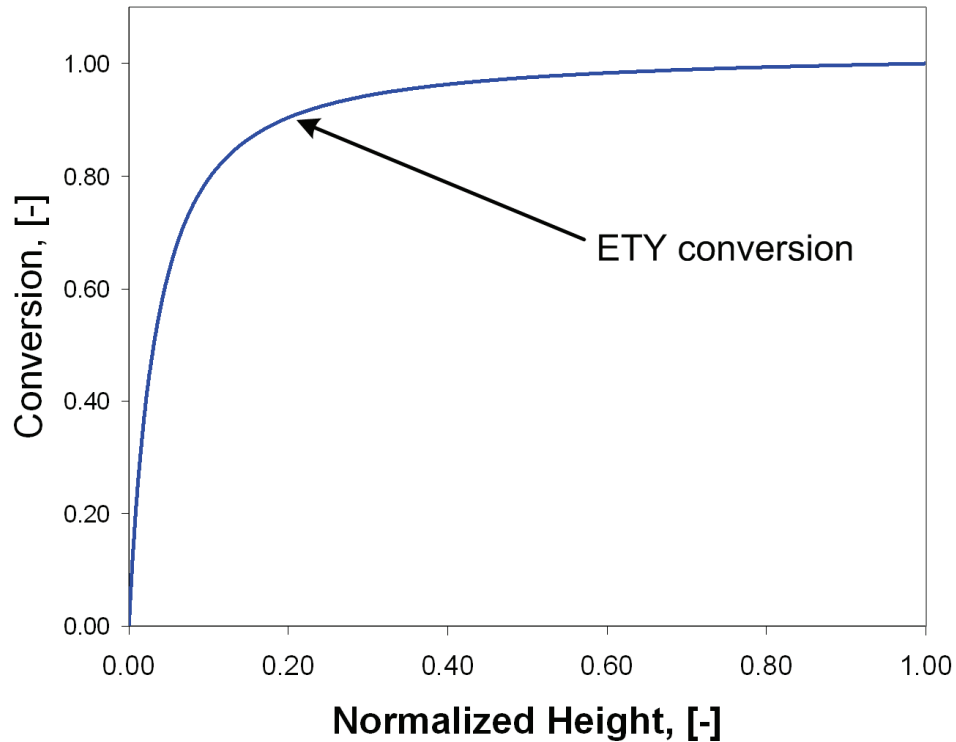


Figure 7.9. Predicted axial profile of steady-state overall ETY conversion. For operating conditions see Table 7.1. Values are normalized by their maximum value.

produced. Although about 90% of the final product concentration is predicted to be achieved at a height of ~2 m, the concentration continues to increase asymptotically until the exit is reached. This behaviour agrees quite well with earlier predictions of Abba *et al.* (2002) and is consistent with industrial experience.

Most of the reactions take place in the high-density pseudo-phase. In order to leave the reactor, the gaseous products have to diffuse to the low-density phase due to the concentration difference between the phases. The interphase diffusion is quite fast, making the concentrations relatively uniform in both pseudo-phases after passing the lowest section of the bed. Moreover, the flow rates in the two pseudo-phases differ, as expected, since the low-density phase contains most of the gas and accounts for most of the molar flow of gases through the reactor. (Note that the difference between the molar flows in the two pseudo-phases cannot be appreciated in normalized form).

Figure 7.8 shows the pressure drop along the reactor. As expected from the model equation, this pressure drop varies in a linear way with height.

Figure 7.9 shows the rapid conversion of ETY along the reactor. The value of the conversion, appears to asymptotically approach a value of about 98%. The results are very similar to those of Abba *et al.* (2002) and give good agreement with industrial reactor measured results (these values are confidential).

7.5. Conclusions

As a case study, a simplified version of the generic fluidized-bed reactor model was applied to simulate an oxychlorination fluidized-bed reactor for the production of ethylene dichloride from ethylene. The results were similar to those from the model of Abba *et al.* (2002) and in good agreement with industrial findings. The model is able to describe fluidized bed reactor systems relying on fewer assumptions than other models in the literature. When different combinations of assumptions are incorporated in the model, it simplifies to a number of fluid bed reactor models previously presented in the literature. Simulations including transient behaviour are also available in Video format using the computational package *COMSOL Multiphysics*.

7.6. References

- Abba, I.A., Grace, J.R. and Bi, H.T. (2002). Variable-gas-density fluidized bed reactor model for catalytic processes. *Chem. Eng. Sci.*, 57, 4797-4807.
- Al-Zahrani, S.M., Aljodai, A.M. and Wagialla, K.M. (2001). Modelling and simulation of 1,2-dichloroethane production by ethylene oxychlorination in fluidized-bed reactor. *Chem. Eng. Sci.*, 56, 621-626.
- Alaee, M. and Wenning, R. (2002). The Significance of Brominated Flame Retardants in the Environment: Current understanding, issues and challenges. *Chemosphere*, 46, 579-582.
- Allen, D.T. and Butner, R.S. (2002). Industrial Ecology: A Chemical Engineering Challenge. Environmental Protection, from <http://www.cepmagazine.org>.
- Allen, J.A. and Clark, A.J. (1971). Oxychlorination catalysts. *Pure and Appl. Chem*, 21, 145-166.
- Carrubba, R.V. and Spencer, J.L. (1970). Kinetics of the oxychlorination of ethylene. *Ind. Eng. Chem. Process Des. Develop.*, 9, 414-419.
- Chanania, F. and Austin, J. (1999). Best demonstrated available technology (BDAT) background document for chlorinated aliphatics production wastes. Washington, D.C., U.S. Environmental Protection Agency. Office of Solid Waste.

Dana, L.I., Burdick, J.N. and Jenkis, A.C. (1927). Some physical properties of vinyl chloride, Laboratory of the linde air products company: 2801-2806.

Ellis, N., Abba, I.A., Bi, H.T. and Grace, J.R. (2000). Modelling and scale up of O₂-feed oxy-chlorination fluidized bed reactors. Vancouver, Canada, Report submitted to Mitsubishi Chemical Corporation. University of British Columbia.

Hansson, M., Barregard, L., Sallsten, G., Svensson, B.G. and Rappe, C. (1997). Polychlorinated dibenzo- p-dioxin and dibenzofuran levels and patterns in polyvinylchloride and chloralkali industry workers. *Int. Arch. Occup. Environ. Health*, 70, 51-56.

Lakshmanan, A. and Biegler, L.T. (1997). A case study for reactor network synthesis: the vinyl chloride process. *Comput. Chem. Eng.* , 21 Suppl, S785-S790.

Lakshmanan, A., Rooney, W.C. and Biegler, L.T. (1999). A case study for reactor network synthesis: the vinyl chloride process. *Comput. Chem. Eng.* , 23, 479-495.

Magistro, A.J. (1976). Catalyst and process for the preparation of ethylene and vinyl chloride from ethane. United States Patent. U.S.A.

Magistro, A.J. and Cowfer, J.A. (1986). Oxychlorination of ethylene. *J. Chem. Educ.* , 63, 1056-1058.

Mahecha-Botero, A., Grace, J.R., Elnashaie, S.S.E.H. and Lim, C.J. (2006a). Comprehensive modelling of gas fluidized-bed reactors allowing for transients, multiple flow regimes and selective removal of species. *Int. J. Chem. Reactor Eng.*, 4, A11.

Naqvi, S. (2004). Process Economics Program Report: Vinyl Polymers. SRI Consulting.

Orejas, J.A. (1999). Modelling and simulation of a bubble-column reactor with external loop: Application to the direct chlorination of ethylene. *Chem. Eng. Sci.*, 54, 5299-5309.

Orejas, J.A. (2001). Model evaluation for an industrial process of direct chlorination of ethylene in a bubble-column reactor with external recirculation loop. *Chem. Eng. Sci.*, 56, 513-522.

Schittkowski, K. (2004). Data fitting in partial differential algebraic equations: some academic and industrial applications K. . *J. Comput. Appl. Math.* , 163, 29-57.

8. TIME-SCALE ANALYSIS OF MALEIC ANHYDRIDE FLUIDIZED-BED CATALYTIC REACTOR BASED ON DYNAMIC MODEL ⁸

8.1. Introduction

Fluidized-bed reactors, like many other industrial and natural processes, involve multiple phenomena that occur at different rates. In a fluidized-bed reactor, phenomena such as multi-phase flow, mass transfer/reaction and heat transfer take place in coupled non-linear ways. Dynamic modelling for such phenomena requires mathematical relations that describe the interaction between the system state variables and parameters, accounting for their evolution in time. In this chapter, a dynamic model is implemented to identify different time scales and to gain insight into the dynamic behaviour of fluidized-beds.

The dynamic behaviour of complex systems often contains multiple time scales (Okino and Mavrovouniotis, 1998). After an initial transient period, it may be possible to consider some fast phenomena as if they were instantaneous relative to slower ones (Okino and Mavrovouniotis, 1998). For instance, hydrodynamic phenomena may reach a pseudo-steady-state much more quickly than heat transfer in fluidized bed reactors. The identification of different time scales may then be used to simplify the numerical solution of system models (Muralidhar and Ramkrishna, 1986; Thompson and Larter, 1995; Strier and Dawson, 2000; Vora and Daoutidis, 2001).

8.2. Application to an Industrial MA Fluidized-Bed Reactor

Maleic Anhydride (MA) is an important intermediate in the production of fumaric and tartaric acids, unsaturated polyester resins, chemicals for agriculture, alkyd resins, lubricant oils, copolymers, food additives and NutraSweet (Dente *et al.*, 2003). Initially, MA was produced

⁸ *A version of this Chapter was published as: Mahecha-Botero, A., Grace, J.R., Elnashaie, S.S.E.H. and Lim, C.J. (2007). "Time scale analysis of a fluidized-bed reactor based on a generalized dynamic model". in Fluidization XII. Eds. Bi, X.T., Berruti, F. and Pugsley, T., ECI Symposium Series. United Engineering Conferences, Brooklyn, pp. 623-630.*

from benzene (Pugsley *et al.*, 1992), but due to environmental and economic constraints, it is currently produced commercially by partial oxidation of n-butane over a vanadium phosphorous oxide (VPO) catalyst (Golbig and Werther, 1997), involving complex heterogeneously-catalyzed reactions (Alonso *et al.*, 2001) and the only alkane-selective oxidation reaction used in industry (Huang *et al.*, 2002). The catalytic reactions occur through sequential reduction-oxidation of the catalyst surface and selective generation of MA (Wang and Barteau, 2002). Fluidized bed reactors play a major role in MA synthesis, facilitating excellent heat transfer and avoiding hot spots. As well, higher reactant concentrations can be fed without generating explosive mixtures because the fluidized catalyst acts as a flame arrester (Contractor, 1999). The dimensions and operating conditions given in Table 8.1 are similar to those in some industrial units.

Table 8-1. Key reactor parameters.

Parameter	Value	Parameter	Value
Gas inlet temperature	613 [K]	Catalyst density	2000 [kg/m ³]
Pressure at distributor level	1500 [kPa]	Inner diameter	0.8 [m]
Expanded bed height	6 [m]	Butane feed	40 [Nm ³ /h]
Superficial gas velocity	0.6 [m/s]	Oxygen feed	200 [Nm ³ /h]
Mean particle diameter	50 [μm]	Nitrogen feed	800 [Nm ³ /h]
Reactor shell preheat temperature	513 [K]		

8.2.1. Reaction Kinetics

A triangular reaction scheme commonly appears in the literature, based on the work of Centi *et al.* (1985). These kinetics were employed in our simulations. These are widely used (Pugsley *et al.*, 1992; Roy *et al.*, 2000) and can produce accurate species conversion predictions (Mostoufi *et al.*, 2001). The reaction rates are then described by:

$$r_1 = r_{C_4H_2O_3} = \frac{k_1 C_{C_4H_{10}} C_{O_2}^\alpha}{1 + K_B C_{C_4H_{10}}} \quad (8.1)$$

$$r_2 = r_{CO_x} = k_2 C_{O_2}^\beta, \quad (8.2)$$

$$r_3 = k_3 C_{C_4H_2O_3} \left(\frac{C_{O_2}^\gamma}{C_{C_4H_{10}}^\delta} \right), \quad (8.3)$$

where r_1 is the rate of MA formation, r_2 the rate of butane total oxidation, and r_3 the rate of MA total oxidation. The corresponding kinetic constants (Centi *et al.*, 1985) appear in Table 8.2.

Table 8-2. Maleic anhydride kinetic parameters from Centi *et al.* (1985).

Temperature [K]	k_1 [$\text{mol}^{1-\alpha} \text{L}^\alpha \text{g}^{-1} \text{s}^{-1}$]	k_2 [$\text{mol}^{1-\beta} \text{L}^\beta \text{g}^{-1} \text{s}^{-1}$]	k_3 [$\text{mol}^{\gamma-\delta} \text{L}^{1-\gamma-\delta} \text{g}^{-1} \text{s}^{-1}$]
573.15	3.357×10^{-7}	2.001×10^{-7}	4.400×10^{-8}
593.15	4.621×10^{-7}	4.364×10^{-7}	6.606×10^{-8}
613.15	6.230×10^{-7}	9.040×10^{-7}	9.658×10^{-8}
Other parameters:	$K_B=2616$ [L mol^{-1}]; $\alpha = \beta = 0.2298$ [-]; $\gamma = 0.6345$ [-]; $\delta = 1.151$ [-]		

8.2.2. Proposed Stoichiometry

The following stoichiometry is assumed for this modeling work. The CO:CO₂ molar ratio is assumed to be 1, similar to values reported by Lorences *et al.* (Lorences *et al.*, 2003).



8.2.3. Implementation of General Model

The general model described above is applied to a MA reactor. The dynamic model is solved by *COMSOL Multiphysics* 3.2b in a one-dimensional geometry as described by equations 1.9, 1.18 and 1.21. The following assumptions are adopted:

- Unidirectional flow.
- Interphase balancing mass-transfer is neglected*.
- Terms such as feed distribution, sorption of species and solid chemisorption are not considered. Effectiveness factors and catalyst activity assumed to be 100%, i.e. $\Omega_{j_{cat,\varphi}} \cdot a_{j_{cat,\varphi}} = 1.0$.
- Time-dependent (dynamic) operation.

* The importance of this term was studied later in the project (i.e. in the chapters dealing with steam methane reforming).

Additionally, a heat exchange term between the gas and reaction vessel is included on the left side of form: $+U_{(R)}(T_{(R)} - T_{(\varphi)})$. A heat balance for the reactor vessel (made of steel) is developed based on Equation 1.18 by eliminating all reaction and flow terms:

$$-\bar{\nabla} \cdot \left(-\langle K_{(R)} \rangle \bar{\nabla} \cdot (T_{(R)}) \right) + U_{(R)} a_R (T_{(\varphi)} - T_{(R)}) + U_{(Cool)} a_{cool} (T_{(Cool)} - T_{(R)}) = \frac{\partial}{\partial t} \left(\langle \rho_{(R)} \rangle \langle C_{P(R)} \rangle T_{(R)} \right) \quad (8.4)$$

where subscript “R” denotes the reactor shell. The reactor shell Biot number is low enough to ensure that the radial variation in temperature can be safely neglected, allowing for the adoption of a radially lumped capacitance (1-D) model. The start-up policy for solving the model requires that all species concentrations inside the reactor are equal to their input values. At $t=0$, all concentration profiles are flat along the reactor height. Suddenly, at $t=0$ the reaction and convection start, and the conversion increases gradually as time progresses. The shell is assumed to be externally preheated to 513 K, as well as insulated to prevent heat loss. The reactor is then simulated assuming an average (i.e. weighted by their fractions in the bed) temperature for the high- and low- density pseudo-phases as the reactor temperature.

8.3. Results and Discussion

Numerical simulation of the system dynamics revealed two very different time scales:

8.3.1. Mass Transfer/Reaction Time Scale

System dynamics based on the mole balances for the chemical species inside the reactor are very quick. The time step for the numerical simulations needs to be kept below 0.0001 s to assure numerical stability due the speed of the convection-diffusion processes. The time-step required to solve the model was estimated by trial and error. The time scale in this case is ~ 10 s. On the other hand, heat transfer to/from the reactor vessel is very slow and has very little influence on the system dynamics for the above time scale. Conversion profiles at different times for the reactor are depicted in Figure 8.1. For these curves, all heat transfer processes can be assumed to be at pseudo-steady-state. The shape of the profiles is similar to earlier findings (Mostoufi *et al.*, 2001).

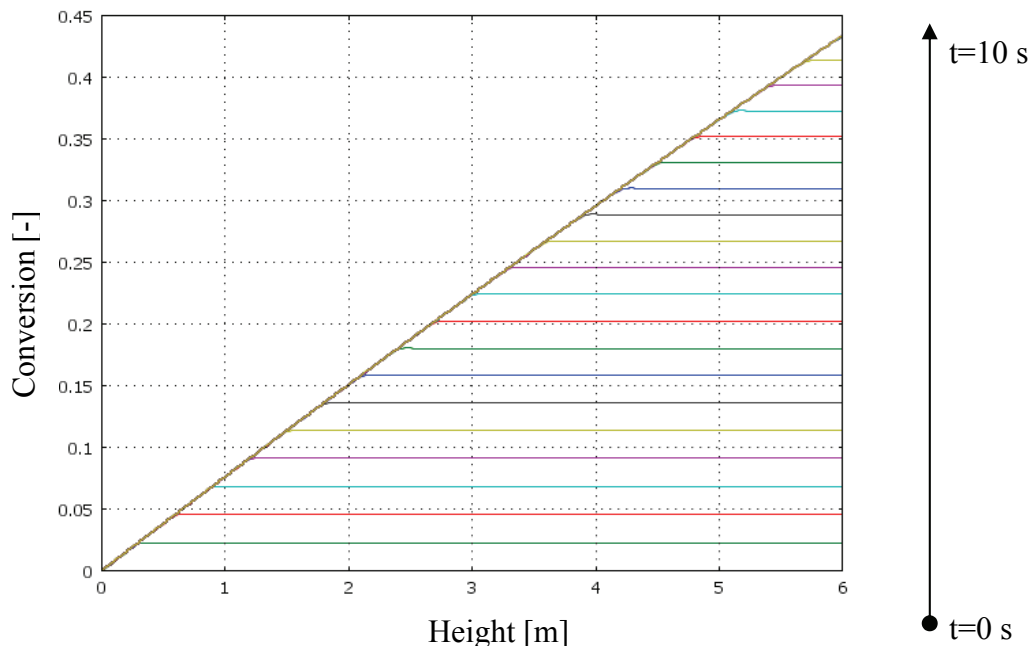


Figure 8.1. Conversion vs Height [m] for different times (one profile every 0.5 s).

8.3.2. Heat Transfer Time Scale

Because of the thermal inertia of the reactor and its contents, heat transfer involves a time scale many orders of magnitude larger than the mass transfer/reaction time scale. Our simulations adopt values of the state variables and parameters from Section 8.3.1 simulations after 10 s (i.e. when the mass transfer/reaction processes have essentially reached steady state). The system is then simulated by two coupled energy balances (one for the reactor contents, the other for the vessel), with species concentration profiles, rates of reaction profiles and heat generation profiles from Section 8.3.1 above. It was verified that this procedure gave overall solutions very similar to those where all of the dynamic equations were solved simultaneously.

When the time step was increased to ~ 0.1 s, with numerical stability conserved, 150,000 s were required to reach steady-state. This confirms that the shell temperature profile evolves slowly, trying to equilibrate with the reactor temperature. The heat transfer is much slower than the mass transfer/reaction phenomena. Figures 8.2 and 8.3 depict temperature profiles at different times for the reactor and shell temperature respectively.

From Figure 8.2 it is clear that the temperature of the contents of the reactor has faster dynamics than the reactor shell since it reaches almost its final value after ~ 1000 s. In this mode of operation it is safe to assume that the mass transfer/reaction processes are at pseudo-steady-state.

The time scale for the heat transfer phenomena depend on the size of the equipment and also on whether the vessel is externally insulated or refractory-lined. Neglecting the heat effects of the reactor shell in Section 8.3.1 does not affect the results significantly. However, this assumption is not appropriate when estimating the time to reach thermal steady state.

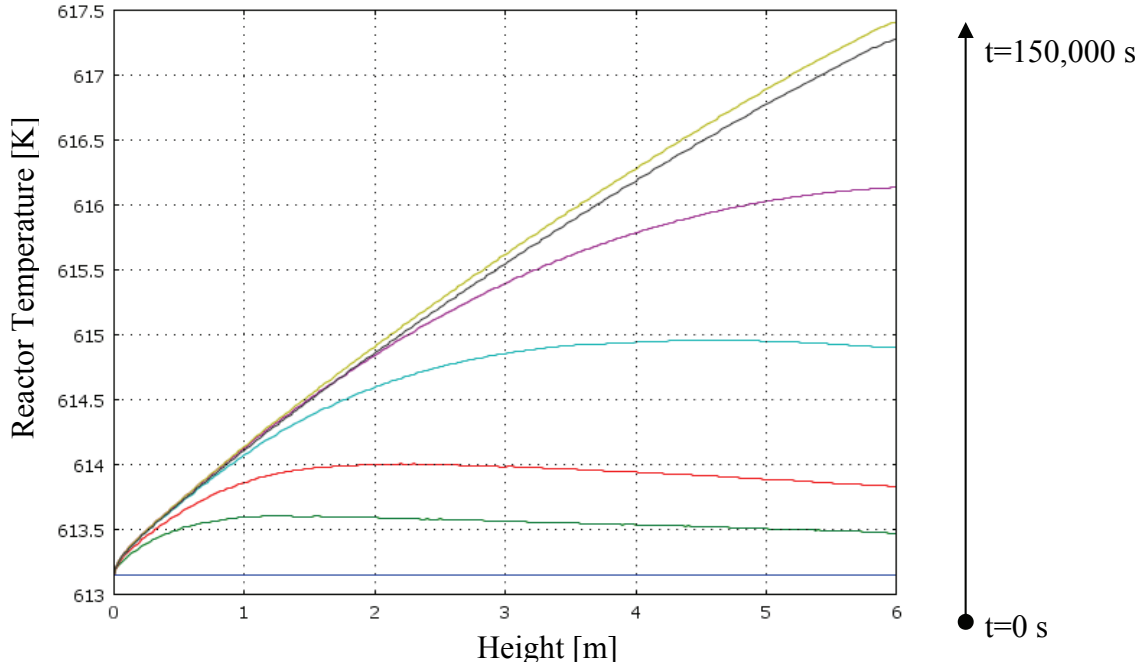


Figure 8.2. Reactor temperature vs height for different times (profiles at: $t = 0$ s, $t = 1$ s, $t = 2$ s, $t = 5$ s, $t = 10$ s, $t = 1,000$ s and $t = 150,000$ s).

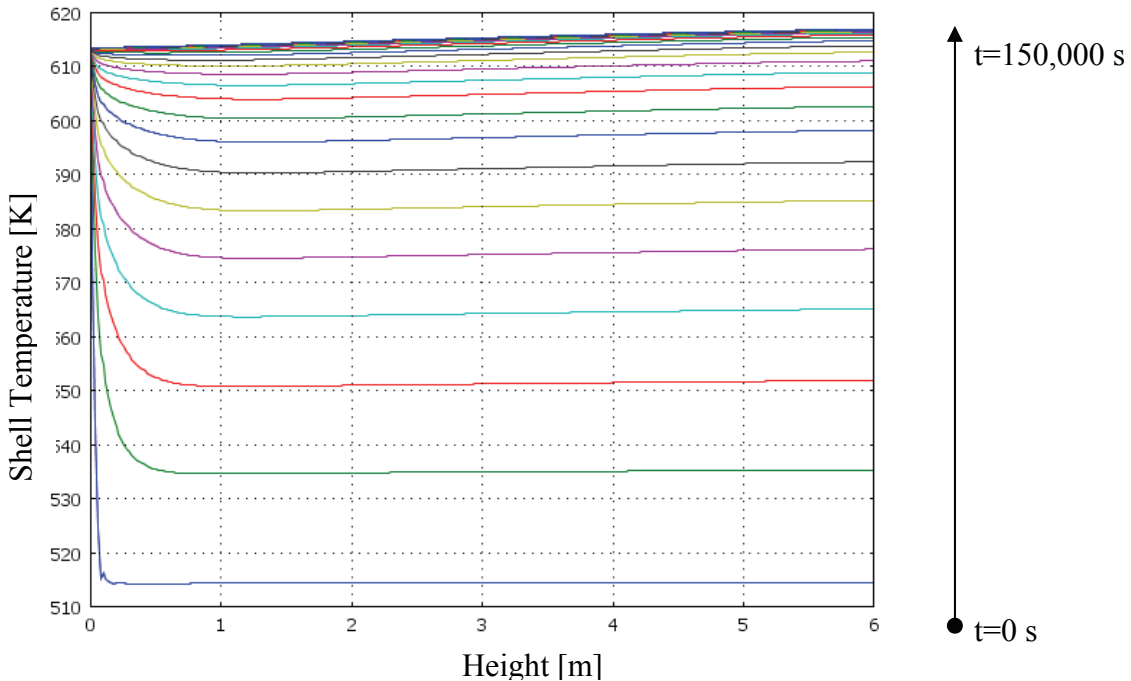


Figure 8.3. Reactor shell temperature vs height at different times (one profile every 3,000 s).

8.4. Conclusions

Different time scales are identified for an industrial MA reactor, providing insight into the dynamic behaviour of the system. The generalized model may be simplified depending on the desired degree of sophistication for a given period. The model predicts very different time scales for key dynamic phenomena inherent to the process. The mass transfer/reaction time scale was found to be close to the residence time of the gas molecules in the reactor. Furthermore, a heat transfer time scale several orders of magnitude larger was revealed for the current system. Heat transfer calculations may be carried out assuming that the mass transfer/reaction phenomena have reached pseudo-steady state. In addition, it is safe to neglect heat transfer dynamics for the initial few seconds required for the mass transfer/reaction phenomena to stabilize. This type of time-scale analysis may be a useful tool to identify the appropriate degree of sophistication to predict the dynamics of some complex reacting systems. Some assumptions are valid for a determined interval of time, whereas the same assumption may be invalid if applied when considering different time scales.

8.5. References

- Alonso, M., Lorences, M.J., Pina, M.P. and Patience, G.S. (2001). Butane partial oxidation in an externally fluidized bed-membrane reactor. *Catal. Today*, 67, 151–157.
- Centi, G., Fornasari, G. and Trifiro, F. (1985). n-butane oxidation to maleic anhydride on vanadium-phosphorous oxides: Kinetic analysis with a tubular flow stacked-pellet reactor. *Ind. Eng. Chem. Prod. Res. Dev.*, 24, 32-37.
- Contractor, R.M. (1999). Dupont's CFB technology for maleic anhydride. *Chem. Eng. Sci.*, 54, 5627-5632.
- Dente, M., Pierucci, S., Tronconi, E., Cecchini, M. and Ghelfi, F. (2003). Selective oxidation of n-butane to maleic anhydride in fluid bed reactors: detailed kinetic investigation and reactor modelling. *Chem. Eng. Sci.*, 58, 643-648.
- Golbig, K.G. and Werther, J. (1997). Selective synthesis of maleic anhydride by spatial separation of n-butane oxidation and catalyst reoxidation. *Chem. Eng. Sci.*, 52, 583-595.
- Huang, X., Li, C., Chen, B. and Silveston, P.L. (2002). Transient kinetics of n-butane oxidation to maleic anhydride over a VPO catalyst. *AIChE J.*, 48, 846-855.
- Lorences, M.J., Patience, G.S., Diez, F.V. and Coca, J. (2003). Butane oxidation to maleic anhydride: Kinetic modeling and byproducts. *Ind. Eng. Chem. Res.*, 42, 6730-6742.

Mahecha-Botero, A., Grace, J.R., Elnashaie, S.S.E.H. and Lim, C.J. (2007b). Time scale analysis of a fluidized-bed reactor based on a generalized dynamic model. in Fluidization XII. Eds. Bi, X., F., B. and Pugsley, T. Harrison Hot Springs, BC, Canada., ECI Symposium Series. United Engineering Conferences, Brooklyn. http://services.bepress.com/eci/fluidization_xii/76.

Mostoufi, N., Cui, H. and Chaouki, J. (2001). A comparison of two- and single-phase models for fluidized-bed reactors. *Ind. Eng. Chem. Res.*, 40, 5526-5532.

Muralidhar, R. and Ramkrishna, D. (1986). Analysis of droplet coalescence in turbulent liquid-liquid dispersions. *Ind. Eng. Chem. Fundam.*, 25, 554-560.

Okino, M.S. and Mavrovouniotis, M.L. (1998). Simplification of mathematical models of chemical reaction systems. *Chem. Rev.*, 98, 391-408.

Pugsley, T.S., Patience, G.S., Berruti, F. and Chaouki, J. (1992). Modeling the catalytic oxidation of n-butane to maleic anhydride using a circulating fluidized bed reactor. *Ind. Eng. Chem. Res.*, 31, 2652-2660.

Roy, S., Dudukovic, M.P. and Mills, P.L. (2000). A two-phase compartments model for the selective oxidation of n-butane in a circulating fluidized bed reactor. *Catal. Today* 61, 73–85.

Strier, D.E. and Dawson, S.P. (2000). Rescaling of diffusion coefficients in two-time scale chemical systems. *J. Chem. Phys.*, 112, 825-834.

Thompson, D.R. and Larter, R. (1995). Multiple time scale analysis of two models for the peroxidase-oxidase reaction. *Chaos*, 5, 448-457.

Vora, N. and Daoutidis, P. (2001). Nonlinear model reduction of chemical reaction systems. *AIChE J.*, 47, 2320-2332.

Wang, D. and Barteau, M.A. (2002). Oxidation kinetics of partially reduced vanadyl pyrophosphate catalyst. *Appl. Catal. A*, 223 205–214.

9. FLUIDIZED-BED REACTOR FOR PRODUCTION OF PHTHALIC ANHYDRIDE⁹

9.1. Introduction

In this chapter, the generic model is applied for the simulation of an industrial scale process. A two-phase distributed fluidized-bed reactor model is used for the production of phthalic anhydride with naphthalene as feedstock (Johnsson *et al.*, 1987). The reactor model developed in Section 1.2 is simplified using the assumptions:

- Unidirectional flow.
- Interphase balancing mass-transfer is neglected*.
- Terms such as feed distribution, sorption of species and solid chemisorption are not considered. Effectiveness factors and catalyst activity assumed to be 100%, i.e.

$$\Omega_{j_{cat,\phi}} \cdot a_{j_{cat,\phi}} = 1.0.$$

- Steady state operation.
- Isothermal operation.

The main reactor parameters and operating conditions are described in Table 9.1.

9.2. Reaction Kinetics

A reaction kinetic model for the oxidation of naphthalene was proposed by DeMaria *et al.* (1961) and refined by Johnsson *et al.* (1987).

⁹ A version of this chapter was published as: Mahecha-Botero, A., Grace, J.R., Elnashaie, S.S.E.H. and Lim, C.J. (2007). "A comprehensive approach to reaction engineering". International Journal of Chemical Reactor Engineering, 5: A17.

* The importance of this term was studied later in the project (i.e. in the chapters dealing with steam methane reforming).



where MA, NQ, NA and PA denote maleic anhydride, naphthoquinone, naphthalene and phthalic anhydride, respectively.

Table 9-1. Key reactor parameters.

Parameter	Value
Reactor diameter	7.9 m
Input temperature	360 °C
Input pressure	0.26 MPa
Overall equipment height	13.7 m
Expanded bed height	7.9 m
Particle diameter	53 μm
Particle density	1200 Kg.m ⁻³
Naphthalene input flow	1.4 mol.s ⁻¹
Nitrogen input flow	53.4 mol.s ⁻¹
Argon input flow	0.6 mol.s ⁻¹
Oxygen input flow	14.4 mol.s ⁻¹
Water input flow	0.9 mol.s ⁻¹

The corresponding rate expressions are:

$$r_{1\phi} = \rho_{cat} \cdot (1 - \varepsilon_{\phi}) k_1 C_{NA\phi} C_{O_2\phi} \quad \text{(9.1)}$$

$$r_{2\phi} = \rho_{cat} \cdot (1 - \varepsilon_{\phi}) k_2 C_{NA\phi} C_{O_2\phi} \quad \text{(9.2)}$$

$$r_{3\phi} = \rho_{cat} \cdot (1 - \varepsilon_{\phi}) k_3 C_{NQ\phi} \quad \text{(9.3)}$$

$$r_{4\phi} = \rho_{cat} \cdot (1 - \varepsilon_{\phi}) k_4 C_{PA\phi} C_{O_2\phi}^{0.8} \quad \text{(9.4)}$$

The kinetics of DeMaria *et al.* (1961) and Johnsson *et al.* (1987) assume a pseudo-first order form given the low concentration of naphthalene in the reactor. The values of the kinetic parameters are listed in Table 9.2.

Table 9-2. Kinetic parameters from Johnsson *et al.* (1987).

Parameter	Value
$k_1 \cdot C_{O_2}$	1.8 s^{-1}
$k_2 \cdot C_{O_2}$	1.8 s^{-1}
k_3	4.6 s^{-1}
$k_4 C_{O_2}^{0.8}$	0.023 s^{-1}

9.3. Results and Discussion

Figure 9.1 shows the rapid disappearance of naphthalene in both pseudo-phases along the reactor. As naphthalene is consumed, naphthoquinone is generated as an intermediate component. The desired partial oxidation product phthalic anhydride is generated very quickly. Further oxidation consumes all the remaining reactant. The intermediate component, naphthoquinone, reaches a maximum concentration and decreases as the reaction proceeds. Since the product is the phthalic anhydride, it is desirable to consume all intermediate components. The phthalic anhydride reaches a maximum at approximately 1.4 moles per second. Later, some maleic anhydride is produced, decreasing the yield of phthalic anhydride in the reactor. It is important to note that the flow rates in the two pseudo-phases have different values as expected. The low-density pseudo-phase contains most of the gas and accounts for most of the molar flows in the reactor.

From Figure 9.1 and 9.2, it is observed that the profiles in the high-density pseudo-phase, due to its higher solid content and therefore higher reaction rate, develop faster (i.e. achieve their maximum values at a shorter distance) than their low-density counterparts. Most of the reaction products are produced in the emulsion pseudo-phase. The generated product has to diffuse to the low-density pseudo-phase due to a concentration gradient. These products diffuse to the bubbles via inter-phase mass transfer. This is why the concentration profiles in the two phases differ in

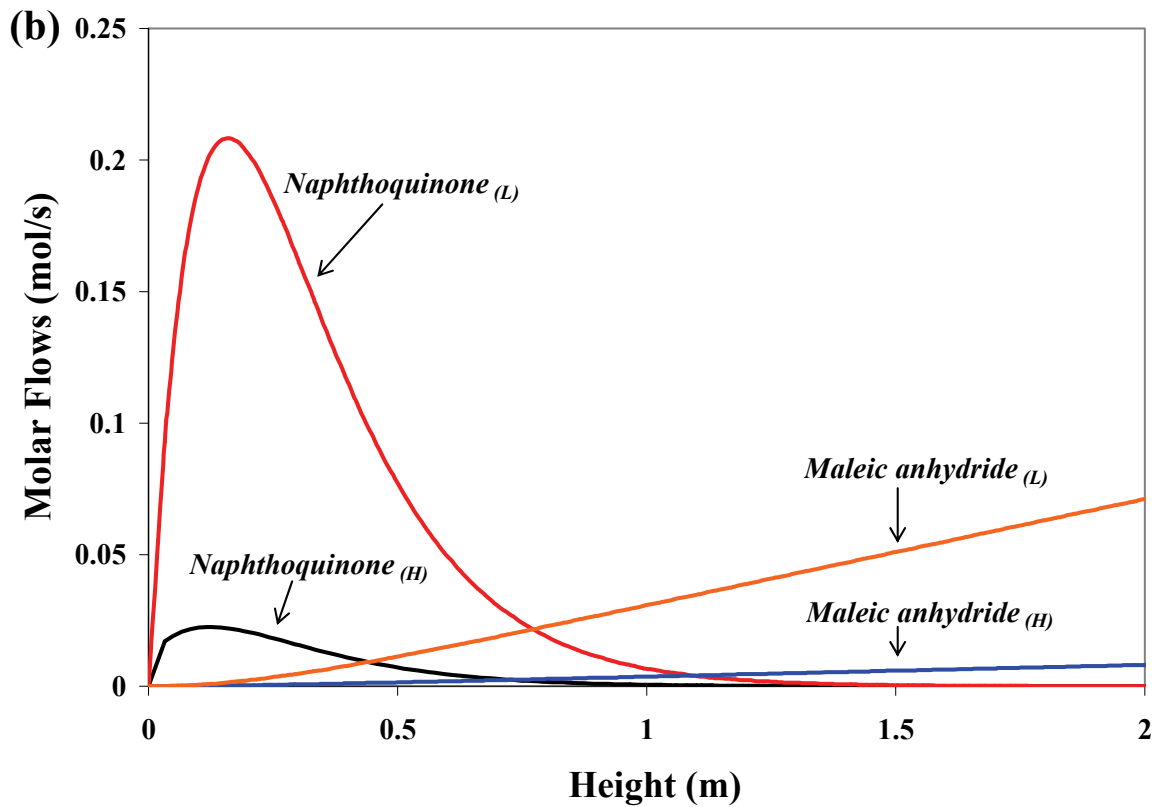
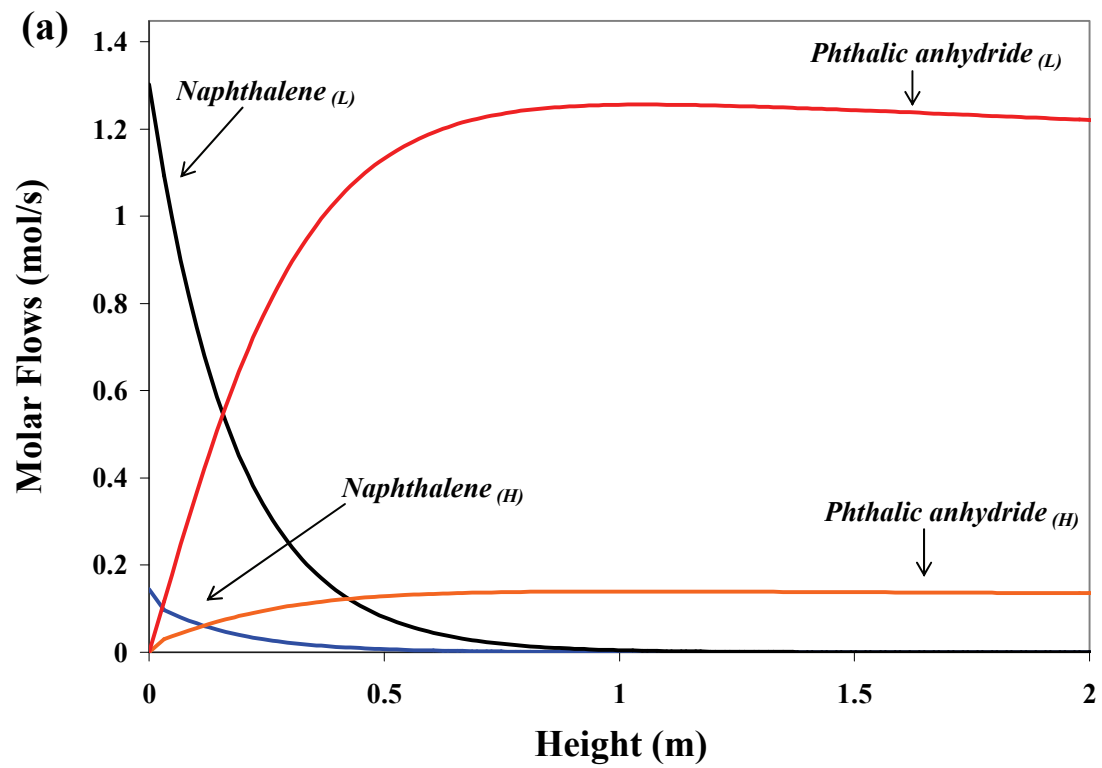


Figure 9.1. Molar flows in the low and high density phases vs reactor height for phthalic anhydride process in fluidized bed reactor. For reactor size and operating conditions, see (Johnsson *et al.*, 1987): (a) Molar flows of naphthalene and phthalic anhydride. (b) Molar flows of maleic anhydride and naphthoquinone.

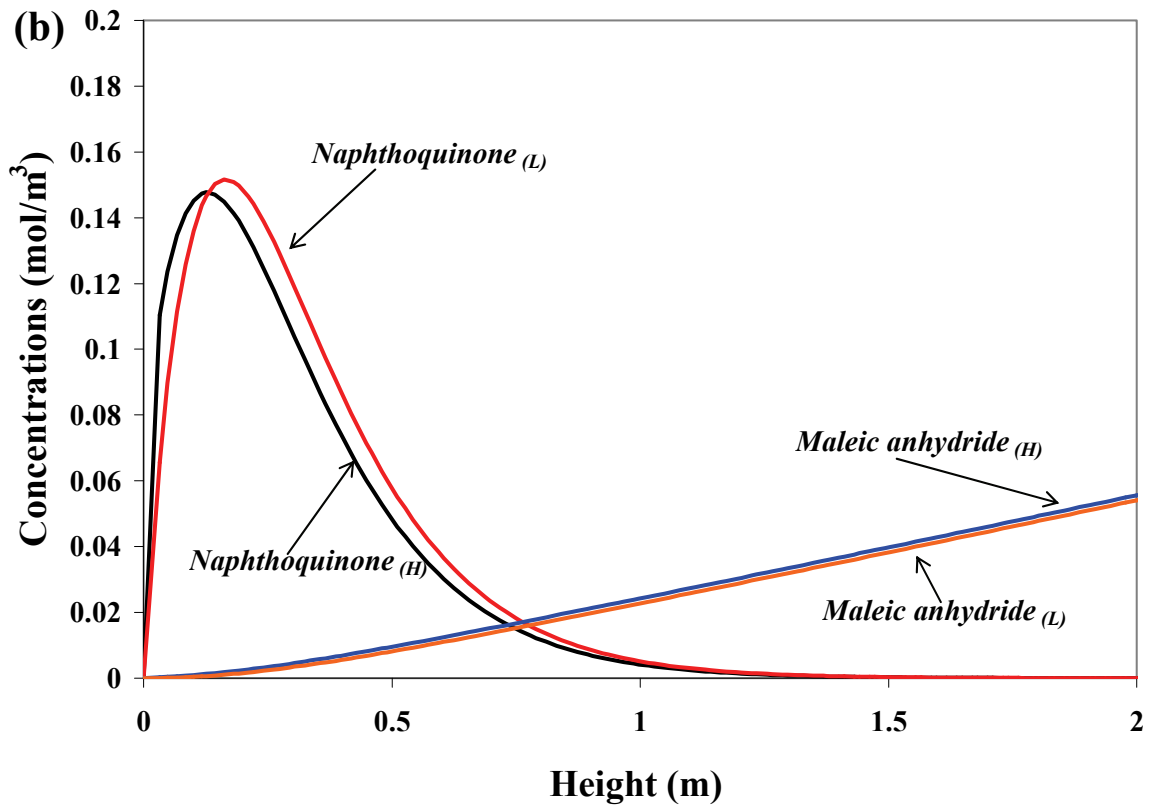
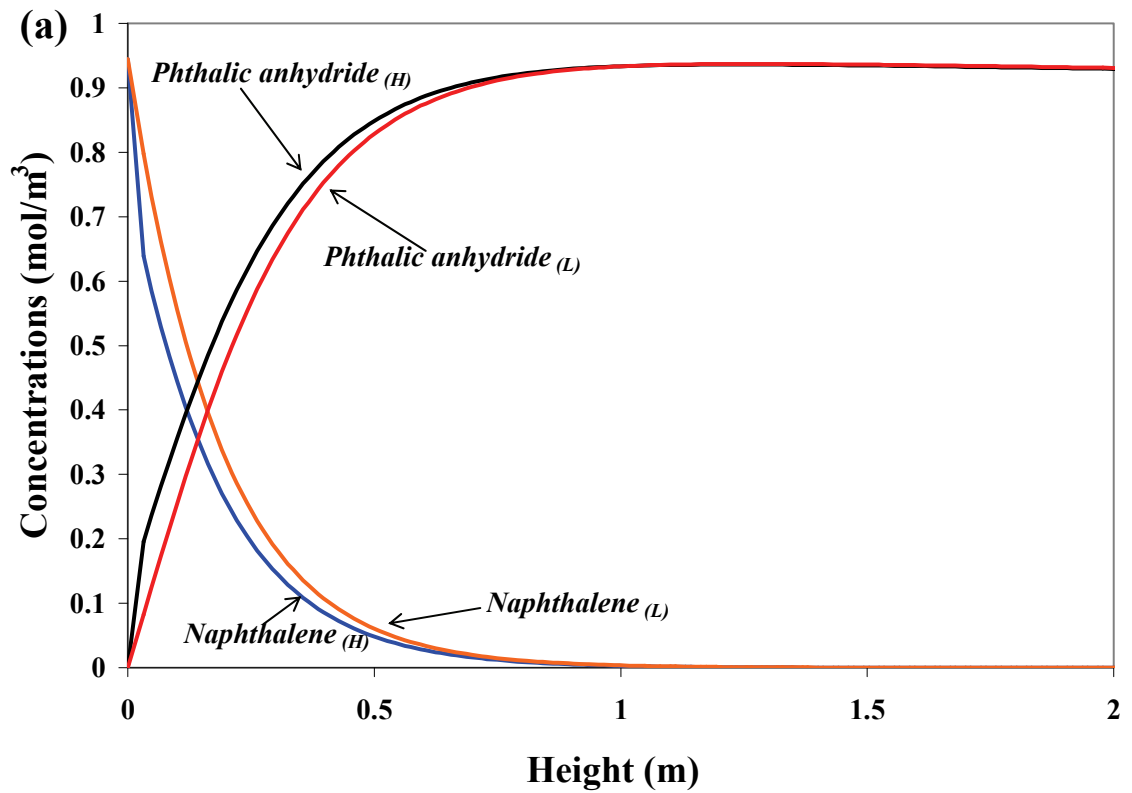


Figure 9.2. Species concentrations in the low and high density phases vs reactor height for phthalic anhydride process in fluidized bed reactor. For reactor size and operating conditions, see (Johnsson *et al.*, 1987): (a) Concentrations of naphthalene and phthalic anhydride. (b) Concentrations of maleic anhydride and naphthoquinone.

the lowest section of the bed. For example, the concentration of phthalic anhydride in the denser pseudo-phase is greater than in the bubbles. As this product diffuses, the concentration in the bubble-phase gradually increases, following the trend of the high-density pseudo-phase until the diffusion driving force dies out. In the case of the intermediate component naphthoquinone, something similar occurs for the initial steps of the reaction phenomena. When $(r_{1(H)} - r_{3(H)})$ is greatest, the concentration of naphthoquinone increases quickly. It is observed that the maximum concentration value for low-density in Figure 9.2 occurs after the maximum for high-density. This is expected since most of the reaction occurs in the emulsion phase. Then naphthoquinone is consumed at a rate $(r_{3(H)} - r_{1(H)})$, decreasing this intermediate concentration faster in the emulsion pseudo-phase. The interphase diffusion turns out to be fast, making the concentrations uniform in both pseudo-phases beyond the lowest section of the bed.

Figure 9.3 shows that the pressure decreases rapidly and linearly with height. The overall pressure drop is modest showing one of the advantages of fluidized bed reactors. Figure 9.3 also shows rapid conversion of naphthalene in the lower part of the reactor. The maximum conversion approaches 100%, in agreement with the values reported in the literature (Johnsson et al., 1987; Bolthrunis, 1989) for this industrial reactor of 99.9%. The predicted phthalic anhydride yield is approximately 75%, in reasonable agreement with measured values (Johnsson et al., 1987; Bolthrunis, 1989) of around 80%.

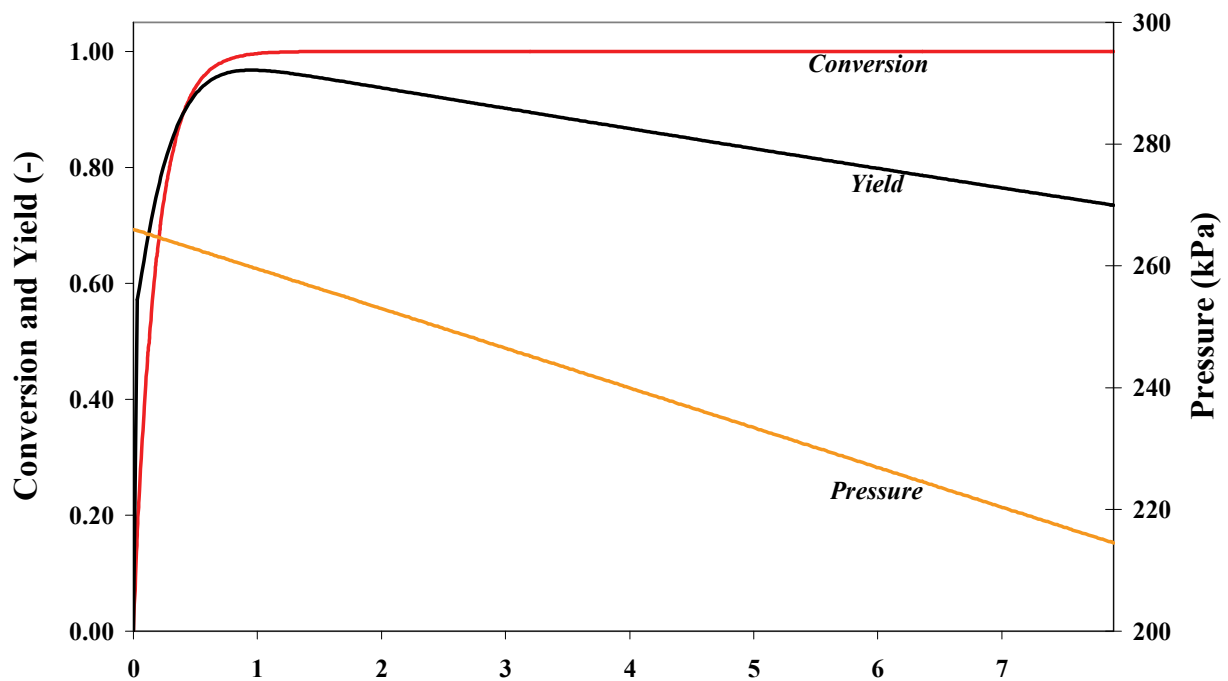


Figure 9.3. Conversion, yield and pressure vs reactor height. For reactor size and operating conditions, see (Johnsson et al., 1987).

From the shape of these curves one might suggest that a shorter reactor may give the same naphthalene conversions reducing the formation of total oxidation products, thus increasing the phthalic anhydride yield. Heat transfer requirements should be considered in order to determine the optimum/safe reactor height.

9.4. Conclusions

A direct application of the generalized model is presented in this chapter. The production of phthalic anhydride from naphthalene in an industrial fluidized-bed reactor is simulated under isothermal conditions. The model usefulness is once again proved for a different reacting system. The results show reasonable agreement with what is available in the literature using simple reaction kinetics.

9.5. References

- Bolthrunis, C.O. (1989). An industrial perspective on fluid bed reactor models. *Chem. Eng. Prog.*, 85, 51-54.
- DeMaria, F., Longfield, J.E. and Butler, G. (1961). Catalytic reactor design. *Ind. Eng. Chem.*, 53, 259.
- Johnsson, J.E., Grace, J.R. and Graham, J.J. (1987). Fluidized-bed reactor model verification on a reactor of industrial scale. *AIChE J.*, 33, 619-627.
- Mahecha-Botero, A., Grace, J.R., Elnashaie, S.S.E.H. and Lim, C.J. (2007a). A comprehensive approach to reaction engineering. *Int. J. Chem. Reactor Eng.*, 5: A17.

10. GLOBAL DISCUSSION, CONCLUSIONS AND RECOMMENDATIONS FOR FUTURE WORK

10.1. Global Discussion

In this thesis a comprehensive methodology is proposed and developed to study fluidized-bed reactors. This methodology starts from basic concepts and is demonstrated to be useful to tackle several complex problems, such as the coupling of modelling and experimental programs. Furthermore the work presented in Appendix G shows how this methodology can be applied to standard reaction engineering problems. A novel sophisticated computational model is developed to study fluidized-bed reactors for various chemical processes with special emphasis on clean energy production in the form of hydrogen fuel. Concomitantly, an experimental program with a pilot prototype reactor for the efficient generation of ultra-pure hydrogen was developed to advance the state of the art on fluidized-bed membrane reactors (FBMR) and to validate the general model.

The novel prototype fluidized-bed membrane reactor was assembled, commissioned and operated under steam methane reforming and autothermal reforming conditions, with and without active membranes, under a variety of operating conditions. The reactor concept was successfully demonstrated, suggesting that it can be applied for larger systems with high performance and efficiency. Introduction of air at the top of the dense bed improved the hydrogen production by reducing the nitrogen penalty during ATR operation. Increasing the pressure difference between the reactor and the permeate side of the membranes favourably affected membrane hydrogen production. The overall reactor performance was dominated by the available membrane area, as demonstrated by the fact that pure hydrogen production almost remained constant when the methane feed rate was changed. Hydrogen purities up to 99.995% were obtained free of carbon monoxide, indicating suitability for PEM fuel cells. Also a H_2/CH_4 yield of 3.03 was achieved under SMR conditions, above the required limit for practical application since the remaining unreacted gases can be easily utilized in a combustor for preheating the feed, making the FBMR promising for energy generation.

A comprehensive fluidized-bed reactor model was developed at a higher level of sophistication than in available literature models, by considering two pseudo-phases (high- and low- density) in two regions (dense bed and freeboard) accounting for local variations of species

concentrations, volumetric flow, solids content, pressure, mass transfer parameters, balancing mass transfer, reactor geometry, membrane permeation and feed distribution, among other phenomena. The model is applied to specific cases by the elimination of all the terms that could be justifiably neglected in a specific case. Model predictions suggest that heat dispersion dominates the fluidized-bed reactor temperature profile during adiabatic operation. For small vessels the temperature profile is dominated by heat losses due to the large surface area. The model demonstrated that equilibrium conversion is affected by local temperature variations when reaction kinetics are fast enough.

The pressure in the reactor decreases nearly linearly with height within the dense region for fluidized-beds operating in the bubbling or turbulent regime, but more gradually in the freeboard region where the solids holdup decays exponentially. Increasing the catalyst content leads to a faster approach to equilibrium.

A novel method for distributing gaseous reactants at different heights was developed and simulated successfully. A numerically generated pulse was introduced to account for additional reactant supply. This method allowed the effect of reactant distribution to be investigated. Numerical simulation confirms that introducing some air above the membranes successfully reduces the nitrogen dilution penalty, with positive impact on reactor performance. The simulation also provides a means of determining the optimal number and location of membrane surfaces in FBMRs.

Balancing interphase mass transfer was found to be essential for the model predictions to avoid issues such as bed de-fluidization. The model does not require any adjustable parameters. Its predictions result from fundamental derivations, two-phase theory analysis and hydrodynamic correlations from the literature. It is likely that the accuracy of the model could be further improved by introducing more realistic membrane parameters for fluidization conditions. When comparing experimental measurements with model predictions, the match is reasonably good given the limitations of the experimental data (e.g. reverse reaction in plant data, as well as limitations in characterizing the hydrogen removal). Modelling was also carried out to determine the best flow regime for operating fluidized-bed membrane reactors. It was found that turbulent fluidized-beds give some performance improvement over bubbling beds since they are not limited by interphase mass transfer. Nevertheless, the bubbling regime has some advantages in providing a less abrasive environment for the membranes.

The generalized model was applied to a variety of systems. When dynamic simulations were required, different time scales were found to be important. Knowledge of the underlying time scales was used to simulate the slower phenomena assuming that the faster dynamics reached a pseudo-steady state without introducing significant errors. Overall, comprehensive modelling is shown to be a powerful tool for simulating complex processes like FBMR steam methane reforming.

10.2. Conclusions

The main conclusions of the thesis are:

- An original methodology is developed to investigate fluidized-bed reactors. This describes the required steps to an experimental design for model validation.
- A novel experimental fluidized-bed membrane reactor concept was successfully demonstrated, providing high performance and efficiency. Process variables such as top air flow, membrane area and pressure diving force between the reactor and membranes had a positive effect on hydrogen production and process efficiency. Hydrogen purities $\geq 99.995\%$, and H_2/CH_4 yield of 3.03 were obtained.
- A novel comprehensive fluidized-bed computational reactor model was developed without any adjustable parameters. It considers two pseudo-phases (high- and low-density) in two regions (dense bed and freeboard) accounting for local variations of species concentrations, volumetric flow, solids content, pressure, mass transfer parameters, balancing mass transfer, reactor geometry, membrane permeation and feed distribution.
- The general model is applied to several specific processes.
- The model predicts distributed temperature profiles that for adiabatic cases are dominated by heat dispersion due to the circulation of hot solids inside the reactor.
- Fast chemical kinetics allow for equilibrium conversions just above the distributor in steam reformers. When membranes are introduced, the chemical equilibrium is shifted forward. If complete conversion is achieved below a certain membrane level, membrane utilization at higher levels becomes negligible.

- Model predictions as well as experimental data confirm that introducing air above the membranes increases reactor performance.
- Balancing interphase mass transfer is required to correctly represent the fluidization conditions of a reactor if there is a large change in volumetric flow.
- Phase specific variables such as the solids content, volumetric flow and membrane removal determine the chemical reactions in both phases. For instance the H-phase is predicted to have faster conversion due to its large solids content, small volumetric flow and large contact with membrane surfaces.
- Modelling suggests that turbulent beds give better performance than other flow regimes since they are not limited by mass transfer to the H-phase.
- Different time scales apply to heat transfer and diffusion-reaction. Understanding these time scales can be useful for model reduction.
- Overall model predictions match reasonably well with experimental data. The new general model is a powerful tool for simulating complex fluidized-bed reactors.

10.3. Outlook and Recommendations for Future Work

10.3.1. Modelling

1) The comprehensive model accounts for most features encountered in catalytic fluidized-bed reactors. Improvements to the software are needed to apply the model in a user-friendly manner. Simulations based on *COMSOL Multiphysics* suffered from limitations in numerical solvers. For instance, features such as fast chemical kinetics, non-linear expressions, multidimensional/complex geometries, stream recycling and wide-range case studies (e.g. large variation of dimensionless groups such as Péclet and Reynolds numbers) were problematic due to software crashes. Computational considerations such as RAM and simulation time also continued to be issues. Work is needed to create a more robust platform that can provide comprehensive modelling executing a graphical user interface (GUI).

2) The current model does not rely on adjustable parameters, but some issues are problematic, and have not been resolved by the fluidization community. Considerable developments are needed to characterize such phenomena as:

- *Solids content of the L-phase*: This parameter does not have a robust correlation, but it can have a significant impact on the simulation results, especially for fast reactions.
- *Interphase balancing interphase mass transfer (crossflow)*: This phenomenon is critical for the model predictions as explained above, but not fully understood.
- *Membrane characterization*: Membrane reformers are typically limited by the available membrane flux. Membrane characterization available to date comes from environments free of particles.

10.3.2. Future of Reactor Modelling

This thesis deals with a model that can tackle complex reacting systems. Nevertheless, its momentum/pressure balance is highly oversimplified. It relies on a compilation of correlations to calculate hydrodynamic parameters. A more fundamental approach to the gas/solid momentum balance is desirable. Although the vast majority of computational fluid dynamic (CFD) models deal only with hydrodynamic analysis of fluidized beds (Enwald *et al.*, 1996), considerable progress with reacting flow has been realized in recent years. However, most progress has been for simple chemical systems (Das *et al.*, 2004) such as ozone decomposition (Syamlal and O'Brien, 2003; Therdthianwong *et al.*, 2003; Hansen *et al.*, 2004; Dong *et al.*, 2008) and chemical vapour deposition of silicon (Cadoret *et al.*, 2007; Reuge *et al.*, 2009). This is probably due to the numerical and computational demands associated with such issues as the number of mole balances, varying total molar flowrate, nonlinear reaction kinetics, fluid expansion/compression due to reaction and non-isothermal considerations. In addition, Grace and Taghipour (2004) identified a number of issues regarding validation of CFD codes, suggesting that simpler hydrodynamic calculations, similar to those implemented in this thesis currently give at least the same level of accuracy. A number of recent works tackle more complex chemical systems (Gao *et al.*, 1999; Mao *et al.*, 2004; Jung and Gamwo, 2008). Deen *et al.* (2007) suggest that discrete particle models could play a key role in future fluidized-bed hydrodynamic modelling.

The rapid increase in computational hardware power capability and the improvement and refinement of numerical techniques provide an exciting environment for more predictive CFD models. Future fluidized-bed reactor modelling will likely require the implementation of CFD models coupled with the reaction engineering models (mole and energy balances) based on models similar to those presented in this thesis.

10.3.3. Experimental Set-up

The following suggestions may help future experimental campaigns:

- 1) Membranes characterization should be characterized in a hot environment containing the chemical mixture and catalyst powder encountered during reforming.
- 2) The residence time in the sampling lines was high in our experiments. Multiple gas chromatographs are recommended located as close as possible to the reformer with very fine sintered metal filters to remove all catalyst in the lines.
- 3) This thesis predicts the influence of fluidization flow regimes on FBMR performance. It would be desirable to determine whether turbulent and fast fluidization could be viable alternatives to bubbling fluidization by conducting an experimental program at higher gas velocities.
- 4) Considerable reverse reaction occurred in the freeboard region of the experimental reactor in this project. This should be addressed to increase reactor conversion, e.g. by:
 - *Heating the freeboard.* This may be done with external ring heaters similar to those at the base of the reactor. An internal coiled heater could also be installed.
 - *Quenching reactor off-gas (ROG) line.* The current line is well insulated. If the insulation is removed, the output gas can be cooled quickly.
 - *Improving the ROG filters.* This could avoid catalyst fines in the ROG line.

10.3.4. Future of Reforming Technologies

More studies are required for the technology introduced in Appendix F. The ability to produce pure hydrogen, coupled with CO₂ capture, could be a major breakthrough in the future of the energy industry. The production of hydrogen is the most greenhouse-gas-intensive stage in a hydrogen economy. If most of the carbon dioxide can be captured at source, it could facilitate more acceptable use of hydrocarbons for energy generation.

10.4. References

- Cadoret, L., Reuge, N., Pannala, S., Syamlal, M., Coufort, C. and Caussat, B. (2007). Silicon CVD on powders in fluidized bed: Experimental and multifluid Eulerian modelling study. *Surf. Coat. Technol.*, 201, 8919-8923.
- Das, A.K., De Wilde, J., Heynderickx, G.J., Marin, G.B., Vierendeels, J. and Dick, E. (2004). CFD simulation of dilute phase gas–solid riser reactors: Part I-a new solution method and flow model validation *Chem. Eng. Sci.*, 59, 167-186.
- Deen, N.G., Van Sint Annaland, M., Van der Hoef, M.A. and Kuipers, J.A.M. (2007). Review of discrete particle modeling of fluidized beds. *Chem. Eng. Sci.*, 62, 28-44.
- Dong, W., Wang, W. and Li, J. (2008). A multiscale mass transfer model for gas-solid riser flows: Part II - Sub-grid simulation of ozone decomposition. *Chem. Eng. Sci.*, 63, 2811-2823.
- Enwald, H., Peirano, E. and Almstedt, A.E. (1996). Eulerian two-phase flow theory applied to fluidization. *Int. J. Multiphase Flow*, 22, 24-66.
- Gao, J., Xu, C., Lin, S., Yang, G. and Guo, Y. (1999). Advanced model for turbulent gas–solid flow and reaction in FCC riser reactors. *AIChE J.*, 45, 1095-1013.
- Grace, J.R. and Taghipour, F. (2004). Verification and validation of CFD models and dynamic similarity for fluidized beds. *Powd. Technol.*, 139, 99-110.
- Hansen, K.G., Solberg, T. and Hjertager, B.H. (2004). A three-dimensional simulation of gas/particle flow and ozone decomposition in the riser of a circulating fluidized bed *Chem. Eng. Sci.*, 59, 5217-5224.
- Jung, J. and Gamwo, I.K. (2008). Multiphase CFD-based models for chemical looping combustion process: Fuel reactor modeling. *Powd. Technol.*, 183, 401-409.
- Mao, D., Edwards, J.R., Kuznetsov, A.V. and Srivastava, R.K. (2004). Three-dimensional numerical simulation of a circulating fluidized bed reactor for multi-pollutant control. *Chem. Eng. Sci.*, 59, 4279-4289.

Reuge, N., Cadoret, L. and Caussat, B. (2009). Multifluid Eulerian modelling of a silicon fluidized bed chemical vapor deposition process: Analysis of various kinetic models. *Chem. Eng. J.*, 148, 506-516.

Syamlal, M. and O'Brien, T.J. (2003). Fluid dynamic simulation of O₃ decomposition in a bubbling fluidized bed. *AIChE J.*, 49, 2793-2801.

Therdthianwong, A., Pantarak, P. and Therdthianwong, S. (2003). Modeling and simulation of circulating fluidized bed reactor with catalytic ozone decomposition reaction. *Powd. Technol.*, 133, 1-14.

APPENDIX A. NUMERICAL SOLVERS

A.1. Introduction

This appendix presents a concise description of the numerical solvers implemented for the solution of the models presented in this thesis. The main features of the Matlab and COMSOL Multiphysics equation solvers are described below.

A.2. Solution of Systems of Ordinary Differential Equations (ODEs)

When a model is represented by a system of ordinary differential equations, it can be solved using *ode* Matlab routines. These routines have been optimized for solving different types of systems depending on their stiffness (Matlab, 2007). Most of these routines are variations of the classic Runge-Kutta integration formula (Elnashaie and Uhlig, 2007). Details about other integration methods (including many features such as adaptive step-size) are described in the Matlab documentation as well as in: (Shampine and Reichelt, 1997; Ashino *et al.*, 2000; Shampine *et al.*, 2005). Although the most common Runge-Kutta method is of order four (Press *et al.*, 2007), its formula can be generalized as follows:

To solve a system of differential equations such as:

$$\frac{dY}{dt} = f(t, Y), \tag{A.1}$$

with the initial condition: $Y(t_0) = Y_0$

where Y is the vector of state variables and t is the independent variable. The Runge-Kutta method suggests that:

$$Y_{n+1} = Y_n + h \cdot \sum_{i=1}^s b_i \cdot k_i, \tag{A.2}$$

$$t_{n+1} = t_n + h,$$

where Y_{n+1} is the numerical approximation of $Y(t_{n+1})$ and h is the integration step-size.

Additionally:

$$k_1 = f(t_n, Y_n), \tag{A.3}$$

$$\begin{aligned}
k_2 &= f(t_n + c_2.h, Y_n + a_{21}.h.k_1), \\
k_3 &= f(t_n + c_3.h, Y_n + a_{31}.h.k_1 + a_{32}.h.k_2), \\
&\vdots \\
k_s &= f(t_n + c_s.h, Y_n + a_{s1}.h.k_1 + a_{s2}.h.k_2 + \dots + a_{s,s-1}.h.k_{s-1})
\end{aligned}$$

where a_{ij} , b_i and c_i are coefficients specific to each variation of the Runge-Kutta method.

A.3. Solution of Systems of Partial Differential Equations (PDEs)

A system must be represented by a set of partial differential equations if its number of independent variables is greater than one. To solve systems of PDEs on a given geometry, a mesh should be defined (an example of a mesh created using COMSOL Multiphysics is given in Figure A.1.). Subsequently, the finite element method (FEM) discretizes the equations on the mesh and builds equations for the discrete approximation of the solution (Zimmerman, 2004). After a process called the FE-assembly, PDEs are transformed into a system of algebraic equations. Other details about this process can be found in: (Owen and Hinton, 1980; Zimmerman, 2004; COMSOL, 2006; Zimmerman, 2006). COMSOL Multiphysics includes the PDE solvers described in Table A.1 which can use one of the linear system solvers from Table A.2.

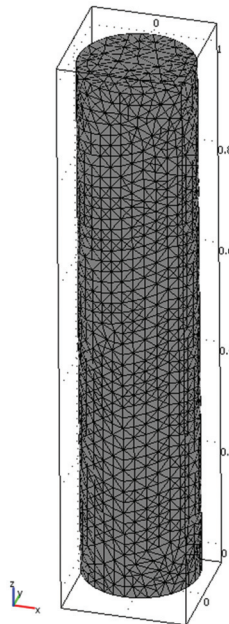


Figure A. 1. Example of a three-dimensional mesh created using COMSOL Multiphysics.

Table A. 1. COMSOL Multiphysics PDE solvers. Adapted from (COMSOL, 2006).

PDE Solver	Solver Applicability
Stationary linear	Linear steady-state models
Stationary nonlinear	Non-linear steady-state models
Time-dependent	Time-dependent (dynamic) models (linear or non-linear)
Eigenvalue solver	Eigenvalue problems
Parametric linear	Linear steady state models depending on a parameter
Parametric nonlinear	Non-linear steady-state models depending on a parameter
Adaptive	Steady-state models (linear or non-linear) using adaptive mesh refinement

*The models of this thesis were solved using parametric nonlinear, time-dependent or stationary nonlinear solvers.

Table A. 2. COMSOL Multiphysics linear system solvers. Adapted from (COMSOL, 2006).

Linear System Solver	Abbreviation	Type of Solver	Solver Applicability*
Unsymmetric multifrontal sparse LU factorization package	UMFPACK	Direct	Unsymmetric models
Sparse object oriented linear equations solver	SPOOLES	Direct	Symmetric and unsymmetric models
Cholesky	TAUCS	Direct	Positive-definite models
Generalised minimum residual	GMRES	Iterative	Unsymmetric models
Conjugate gradients	N/A	Iterative	Positive-definite models
Geometric multigrid	N/A	Iterative	Elliptic or parabolic models

*The models of this thesis were commonly solved using GMRES when RAM was limiting. In some cases UMFPACK was also implemented.

A.4. Conclusions

An overview of key numerical solvers is presented in this appendix. Furthermore, references to important numerical techniques are also included for the solution of partial and ordinary differential equations.

A.5. References

Ashino, R., Nagase, M. and Vaillancourt, R. (2000). Behind and beyond the Matlab ODE suite. *Computers & Math. Appl.*, 40, 491-512.

COMSOL (2006). COMSOL documentation and multiphysics user's guide.

Elnashaie, S.S.E.H. and Uhlig, F. (2007). Numerical techniques for chemical and biological engineers using Matlab. A simple bifurcation approach. Springer, New York.

Matlab (2007). Matlab documentation.

Owen, D.R.J. and Hinton, E. (1980). A simple guide to finite elements. Pineridge Press, Swansea, U.K.

Press, W.H., Teukolsky, S.A., Vetterling, W.T. and B.P., F. (2007). Numerical recipes: The art of scientific computing. Cambridge University Press, New York.

Shampine, L.F. and Reichelt, M.W. (1997). The Matlab ODE suite. Siam J. Sci. Comput., 18, 1-22.

Shampine, L.F., Thompson, S., Kierzenka, J.A. and Byrne, G.D. (2005). Non-negative solutions of ODEs. Appl. Math. Comput., 170, 556-569.

Zimmerman, W.B.J. (2004). Process modelling and simulation with finite element methods. World Scientific Publishing, Singapore.

Zimmerman, W.B.J. (2006). Multiphysics modeling with finite element methods. World Scientific Publishing, Singapore.

APPENDIX B. PRESSURE VESSEL CALCULATIONS FOR FLUIDIZED-BED MEMBRANE REACTOR

B.1. Introduction

In this appendix, a pressure vessel calculation is presented for the FBMR of Chapter 3. This study was performed to estimate the approximate mechanical requirements of a reactor with flat flanges on the sides supported by bolts, in a non-conventional design. These calculations are initial estimates for the material mechanics of the vessel. Ultimately the mechanical design was performed by certified professionals with a much more complex/reinforced geometry as seen in Chapter 3. They also performed several pressure tests filling the vessel with pressurized water to ensure the safety of the vessel.

The vessel is designed to withstand a pressure of 1.0 MPa at a temperature of 650°C. The vessel dimensions are $X_R=50.8$ mm, $Z_R=95.25$ mm and $Z_R=2$ m as depicted in Figure B.1. The objectives of the present calculations are:

- 1) Find the required thickness of the walls for the vessel (W_R).
- 2) Find the number of bolts required to hold the walls (N_B).
- 3) Find the required thickness of the bolts.

B.2. Calculations

B.2.1. Wall Thickness

The reactor pressure (P) exerts a force on the walls. The effect of this pressure requires a mechanics of materials analysis. The mechanical analysis is done for a steel flange of cross-sectional area $X_R * W_R$. A schematic diagram is presented in Figure B.2.

The applied pressure consists of a distributed force (F) along the walls. This force produces a bending moment (M).

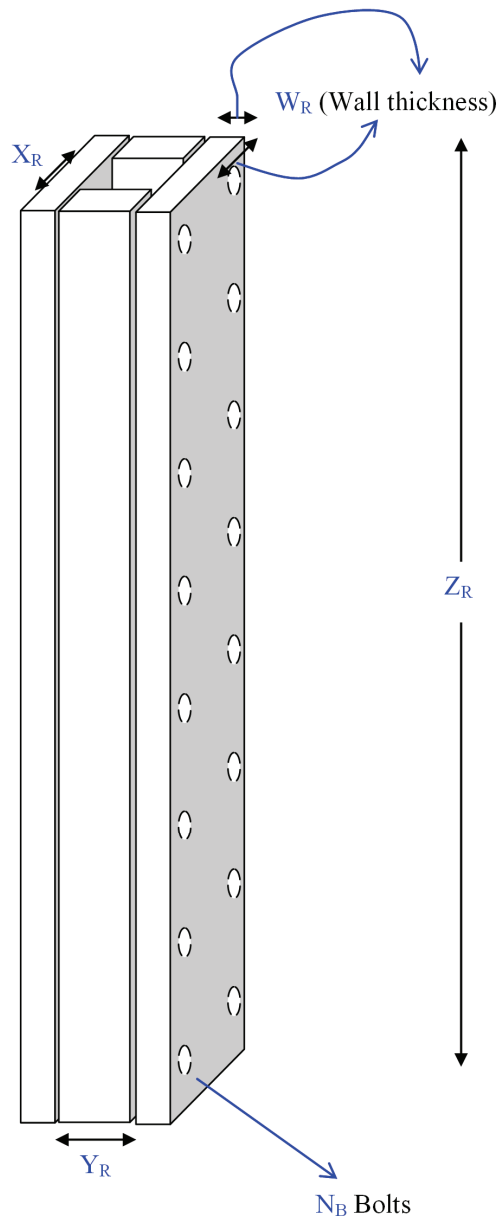


Figure B. 1. Schematic representation of FBMR flange.

A steady state forces balance on the material yields:

$$\sum Moments_z = 0$$

$$M_z + \int (-y\sigma_x)dA = 0, \text{ or,}$$

$$M = \int (y\sigma_x)dA$$

where σ_x is the applied normal stress. From mechanics of materials theory (Beer and Johnston, 1992) we have:

$$M = \frac{\sigma_m I}{C}$$

where σ_m is the normal stress exerted by the material subject to bending. For the rectangular section of material, its Moment of inertia is given by:

$$I = \frac{X_R \cdot W_R^3}{12}$$

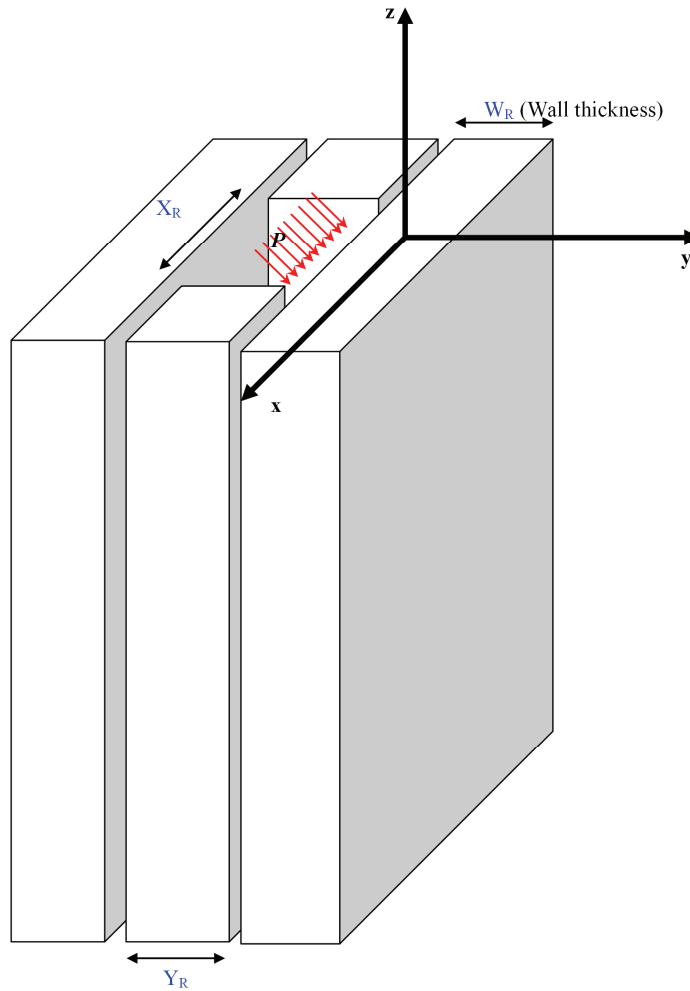


Figure B. 2. Schematic representation of the pressure force acting on the reactor walls.

The bending moment is given by:

$$M = \frac{\sigma_m \left(\frac{X_R \cdot W_R^3}{12} \right)}{\left(\frac{W_R}{2} \right)}$$

Solving for the wall thickness, we obtain:

$$W_R = \sqrt{\frac{6.M}{\sigma_m.X_R}}$$

The flange bending moment is illustrated in Figure B.3, and it is defined as:

$$M = F.\left(\frac{X_R}{2}\right)$$

where F is the effective force on the walls due to pressurization.

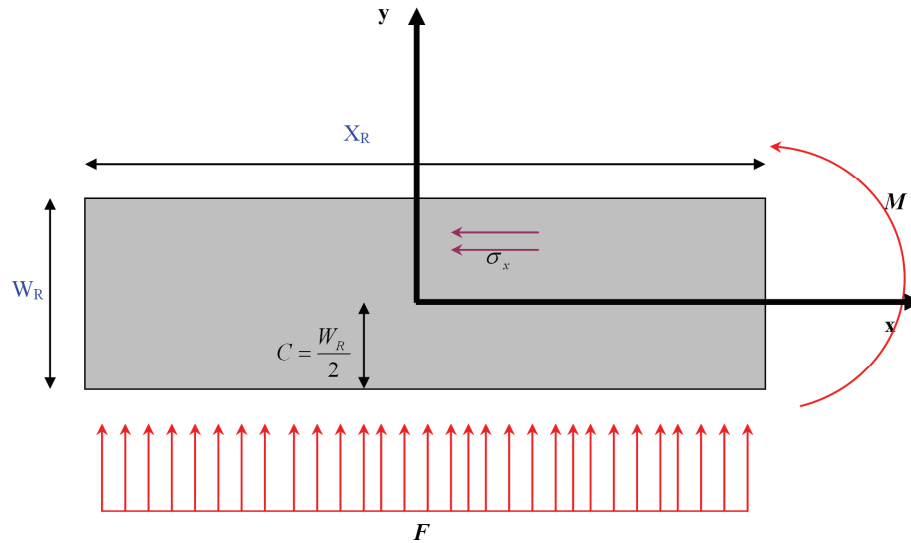


Figure B. 3. Bending moment on reactor walls.

$$M = P.A.\left(\frac{X_R}{2}\right), \text{ or,}$$

$$M = P.(X_R.Z_R).\left(\frac{X_R}{2}\right)$$

Also for σ_m we have from mechanics of materials theory:

$$\sigma_m = \frac{\sigma_F}{F_s}$$

where F_s and σ_F are taken from the literature. The properties of stainless steel AISI 316 are taken from (ssina.com, 2008). The Safety factor is recommended by Beer and Johnston (1992) to be in the range of 1.5 - 2.0. Here a safety factor of 2.0 is taken.

$$S_F = 2$$

$\sigma_F = 290$ MPa at room temperature, 152 MPa at 650°C

Replacing M and σ_m in the expression for the wall thickness we obtain:

$$W_R = \sqrt{\frac{6 \cdot \left(P \cdot (X_R \cdot Z_R) \cdot \left(\frac{X_R}{2} \right) \right)}{\left(\frac{\sigma_F}{F_s} \right) \cdot X_R}}$$

The above expression allows us to calculate the required wall thickness for a given set of design conditions. Using the required data we obtain:

$$W_R = \sqrt{\frac{6 \cdot \left(10 \cdot 101325 \text{ Pa} \cdot (5.08 \cdot 10^{-2} \text{ m} \cdot 2 \text{ m}) \cdot \left(\frac{5.08 \cdot 10^{-2} \text{ m}}{2} \right) \right)}{\left(\frac{290 \cdot 10^6 \text{ Pa}}{2} \right) (5.08 \cdot 10^{-2} \text{ m})}} = 0.47 \text{ m}$$

We conclude that the minimum required wall thickness is ~47 mm assuming room temperature. At an operating temperature of 650°C, the required wall thickness will be ~63 mm, which is close to the final flange thickness utilized in the FBMR.

B.2.1.1. Effect of temperature

Temperature reduces the mechanical strength of stainless steel. Figure B.4 depicts the decrease in tensile strength as temperature is increased. All calculations should keep in mind the dependence of mechanical properties on temperature. The dependence of required wall thickness on operating temperature is depicted on Figure B.5.

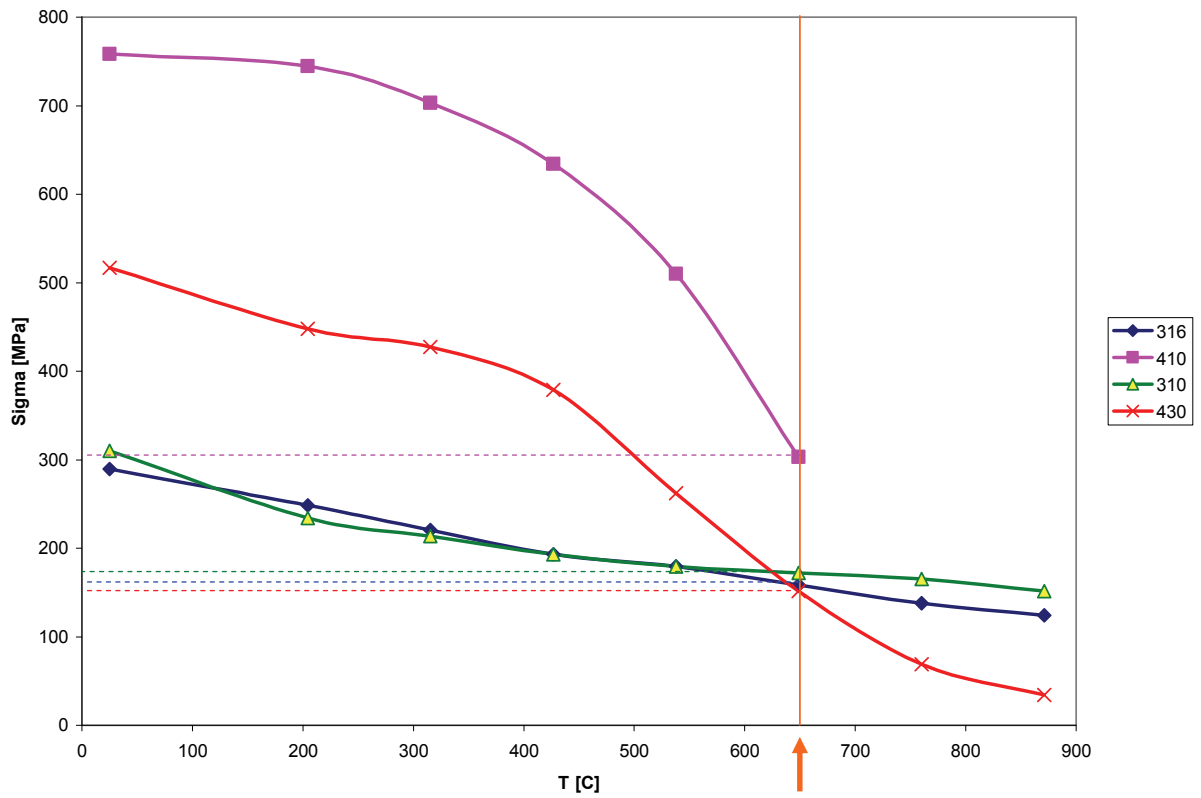


Figure B. 4. Tensile strength vs temperature for stainless steel. (The orange line is the maximum temperature tolerable by the H₂ membranes).

Wall thickness vs Temperature

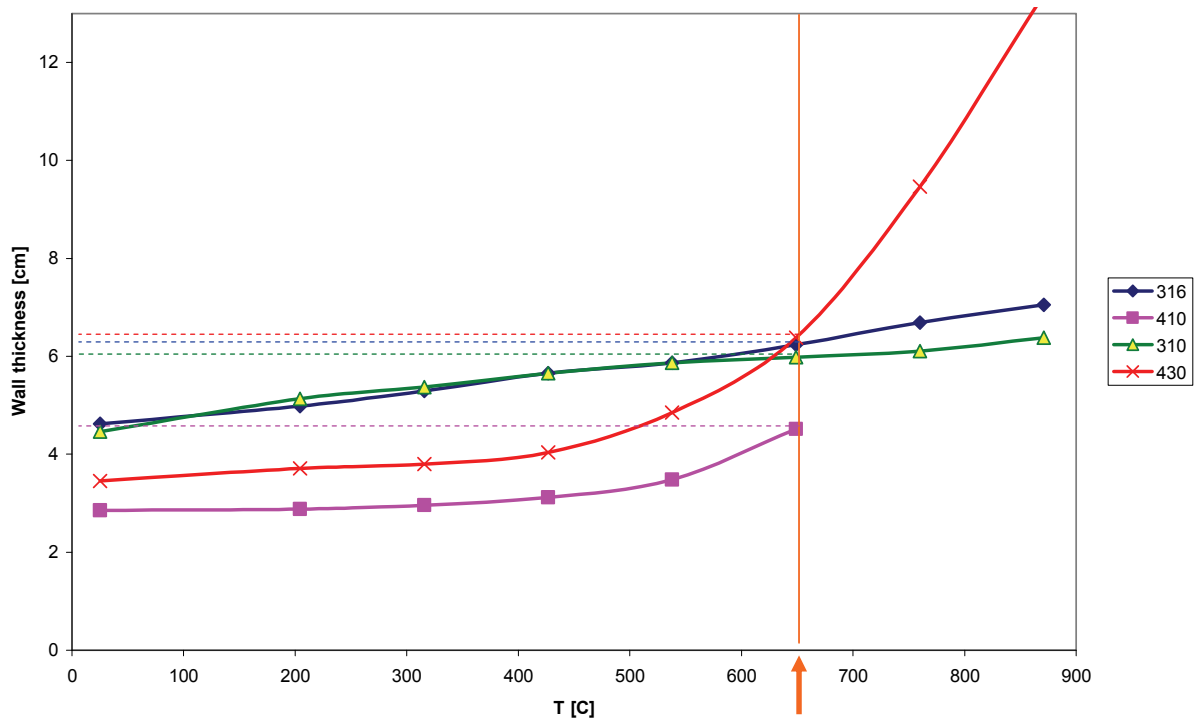


Figure B. 5. Required wall thickness vs temperature for stainless steel. (The orange line is the maximum temperature tolerable by the H₂ membranes).

B.2.2. Distance Between Bolts

Using the above equations, we have:

$$M = \frac{\sigma_m \cdot \left(\frac{dist_B \cdot W_R^3}{12} \right)}{\left(\frac{W_R}{2} \right)}$$

For our case the bending moment is defined as:

$$M = F \cdot \left(\frac{Z_R}{2} \right)$$

where F is the effective force on the walls due to pressurization.

$$M = P \cdot A \cdot \left(\frac{Z_R}{2} \right)$$

which is equivalent to:

$$M = P \cdot (X_R \cdot Z_R) \cdot \left(\frac{Z_R}{2} \right)$$

Solving for the distance between bolts we obtain:

$$dist_B = \frac{6 \cdot \left(P \cdot (X_R \cdot Z_R) \cdot \left(\frac{Z_R}{2} \right) \right)}{\left(\frac{\sigma_F}{F_s} \right) \cdot W_R^2}$$

The above expression allows the calculation of the required distance between bolts for a given set of design conditions. Using the required data we obtain:

$$dist_B = \frac{6 \cdot \left(10 \cdot 101325 \text{ Pa} \cdot \left(5.08 \cdot 10^{-2} \text{ m} \cdot 2 \text{ m} \right) \cdot \left(\frac{2 \text{ m}}{2} \right) \right)}{\left(\frac{152 \cdot 10^6 \text{ Pa}}{2} \right) \cdot (6.3 \cdot 10^{-2} \text{ m})^2} = 0.34 \text{ m}$$

We can conclude that the required distance between bolts is 0.34 m. According to the actual number of bolts (See section below B.2.3) the minimum distance required would be 0.28 m.

B.2.3. Number of Bolts

The required number of bolts is:

$$N_B = \left\lceil 2 \cdot \left(\frac{Z_R}{dist_B} \right) \right\rceil + 2$$

It is then recommended to have 14 bolts distributed in 7 pairs on both sides of the walls.

B.2.4. Bolt Size

In order to size each bolt, we distribute the force applied to the reactor walls among the number of available bolts.

$$F_B = \frac{F}{N_B}$$

The force applied to each bolt is given by:

$$F_B = A_B \cdot \sigma_B$$

Including the cross-sectional area of each bolt, we obtain:

$$F_B = \left(\frac{\pi}{4} d_B^2 \right) \cdot \sigma_B$$

Solving for the diameter of the bolt, we obtain:

$$d_B = \sqrt{\left(\frac{4 \cdot F_B}{\pi \cdot \sigma_B} \right)}$$

Replacing the value of F_B and σ_B , we obtain:

$$d_B = \sqrt{\left(\frac{4}{\pi} \right) \cdot \left(\frac{F}{N_B} \right) \cdot \left(\frac{1}{\sigma_F \cdot S_F} \right)} = \sqrt{\left(\frac{4}{\pi} \right) \cdot \left(\frac{P \cdot (X_R \cdot Z_R)}{N_B} \right) \cdot \left(\frac{1}{\sigma_F \cdot S_F} \right)}$$

The above expression allows us to calculate the required bolt diameter for a given set of design conditions. Using the required data we obtain:

$$d_B = \sqrt{\left(\frac{4}{\pi} \right) \cdot \left(\frac{10 * 101325 \text{ Pa} \cdot (5.08 * 10^{-2} \text{ m} \cdot * 2 \text{ m})}{14} \right) \cdot \left(\frac{1}{152 * 10^6 \text{ Pa} * 2} \right)} = 0.0056 \text{ m}$$

We can conclude that the required diameter of bolts is 5.6 mm. This number should be increased to match a commercial value.

B.3 Notation

A	Area, (m ²)
C	Distance to the neutral plane (m)
d_B	Diameter of bolt (m)
dis_B	Distance between bolts (m)
I	Moment of inertia of the material's surface (m ⁴)
F	Force (N)
M	Bending moment (N.m)
N_B	Number of bolts (dimensionless)
P	Pressure (Pa)
W_R	Flange thickness (m)
X_R	Reactor depth (m)
Y_R	Reactor width (m)
Z_R	Reactor height (m)
x, y, z	Rectangular coordinates, (m)
Greek Symbols	
σ	Normal stress (N/m ²)
Subscripts	
B	Bolt
m	Material
R	Reactor

B.4. Conclusions

Preliminary calculations for the pilot fluidized-bed membrane reactor are described in this appendix. A number of mechanical variables are calculated based on basic mechanics of materials calculations. It is found that the required flange thickness is proportional to the square root of the reactor pressure. Furthermore this wall thickness is also proportional to the square root of the reactor vessel width and height. The final width implemented in the FBMR using a design by pressure vessel design professionals is ~70 mm, which is very similar to the size found in these calculations. Nevertheless, the actual design includes many more bolts in a different layout.

B.5. References

Beer, F.P. and Johnston, E.R. (1992). Mechanics of materials. McGraw-Hill.

ssina.com. (2008). Properties of stainless steel. Retrieved December 10, from <http://www.ssina.com/composition/temperature.html>.

APPENDIX C. COMMISSIONING OF FLUIDIZED-BED MEMBRANE REACTOR

C.1. Introduction

In this appendix, a concise description of reactor commissioning is presented for the FBMR described in Chapter 3. The commissioning process tests the performance of the pilot reactor components and systems at *Membrane Reactor Technologies Ltd* (MRT). The consistency of the constructed parts is tested as well as their safety requirements to ensure that it meets its design specifications.

C.2. Cold Commissioning

The major concern about a pressurized vessel is its safety. The reactor operates at a pressure of 1.0 MPa, and a number of tests should be made in order to warrant a safe operation. In addition to the obvious safety concerns, the occurrence of leaks should also be tested at the many flanges and compression fittings. Due to the small scale reactor and more importantly, the presence of flammable gases, leaks must be prevented at all times. The proposed steps in order to safely test the reactor for leaks are summarized in Table C.1.

Table C. 1. Cold commissioning test procedure

#	Test	Procedure
(1)	Hydro-Test for the reactor vessel	The constructed reactor vessel is pressurized using water. Water is chosen for safety reasons due to its very low compressibility. The vessel may be exposed to several times its operating pressure to check the reliability of the welding. This test is performed by the constructors of the pressure vessel.
(2)	Pressurize to 30% of the operating pressure	Increase the reactor pressure to 0.3 MPa. Afterwards, depressurize the system. Use Snoop.
(3)	Pressurize to 60% of the operating pressure	Increase the reactor pressure to 0.6 MPa. Afterwards, depressurize the system. Use Snoop.
(4)	Pressurize to 100% of the operating pressure	Increase the reactor pressure to 1.0 MPa. Afterwards, depressurize the system. Use Snoop.

Tests #2 and higher were performed after the installation of the reactor vessel. The pressure is increased using nitrogen and decreased gradually to allow for compression/expansion of parts. No catalyst is introduced to the reactor. This procedure verifies if there are any leaks in the

fittings and pipe connections. During each test, Snoop was used (or a soap/water solution) to check for bubbles on the connections.

C.3. Hot Commissioning

Stainless steel strength is greatly reduced at high temperatures. It is important to verify the integrity of the system when the temperature is elevated. The decay in the tensile strength of different stainless steel metals is depicted in Figure A.4. At temperatures as high as 650°C, the material strength is much lower than at room temperature. Figure A.5 is included to show the required wall thickness for a square pressure vessel as a function of temperature.

The proposed steps in order to safely test the reactor are summarized in Table C.2. The temperature is increased using electrical heaters and decreased gradually to allow for compression/expansion of parts. No catalyst is introduced to the reactor. This procedure verifies the integrity of the system at high temperature. In addition, an emergency reactor shut-down was tested.

Table C. 2. Hot commissioning test procedure

#	Test	Procedure
(1)	Heat up to 30% of the operating temperature	Increase the reactor temperature to 160°C at 0.1 MPa. Afterwards, pressurize the system to 1.0 MPa.
(2)	Heat up to 60% of the operating temperature	Increase the reactor temperature to 330°C at 0.1 MPa. Afterwards, pressurize the system to 1.0 MPa.
(3)	Heat up to 100% of the operating temperature	Increase the reactor temperature to 600°C at 0.1 MPa. Afterwards, pressurize the system to 1.0 MPa.

C.4. Start-Up and Experimental Runs

After all the commissioning tests are completed and the ability to operate safely is confirmed, the steam-reforming unit is started-up. Detailed start-up policies are proprietary of MRT and are not presented here. The results from the experimental runs are presented in Chapter 3.

C.5. Conclusion

The commissioning and start-up plan is described for the MRT reactor. Cold and hot commissioning are performed to assure the safety of the system.

APPENDIX D. DETAILS OF PILOT FLUIDIZED-BED MEMBRANE REACTOR

D.1. Overview

This appendix presents a variety of illustrations for the pilot fluidized-membrane reactor assembled at Membrane Reactor Technologies Ltd. The pilot reactor is presented in its form of operation in Figure D.1. During the commissioning, three different insulation techniques were implemented to reduce heat losses of a vessel of high surface-to-volume ratio. Figure D.2. illustrates the improvements in insulation with four photographs taken at different dates. Figure D.3. is a macro photograph of the palladium foil affixed to steel supports on the membrane. A normal view of a membrane panel is presented in Figure D.4. The reactor contained three side flanges attached to the sides. Each flange contained up to two membrane panels as depicted in Figure D.5. Figures D.6 and D.7 illustrate the top of the reactor, presenting the top flange and the top air distributor respectively. The external electrical heaters that provide heat are photographed in Figures D.8 and D.9. The crushed powders fluidized in the experimental runs are presented in Figure D.10. D.11 contains a complete PID of the pilot plant.



Figure D. 1. Pilot reactor under operation.

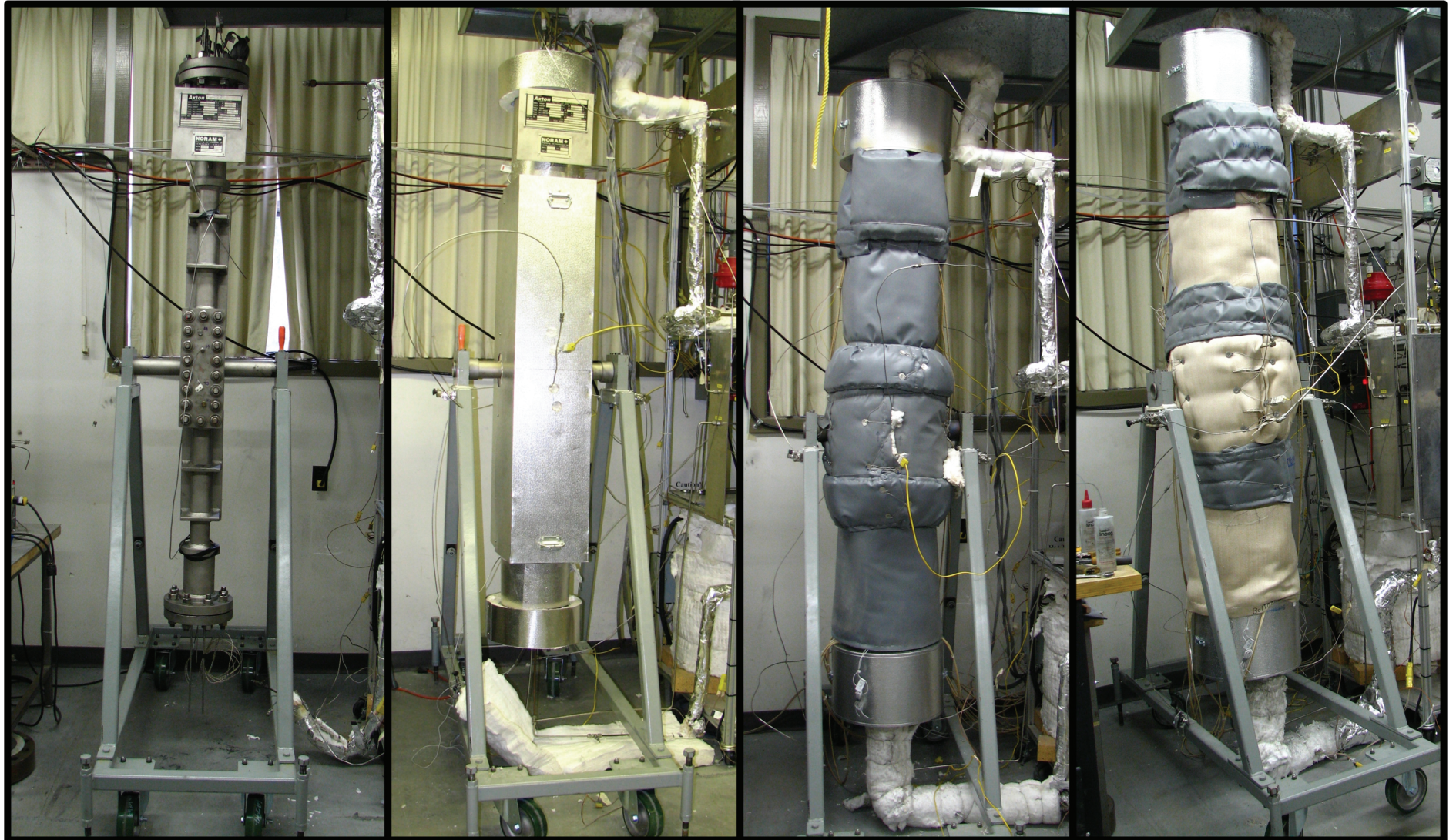


Figure D. 2. Fluidized-bed reactor insulation at different stages of the project.



Figure D. 3. Close-up photo of membrane panel.

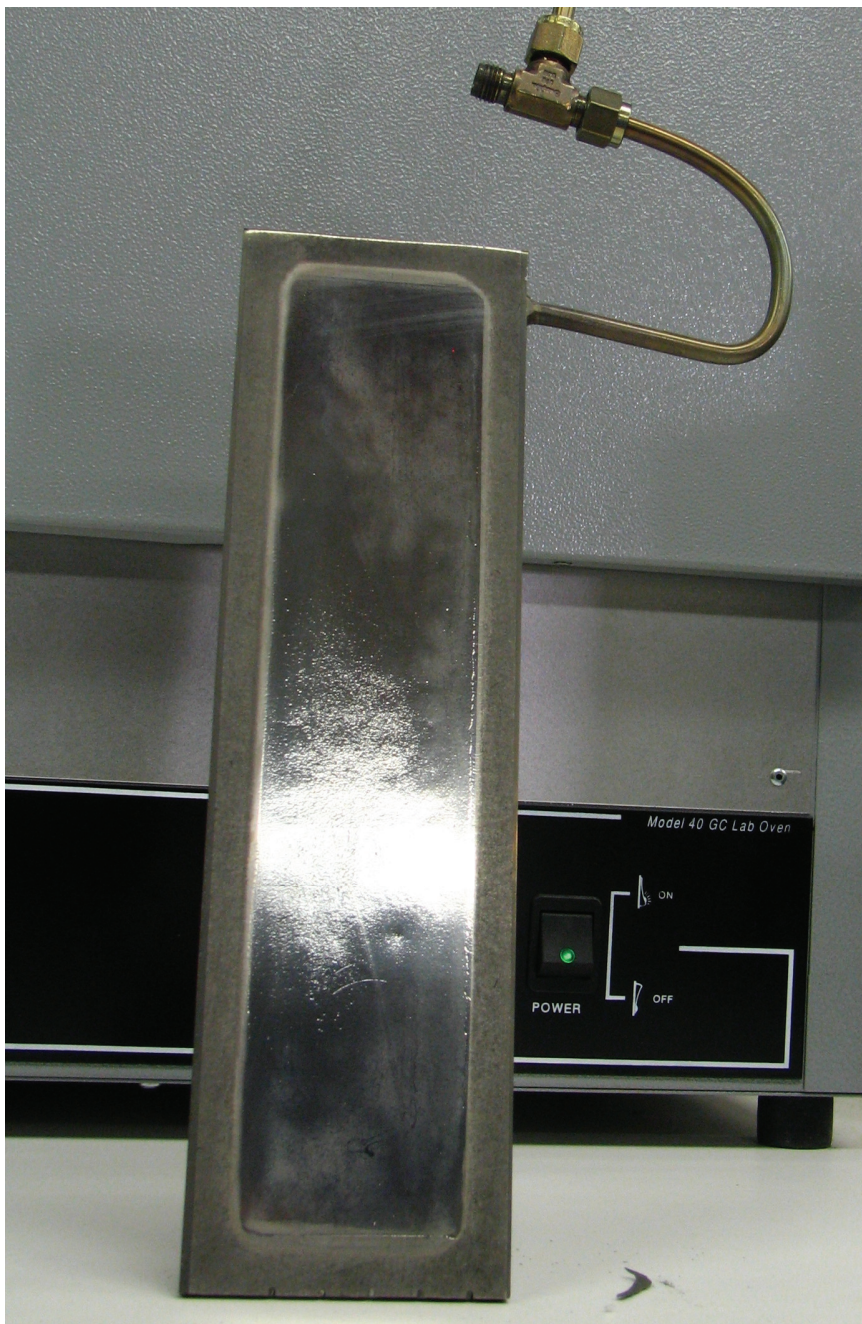


Figure D. 4. Palladium membrane panel.

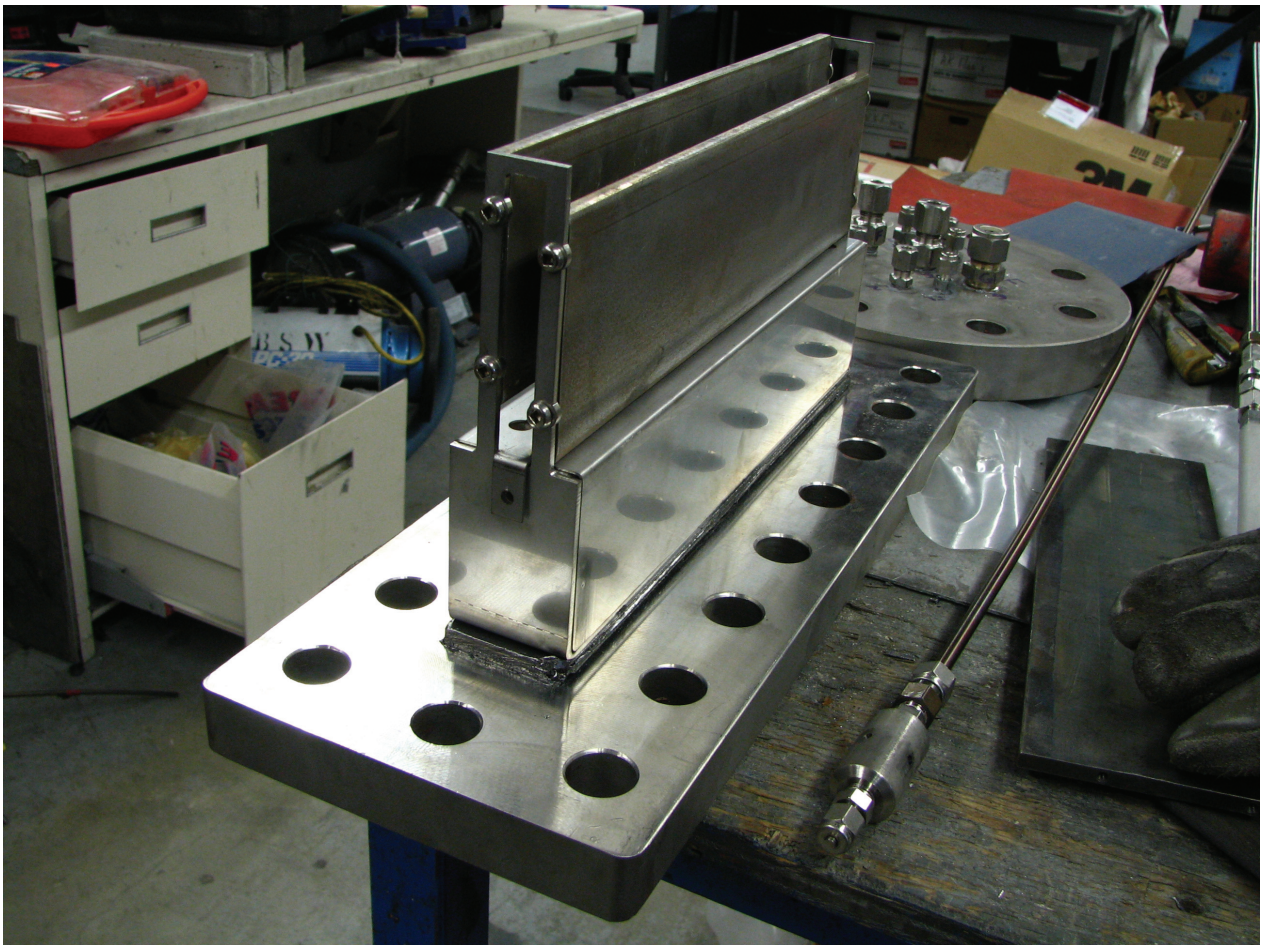


Figure D. 5. Side flange supporting two panels.

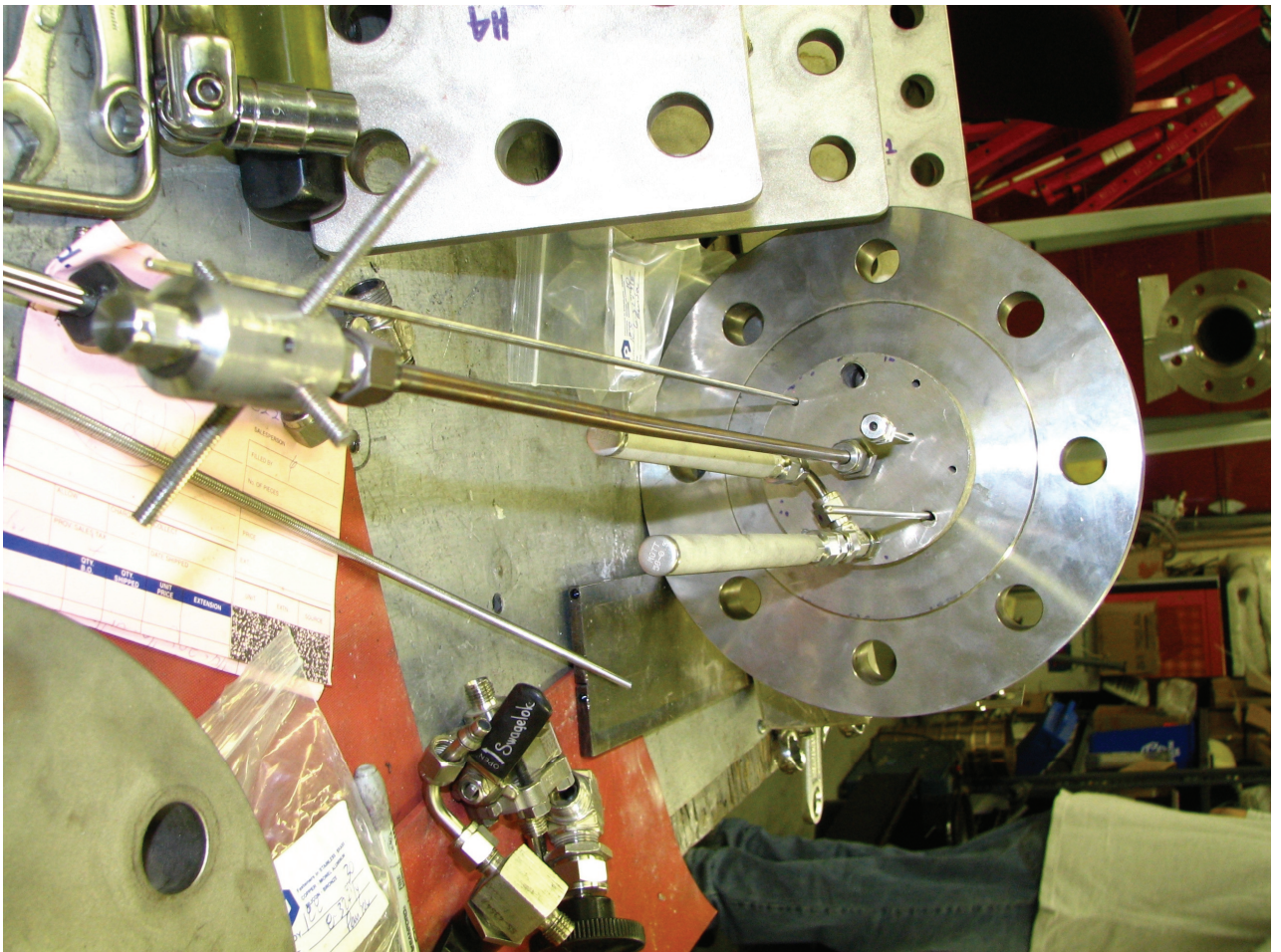


Figure D. 6. Top flange with gas filters and air distributor.

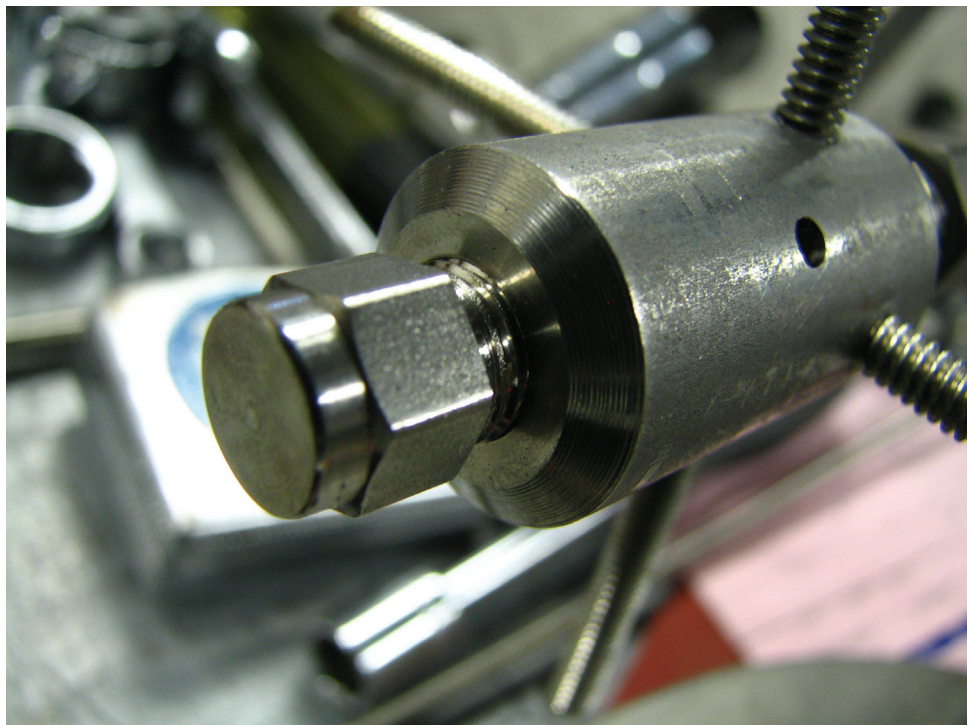


Figure D. 7. Close-up of top air distributor.

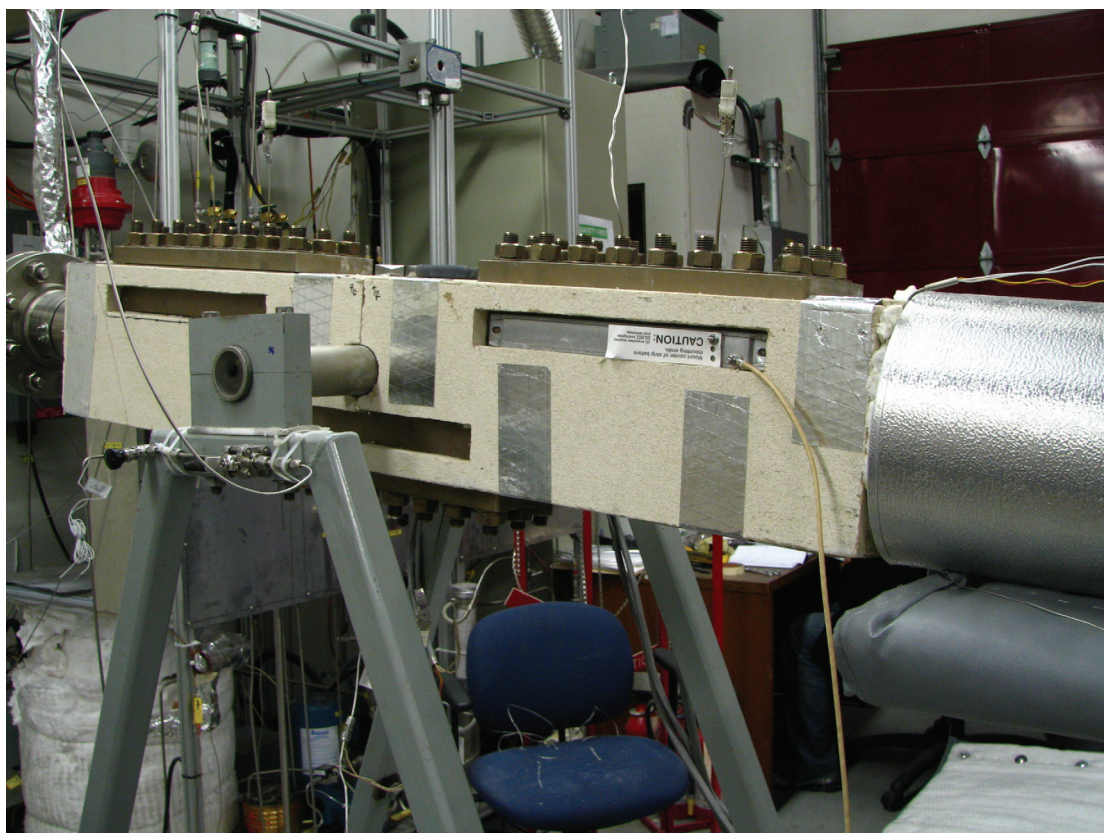


Figure D. 8. Placement of external electrical heaters.

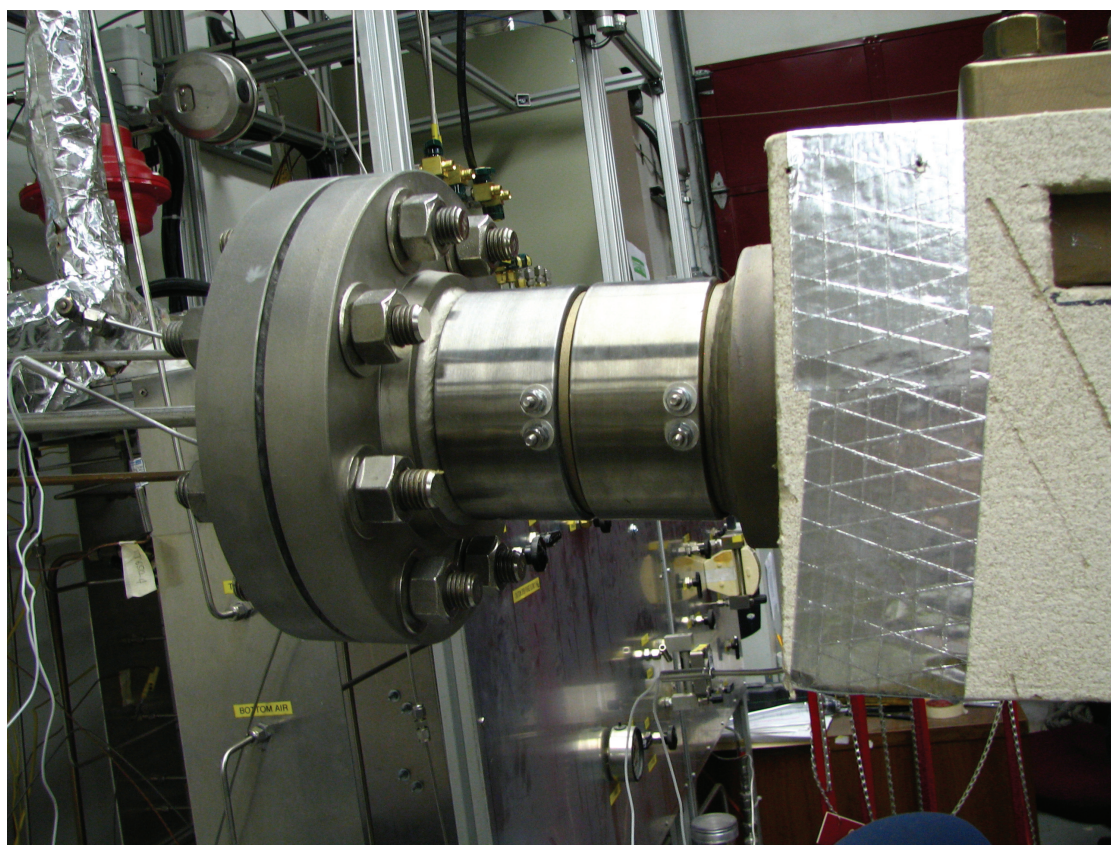


Figure D. 9. External heaters above the gas distributor.



Figure D. 10. Fluidization catalysts.

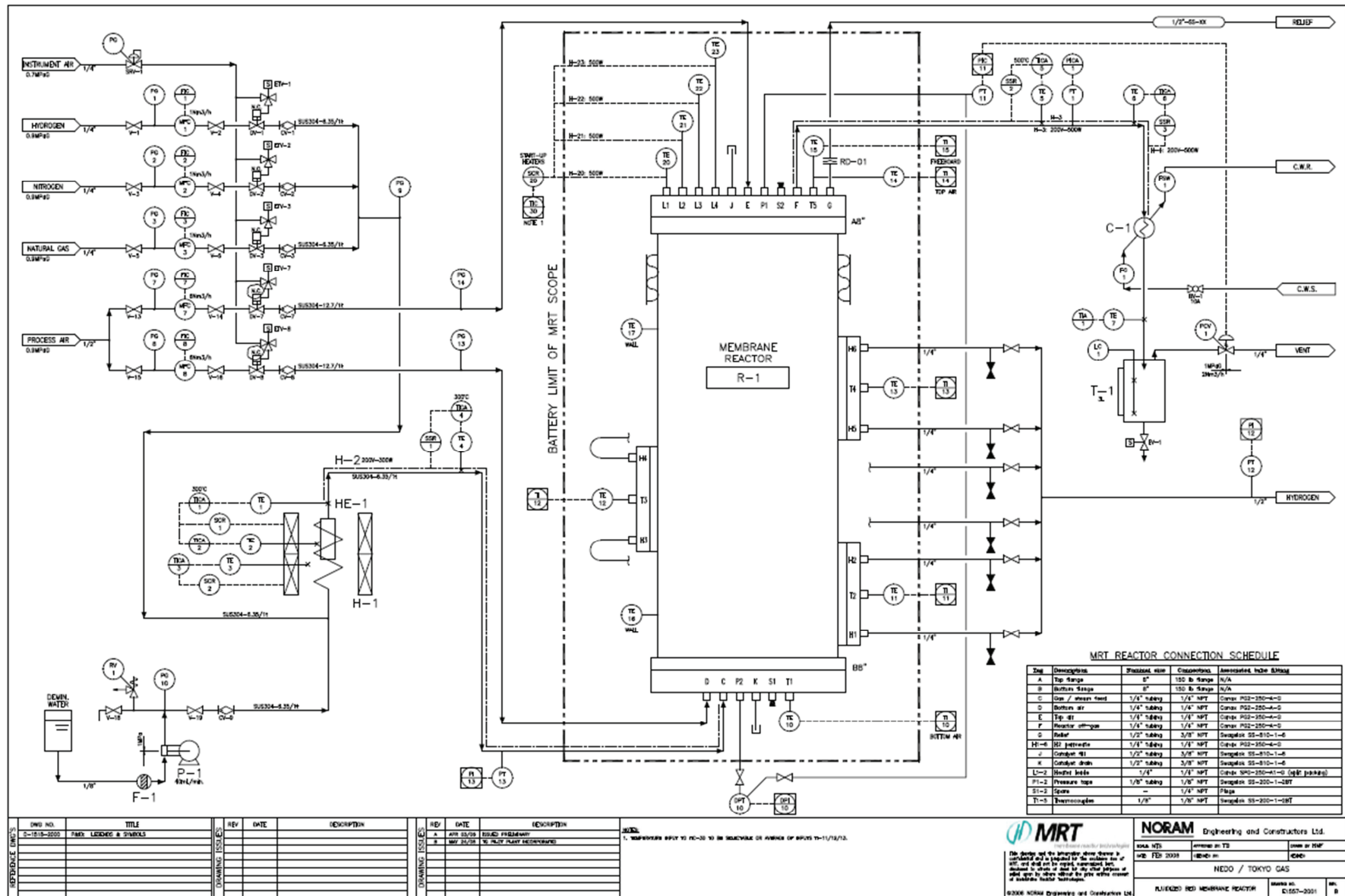


Figure D. 11. PID diagram for pilot reactor.

APPENDIX E. EFFECT OF AIR SPLIT IN A MULTI-STAGE MODEL WITH INTERNAL RECYCLE

E.1. Introduction

This section investigates the effect of modulating the split of air in an autothermal fluidized-bed membrane reformer. The reactor model developed by Boyd (2007) is modified to study the penalty associated with introducing nitrogen at different levels in the membrane reactor. The model is based on a commercial process simulator, HYSYS, to simulate a steam methane reformer with internal circulation of catalyst, with some gas dragged downward in an outer annulus region while upflow occurs in the reactor core (Boyd *et al.*, 2005). In addition, oxygen is introduced at the top of the reactor in order to burn the reactor off-gases and recycle the generated heat via the recirculating catalyst particles. More details about this system are provided by Boyd, (2007).

E.2. Results and Discussion

The base case simulation conditions can be found in Table E.1. An industrial scale system designed to produce 30 Nm³/h of pure hydrogen was simulated under different conditions. Three different scenarios were simulated as described in Table E.2. Simulations were carried out with a commercial process simulator (HYSYS). Air is introduced to supply the required heat for the steam reforming. The circulating reforming catalyst acts as the heat carrier.

The effective membrane area (A_{eff}) for each case can then be calculated from the simulation output using the equation:

$$A_{eff} = \sum_{i=1}^{N_z} A_{eff_i} \quad (\text{E.1})$$

where N_z is the number of permeation zones (10 zones here) and A_{eff_i} is the required membrane area for permeation zone i . The effective membrane area for each permeation zone can then be calculated from the simulation output using the Sievert's law hydrogen flux equation:

$$A_{eff_i} = \frac{\Delta_{H_2} Q_H}{k_H} \exp\left(\frac{-E_p}{RT}\right) (\sqrt{p_{HH}} - \sqrt{p_{HI}}) \quad (\text{E.2})$$

where δ_{H_2} is the membrane thickness (base case 50E-6 m), Q_H is the H₂ permeation per stage (base case 30 Nm³/h/10 stages = 0.037 mol/s), $k_H = 1.08E-7$ mol/m s Pa^{0.5}, $E_p = 9,180$ J/mol, T is the permeation temperature, assumed to be equal to the temperature of the reactor gas entering each membrane separation stage, P_{Hh} is the hydrogen partial pressure in the reactor, and P_{Hl} is the hydrogen partial pressure in the permeate stream (the base case being atmospheric pressure with no sweep gas).

Table E. 1. Simulation conditions.

Variable	Design Conditions
Reactor pressure	2,500 kPa
Total permeate H2 flow	30 Nm3/h
H2O:CH4 molar ratio of feed	3.00
Superficial core velocity	0.25 m/s
Membrane temperature	600°C
preheat temperature	600°C
Reactor heat losses	2 kW
CH4 flow	12 Nm3/h
Solids circulation	1,356 kg/h
Oxidation zone temperature	618°C
Membrane thickness	50E-6 m
Permeate sweep gas	None
Permeate pressure	101 kPa
Membrane Parameters	
Membrane efficiency	100%
Ep (J/mol)	9180
Kh (mol/m s Pa ^{0.5})	1.08E-07
QH per Membrane (mol/s)	0.037
t (m)	5.00E-05
R (J/mol K)	8.3145

Table E. 2. Simulation conditions for different cases.

CASE	Conditions
(1)	100% air at top
(2)	50% air split top/bottom
(3)	100% air at bottom

Figure E.1 depicts the overall membrane requirements for the different cases. Simulation results for Case 1 are presented in Tables E.3 and E.4. Tables E.5 and E.6 include the results for Case 2, whereas Tables E.7 and E.8 present results for Case 3. These results clearly indicate that reactor performance increases when nitrogen is fed at the top of the bed to reduce the dilution caused by nitrogen.

Table E. 3. Case 1 Simulation results. Input and output streams.

CASE 1 All Air at Top		Input Streams				Output Streams	
		NG (Input at Bottom)	Steam (Input at Bottom)	Air (Input at Bottom)	Air (Input at Top)	ROG (Reactor Off Gas)	Total H2 (Product)
Stream	Variable						
	Mass Flow (kg/h)	8.594	24.127	N.A.	25.464	55.488	2.698
	Molar Flow (Nm ³ /h)	12.008	30.019	N.A.	19.783	49.211	29.993
	Temperature C	600	600	N.A.	600	613	590
	Pressure (KPa)	2750	2750	N.A.	2750	2750	120
Composition	Vapour fraction	1.000	1.000	N.A.	1.000	1.000	1.000
	Methane mole fraction	1.000	0.000	N.A.	0.000	0.025	0.000
	CO mole fraction	0.000	0.000	N.A.	0.000	0.019	0.000
	CO ₂ mole fraction	0.000	0.000	N.A.	0.000	0.200	0.000
	H ₂ O mole fraction	0.000	1.000	N.A.	0.000	0.360	0.000
	Nitrogen mole fraction	0.000	0.000	N.A.	0.790	0.318	0.000
	Oxygen mole fraction	0.000	0.000	N.A.	0.210	0.000	0.000
	Hydrogen mole fraction	0.000	0.000	N.A.	0.000	0.079	1.000

CH₄ Conversion	0.897
H₂:CH₄ Recovery	2.498

Table E. 4. Case 1 Simulation results. Permeation zones.

CASE 1 All Air at Top		All Membranes				
		Membrane #1	Membrane #2	Membrane #3	Membrane #4	Membrane #5
Membrane	Mass Flow (kg/h)	0.270	0.270	0.270	0.270	0.269
	Molar Flow (Nm ³ /h)	3.022	3.028	3.030	3.030	3.013
	Molar Flow (mol/s)	0.037	0.038	0.038	0.038	0.037
	Temperature C	606	603	599	596	592
	Pressure (KPa)	120	120	120	120	120
	Vapour fraction	1.000	1.000	1.000	1.000	1.000
Composition	Methane mole fraction	0.000	0.000	0.000	0.000	0.000
	CO mole fraction	0.000	0.000	0.000	0.000	0.000
	CO ₂ mole fraction	0.000	0.000	0.000	0.000	0.000
	H ₂ O mole fraction	0.000	0.000	0.000	0.000	0.000
	Nitrogen mole fraction	0.000	0.000	0.000	0.000	0.000
	Oxygen mole fraction	0.000	0.000	0.000	0.000	0.000
	Hydrogen mole fraction	1.000	1.000	1.000	1.000	1.000
Reactor	Pressure (Reactor side) (Kpa)	2750	2750	2750	2750	2750
	Temperature (Reactor side) C	600	597	593	589	585
	Hydrogen Mole frac (Reactor side)	0.194	0.181	0.168	0.155	0.278
	Area of Membrane (m ²)	0.160	0.173	0.187	0.204	0.118
	Membrane #6	Membrane #7	Membrane #8	Membrane #9	Membrane #10	
Membrane	Mass Flow (kg/h)	0.268	0.270	0.269	0.270	0.270
	Molar Flow (Nm ³ /h)	3.005	3.027	3.008	3.024	3.029
	Molar Flow (mol/s)	0.037	0.038	0.037	0.037	0.038
	Temperature C	588	584	580	576	572
	Pressure (KPa)	120	120	120	120	120
	Vapour fraction	1.000	1.000	1.000	1.000	1.000
Composition	Methane mole fraction	0.000	0.000	0.000	0.000	0.000
	CO mole fraction	0.000	0.000	0.000	0.000	0.000
	CO ₂ mole fraction	0.000	0.000	0.000	0.000	0.000
	H ₂ O mole fraction	0.000	0.000	0.000	0.000	0.000
	Nitrogen mole fraction	0.000	0.000	0.000	0.000	0.000
	Oxygen mole fraction	0.000	0.000	0.000	0.000	0.000
	Hydrogen mole fraction	1.000	1.000	1.000	1.000	1.000
Reactor	Pressure (Reactor side) (Kpa)	2750	2750	2750	2750	2750
	Temperature (Reactor side) C	581	577	573	569	564
	Hydrogen Mole frac (Reactor side)	0.246	0.122	0.111	0.101	0.092
	Area of Membrane (m ²)	0.132	0.274	0.308	0.355	0.416
TOTAL Area Required (m²)			2.327			

Table E. 5. Case 2 Simulation results. Input and output streams.

CASE 2 50% Air Split		Input Streams				Output Streams	
		NG (Input at Bottom)	Steam (Input at Bottom)	Air (Input at Bottom)	Air (Input at Top)	ROG (Reactor Off Gas)	Total H2 (Product)
Stream	Variable						
	Mass Flow (kg/h)	8.594	24.127	12.732	12.732	55.234	2.723
	Molar Flow (Nm3/h)	12.008	30.019	9.891	9.891	48.410	30.276
	Temperature C	600	600	600	600	584	590
	Pressure (KPa)	2750	2750	2750	2750	2750	120
	Vapour fraction	1.000	1.000	1.000	1.000	1.000	1.000
Composition	Methane mole fraction	1.000	0.000	0.000	0.000	0.029	0.000
	CO mole fraction	0.000	0.000	0.000	0.000	0.013	0.000
	CO2 mole fraction	0.000	0.000	0.000	0.000	0.205	0.000
	H2O mole fraction	0.000	1.000	0.000	0.000	0.366	0.000
	Nitrogen mole fraction	0.000	0.000	0.790	0.790	0.321	0.000
	Oxygen mole fraction	0.000	0.000	0.210	0.210	0.000	0.000
	Hydrogen mole fraction	0.000	0.000	0.000	0.000	0.066	1.000

CH4 Conversion	0.884
H2:CH4 Recovery	2.521

Table E. 6. Case 2 Simulation results. Permeation zones.

CASE 2 50% Air Split		All Membranes				
		Membrane #1	Membrane #2	Membrane #3	Membrane #4	Membrane #5
Membrane	Mass Flow (kg/h)	0.270	0.272	0.271	0.267	0.270
	Molar Flow (Nm ³ /h)	3.024	3.046	3.039	2.994	3.024
	Molar Flow (mol/s)	0.038	0.038	0.038	0.037	0.037
	Temperature C	606	603	599	596	592
	Pressure (KPa)	120	120	120	120	120
	Vapour fraction	1.000	1.000	1.000	1.000	1.000
Composition	Methane mole fraction	0.000	0.000	0.000	0.000	0.000
	CO mole fraction	0.000	0.000	0.000	0.000	0.000
	CO ₂ mole fraction	0.000	0.000	0.000	0.000	0.000
	H ₂ O mole fraction	0.000	0.000	0.000	0.000	0.000
	Nitrogen mole fraction	0.000	0.000	0.000	0.000	0.000
	Oxygen mole fraction	0.000	0.000	0.000	0.000	0.000
Reactor	Hydrogen mole fraction	1.000	1.000	1.000	1.000	1.000
	Pressure (Reactor side) (Kpa)	2750	2750	2750	2750	2750
	Temperature (Reactor side) C	600	597	593	589	585
	Hydrogen Mole frac (Reactor side)	0.167	0.155	0.144	0.134	0.296
Area of Membrane (m ²)	0.186	0.203	0.220	0.238	0.113	
		Membrane #6	Membrane #7	Membrane #8	Membrane #9	Membrane #10
Membrane	Mass Flow (kg/h)	0.270	0.281	0.280	0.271	0.270
	Molar Flow (Nm ³ /h)	3.024	3.148	3.141	3.036	3.024
	Molar Flow (mol/s)	0.037	0.039	0.039	0.038	0.037
	Temperature C	588	585	580	576	572
	Pressure (KPa)	120	120	120	120	120
	Vapour fraction	1.000	1.000	1.000	1.000	1.000
Composition	Methane mole fraction	0.000	0.000	0.000	0.000	0.000
	CO mole fraction	0.000	0.000	0.000	0.000	0.000
	CO ₂ mole fraction	0.000	0.000	0.000	0.000	0.000
	H ₂ O mole fraction	0.000	0.000	0.000	0.000	0.000
	Nitrogen mole fraction	0.000	0.000	0.000	0.000	0.000
	Oxygen mole fraction	0.000	0.000	0.000	0.000	0.000
Reactor	Hydrogen mole fraction	1.000	1.000	1.000	1.000	1.000
	Pressure (Reactor side) (Kpa)	2750	2750	2750	2750	2750
	Temperature (Reactor side) C	581	577	573	569	564
	Hydrogen Mole frac (Reactor side)	0.263	0.104	0.095	0.086	0.077
Area of Membrane (m ²)	0.125	0.349	0.404	0.466	0.571	
TOTAL Area Required (m²)		2.877				

Table E. 7. Case 3 Simulation results. Input and output streams.

CASE 3 All Air at Bottom		Input Streams				Output Streams	
		NG (Input at Bottom)	Steam (Input at Bottom)	Air (Input at Bottom)	Air (Input at Top)	ROG (Reactor Off Gas)	Total H2 (Product)
Variable							
Stream	Mass Flow (kg/h)	8.594	24.127	25.464	N.A.	55.032	2.710
	Molar Flow (Nm³/h)	12.008	30.019	19.783	N.A.	47.908	30.135
	Temperature C	600	600	600	N.A.	555	589
	Pressure (KPa)	2750	2750	2750	N.A.	2750	120
	Vapour fraction	1.000	1.000	1.000	N.A.	1.000	1.000
Composition	Methane mole fraction	1.000	0.000	0.000	N.A.	0.034	0.000
	CO mole fraction	0.000	0.000	0.000	N.A.	0.009	0.000
	CO2 mole fraction	0.000	0.000	0.000	N.A.	0.206	0.000
	H2O mole fraction	0.000	1.000	0.000	N.A.	0.373	0.000
	Nitrogen mole fraction	0.000	0.000	0.790	N.A.	0.324	0.000
	Oxygen mole fraction	0.000	0.000	0.210	N.A.	0.000	0.000
	Hydrogen mole fraction	0.000	0.000	0.000	N.A.	0.055	1.000

CH4 Conversion	0.866
H2:CH4 Recovery	2.510

Table E. 8. Case 3 Simulation results. Permeation zones.

CASE 3 All Air at Bottom		All Membranes				
		Membrane #1	Membrane #2	Membrane #3	Membrane #4	Membrane #5
Membrane	Mass Flow (kg/h)	0.270	0.272	0.272	0.270	0.269
	Molar Flow (Nm ³ /h)	3.024	3.042	3.042	3.024	3.009
	Molar Flow (mol/s)	0.038	0.038	0.038	0.038	0.037
	Temperature C	606	602	599	596	592
	Pressure (KPa)	120	120	120	120	120
	Vapour fraction	1.000	1.000	1.000	1.000	1.000
Composition	Methane mole fraction	0.000	0.000	0.000	0.000	0.000
	CO mole fraction	0.000	0.000	0.000	0.000	0.000
	CO2 mole fraction	0.000	0.000	0.000	0.000	0.000
	H2O mole fraction	0.000	0.000	0.000	0.000	0.000
	Nitrogen mole fraction	0.000	0.000	0.000	0.000	0.000
	Oxygen mole fraction	0.000	0.000	0.000	0.000	0.000
Reactor	Hydrogen mole fraction	1.000	1.000	1.000	1.000	1.000
	Pressure (Reactor side) (Kpa)	2750	2750	2750	2750	2750
	Temperature (Reactor side) C	600	597	593	589	586
	Hydrogen Mole frac (Reactor side)	0.146	0.136	0.126	0.117	0.307
	Area of Membrane (m ²)	0.214	0.234	0.257	0.282	0.109
		Membrane #6	Membrane #7	Membrane #8	Membrane #9	Membrane #10
Membrane	Mass Flow (kg/h)	0.269	0.289	0.269	0.269	0.268
	Molar Flow (Nm ³ /h)	3.011	3.234	3.010	3.010	3.003
	Molar Flow (mol/s)	0.037	0.040	0.037	0.037	0.037
	Temperature C	588	584	580	576	572
	Pressure (KPa)	120	120	120	120	120
	Vapour fraction	1.000	1.000	1.000	1.000	1.000
Composition	Methane mole fraction	0.000	0.000	0.000	0.000	0.000
	CO mole fraction	0.000	0.000	0.000	0.000	0.000
	CO2 mole fraction	0.000	0.000	0.000	0.000	0.000
	H2O mole fraction	0.000	0.000	0.000	0.000	0.000
	Nitrogen mole fraction	0.000	0.000	0.000	0.000	0.000
	Oxygen mole fraction	0.000	0.000	0.000	0.000	0.000
Reactor	Hydrogen mole fraction	1.000	1.000	1.000	1.000	1.000
	Pressure (Reactor side) (Kpa)	2750	2750	2750	2750	2750
	Temperature (Reactor side) C	582	578	574	569	565
	Hydrogen Mole frac (Reactor side)	0.274	0.091	0.083	0.074	0.066
	Area of Membrane (m ²)	0.120	0.442	0.489	0.616	0.824
TOTAL Area Required (m²)		3.588				

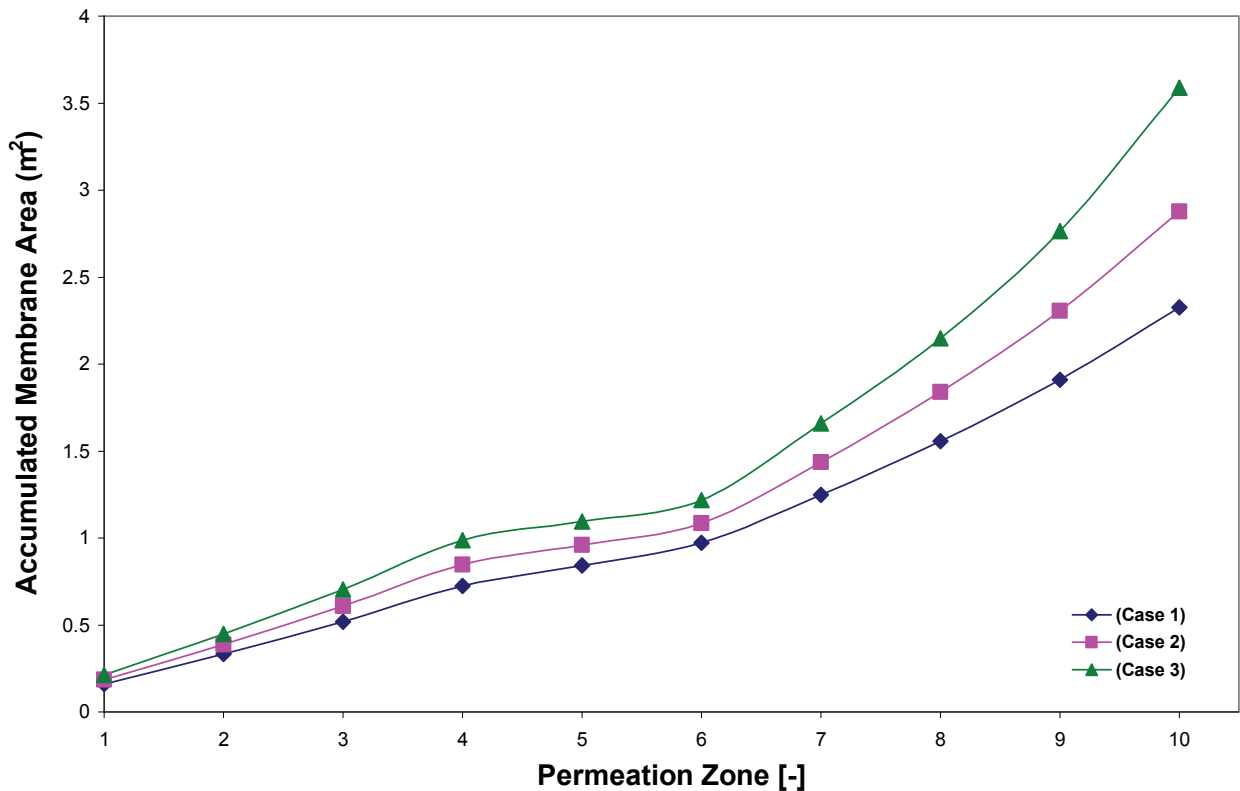


Figure E. 1. Required membrane area for different configurations. Gibbs reactors in series with 10 permeation zones are used to simulate the fluidized-bed membrane reformer.

E.3. Conclusions

The effects of the nitrogen penalty are illustrated implementing a staged model for an internally circulating fluidized-bed membrane reactor. Nitrogen dilutes the reactor gases lowering the hydrogen partial pressure. This inert gas reduces the driving force required for permeation. It is preferable to add most of the air at the top of the reactor to reduce this nitrogen penalty. Other heat transfer effects should be considered to define the air split ratio since unsafe local temperatures could occur when all of the oxidant gas is supplied at a single level in the reactor.

E.4. References

- Boyd, T. (2007). Hydrogen from an internally circulating fluidized bed membrane reactor Department of Chemical and Biological Engineering. Vancouver, University of British Columbia. Ph.D. Thesis.
- Boyd, T., Grace, J.R., Lim, C.J. and Adris, A. (2005). Hydrogen from an internally circulating fluidized bed membrane reactor. *Int. J. Chem. Reactor Eng.*, 3, A58.

APPENDIX F. DESIGN OF A SOLIDS CIRCULATION LOOP FOR A REFORMER-CALCINER SYSTEM

F.1. Introduction

In this section a looping system is designed for a fluidized-bed membrane reformer coupled with a calcination system for integrated hydrogen production and carbon dioxide capture. The reformer is a modification of the membrane reformer presented in Chapter 3 (i.e. removing its top membrane section). The reformer-calciner system is presented in Figure F.1. Both vessels are pressurized to 1.0 MPa. The reformer operates at $\sim 550^{\circ}\text{C}$, while the calciner operates at $\sim 800^{\circ}\text{C}$. Calcium carbonate is continuously recalculated between the two vessels to remove carbon dioxide from the reformer (Chen *et al.*, 2008).

F.2. Practical Considerations

The solids circulation system consists of a J-Valve and a return leg. The J-Valve actively controls the solids motion by injecting transport gas at different angles and therefore pushing the solids upwards from the calciner to the reformer. The return leg brings spent solid sorbent (CaCO_3) to the calciner with the aid of gravity. This tube is accommodated at a vertical angle larger than 70° to allow for free downwards solids flow. The transport lines are as straight as possible to avoid fouling. The location of solids input and output nozzles for each vessel are carefully separated from each other to avoid bypassing. The entry ports of the transport lines are expanded to collect solids more efficiently (Rusnell *et al.*, 2007).

The J-valve is designed by mapping the possible flow regimes inside its main tube. The idea behind this is to identify the minimum pipe diameter required to operate in the fast fluidization regime inside the J-Valve as seen in Figure F.2. From this figure, it is concluded that the diameter of the J-valve should be smaller than 13 mm. A personal communication with Ted Knowlton (July 21, 2007) confirmed the feasibility of operating at such small diameter with group A particles. The final PID diagram of the calciner coupled with the solids recirculation is presented in Figure F.3.

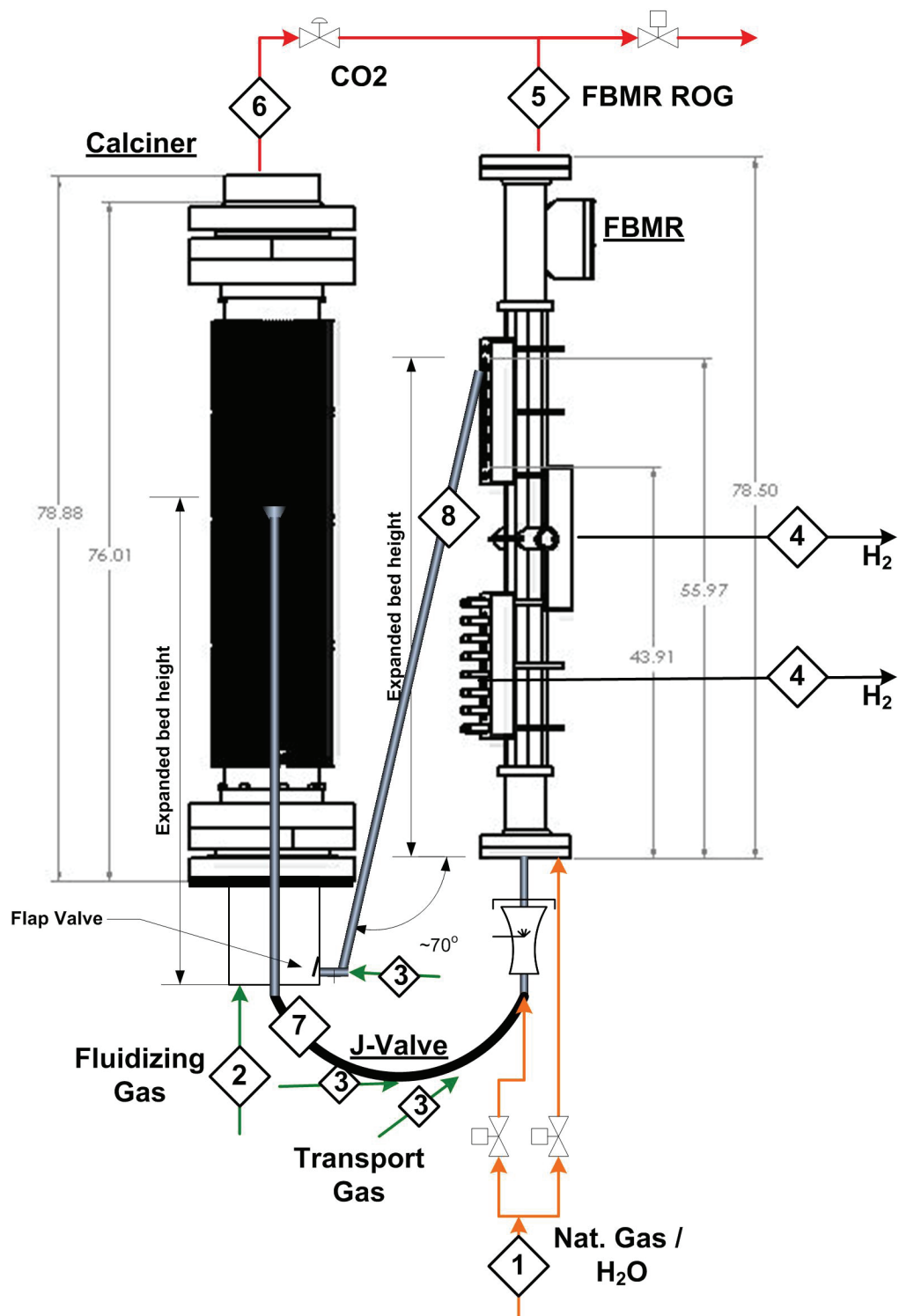


Figure F. 1. Reformer-calciner system.

F.3. Conclusions

This appendix summarizes the design of a solids recirculation system. A final design is suggested to be applied in a reformer-calciner unit to produce separate streams of ultrapure hydrogen and high concentration carbon dioxide.

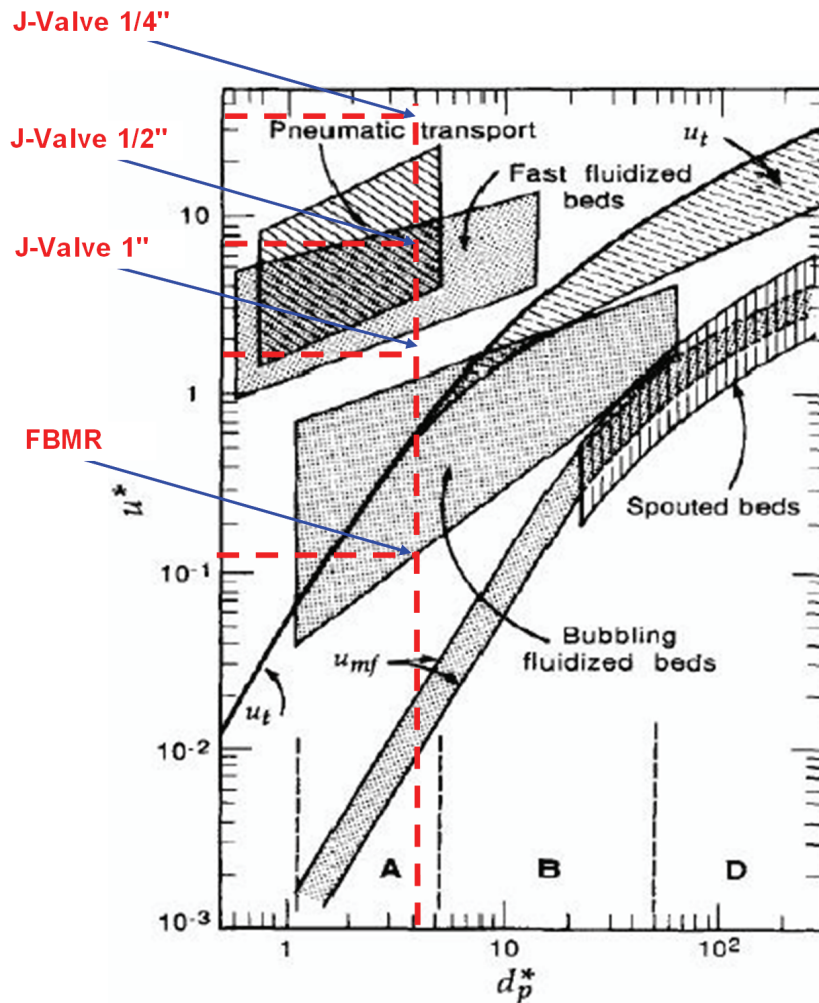


Figure F. 2. Mapping for J-valve.

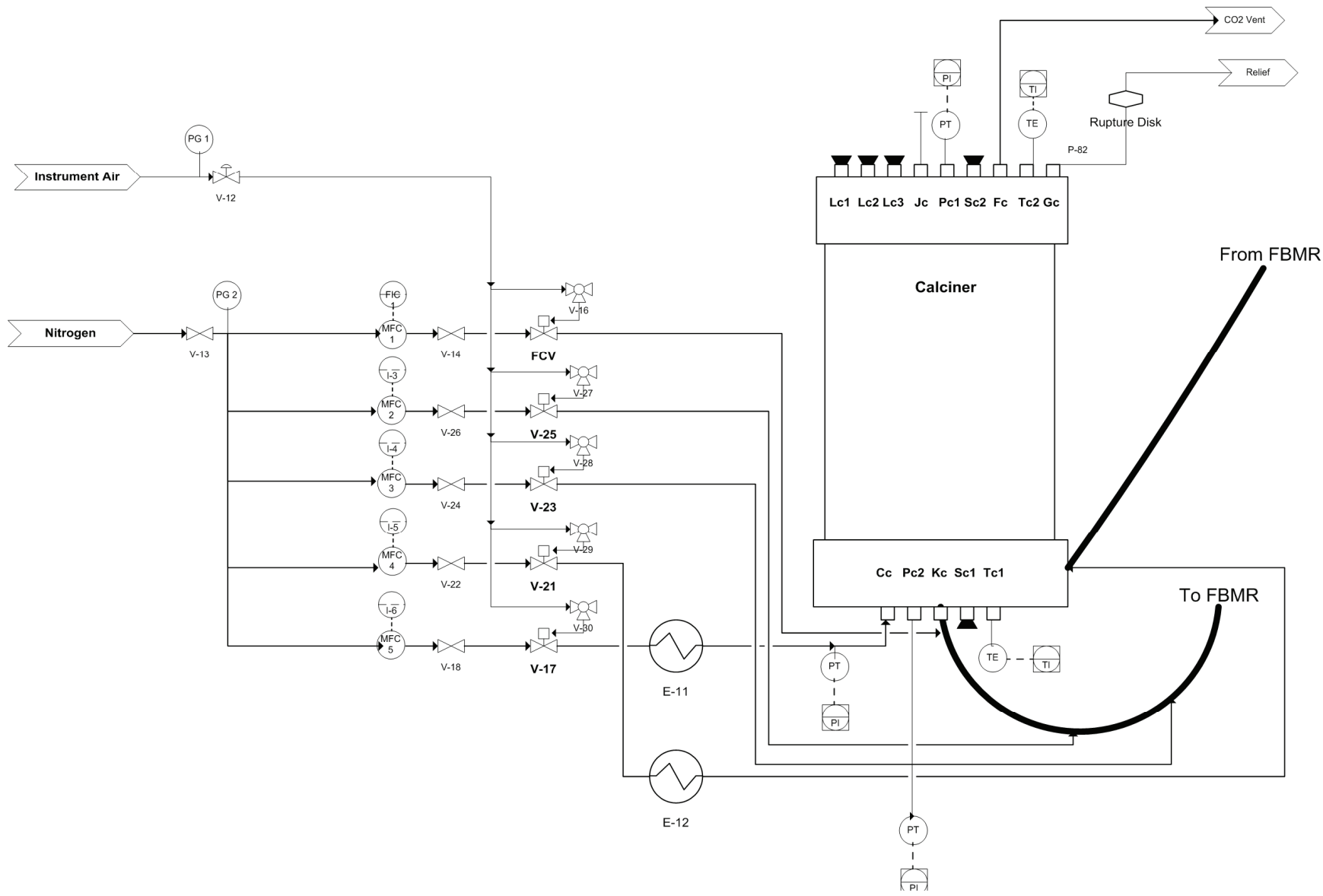


Figure F. 3. PID for calciner and solids circulation system.

F.4. References

Chen, Z., Po, F., Grace, J.R., Lim, C.J., Elnashaie, S.S.E.H., Mahecha-Botero, A., Rakib, M., Shirasaki, Y. and Yasuda, I. (2008). Sorbent enhanced/membrane-assisted steam methane reforming. *Chem. Eng. Sci.*, 63, 170-182.

Knowlton, T.M. (July 21, 2007). J- valve diameter. Personal communication with. Grace, J.R. and Mahecha-Botero, A. PSRI, Chicago.

Rusnell, D., Grace, J.R., Bi, H.T., Lim, C.J., Ronan, P. and McKnight, C.A. (2007). Improved transfer line entrance for stable high-flux solids flow. in *Fluidization XII*. Eds. Bi, X., F., B. and Pugsley, T. Harrison Hot Springs, BC, Canada, ECI Symposium Series. United Engineering Conferences, Brooklyn.

APPENDIX G. A COMPREHENSIVE APPROACH TO REACTION ENGINEERING ¹⁰

G.1. Introduction

In the teaching of science and engineering, it is very important to provide a solid background to students. This allows a better understanding of the underlying physical/chemical phenomena and encourages students to advance their knowledge in this field of study. It is difficult to formulate a robust modeling approach in chemical engineering education. Most learning has been oriented to particular cases. Although individual case analysis is essential to the development of an engineer, this could limit the attainment of an overall integrated picture of physical and chemical phenomena.

A systematic approach is introduced here which we believe can facilitate student understanding of multiple phenomena encountered in chemical engineering systems. This appendix should be used in combination with Section 1.2. The final model presented includes standard forms found in the literature as special cases, allowing for clear connections to be established among the models and showing the significance and implications of each simplifying assumption. This approach for solving chemical reaction engineering problems should encourage students to build more sophisticated models and simulate more complex systems.

G.2. Generalized Governing Equations for Reaction Engineering

The backbone for any reactor engineering model is developed in this section. This backbone may be enriched with many additional relations in order to describe the reacting system. In order to write a single set of equations for many different cases, multidimensional control indices are used in the mole and energy balances. These control indices act as switches to include or discard

¹⁰ *This appendix presents a systematic algorithm for formulating and solving chemical/biochemical reaction engineering problems. A version of this appendix was published as: Mahecha-Botero, A., Grace, J.R., Elnashaie, S.S.E.H. and Lim, C.J. (2007). "A comprehensive approach to reaction engineering". International Journal of Chemical Reactor Engineering, 5: A17.*

terms in the balance equations. These indices may then have a value of 0 or 1, depending on the degree of complexity of the model equations.

In Section G.2.1 a set of balances is developed for a lumped system. These balances are extended to one-dimensional distributed systems in Section G.2.2. The systems of equations derived in this section are intended for *multi-phase systems*. Equations for a general pseudo-phase (φ) are derived below allowing for exchange of mass and heat with other pseudo-phases nearby. The *pseudo-phase* may contain matter in any physical state such as solid, liquid and gas, as well as a combination of them. The balance equations described below should be applied to all pseudo-phases involved in the system of study.

G.2.1. Lumped Systems (Continuous Stirred Tank Reactors, Stirred Batch and Semi-Batch Reactors)

G.2.1.1. Mole balance

The mole balances for each species in pseudo-phase (φ) (Figure G.1) are given by:

$$[\text{Input} - \text{Output}]_{(\varphi)} + [\text{Chemical reaction generation/consumption}]_{(\varphi)} + [\text{Exchange with other pseudo-phases}]_{(\varphi)} = [\text{Molar accumulation rate}]_{(\varphi)}$$

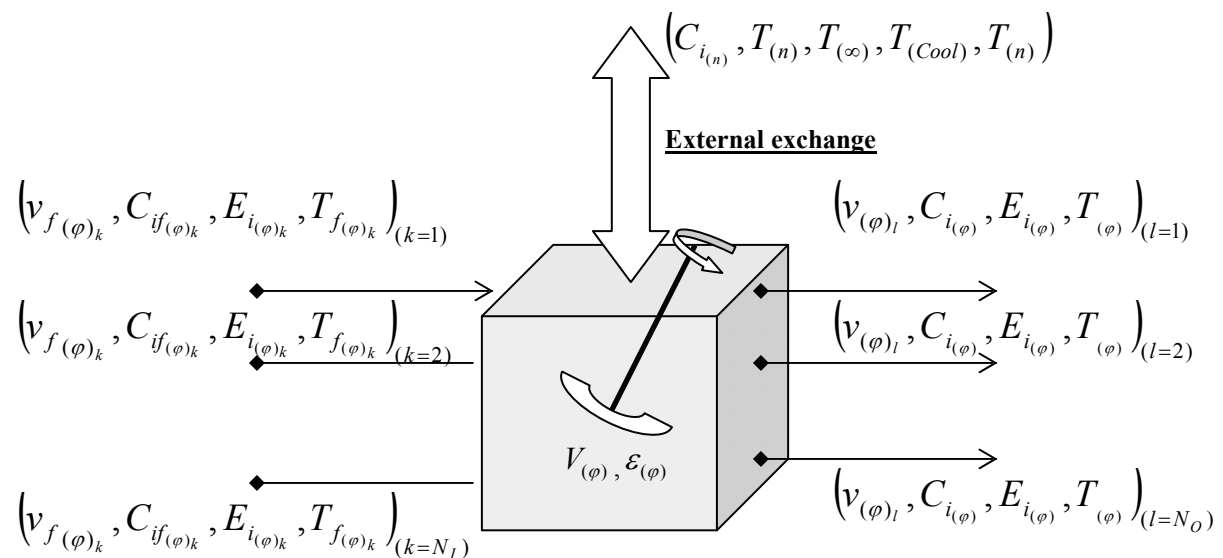


Figure G. 1. Mole and energy fundamental balances for lumped systems.

Initially the mole balance is developed in terms of concentrations as follows:

$$\left[\sum_{k=1}^{N_I} v_{f(\varphi)_k} \cdot C_{if(\varphi)_k} - \sum_{l=1}^{N_O} v_{(\varphi)_l} \cdot C_{i(\varphi)_l} \right] + \left[V_{(\varphi)} \cdot \sum_{j=1}^{N_R} v_{ij} \cdot \Omega_{j(\varphi)} \cdot a_{j(\varphi)} \cdot r_{j(\varphi)} \right] + \left[V_{(\varphi)} \cdot \sum_{\substack{n=1 \\ n \neq \varphi}}^{N_\varphi} a_{I(n \rightarrow \varphi)} \cdot k_{c_i} \cdot (C_{i(n)} - C_{i(\varphi)}) \right] \quad (\text{G.1})$$

$$= \left[\frac{d}{dt} (\varepsilon_{(\varphi)} \cdot V_{(\varphi)} \cdot C_{i(\varphi)}) \right]$$

$i = 1, 2, \dots, N_C$

where for pseudo-phase (φ): $v_{(\varphi)}$ is the volumetric flow rate, $C_{i(\varphi)}$ the concentration of species i in the fluid part of pseudo-phase (φ), $V_{(\varphi)}$ the total volume, $\varepsilon_{(\varphi)}$ the void fraction, v_{ij} the stoichiometric coefficient of species i in reaction j , $\Omega_{j(\varphi)}$ the overall effectiveness factor, $a_{j(\varphi)}$ the catalyst activity, $r_{j(\varphi)}$ the rate of reaction j , $a_{I(n \rightarrow \varphi)}$ the interphase transfer area per unit volume between phases (φ) and (n), k_c the interphase mass transfer coefficient, and $C_{i(n)}$ is the concentration of species i in an adjacent pseudo-phase (n) in contact with pseudo-phase (φ). N_C is the number of chemical species, whereas N_φ is the number of phases.

The following expressions are obtained after expanding the time derivatives and introducing control indices α_m for future simplifications:

$$\alpha_1 \cdot \sum_{k=1}^{N_I} v_{f(\varphi)_k} \cdot C_{if(\varphi)_k} - \alpha_2 \cdot \sum_{l=1}^{N_O} v_{(\varphi)_l} \cdot C_{i(\varphi)_l} + \alpha_3 \cdot V_{(\varphi)} \cdot \sum_{j=1}^{N_R} v_{ij} \cdot \Omega_{j(\varphi)} \cdot a_{j(\varphi)} \cdot r_{j(\varphi)} + \alpha_4 \cdot V_{(\varphi)} \cdot \sum_{\substack{n=1 \\ n \neq \varphi}}^{N_\varphi} a_{I(n \rightarrow \varphi)} \cdot k_{c_i} \cdot (C_{i(n)} - C_{i(\varphi)}) = \alpha_5 \cdot \varepsilon_{(\varphi)} \cdot V_{(\varphi)} \cdot \frac{d}{dt} (C_{i(\varphi)}) + \alpha_6 \cdot C_{i(\varphi)} \cdot \frac{d}{dt} (\varepsilon_{(\varphi)} \cdot V_{(\varphi)}) \quad (\text{G.2})$$

$$i = 1, 2, \dots, N_C$$

In order to account for changes in the volume and/or number of moles, the mole balances can be re-written in terms of molar flow-rates. This form of the equations simplifies the simulations when the overall volume and/or number of moles vary significantly over the course of

time. It is advisable to express the concentrations of species as: $C_{i(\varphi)} = \left(\frac{F_{i(\varphi)}}{v_{(\varphi)}} \right)$ to obtain:

$$\begin{aligned}
& \alpha_1 \cdot \sum_{k=1}^{N_I} F_{if(\varphi)_k} - \alpha_2 \cdot \sum_{l=1}^{N_O} F_{i(\varphi)_l} + \alpha_3 \cdot V_{(\varphi)} \cdot \sum_{j=1}^{N_R} v_{ij} \cdot \Omega_{j(\varphi)} \cdot a_{j(\varphi)} \cdot r_{j(\varphi)} + \alpha_4 \cdot V_{(\varphi)} \cdot \sum_{\substack{n=1 \\ n \neq \varphi}}^{N_\varphi} a_{I(n \rightarrow \varphi)} \cdot k_{c_i} \cdot \left(\frac{F_{i(n)}}{v_{(n)}} - \frac{F_{i(\varphi)}}{v_{(\varphi)}} \right) \\
& = \alpha_5 \cdot \varepsilon_{(\varphi)} \cdot V_{(\varphi)} \cdot \frac{d}{dt} \left(\frac{F_{i(\varphi)}}{v_{(\varphi)}} \right) + \alpha_6 \cdot \left(\frac{F_{i(\varphi)}}{v_{(\varphi)}} \right) \cdot \frac{d}{dt} (\varepsilon_{(\varphi)} \cdot V_{(\varphi)})
\end{aligned} \tag{G.3}$$

$$i = 1, 2, \dots, N_C$$

where $F_{i(\varphi)}$ represents the molar flow rate of species i .

G.2.1.2. Energy balance

The energy balance based on the First Law of thermodynamics for pseudo-phase (φ) (Figure G.1) gives

$$[Rate\ of\ flow\ of\ heat\ to\ the\ system]_{(\varphi)} - [Rate\ of\ work\ done\ by\ the\ system]_{(\varphi)} + [Energy\ input\ by\ mass\ flow - Energy\ output\ by\ mass\ flow]_{(\varphi)} = [Heat\ accumulation\ rate]_{(\varphi)}$$

Initially the mole balance is developed in terms of concentrations and internal energy:

$$\begin{aligned}
& \left[V_{(\varphi)} \cdot \sum_{\substack{n=1 \\ n \neq \varphi}}^{N_\varphi} a_{I(n \rightarrow \varphi)} \cdot U_I \cdot (T_{(n)} - T_{(\varphi)}) + U_{SR} \cdot V_{(\varphi)} \cdot a_{SR} \cdot (T_\infty - T_S) + \varepsilon_M \cdot V_{(\varphi)} \cdot a_{SR} \cdot \sigma \cdot (T_\infty^4 - T_S^4) + U_{Cool} \cdot V_{(\varphi)} \cdot a_{Cool} \cdot (T_{Cool} - T_{(\varphi)}) \right] \\
& - \left[\dot{W}_s \right] + \left[\sum_{k=1}^{N_I} \left(\sum_{i=1}^{N_C} v_{f(\varphi)_k} \cdot C_{if(\varphi)_k} \cdot E_{if(\varphi)_k} + v_{fSolids(\varphi)_k} \cdot \rho_{Solids} \cdot E_{fSolids(\varphi)_k} \right) - \sum_{l=1}^{N_O} \left(\sum_{i=1}^{N_C} v_{f(\varphi)_l} \cdot C_{i(\varphi)_l} \cdot E_{i(\varphi)_l} + v_{Solids(\varphi)_l} \cdot \rho_{Solids} \cdot E_{Solids(\varphi)_l} \right) \right] \\
& = \left[\frac{d}{dt} \left(\sum_{i=1}^{N_C} \varepsilon_{(\varphi)} \cdot V_{(\varphi)} \cdot C_{i(\varphi)} \cdot E_{i(\varphi)} + (1 - \varepsilon_{(\varphi)}) V_{(\varphi)} \cdot \rho_{Solids} \cdot E_{Solids(\varphi)} \right) \right]
\end{aligned} \tag{G.4}$$

where U_I , U_{SR} and U_{Cool} are the interphase, surroundings and cooling heat transfer coefficients respectively. $T_{(\varphi)}$ represents the temperature, $E_{i(\varphi)}$ is the internal energy of species i , $E_{Solids(\varphi)}$ is the internal energy of the solids in pseudo-phase (φ) and $v_{Solids(\varphi)}$ is the volumetric flow rate of solids.

The fundamental thermodynamic relation, $E_{i(\varphi)} = H_{i(\varphi)} - P \cdot V_{i(\varphi)}$, is introduced. Assuming that the residual value of the internal energy (i.e. $-\frac{d}{dt} \sum_{i=1}^{N_C} C_{i(\varphi)} \cdot P \cdot V_{i(\varphi)}$) is negligible and expanding the time derivative we obtain:

$$\begin{aligned}
& \left[V_{(\varphi)} \cdot \sum_{\substack{n=1 \\ n \neq \varphi}}^{N_{\varphi}} a_{I(n \rightarrow \varphi)} U_I \cdot (T_{(n)} - T_{(\varphi)}) + U_{SR} \cdot V_{(\varphi)} \cdot a_{SR} \cdot (T_{\infty} - T_S) + \epsilon_M \cdot V_{(\varphi)} \cdot a_{SR} \cdot \sigma \cdot (T_{\infty}^4 - T_S^4) + U_{Cool} \cdot V_{(\varphi)} \cdot a_{Cool} \cdot (T_{Cool} - T_{(\varphi)}) \right] \\
& - \left[\dot{W}_s \right] + \left[\sum_{k=1}^{N_i} \left(\sum_{i=1}^{NC} v_{f(\varphi)_k} \cdot C_{if(\varphi)_k} \cdot H_{if(\varphi)_k} + v_{fSolids(\varphi)_k} \cdot \rho_{Solids} \cdot H_{fSolids(\varphi)_k} \right) - \sum_{l=1}^{N_o} \left(\sum_{i=1}^{NC} v_{f(\varphi)_l} \cdot C_{i(\varphi)} \cdot H_{i(\varphi)} + v_{Solids(\varphi)_l} \cdot \rho_{Solids} \cdot E_{Solids(\varphi)} \right) \right] \\
& = \left[\sum_{i=1}^{NC} \epsilon_{(\varphi)} \cdot V_{(\varphi)} \cdot C_{i(\varphi)} \cdot \frac{d}{dt} (H_{i(\varphi)}) + \sum_{i=1}^{NC} H_{i(\varphi)} \cdot \frac{d}{dt} (\epsilon_{(\varphi)} \cdot V_{(\varphi)} \cdot C_{i(\varphi)}) \right] \\
& + \left[(1 - \epsilon_{(\varphi)}) V_{(\varphi)} \cdot \rho_{Solids} \cdot \frac{d}{dt} (H_{Solids(\varphi)}) + H_{Solids(\varphi)} \cdot \frac{d}{dt} ((1 - \epsilon_{(\varphi)}) V_{(\varphi)} \cdot \rho_{Solids}) \right]
\end{aligned} \tag{G.5}$$

where $H_{i(\varphi)}$ is the enthalpy of species i and $H_{Solids(\varphi)}$ is the enthalpy of solids in pseudo-phase (φ) .

Next we substitute $\frac{d}{dt} (\epsilon_{(\varphi)} \cdot V_{(\varphi)} \cdot C_{i(\varphi)})$ from Equation G.1 and add it to Equation G.5. Using the definition of heat of reaction (ΔH_{RXj}) and rearranging, we obtain:

$$\begin{aligned}
& V_{(\varphi)} \cdot \sum_{\substack{n=1 \\ n \neq \varphi}}^{N_{\varphi}} a_{I(n \rightarrow \varphi)} U_I \cdot (T_{(n)} - T_{(\varphi)}) + U_{SR} \cdot V_{(\varphi)} \cdot a_{SR} \cdot (T_{\infty} - T_S) + \epsilon_M \cdot V_{(\varphi)} \cdot a_{SR} \cdot \sigma \cdot (T_{\infty}^4 - T_S^4) + U_{Cool} \cdot V_{(\varphi)} \cdot a_{Cool} \cdot (T_{Cool} - T_{(\varphi)}) \\
& - \dot{W}_s - \sum_{k=1}^{N_i} \left(\sum_{i=1}^{NC} v_{f(\varphi)_k} \cdot C_{if(\varphi)} \cdot (H_{i(\varphi)} - H_{if(\varphi)}) \right) + V_{(\varphi)} \cdot \sum_{j=1}^{N_R} (-\Delta H_{RXj}) \Omega_{j(\varphi)} \cdot a_{j(\varphi)} \cdot r_{j(\varphi)} \\
& = \sum_{i=1}^{NC} \epsilon_{(\varphi)} \cdot V_{(\varphi)} \cdot C_{i(\varphi)} \cdot \frac{d}{dt} (H_{i(\varphi)}) + (1 - \epsilon_{(\varphi)}) V_{(\varphi)} \cdot \rho_{Solids} \cdot \frac{d}{dt} (H_{Solids(\varphi)}) + H_{Solids(\varphi)} \cdot \frac{d}{dt} ((1 - \epsilon_{(\varphi)}) V_{(\varphi)} \cdot \rho_{Solids}) \\
& + \sum_{i=1}^{NC} H_{i(\varphi)} \left(V_{(\varphi)} \cdot \sum_{\substack{n=1 \\ n \neq \varphi}}^{N_{\varphi}} a_{I(n \rightarrow \varphi)} \cdot k_{c_i} \cdot (C_{i(n)} - C_{i(\varphi)}) \right) + \left(\sum_{k=1}^{N_i} (v_{fSolids(\varphi)_k} \cdot \rho_{Solids} \cdot H_{fSolids(\varphi)_k}) - \sum_{l=1}^{N_o} (v_{Solids(\varphi)_l} \cdot \rho_{Solids} \cdot H_{Solids(\varphi)_l}) \right)
\end{aligned} \tag{G.6}$$

The following expression is obtained after introducing the definition of enthalpy and control indices β_m to facilitate future simplifications:

$$\begin{aligned}
& \beta_1 \cdot V_{(\varphi)} \cdot \sum_{\substack{n=1 \\ n \neq \varphi}}^{N_\varphi} a_{I(n \rightarrow \varphi)} U_I \cdot (T_{(n)} - T_{(\varphi)}) + \beta_2 \cdot U_{SR} \cdot V_{(\varphi)} \cdot a_{SR} \cdot (T_\infty - T_S) + \beta_3 \cdot \epsilon_M \cdot V_{(\varphi)} \cdot a_{SR} \cdot \sigma \cdot (T_\infty^4 - T_S^4) \\
& + \beta_4 \cdot U_{Cool} \cdot V_{(\varphi)} \cdot a_{Cool} \cdot (T_{Cool} - T_{(\varphi)}) - \beta_5 \cdot W_s - \beta_6 \cdot \sum_{k=1}^{N_I} \left(\sum_{i=1}^{NC} v_{f(\varphi)_k} \cdot C_{p_{i(\varphi)}} \cdot (T_{(\varphi)} - T_{f(\varphi)_k}) \right) \\
& + \beta_7 \cdot V_{(\varphi)} \cdot \sum_{j=1}^{N_R} (-\Delta H_{RXj}) \Omega_{j(\varphi)} \cdot a_{j(\varphi)} \cdot r_{j(\varphi)} = \beta_8 \cdot \sum_{i=1}^{NC} \epsilon_{(\varphi)} \cdot V_{(\varphi)} \cdot C_{p_{i(\varphi)}} \cdot \frac{d}{dt} (T_{(\varphi)}) \\
& + \beta_9 \cdot \left((1 - \epsilon_{(\varphi)}) V_{(\varphi)} \cdot \rho_{Solids} \cdot C_{p_{Solids(\varphi)}} \cdot \frac{d}{dt} (T_{(\varphi)}) + C_{p_{Solids(\varphi)}} \cdot T_{(\varphi)} \cdot \frac{d}{dt} \left((1 - \epsilon_{(\varphi)}) V_{(\varphi)} \cdot \rho_{Solids} \right) \right) \\
& - \beta_{10} \cdot \left(\sum_{k=1}^{N_I} \left(v_{f_{Solids(\varphi)_k}} \cdot \rho_{Solids} \cdot C_{p_{Solids(\varphi)}} \cdot T_{f(\varphi)_k} \right) - \sum_{l=1}^{N_O} \left(v_{Solids(\varphi)_l} \cdot \rho_{Solids} \cdot C_{p_{Solids(\varphi)}} \cdot T_{(\varphi)} \right) \right) \\
& + \beta_{11} \cdot \sum_{i=1}^{NC} C_{p_{i(\varphi)}} \cdot T_{(\varphi)} \cdot \left(V_{(\varphi)} \cdot \sum_{\substack{n=1 \\ n \neq \varphi}}^{N_\varphi} a_{I(n \rightarrow \varphi)} \cdot k_{c_i} \cdot (C_{i(n)} - C_{i(\varphi)}) \right)
\end{aligned} \tag{G.7}$$

where $C_{p_{i(\varphi)}}$ is the heat capacity of species i in pseudo-phase (φ) .

The energy balance is re-written in terms of molar flow-rates in order to account for changes in volume or molar flow rate/number:

$$\begin{aligned}
& \beta_1 \cdot V_{(\varphi)} \cdot \sum_{\substack{n=1 \\ n \neq \varphi}}^{N_\varphi} a_{I(n \rightarrow \varphi)} U_I \cdot (T_{(n)} - T_{(\varphi)}) + \beta_2 \cdot U_{SR} \cdot V_{(\varphi)} \cdot a_{SR} \cdot (T_\infty - T_S) + \beta_3 \cdot \epsilon_M \cdot V_{(\varphi)} \cdot a_{SR} \cdot \sigma \cdot (T_\infty^4 - T_S^4) \\
& + \beta_4 \cdot U_{Cool} \cdot V_{(\varphi)} \cdot a_{Cool} \cdot (T_{Cool} - T_{(\varphi)}) - \beta_5 \cdot W_s - \beta_6 \cdot \sum_{k=1}^{N_I} \left(\sum_{i=1}^{NC} F_{if(\varphi)_k} \cdot C_{p_{i(\varphi)}} \cdot (T_{(\varphi)} - T_{f(\varphi)_k}) \right) \\
& + \beta_7 \cdot V_{(\varphi)} \cdot \sum_{j=1}^{N_R} (-\Delta H_{RXj}) \Omega_{j(\varphi)} \cdot a_{j(\varphi)} \cdot r_{j(\varphi)} = \beta_8 \cdot \sum_{i=1}^{NC} \epsilon_{(\varphi)} \cdot V_{(\varphi)} \cdot \left(\frac{F_{i(\varphi)}}{v_{(\varphi)}} \right) \cdot C_{p_{i(\varphi)}} \cdot \frac{d}{dt} (T_{(\varphi)}) \\
& + \beta_9 \cdot \left((1 - \epsilon_{(\varphi)}) V_{(\varphi)} \cdot \rho_{Solids} \cdot C_{p_{Solids(\varphi)}} \cdot \frac{d}{dt} (T_{(\varphi)}) + C_{p_{Solids(\varphi)}} \cdot T_{(\varphi)} \cdot \frac{d}{dt} \left((1 - \epsilon_{(\varphi)}) V_{(\varphi)} \cdot \rho_{Solids} \right) \right) \\
& - \beta_{10} \cdot \left(\sum_{k=1}^{N_I} \left(v_{f_{Solids(\varphi)_k}} \cdot \rho_{Solids} \cdot C_{p_{Solids(\varphi)}} \cdot T_{f(\varphi)_k} \right) - \sum_{l=1}^{N_O} \left(v_{Solids(\varphi)_l} \cdot \rho_{Solids} \cdot C_{p_{Solids(\varphi)}} \cdot T_{(\varphi)} \right) \right) \\
& + \beta_{11} \cdot \sum_{i=1}^{NC} C_{p_{i(\varphi)}} \cdot T_{(\varphi)} \cdot \left(V_{(\varphi)} \cdot \sum_{\substack{n=1 \\ n \neq \varphi}}^{N_\varphi} a_{I(n \rightarrow \varphi)} \cdot k_{c_i} \cdot \left(\frac{F_{i(n)}}{v_{(n)}} - \frac{F_{i(\varphi)}}{v_{(\varphi)}} \right) \right)
\end{aligned} \tag{G.8}$$

G.2.1.3. Initial conditions

Except when there is steady-state, the initial conditions to solve this set of ODEs must be specified, i.e. we need to specify the concentrations and temperature inside the reactor at $t=0$.

G.2.1.4. Simplifications

The general model for lumped systems consists of two main balances (Equations G.2 and G.7). These general mole and energy balances can be simplified in many special cases by means of control indexes. Some common simplification strategies are listed below. In real problems, a combination of these simplifications is commonly applicable:

a) Continuous stirred tank reactor (CSTR)

In this case the change in total volume is negligible: Set $\alpha_6 = 0$.

b) Fluid pseudo-phase (No solids)

In this case the void fraction $\varepsilon_{(\varphi)} = 1$. Also set $\beta_9 = \beta_{10} = 0$

c) Batch reactor (Closed system)

Set $\alpha_1 = \alpha_2 = \beta_6 = 0$. If the change in total reactor volume is negligible: Set $\alpha_6 = 0$.

d) Semi-batch reactor (No output)

Set $\alpha_2 = 0$ and $\frac{d}{dt}(\varepsilon_{(\varphi)} \cdot V_{(\varphi)}) = v_{f(\varphi)}$.

e) Steady state operation

Set $\alpha_5 = \alpha_6 = \beta_8 = 0$.

f) Isothermal system

Set $T_{(\varphi)} = T_{f(\varphi)}$. There is no need for an energy balance.

g) Adiabatic operation

Set $\beta_2 = \beta_3 = \beta_4 = 0$.

h) Isolated system

This means that the system is *adiabatic* and *closed*, as seen in c) and g).

i) Single phase

Set $N_\varphi = 1$ or $\alpha_4 = \beta_1 = \beta_{11} = 0$ (For multi-phase systems it is necessary to account for mass and heat transfer between phases).

j) Single reaction

Set $N_R = 1$.

k) Single input/output

Set $N_I = 1$ or/and $N_O = 1$.

l) Appreciable change in number of moles

Equations G.3 and G.8 should be utilized in order to work with molar flows as state variables.

G.2.2. Distributed Systems (Plug Flow Reactors, Packed Beds, Fluidized-Beds, etc)

In order to account for axial variation, we implement the balances developed in the previous section with the addition of axial dispersion into a differential control volume of length Δz :

G.2.2.1. Mole balance

The mole balances for each species in pseudo-phase (φ) (Figure G.2):

$[Convective\ input - Convective\ output]_{(\varphi)} + [Diffusive\ input - Diffusive\ output]_{(\varphi)} + [Chemical\ reaction\ generation/consumption]_{(\varphi)} + [Exchange\ with\ other\ pseudo-phases]_{(\varphi)} = [Molar\ accumulation\ rate]_{(\varphi)}$

Initially the mole balance is developed in terms of concentrations:

$$\begin{aligned}
 & \left[\left(v_{(\varphi)} \cdot C_{i(\varphi)} \right)_{(z)} - \left(v_{(\varphi)} \cdot C_{i(\varphi)} \right)_{(z+\Delta z)} \right] + \varepsilon_{(\varphi)} \cdot A_{(\varphi)} \cdot \left[\left(N_{i(\varphi)} \right)_{(z)} - \left(N_{i(\varphi)} \right)_{(z+\Delta z)} \right] \\
 & + \left[A_{(\varphi)} \cdot \Delta z \cdot \sum_{j=1}^{N_R} v_{ij} \cdot \Omega_{j(\varphi)} \cdot a_{j(\varphi)} \cdot r_{j(\varphi)} \right] + \left[A_{(\varphi)} \cdot \Delta z \cdot \sum_{\substack{n=1 \\ n \neq \varphi}}^{N_\varphi} a_{I(n \rightarrow \varphi)} \cdot k_{c_i} \cdot \left(C_{i(n)} - C_{i(\varphi)} \right) \right] \quad \text{(G.9)} \\
 & = \left[\varepsilon_{(\varphi)} \cdot A_{(\varphi)} \cdot \Delta z \cdot \frac{d}{dt} \left(C_{i(\varphi)} \right) \right]
 \end{aligned}$$

$$i = 1, 2, \dots, N_C$$

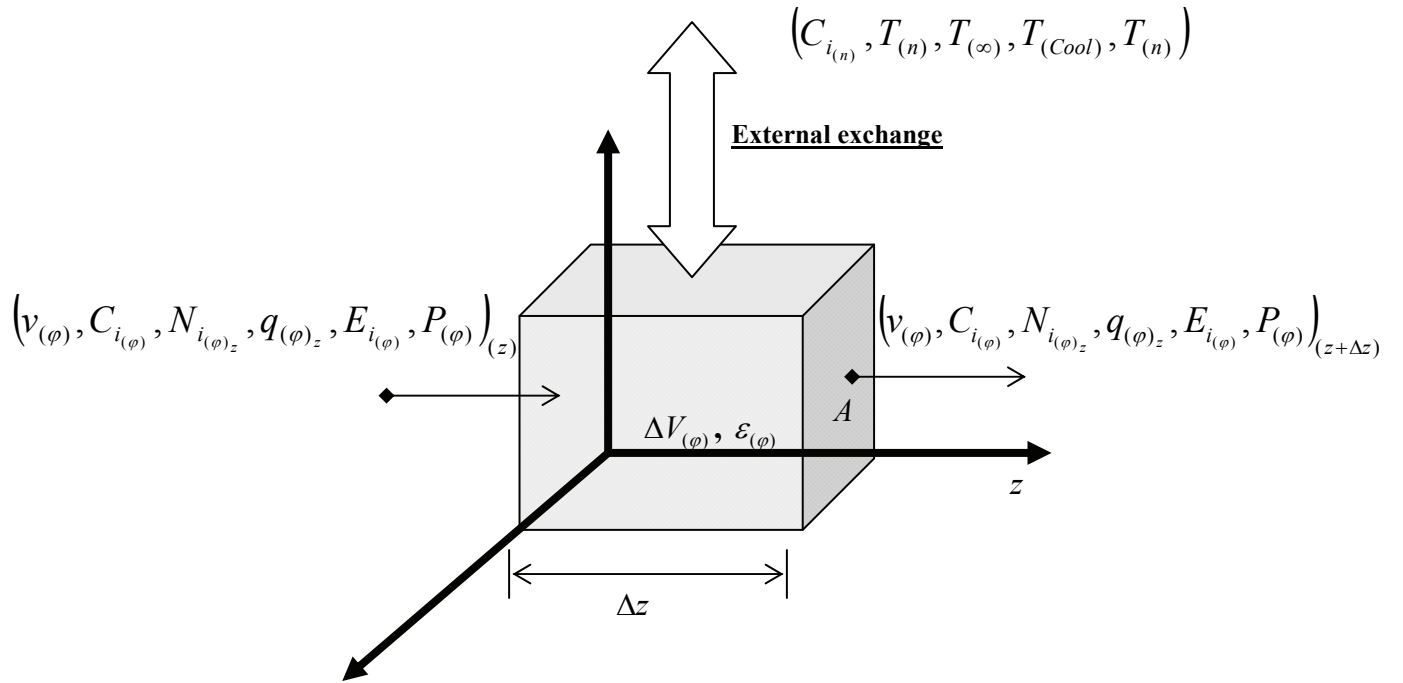


Figure G. 2. Mole and energy balances for distributed systems.

Replacing the diffusive mass flux by its corresponding Fickian form

$$\left(N_{i(\varphi)} = -D_{i(\varphi)} \cdot \frac{\partial C_{i(\varphi)}}{\partial z} \right), \text{ dividing by } \Delta z \text{ and taking the limit as } \Delta z \rightarrow 0 \text{ (with } \Delta V = A_{(\varphi)} \cdot \Delta z \text{) the}$$

following expression is obtained:

$$\begin{aligned} & -\frac{1}{A_{(\varphi)}} \cdot \frac{\partial}{\partial z} (v_{(\varphi)} \cdot C_{i(\varphi)}) + \varepsilon_{(\varphi)} \cdot \frac{\partial}{\partial z} \left(D_{i(\varphi)} \cdot \frac{\partial C_{i(\varphi)}}{\partial z} \right) + \sum_{j=1}^{N_R} v_{ij} \cdot \Omega_{j(\varphi)} \cdot a_{j(\varphi)} \cdot r_{j(\varphi)} \\ & + \sum_{\substack{n=1 \\ n \neq \varphi}}^{N_\varphi} a_{I(n \rightarrow \varphi)} \cdot k_{c_i} \cdot (C_{i(n)} - C_{i(\varphi)}) = \frac{\partial}{\partial t} (\varepsilon_{(\varphi)} \cdot C_{i(\varphi)}) \end{aligned} \quad (\text{G.10})$$

$$i = 1, 2, \dots, N_C$$

where $D_{i(\varphi)}$ is the diffusion coefficient of species i in pseudo-phase (φ) . The following expressions are obtained after expanding the time derivatives and introducing control indices α_m to allow for future simplifications:

$$\begin{aligned}
& -\alpha_1 \cdot \frac{1}{A_{(\varphi)}} \cdot \frac{\partial}{\partial z} (v_{(\varphi)} \cdot C_{i_{(\varphi)}}) + \alpha_2 \cdot \varepsilon_{(\varphi)} \cdot \frac{\partial}{\partial z} \left(D_{i_{(\varphi)}} \cdot \frac{\partial C_{i_{(\varphi)}}}{\partial z} \right) + \alpha_3 \cdot \sum_{j=1}^{N_R} v_{ij} \cdot \Omega_{j_{(\varphi)}} \cdot a_{j_{(\varphi)}} \cdot r_{j_{(\varphi)}} \\
& + \alpha_4 \cdot \sum_{\substack{n=1 \\ n \neq \varphi}}^{N_\varphi} a_{I_{(n \rightarrow \varphi)}} \cdot k_{c_i} \cdot (C_{i_{(n)}} - C_{i_{(\varphi)}}) = \alpha_5 \cdot \varepsilon_{(\varphi)} \cdot \frac{\partial}{\partial t} (C_{i_{(\varphi)}})
\end{aligned} \tag{G.11}$$

$$i = 1, 2, \dots, N_C$$

Alternatively, the mole balances can be expressed in terms of molar flow-rates in order to account for changes in volume/number of moles:

$$\begin{aligned}
& -\alpha_1 \cdot \frac{1}{A_{(\varphi)}} \cdot \frac{\partial}{\partial z} (F_{i_{(\varphi)}}) + \alpha_2 \cdot \frac{\partial}{\partial z} \left(D_{i_{(\varphi)}} \cdot \frac{\partial}{\partial z} \left(\frac{F_{i_{(\varphi)}}}{v_{(\varphi)}} \right) \right) + \alpha_3 \cdot \sum_{j=1}^{N_R} v_{ij} \cdot \Omega_{j_{(\varphi)}} \cdot a_{j_{(\varphi)}} \cdot r_{j_{(\varphi)}} \\
& + \alpha_4 \cdot \sum_{\substack{n=1 \\ n \neq \varphi}}^{N_\varphi} a_{I_{(n \rightarrow \varphi)}} \cdot k_{c_i} \cdot \left(\frac{F_{i_{(n)}}}{v_{(n)}} - \frac{F_{i_{(\varphi)}}}{v_{(\varphi)}} \right) = \alpha_5 \cdot \varepsilon_{(\varphi)} \cdot \frac{\partial}{\partial t} \left(\frac{F_{i_{(\varphi)}}}{v_{(\varphi)}} \right)
\end{aligned} \tag{G.12}$$

$$i = 1, 2, \dots, N_C$$

G.2.2.2. Energy balance

The energy balance based on the first law of thermodynamics for pseudo-phase (φ) (Figure G.2) can be written:

$$\begin{aligned}
& \text{[Rate of flow of heat to the system]}_{(\varphi)} - \text{[Rate of work done by the system]}_{(\varphi)} + \text{[Energy input} \\
& \text{by mass flow - Energy output by mass flow]}_{(\varphi)} + \text{[Chemical reaction heat} \\
& \text{generation/consumption]}_{(\varphi)} + \text{[Diffusive heat input - Diffusive heat output]}_{(\varphi)} = \text{[Heat} \\
& \text{accumulation rate]}_{(\varphi)}
\end{aligned}$$

Initially the mole balance is developed in terms of concentrations and internal energy:

$$\begin{aligned}
& \left[A_{(\varphi)} \cdot \Delta z \cdot \sum_{\substack{n=1 \\ n \neq \varphi}}^{N_\varphi} a_{I_{(n \rightarrow \varphi)}} \cdot U_{I_{(n)}} \cdot (T_{(n)} - T_{(\varphi)}) + U_{SR} \cdot A_{(\varphi)} \cdot \Delta z \cdot a_{SR} \cdot (T_\infty - T_S) + \varepsilon_M \cdot A_{(\varphi)} \cdot \Delta z \cdot a_{SR} \cdot \sigma \cdot (T_\infty^4 - T_S^4) + U_{Cool} \cdot A_{(\varphi)} \cdot \Delta z \cdot a_{Cool} \cdot (T_{Cool} - T_{(\varphi)}) \right] \\
& - \left[A_{(\varphi)} \cdot \Delta z \cdot W_s \right] + \left[\left(\sum_{i=1}^{N_C} v_{(\varphi)} \cdot C_{i_{(\varphi)}} \cdot E_{i_{(\varphi)}} + v_{Solids(\varphi)} \cdot \rho_{Solids} \cdot E_{Solids(\varphi)} \right)_{(z)} - \left(\sum_{i=1}^{N_C} v_{(\varphi)} \cdot C_{i_{(\varphi)}} \cdot E_{i_{(\varphi)}} + v_{Solids(\varphi)} \cdot \rho_{Solids} \cdot E_{Solids(\varphi)} \right)_{(z+\Delta z)} \right] \\
& + \left[A_{(\varphi)} \cdot \Delta z \cdot \sum_{j=1}^{N_R} (-\Delta H_{RXj}) \cdot \Omega_{j_{(\varphi)}} \cdot a_{j_{(\varphi)}} \cdot r_{j_{(\varphi)}} \right] + A_{(\varphi)} \cdot \left[(q_{(\varphi)})_{(z)} - (q_{(\varphi)})_{(z+\Delta z)} \right] \\
& = \left[\frac{d}{dt} \left(\varepsilon_{(\varphi)} \cdot A_{(\varphi)} \cdot \Delta z \cdot \sum_{i=1}^{N_C} C_{i_{(\varphi)}} \cdot E_{i_{(\varphi)}} + (1 - \varepsilon_{(\varphi)}) \cdot A_{(\varphi)} \cdot \Delta z \cdot \rho_{Solids} \cdot E_{Solids(\varphi)} \right) \right]
\end{aligned} \tag{G.13}$$

$$(G.13)$$

Replacing the diffusive heat flux by its corresponding Fourier form $\left(q_{(\varphi)} = -K_{(\varphi)} \cdot \frac{\partial T_{(\varphi)}}{\partial z} \right)$,

dividing by Δz and taking the limit as $\Delta z \rightarrow 0$ (with $\Delta V = A_{(\varphi)} \cdot \Delta z$), we obtain:

$$\begin{aligned} & \sum_{\substack{n=1 \\ n \neq \varphi}}^{N_\varphi} a_{I_{(n-\varphi)}} U_{I_{(n-\varphi)}} (T_{(n)} - T_{(\varphi)}) + U_{SR} \cdot a_{SR} \cdot (T_\infty - T_S) + \epsilon_M \cdot a_{SR} \cdot \sigma \cdot (T_\infty^4 - T_S^4) + U_{Cool} \cdot a_{Cool} \cdot (T_{Cool} - T_{(\varphi)}) - \dot{w}_s \\ & - \frac{1}{A_{(\varphi)}} \cdot \frac{\partial}{\partial z} \left(\sum_{i=1}^{NC} v_{(\varphi)} \cdot C_{i(\varphi)} \cdot E_{i(\varphi)} + v_{Solids(\varphi)} \cdot \rho_{Solids} \cdot E_{Solids(\varphi)} \right) + \sum_{j=1}^{N_R} (-\Delta H_{RX j}) \Omega_{j(\varphi)} \cdot a_{j(\varphi)} \cdot r_{j(\varphi)} + \frac{\partial}{\partial z} \left(K_{(\varphi)} \cdot \frac{\partial T_{(\varphi)}}{\partial z} \right) \quad (\text{G.14}) \\ & = \frac{\partial}{\partial t} \left(\sum_{i=1}^{NC} \epsilon_{(\varphi)} \cdot C_{i(\varphi)} \cdot E_{i(\varphi)} + (1 - \epsilon_{(\varphi)}) \cdot \rho_{Solids} \cdot E_{Solids(\varphi)} \right) \end{aligned}$$

where $K_{(\varphi)}$ is the thermal conductivity of pseudo-phase (φ) .

After plugging in the fundamental thermodynamic relation: $E_{i(\varphi)} = H_{i(\varphi)} - P \cdot V_{i(\varphi)}$, assuming that the residual value of the internal energy (i.e. $-\frac{d}{dt} \sum_{i=1}^{NC} C_{i(\varphi)} \cdot P \cdot V_{i(\varphi)}$) is negligible and expanding the time derivative, we may write:

$$\begin{aligned} & \sum_{\substack{n=1 \\ n \neq \varphi}}^{N_\varphi} a_{I_{(n-\varphi)}} U_{I_{(n-\varphi)}} (T_{(n)} - T_{(\varphi)}) + U_{SR} \cdot a_{SR} \cdot (T_\infty - T_S) + \epsilon_M \cdot a_{SR} \cdot \sigma \cdot (T_\infty^4 - T_S^4) + U_{Cool} \cdot a_{Cool} \cdot (T_{Cool} - T_{(\varphi)}) - \dot{w}_s \\ & - \frac{1}{A_{(\varphi)}} \cdot \frac{\partial}{\partial z} \left(\sum_{i=1}^{NC} v_{(\varphi)} \cdot C_{i(\varphi)} \cdot H_{i(\varphi)} + v_{Solids(\varphi)} \cdot \rho_{Solids} \cdot H_{Solids(\varphi)} \right) + \sum_{j=1}^{N_R} (-\Delta H_{RX j}) \Omega_{j(\varphi)} \cdot a_{j(\varphi)} \cdot r_{j(\varphi)} + \frac{\partial}{\partial z} \left(K_{(\varphi)} \cdot \frac{\partial T_{(\varphi)}}{\partial z} \right) \quad (\text{G.15}) \\ & = \epsilon_{(\varphi)} \cdot \sum_{i=1}^{NC} C_{i(\varphi)} \cdot \frac{\partial}{\partial t} (H_{i(\varphi)}) + \epsilon_{(\varphi)} \cdot \sum_{i=1}^{NC} H_{i(\varphi)} \cdot \frac{\partial}{\partial t} (C_{i(\varphi)}) + \frac{\partial}{\partial t} ((1 - \epsilon_{(\varphi)}) \cdot \rho_{Solids} \cdot H_{Solids(\varphi)}) \end{aligned}$$

The following expression is obtained after introducing the definition of enthalpy and the control indices β_m to facilitate future simplifications:

$$\begin{aligned} & \beta_1 \cdot \sum_{\substack{n=1 \\ n \neq \varphi}}^{N_\varphi} a_{I_{(n-\varphi)}} U_{I_{(n-\varphi)}} (T_{(n)} - T_{(\varphi)}) + \beta_2 \cdot U_{SR} \cdot a_{SR} \cdot (T_\infty - T_S) + \beta_3 \cdot \epsilon_M \cdot a_{SR} \cdot \sigma \cdot (T_\infty^4 - T_S^4) + \beta_4 \cdot U_{Cool} \cdot a_{Cool} \cdot (T_{Cool} - T_{(\varphi)}) \\ & - \beta_5 \cdot \dot{w}_s - \beta_6 \cdot \frac{1}{A_{(\varphi)}} \cdot \frac{\partial}{\partial z} \left(\sum_{i=1}^{NC} v_{(\varphi)} \cdot C_{i(\varphi)} \cdot H_{i(\varphi)} \right) + \beta_7 \cdot \sum_{j=1}^{N_R} (-\Delta H_{RX j}) \Omega_{j(\varphi)} \cdot a_{j(\varphi)} \cdot r_{j(\varphi)} + \beta_8 \cdot \frac{\partial}{\partial z} \left(K_{(\varphi)} \cdot \frac{\partial T_{(\varphi)}}{\partial z} \right) \quad (\text{G.16}) \\ & = \beta_9 \cdot \epsilon_{(\varphi)} \cdot \sum_{i=1}^{NC} C_{i(\varphi)} \cdot \frac{\partial}{\partial t} (H_{i(\varphi)}) + \beta_{10} \cdot \epsilon_{(\varphi)} \cdot \sum_{i=1}^{NC} H_{i(\varphi)} \cdot \frac{\partial}{\partial t} (C_{i(\varphi)}) + \beta_{11} \cdot \frac{1}{A_{(\varphi)}} \cdot \frac{\partial}{\partial z} (v_{Solids(\varphi)} \cdot \rho_{Solids} \cdot H_{Solids(\varphi)}) \\ & + \beta_{12} \cdot \frac{\partial}{\partial t} ((1 - \epsilon_{(\varphi)}) \cdot \rho_{Solids} \cdot H_{Solids(\varphi)}) \end{aligned}$$

The energy balance can again be expressed in terms of molar flow-rates, in order to facilitate accounting for changes in volume and number of moles:

$$\begin{aligned}
& \beta_1 \cdot \sum_{\substack{n=1 \\ n \neq \varphi}}^{N_\varphi} a_{I(n-\varphi)} U_I (T_{(n)} - T_{(\varphi)}) + \beta_2 \cdot U_{SR} \cdot a_{SR} (T_\infty - T_S) + \beta_3 \cdot \epsilon_M \cdot a_{SR} \cdot \sigma (T_\infty^4 - T_S^4) + \beta_4 \cdot U_{Cool} \cdot a_{Cool} (T_{Cool} - T_{(\varphi)}) \\
& - \beta_5 \cdot \dot{w}_s - \beta_6 \cdot \frac{1}{A_{(\varphi)}} \cdot \frac{\partial}{\partial z} \left(\sum_{i=1}^{NC} F_{i(\varphi)} \cdot C_{P_{i(\varphi)}} \cdot T_{(\varphi)} \right) + \beta_7 \cdot \sum_{j=1}^{N_R} (-\Delta H_{RXj}) \Omega_{j(\varphi)} \cdot a_{j(\varphi)} \cdot r_{j(\varphi)} + \beta_8 \cdot \frac{\partial}{\partial z} \left(K_{(\varphi)} \cdot \frac{\partial T_{(\varphi)}}{\partial z} \right) \\
& = \beta_9 \cdot \epsilon_{(\varphi)} \cdot \sum_{i=1}^{NC} \left(\frac{F_{i(\varphi)}}{v_{(\varphi)}} \right) \cdot \frac{\partial}{\partial t} (C_{P_{i(\varphi)}} \cdot T_{(\varphi)}) + \beta_{10} \cdot \epsilon_{(\varphi)} \cdot \sum_{i=1}^{NC} C_{P_{i(\varphi)}} \cdot T_{(\varphi)} \cdot \frac{\partial}{\partial t} \left(\frac{F_{i(\varphi)}}{v_{(\varphi)}} \right) + \beta_{11} \frac{1}{A_{(\varphi)}} \cdot \frac{\partial}{\partial z} (v_{Solids(\varphi)} \cdot \rho_{Solids} \cdot C_{P_{Solids(\varphi)}} \cdot T_{(\varphi)}) \\
& + \beta_{12} \frac{\partial}{\partial t} \left((1 - \epsilon_{(\varphi)}) \cdot \rho_{Solids} \cdot C_{P_{Solids(\varphi)}} \cdot T_{(\varphi)} \right)
\end{aligned} \tag{G.17}$$

G.2.2.3. Initial and boundary conditions

The initial conditions for solving this set of partial differential equations include specification of the concentrations and temperature inside the reactor at $t=0$. The boundary conditions for distributed systems depend on the degree of complexity in the balance equations. The boundary conditions may assume axial symmetry, zero flux at the walls and/or Danckwerts (1953) criteria when diffusion in the fore and aft sections is negligible.

G.2.2.4. Simplifications

The general model for distributed systems consists of two main balances (Equation G.11 and G.16). These general mole and energy balances can be simplified to special cases using the control indexes. Some common simplifications are listed below. In real problems, a combination of these simplifications is commonly appropriate.

a) Plug flow reactor (PFR)

If axial dispersion is negligible, set $\alpha_2 = 0$.

b) Fluid pseudo-phase (No solids)

In this case the void fraction $\epsilon_{(\varphi)} = 1$. Also set $\beta_{11} = \beta_{12} = 0$.

c) Packed bed reactor (PBR)

If axial dispersion is negligible, set $\alpha_2 = 0$. Everything should be expressed per unit mass of catalyst. This can be accomplished by using r_j' , which can be calculated by: $r_j = \rho_{cat} \cdot (1 - \epsilon_{(\varphi)}) r_j'$. Special attention should be paid to the reactor pressure drop as discussed in section G.2.3, below.

d) Fluidized bed reactor (FBR)

This type of reactor is very complex to model, but a simple modeling approach can be based on the above development. At least two phases should be considered, i.e. $N_\phi = 2$. Two sets of balances should be carried out for the high and low-density phases. Many hydrodynamic considerations must be included. For catalytic fluidized bed reactions $r_j = \rho_{cat} \cdot (1 - \varepsilon_{(\phi)}) r'_j$.

e) Steady state operation

Set $\alpha_5 = \beta_9 = \beta_{10} = 0$. The governing equations then become ordinary differential equations.

f) Isothermal system

Set $T_{(\phi)} = T_{f(\phi)}$. There is no longer any need for an energy balance.

g) Adiabatic operation

Set $\beta_2 = \beta_3 = \beta_4 = 0$.

h) No shaft work

Set $\beta_5 = 0$.

i) Single phase

Set $N_\phi = 1$ or $\alpha_4 = \beta_1 = 0$. For multi-phase systems should account for mass and heat transfer between phases.

j) Single reaction

Set $N_R = 1$.

k) Appreciable change in number of moles

Equations G.12 and G.17 should be used to work with molar flows, rather than concentrations as state variables.

G.2.3. Additional Relations

Predicting the behaviour of reaction engineering systems requires information or assumptions with respect to: reaction kinetics and stoichiometry, thermodynamics, flow patterns, heat and

mass transfer, reactor size and geometry, etc. Several useful relations, some of which may be included in the above balances are:

a) Pressure in lumped systems:

For a lumped system the pressure is assumed to be constant.

b) Pressure balance in distributed systems:

For distributed systems there are many different ways to calculate the pressure drop. For homogeneous pipe flow, empirical relations representing the Moody friction factor diagram are most useful. The Ergun equation should be used for packed beds. For fluidized beds, the pressure drop is assumed to be equal to the weight (less buoyancy) per unit cross-sectional area.

c) Concentration of species i in pseudo-phase (φ):

$$C_{i(\varphi)} = \left(\frac{F_{i(\varphi)}}{v_{(\varphi)}} \right)$$

d) Volumetric flow-rate for gases:

$$v_{(\varphi)} = v_{f(\varphi)} \cdot \left(\frac{F_{T(\varphi)}}{F_{T(\varphi)f}} \right) \cdot \left(\frac{T_{(\varphi)}}{T_{(\varphi)f}} \right) \cdot \left(\frac{P_{(\varphi)f}}{P_{(\varphi)}} \right) \cdot \left(\frac{Z_{(\varphi)}}{Z_{(\varphi)f}} \right)$$

e) Volumetric flow-rate for liquids:

$v_{(\varphi)} = v_{f(\varphi)}$ is often assumed to be constant.

f) Total molar flow-rate:

$$F_{T(\varphi)} = \sum_{i=1}^{NC} F_{i(\varphi)}$$

g) Heat of reaction as a function of temperature for reaction j :

$$\Delta H_{RXj} = \Delta H_{RXj}^0(T_R) + \int_{T_R}^T \Delta Cp_j \cdot dT$$

h) Variation of heat capacity for reaction j :

$$\Delta Cp_j = \sum_{i=1}^{NC} \nu_{ij} \cdot Cp_{i(\varphi)}$$

i) Reaction rates:

$$r_{j(\varphi)} = \text{Function}(C_{i(\varphi)})$$

j) Reaction rates for elementary reaction j:

$$r_{j(\varphi)} = k_0 \cdot e^{\left(\frac{Ea}{R \cdot T(\varphi)}\right)} \cdot \prod_{\text{Reactants}} C_{i(\varphi)}^{U_{ij}} \quad (\text{Arrhenius relation, power law kinetics}).$$

k) Empirical catalyst deactivation function such as:

$$a_{j(\varphi)} = e^{(-\alpha_c \cdot C_{c(\varphi)})}. \quad (\text{This is but one example among many}).$$

G.2.4. Summary of Mechanistic Modeling Algorithm for Reaction Engineering Systems

The following algorithm is useful in the mechanistic model of real reaction engineering systems:

- 1) Identify the system to model. Define whether it is lumped (Section G.2.1) or distributed (Section G.2.2).
- 2) For the lumped systems apply Equations G.2 and G.7. For the distributed systems apply equations G.11 and G.16.
- 3) Introduce the desired simplifications from Sections G.2.1.4 or G.2.2.4 using multidimensional control indexes.
- 4) Introduce additional relations, such as those from section G.2.3 as needed.

G.4. Conclusions

A general modeling procedure is developed for reaction engineering systems. This procedure may be employed in teaching introductory and advanced reaction engineering. It provides students with a powerful “toolkit” to tackle a wide range of academic and industrial engineering problems, as well as a starting point for research projects in this field. It should also provide better understanding of the multiple phenomena encountered in chemical/biochemical engineering systems and encourage a higher level of sophistication.

G.5. References

Danckwerts, P.V. (1953). Continuous flow systems: Distribution of residence times. *Chem. Eng. Sci.*, 2, 1-13.

Mahecha-Botero, A., Grace, J.R., Elnashaie, S.S.E.H. and Lim, C.J. (2007a). A comprehensive approach to reaction engineering. *Int. J. Chem. Reactor Eng.*, 5: A17.

APPENDIX H. PUBLICATIONS

JOURNAL PAPERS	
1.	<u>Andrés Mahecha-Botero</u> , John R. Grace, S.S.E.H. Elnashaie, C. Jim Lim. “Comprehensive modelling of gas fluidized-bed reactors allowing for transients, multiple flow regimes and selective removal of species” . <i>International Journal of Chemical Reactor Engineering (IJCRE)</i> . Vol. 4: A11 (2006).
2.	<u>Andrés Mahecha-Botero</u> , John R. Grace, S.S.E.H. Elnashaie, C. Jim Lim. “A Comprehensive approach to reaction engineering” . <i>International Journal of Chemical Reactor Engineering (IJCRE)</i> . Vol. 5: A17 (2007).
3.	Zhongxiang Chen, Friedrick Po, John R. Grace, C. Jim Lim, Said Elnashaie, <u>Andrés Mahecha-Botero</u> , M. Rakib, Yoshinori Shirasaki, Isamu Yasuda “Sorbent enhanced/membrane-assisted steam methane reforming” . <i>Chemical Engineering Science</i> . Volume 63, issue 1, pages 170-182 (2008).
4.	<u>Andrés Mahecha-Botero</u> , Tony Boyd, Ali Gulamhusein, Nicholas Comyn, C. Jim Lim, John R. Grace, Yoshinori Shirasaki, Isamu Yasuda, “Pure hydrogen generation in a fluidized-bed membrane reactor: Experimental findings” . <i>Chemical Engineering Science</i> . Vol 63, issue 10, pages 2752-2762 (2008).
5.	<u>Andrés Mahecha-Botero</u> , Zhongxiang Chen, John R. Grace, S.S.E.H. Elnashaie, C. Jim Lim, M. Rakib, Isamu Yasuda, Yoshinori Shirasaki. “Comparison of fluidized bed flow regimes for steam methane reforming in membrane reactors: A simulation study” . <i>Chemical Engineering Science</i> , In Review (2008).
6.	<u>Andrés Mahecha-Botero</u> , John R. Grace, C. Jim Lim, S.S.E.H. Elnashaie, Tony Boyd, Ali Gulamhusein. “Pure hydrogen generation in a fluidized-bed membrane reactor: Application of the generalized comprehensive reactor model” . <i>Chemical Engineering Science</i> , In Review (2009).
7.	<u>Andrés Mahecha-Botero</u> , John R. Grace, S.S.E.H. Elnashaie, C. Jim Lim “Advances in modelling of fluidized-bed catalytic reactors: A comprehensive review” . <i>Chemical Engineering Communications</i> , In Press (2009).

INTERNATIONAL CONFERENCE PROCEEDINGS	
1.	<u>Andres Mahecha-Botero</u> , S.S.E.H. Elnashaie, John R. Grace, C. Jim Lim, “FEMLAB simulations using a comprehensive model for gas fluidized-bed reactors” . In proceedings for: “COMSOL Multiphysics (FEMLAB) Conference”. Pages 103-107, (2005). http://cds.comsol.com/access/dl/papers/1179/Mahecha-Botero_paper.pdf .
2.	<u>Andres Mahecha-Botero</u> , John R. Grace, S.S.E.H. Elnashaie, C. Jim Lim, “A generalized dynamic model for fluidized-bed reactors and its application to the production of pure hydrogen” . In proceedings for: “Asian Pacific Confederation of Chemical Engineering Congress”, 11th APCCChE, (2005).

INTERNATIONAL CONFERENCE PROCEEDINGS (Cont'd)

- | | |
|----|------------------------------------------------------------------------------------------------------------------------------------------------------------------------------------------------------------------------------------------------------------------------------------------------------------------------------------------------------------------------------------------------------------------------------------------------------------------------------------------------------------------------------------------------------------|
| 3. | <p><u>Andres Mahecha-Botero</u>, John R. Grace, S.S.E.H. Elnashaie, C. Jim Lim, “Time scale analysis of a fluidized-bed reactor based on a generalized dynamic model”. In proceedings for Fluidization XII "The 12th International Conference on Fluidization - New Horizons in Fluidization Engineering", Franco Berruti, Xiaotao (Tony) Bi, Todd Pugsley, Eds, ECI Symposium Series, Volume RP4, pages 623-630, (2007). http://services.bepress.com/eci/fluidization_xii/76</p> |
|----|------------------------------------------------------------------------------------------------------------------------------------------------------------------------------------------------------------------------------------------------------------------------------------------------------------------------------------------------------------------------------------------------------------------------------------------------------------------------------------------------------------------------------------------------------------|

CONFERENCE PRESENTATIONS

- | | |
|----|------------------------------------------------------------------------------------------------------------------------------------------------------------------------------------------------------------------------------------------------------------------------------------------------------------------------------------------------------------------------------------------------------------------------------|
| 1. | <p><u>Andres Mahecha-Botero</u>, John R. Grace, S.S.E.H. Elnashaie, C. Jim Lim, “Comprehensive modelling of gas fluidized-bed reactors allowing for transients, multiple flow regimes and selective removal of species”. Oral presentation: “CRE X conference, Innovations in Chemical Reactor Engineering”, Zacatecas, Mexico. August 28 to September 2, (2005).</p> |
| 2. | <p><u>Andres Mahecha-Botero</u>, S.S.E.H. Elnashaie, John R. Grace, C. Jim Lim, “FEMLAB simulations using a comprehensive model for gas fluidized-bed reactors”. Oral presentation: “COMSOL Multiphysics (FEMLAB) Conference”, Boston, U.S.A. October 23-25, (2005).</p> |
| 3. | <p><u>Andres Mahecha-Botero</u>, John R. Grace, S.S.E.H. Elnashaie, C. Jim Lim, “A generalized dynamic model for fluidized-bed reactors and its application to the production of pure hydrogen”. Oral presentation: “Asian Pacific Confederation of Chemical Engineering Congress”, 11th APCChE. Kuala Lumpur, Malaysia. August 27-30, (2006).</p> |
| 4. | <p><u>Andrés Mahecha-Botero</u>, Tony Boyd, Ali Gulamhusein, Nicholas Comyn, C. Jim Lim, John R. Grace, Yoshinori Shirasaki, Isamu Yasuda. “Performance of a fluidized-bed membrane reactor for high-purity hydrogen production”. Poster in Fluidization XII, “The 12th International Conference on Fluidization. New Horizons in Fluidization Engineering”. Harrison Hot Springs, BC, Canada. May 13-18, (2007).</p> |
| 5. | <p><u>Andres Mahecha-Botero</u>, John R. Grace, S.S.E.H. Elnashaie, C. Jim Lim, “Time scale analysis of a fluidized-bed reactor based on a generalized dynamic model”. Oral presentation: Fluidization XII “The 12th International Conference on Fluidization. New Horizons in Fluidization Engineering”. Harrison Hot Springs, BC, Canada. May 13-18, (2007).</p> |
| 6. | <p><u>Andrés Mahecha-Botero</u>, Tony Boyd, Ali Gulamhusein, Nicholas Comyn, C. Jim Lim, John R. Grace, Yoshinori Shirasaki, Isamu Yasuda “Performance of a fluidized-bed membrane reactor for high-purity hydrogen production”. Oral presentation: “Chemical Reaction Engineering XI: Green Chemical Reactor Engineering”. Bilbao, Vizcaya, Spain. August 26-31, (2007).</p> |
| 7. | <p><u>Andrés Mahecha-Botero</u>, John R. Grace, C. Jim Lim. “H₂ production with membrane reactors”. Featured keynote presentation: “International Symposium on Green Technologies for the Production and the Sustainable Use of Energy at Instituto Tecnológico de Celaya”. Celaya, Mexico, March 25-27, (2009).</p> |